The role of AQP4 and the astrocytic endfoot in CSF-ISF exchange and brain waste clearance

By

Matthew James Simon

A Dissertation

Presented to the Neuroscience Graduate Program at
Oregon Health & Science University School of Medicine
in partial fulfillment of
the requirements for the degree of

Doctor of Philosophy

May 30th 2019

School of Medicine
Oregon Health & Science University

CERTIFICATE OF APPROVAL

This is to certify that the PhD dissertation of

Matthew James Simon

has been approved

Mentor: Jeffrey Iliff, PhD

Committee Chair: Philip Stork, PhD

Member: Vivek Unni, MD, PhD

Member: Marc Freeman, PhD

Member: Julie Saugstad, PhD

Acknowledgments

The work presented here would not have been possible without the help of many people. First and foremost is my advisor Jeff Iliff. Over the past 4 years I have tried to glean as much information from him as possible about how to become a successful scientist, both inside and outside of the lab. The mentorship and insight he provided me has shaped my view of science.

I would like to thank the members of my thesis committee: Phil Stork, Vivek Unni, Marc Freeman, Detlev Boison and Julie Saugstad. They have provided valuable insights and direction as my project has evolved over the past several years and have always had my best interest and future in mind.

I must also thank the wide network of lab mates and collaborators who have taught me countless approaches and made several of these projects possible despite the profound lack of knowledge I had going into them. This includes Martin Pike, Chad Murchison, Zhongya Wang, Jesica Reemmer, Doug Zeppenfeld, Crystal Chaw, and Stefanie Kaech-Petrie among many more.

Finally, I would like to also thank my friends and family who have supported me and dealt with me over the past several years. Most of all, thank you to Hope McCaffrey who has patiently and graciously been there for me every day along the way, and has provided endless feedback, perspective and motivation.

List of commonly used abbreviations

All abbreviations are defined in text. Below are the most common in alphabetical order.

AAV	Adeno-associated virus
AD	Alzheimer's disease
ANOVA	Analysis of variance
AQP4	Aquaporin-4
Aβ	Amyloid β
BBB	Blood-brain barrier
CSF	Cerebrospinal fluid
CTX	Cortex
DAC	Dystrophin-associated complex
ELISA	Enzyme-linked immunosorbent assay
GFP	Green fluorescent protein
HIP	Hippocampus
ISF	Interstitial fluid
kD	Kilodalton
MRI	Magnetic resonance imaging
NFT	Neurofibrillary tangles (tau)
PD	Parkinson's disease
PFF	Preformed fibrils (α-synuclein)
PVS	Perivascular space
ROI	Region of interest
SAS	Subarachnoid space
SNTA1	α-syntrophin (gene)
TBI	Traumatic brain injury
WB	Western blot
WGCNA	Weighted correlation network analysis

Table of contents

List of tables

List of figures

Abstract

Exchange of cerebrospinal fluid (CSF) with interstitial fluid (ISF) is a recently elaborated pathway by which solutes are trafficked into and out of the brain. This pathway has been implicated as a clearance mechanism for proteins such as amyloid β and tau, prior to pathogenic aggregation, a process characteristic of several neurodegenerative diseases. The mechanisms responsible for CSF-ISF exchange are poorly understood but have been linked to the expression of the astrocytic water channel aquaporin-4 (AQP4). AQP4 is unique in that it exhibits a profound localization to the perivascular spaces at which CSF-ISF exchange occurs, and that pathological states, including aging, dramatically reduce this localization. The significance of this loss of localization for CSF-ISF exchange and neurodegenerative disease has not been articulated. Here, we use imaging and cellular based approaches to study the role of AQP4 and the astrocytic endfoot in CSF-ISF exchange and aggregating protein clearance.

In chapter 2, I assess the significance of perivascular AQP4 localization in CSF-ISF exchange using transgenic mice exhibiting a diffuse membrane distribution of AQP4 (*SNTA1*$^{-/-}$). I demonstrate deficits in both CSF influx and ISF efflux in this model, providing insight into the functional consequence of age-dependent decline in AQP4 perivascular localization. Then following-up on these findings, we find that chronic disruption of the endfoot compartment exacerbates α-synuclein aggregation.

In chapters 3-5, I investigate mechanisms that contribute to the regulation of AQP4 localization. In chapter 3, using a viral overexpression paradigm, I demonstrate that elevating expression of the AQP4-M1 isoform reduces perivascular AQP4 localization at capillaries, but has no effect on CSF-ISF exchange. In chapters 4 and 5, I use a bioinformatic approach, coupled with RNAseq datasets to identify novel contributors to CSF-ISF exchange at the astrocytic endfoot. We found several transporter genes that exhibit perivascular localization and associations with Alzheimer's disease.

We hope that the data provided in these chapters will help to better elaborate the mechanism of CSF-ISF exchange, how they contribute to age-linked pathology, and identify putative targets for therapeutic treatments in neurodegenerative diseases.

Chapter 1: An introduction to CSF-ISF exchange in the brain

Foreword

The information provided in this chapter was investigated and compounded by me. Several sections, particularly those focused on CSF circulation and its role in neurological diseases, have been adapted from a review publication generated by Dr. Iliff and me (Simon and Iliff, 2016).

Introduction

Cerebrospinal fluid (CSF), a clear, secreted fluid filling the cerebral ventricles and surrounding the brain and spinal cord within the subarachnoid space (SAS), serves several homeostatic functions in the central nervous system (CNS). CSF provides buoyancy to support the weight of the brain and acts as a protective layer to cushion it from injury. CSF also serves regulatory functions, including distribution of neurotrophic factors and stabilization of brain pH and chemical gradients. Additionally, it supplies excretory pathway for solutes that cannot cross the blood-brain barrier (BBB).

Throughout the course of the 20th Century, surgical, physiological and biophysical experiments led to the development of a classical description of CSF secretion, circulation and reabsorption that remains the principal model to this day. Within this model, CSF is secreted by the choroid plexuses (CPs) and secretory epithelia in the lateral, third and fourth cerebral ventricles (Brinker et al., 2014). Bulk flow, driven by arterial pulsation and respiration, drives CSF through the ventricular system, then out into the SAS via the foramina of Luschka and Magendie (Hladky and Barrand, 2014). From the SAS, CSF is reabsorbed into the blood stream through arachnoid villi, valve-like structures within the walls of dural sinuses, by traveling along cranial or spinal nerve sheaths, or by exiting into peripheral lymphatic vessels. The excretory function of CSF did not come to prominence until the second half of the 20th century with the work of Davson, who suggested that CSF and the brain interstitial fluid (ISF) interacted, and the CSF serves as a "sink" for solutes from the brain parenchyma (Davson, 1963).

Recent research suggests CSF circulation is not as linear as the classical model suggests, and that CSF and brain ISF exchange rapidly along organized anatomical pathways including perivascular compartments along large caliber blood vessels (Figure 1.1b). Movement of CSF, ISF and associated solutes through and out of the brain parenchyma along perivascular pathways has important implications for current understanding of basic physiological processes such as CNS waste clearance, distribution of trophic factors, nutrients, and neuroactive compounds, and CNS immune surveillance. Derangement of CSF circulation may contribute to the development of a wide range of CNS pathologies, including neurodegenerative diseases such as Alzheimer's disease

(AD), neuroinflammatory conditions like multiple sclerosis (MS) and neurovascular conditions including cerebral ischemia, traumatic brain injury and subarachnoid hemorrhage (Gaberel et al., 2014; Iliff et al., 2014; Iliff et al., 2012; Siler et al., 2014)

Recently, astrocytes and the processes they extend toward the vasculature have been implicated as important facilitators of fluid exchange at the perivascular compartment. At this interface, the astrocytic endfoot domain is highly enriched in expression of the water channel aquaporin-4 (AQP4), which is necessary for CSF-ISF exchange (Iliff et al., 2012). Disruption of the localization of AQP4 to the endfoot compartment is linked to several neurodegenerative processes including AD, Parkinson's Disease (PD) and normal aging.

The goal of this dissertation is to expand upon the role that perivascular AQP4 localization plays in facilitating brain fluid exchange and investigate the mechanisms that regulate perivascular AQP4 localization in healthy and diseased conditions. In the rest of chapter 1, I will provide an overview of known astrocyte physiology and cranial fluid dynamics, moving from very broad concepts such as CSF production, down to known structural features of AQP4. I will then elaborate on known associations between brain disease states and CSF physiology.

CSF production and cranial circulation

The Choroid Plexus and CSF Production

CSF is produced primarily by the CPs which are found in the lateral, third and fourth ventricles (Davson and Segal, 1995). The CPs were identified as the primary source of CSF by Dandy in 1919, when he observed that hydrocephalus induced by the blockage of the foramen of Monro could be prevented by removal of the CP (Dandy, 1918). Further work has identified extrachoroidal sources, including ependymal cells, limited trans-capillary fluid flux, and metabolic water production that contribute to CSF production (Abbott, 2004; Cserr, 1988; Pollay and Curl, 1967). It is widely agreed, however, that approximately 80% of total CSF is secreted by the CP (Hladky and Barrand, 2014; McComb, 1983; Welch, 1963).

In 1960, de Rougemont et al. demonstrated that the electrolyte content of the CSF extracted at the CP was distinct from that of blood plasma, physiologically linking the CPs to CSF production (de Rougemont et al., 1960). The composition of the CSF is tightly regulated by the CPs, which are complex structures comprised of a plexus of fenestrated capillaries surrounded by a layer of cuboidal epithelial cells, with an intervening stromal space. The epithelial cells are polarized, with the apical CSF-facing side possessing microvilli and tight junctions that constitute the blood-CSF barrier (BCSFB), which is in many respects analogous in function to the BBB of the cerebrovascular endothelium (Figure 1.1d) (Wolburg et al., 2001).

Under physiological conditions, CSF is actively secreted, largely independently of choroidal blood flow, through the concerted activity of numerous membrane proteins. These include apical Na+/K+ ATPase, the aquaporin-1 (AQP1) water channel, and secondary ion transporters and channels localized specifically to basolateral and/or apical membranes that facilitate ionic flux comprised largely of Na^{+}, HCO^{3-} and Cl^{-} into the ventricular lumen (Kao et al., 2011; Millar and Brown, 2008; Nielsen et al., 1993). The net result of this secretory process is that CSF is produced with stable ionic composition that is distinct from that of plasma.

The CP also utilizes systems of transporter proteins to coordinate both the entry and efflux of specific solutes essential for neuronal and glial function, into and out of the CNS (Spector, 1989). One example of nutrient delivery is folate transport. Folate receptors (FRα) are localized to the membrane of the CP and package reduced folates (MeTHF) from the blood, into endosomes where they are acidified. The MeTHF is then ferried out of the endosome by a proton-coupled folate transporter (SLC46A1), and is ultimately delivered into the CSF via facilitated diffusion mediated by the reduced folate carrier (RFC) (Spector, 1989; Zhao et al., 2009).

In contrast, CP can also mediate solute clearance from the CSF, as occurs with the removal of L-Glutamate, an excitatory neurotransmitter associated with neuroexcitatory conditions such as epilepsy. Excitatory amino acid transporter 3 (EAAT3) is localized to the apical (CSF) side of the CP and facilitates transport into the CP (Akanuma et al., 2015).

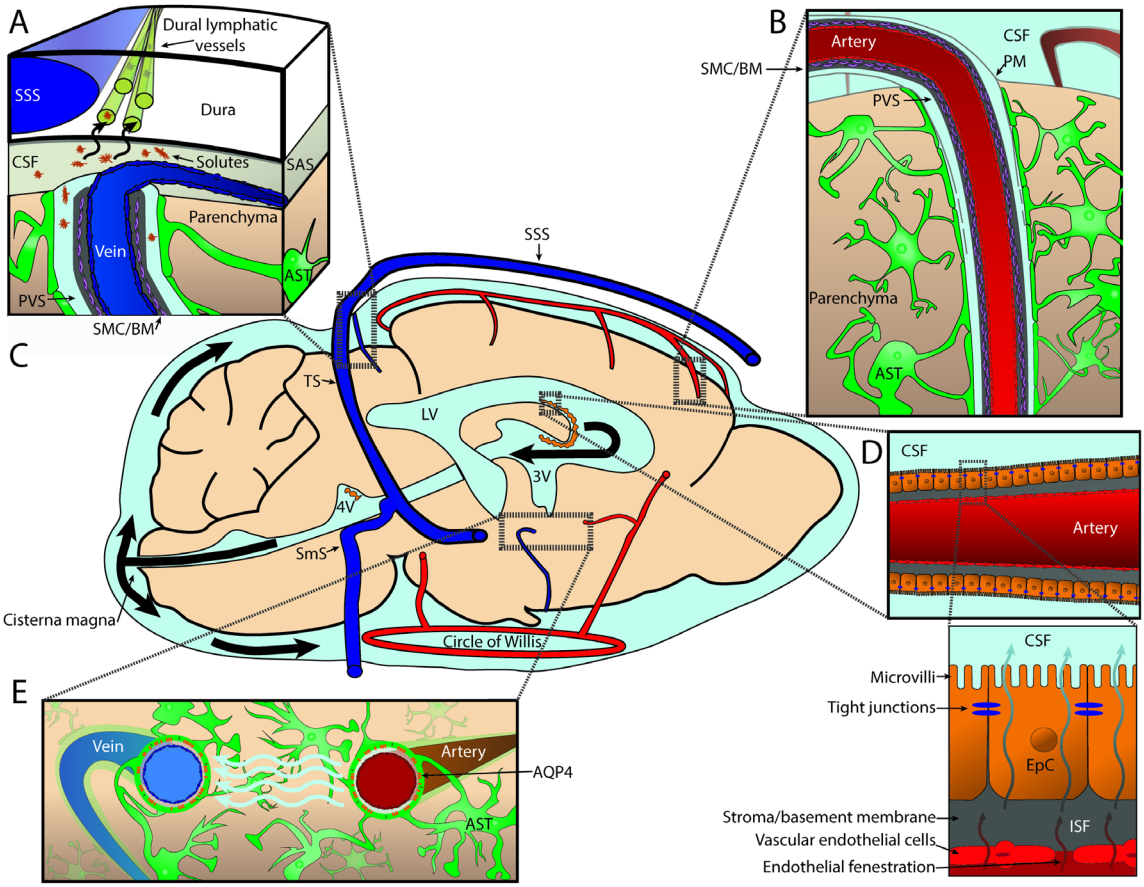

Figure 1.1: Schematic of CSF production and circulation in the brain

(A) Putative interface of ISF exiting the brain along perivascular spaces, and meningeal lymphatic vessels. (B) Representation of the perivascular space along penetrating vessels, bounded internally by the vasculature, and externally by astrocytic endfeet. (C) Brain-wide circulation of CSF. Produced in the ventricles by the choroid plexuses, it exits into the cisterna magna and then circulates through the SAS. (D) Anatomy of the choroid plexus. (E) Putative model of CSF flow through the brain, known as the 'glymphatic' pathway. Abbreviations: Astrocyte (AST), basement membrane (BM), epithelial cells (EpC), pia mater (PM), smooth muscle cell (VSM), sigmoid sinus (SmS), superior sagittal sinus (SSS), transverse sinus (TS).

CSF circulation and exchange with perivascular compartments

Due to the nature of CSF circulation, which occurs dynamically across large anatomical distances, most contemporary research on the topic utilizes phase-contrast

magnetic resonance imaging (PC-MRI). This approach is limited by the scale at which CSF movement occurs. CSF flow is comparatively slow and generally not observed across many voxels during any given measurement. Additionally, the space that CSF travels through is typically very small in any given plane and therefore total voxels for detection are limited. Despite these limitations, PC-MRI has provided key insights into the basic principles of CSF flow. Earlier approaches evaluating rates of CSF production, flow and reabsorption including tracer infusion and CP lesion studies also often produced conflicting or controversial results (Hladky and Barrand, 2014). Here I will attempt to summarize the current leading perspectives in the field.

As detailed above, CSF is largely generated by the CPs. The exact rate of CSF formation varies with neuroendocrine and hormonal modulation (Nilsson et al., 1992), and across species. In humans, the production rate lies between 0.3-0.6 ml/min, with a total daily production of 500-600 ml, while CSF production rate in mice is 400nl/min. approximately 40ul of CSF is found within the ventricles of the mouse, and it takes about 2 hours to turnover completely. These discrepancies are indicative of differences in CSF dynamics between humans and rodent models (Johanson et al., 2008; Oshio et al., 2005).

PC-MRI studies indicate that through the course of each cardiac or respiratory cycle, bi-directional CSF flow through narrow segments of the ventricular system such as the cerebral aqueduct may occur. Net flow of CSF, however, originates in the ventricles (primarily the third and lateral ventricles) and travels through the cerebral aqueduct, to the 4th ventricle where it exits into the SAS through the foramina of Luschka and Magendie (Figure 1.1c) (Dreha-Kulaczewski et al., 2015). Conventional understanding dictates that a portion of the subarachoid CSF continues through the SAS along the spinal cord, exiting along spinal nerve roots, while the remainder exits the cranium via arachnoid villi and the cranial nerves (Damkier et al., 2013). The recently described lymphatic vessels associated with the dural sinuses may also be involved in CSF reabsorption (Figure 1.1a) (Aspelund et al., 2015; Louveau et al., 2015).

Reabsorption of the CP produced CSF circulating through the ventricles and SASs into the lymphatic system is critical to the clearance of metabolites and waste products. The human CSF pool turns over approximately 4 times per day, while the turnover rate in rats has been measured at approximately 11 times a day (Preston, 2001).

CSF bulk flow and reabsorption are driven by pulsations within the cranium but are supported by CSF pressure maintained by equalization of the rates of CSF secretion and reabsorption. Due to enclosure within the cranium, changes in CSF pressure can occur rapidly when the rates of CSF secretion and reabsorption are not balanced, leading to conditions such as hydrocephalus. The pulsations driving CSF from its origin at the CPs to the efflux pathways from the cranium are generated by both the respiratory and cardiac cycles. Utilizing PC-MRI Feinberg and Mark illustrated that CSF velocity at the cerebral aqueduct varies across the cardiac cycle, with peak velocities phase-locked to cardiac systole (Feinberg and Mark, 1987). Recent studies using PC-MRI have also implicated respiration in the bulk flow of CSF as changes in CSF movement through the ventricular system varied with the respiratory cycle and could be manipulated by alterations in the respiratory patterns of study participants (Dreha-Kulaczewski et al., 2015; Yamada et al., 2013). Interestingly, the magnitude of respiration-associated changes in CSF velocity were substantially greater than those occurring in phase with the cardiac cycle.

A longstanding matter of debate has been whether CSF can pass from the subarachnoid compartments into perivascular spaces along leptomeningeal and penetrating arteries. The presence of a sheath of pia mater that surrounds these blood vessels and separates the subarachnoid CSF from these perivascular spaces, provided framework for a model in which access of CSF into the brain along these pathways is limited (Zhang et al., 1990). This report conflicted with a pair of studies carried out in cats and dogs, by Rennels et al. in which it was reported that horseradish peroxidase (a 44kD protein) injected into the ventricular and subarachnoid CSF moved rapidly into the cortex along perivascular spaces surrounding penetrating arteries (Figure 1.1b) (Rennels et al., 1990; Rennels et al., 1985). In an effort to clarify the pathways of flow, Cserr and colleagues injected tracers directly into these perivascular spaces, and observed that the perivascular movement of tracers was slow and variable in direction, but that some tracer did leak out into the SAS (Ichimura et al., 1991). This led to the conclusion that while the perivascular spaces do likely create a viable pathway between the CSF in the SAS and the parenchyma, there was no evidence of it serving as an entry point of directional CSF flow into the parenchyma. The discrepancy between the reports form Cserr's group and

Rennel's group rested primarily in the speed and direction of the flow within the perivascular space and was chalked up to differences in experimental technique.

A hypothesis articulated by Weller, Carare and colleagues proposes that while CSF does not enter the perivascular space, ISF and solutes are cleared along these pathways, moving first along the capillary basal lamina, then vascular smooth muscle basement membrane, then traveling through perivascular spaces to reach the cervical lymphatics along the internal carotid arteries (Weller et al., 2009). This hypothesis is supported by parenchymal tracer injection experiments in which signal is detected along capillaries and within the walls of cortical arteries. Histopathological examination of amyloid depositions along cortical arterioles purported to be an "endogenous" ISF tracer further corroborates the hypothesis (Hawkes et al., 2011).

A series of recent studies, utilizing in vivo approaches that permit the dynamic imaging of CSF tracers suggest that this model may be incorrect. While there is still much disagreement in the field as to the exact mechanism and significance, studies employing dynamic in vivo 2-photon imaging after injection of fluorescent CSF tracers in mice indicates that subarachnoid CSF from the cisternal compartments enters and travels along perivascular spaces surrounding cerebral arteries, gaining access to the brain parenchyma and exchanging with the surrounding ISF (Iliff et al., 2013a; Iliff et al., 2012; Iliff et al., 2013b; Xie et al., 2013). This finding was confirmed in rats and by visualizing brain-wide CSF contrast movement along perivascular pathways by dynamic contrast-enhanced MRI (DCE-MRI) (Gaberel et al., 2014; Iliff et al., 2013a; Yang et al., 2013). The techniques utilized in these studies allowed for a higher time resolution, and therefore a good way to address the discrepancies between the Rennels and Cserr group findings (Ichimura et al., 1991; Rennels et al., 1990; Rennels et al., 1985). Since this description, various groups have reported similar observations of tracer movement into the brain along these pathways across a variety of experimental paradigms and physiological conditions (Mestre et al., 2018a; Pizzo et al., 2018; Smith et al., 2017) (Appendix A).

These studies also investigated the perivascular compartment as an efflux pathway for ISF and its associated solutes. Using intra-parenchymal injections of inert tracer molecules such as fluorescent dextrans, or proteins including amyloid β or tau, it

was observed that ISF and interstitial solutes are cleared from the brain along distinct anatomical pathways, following subcortical white matter tracks and perivascular spaces surrounding large-caliber draining vessels and emerging into cisternal CSF compartments associated with dural sinuses, including the quadrigeminal and basal cisterns (Iliff et al., 2014; Iliff et al., 2012). These data are consistent with some of the earliest studies of waste clearance from the brain (Cserr, 1971; His, 1865)

The anatomical pathway permitting communication of cisternal CSF with CSF flowing along perivascular spaces is still an active topic of investigation. One possibility is that subarachnoid CSF enters perivascular spaces proximally, through fenestrations of the ensheathing pia mater along pial blood vessels. CSF could then be conducted distally through these perivascular spaces to enter the brain parenchyma along penetrating arteries. Supporting this hypothesis is a recent study that investigated the microanatomy of leptomeningeal blood vessel sheaths in rats using scanning electron microscopy (Pizzo et al., 2018). The authors found that along the sheaths there are 'stomata' that are several microns in size. While the physiological significance of these stomata has not yet been determined, these perforations of the meninges may represent a mechanism by which bi-directional exchange of CSF from the cisternal compartments with the ISF throughout the brain parenchyma may occur.

Solute transport in the brain

Fluid and solute movement in the brain: diffusion vs. bulk flow

Classical CSF studies demonstrate that the CSF serves as a sink to interstitial solutes, as tracers injected into different brain regions drain to different CSF compartments (Szentistvanyi et al., 1984). Two modes of movement, diffusion and bulk flow (or convection), could potentially account for the movement of solutes within the brain extracellular space and their clearance either to internal or external CSF compartments. Diffusion results from the thermal motion of a molecule down its concentration gradient. The speed of diffusion is strongly influenced by the mass of the solute, with large macromolecules moving slowly through the brain extracellular space (Sykova and Nicholson, 2008). Bulk flow occurs on a larger scale and refers to

movement in which all solutes travel at the same rate, regardless of size (Abbott, 2004; Cserr, 1971).

To define the mechanism governing solute efflux from the brain interstitium, Cserr and colleagues observed that inert tracers with masses spanning nearly 2 orders of magnitude (900 Da – 69 kD) were cleared from the rat caudate nucleus at the same rate, demonstrating that the efflux of macromolecules from the brain occurs by bulk flow rather than by diffusion (Cserr et al., 1981). These findings were recently confirmed in a radio-tracer study in mice using mannitol (182 Da) and dextran (10kD) (Iliff et al., 2012). Since Cserr's work, a pharmacokinetic study by Groothuis et al. reported that for molecules exhibiting uptake across the blood brain barrier, efflux from the parenchyma was dependent upon local diffusion, while clearance of molecules by bulk flow could be modulated by factors including intramolecular binding interactions, physiological state and the type of anesthesia used (Groothuis et al., 2007). This latter study, which identified solutes that appeared to be cleared from the brain interstitium by a combination of bulk flow and diffusion, reflects several studies that indicate that the contribution of diffusion and bulk flow to the efflux of interstitial solutes may not be uniform throughout the brain parenchyma. Distinct tissue features, including white matter tracts and perivascular spaces, appear to experience rapid bulk flow compared to the wider neuropil (Iliff et al., 2012; Konsman et al., 2000; Proescholdt et al., 2000; Rennels et al., 1985; Rosenberg et al., 1980). One possible alternative to a global role of bulk flow in the efflux of interstitial solutes is the combined influence of diffusion within the dimensions of the brain extracellular space coupled to efflux via bulk flow along 'privileged' long-distance pathways such as white matter tracks and perivascular spaces (Hladky and Barrand, 2014).

CSF-ISF exchange: The 'glymphatic' pathway

The studies detailed above demonstrate that perivascular pathways provide key anatomical routes for the bi-directional exchange of CSF from cisternal compartments with the brain ISF, with CSF entering the brain along perivascular spaces surrounding penetrating arteries to exchange with surrounding ISF, while ISF and interstitial solutes are cleared along perivascular spaces surrounding large caliber vessels to reach CSF

compartments which have access to peripheral lymphatic vessels in the meninges and skull base. The findings reported by Nedergaard and colleagues are in many ways simply a confirmation of earlier tracer studies defining exchange of CSF and ISF along perivascular pathways (Ichimura et al., 1991; Iliff et al., 2013a; Iliff et al., 2012; Iliff et al., 2013b; Rennels et al., 1990; Rennels et al., 1985; Szentistvanyi et al., 1984). These recent studies, however, are unique in that they suggest a central role for astrocytes in facilitating perivascular CSF-ISF exchange. Moreover, they provide strong evidence for the physiological regulation of the dynamics of perivascular fluid exchange that may offer key insight into the interrelationship between CSF-ISF dynamics, physiological brain function, and the development of neurological disease.

One key finding from these studies was the observation that the astrocytic water channel aquaporin-4 (AQP4), which is localized primarily (enriched 10:1) to perivascular astrocytic endfeet ensheathing the cerebral vasculature, supports both perivascular influx of CSF into and through the brain interstitium as well as the clearance of interstitial solutes from the brain parenchyma (Iliff et al., 2012). Owing the dependence of perivascular CSF-ISF exchange upon glial water transport and its assumption of the conventional peripheral lymphatic function of interstitial solute clearance, Nedergaard and colleagues termed this brain-wide glial-vascular network the ‘glymphatic’ system (Figure 1.1e) (Nedergaard, 2013).

In a follow-up study, Xie et al. reported that glymphatic pathway function was a feature of the sleeping, rather than the waking brain (Xie et al., 2013). Compared to both naturally sleeping and anesthetized mice, the rate of perivascular CSF tracer influx into the waking cortex after infusion into the cisterna magna was reduced by ~95%. In parallel experiments, the authors reported that both the clearance of the inert radio-tracer ^{14}C-inulin and radio-labeled ^{125}I-amyloid β were reduced by approximately one half in the waking compared to the sleeping or anesthetized brain. These data are in agreement with the findings of Groothuis et al. who reported that the clearance of the inert tracer ^{14}C-Sucrose from the brain interstitium was markedly slowed in awake behaving rats compared to those under ketamine-xylazine anesthesia (Groothuis et al., 2007). Underlying these changes in perivascular CSF-ISF exchange in interstitial solute clearance appears to be sleep-wake changes in the dimensions of the brain extracellular

spaces. From in vivo electrophysiological recordings collected in mouse cortex using the gold-standard tetramethylammonium (TMA) micro-iontophoresis method (Sykova and Nicholson, 2008), Xie et al. reported that during sleep, the brain extracellular space increases in volume by ~60% (Xie et al., 2013). This effect, as well as the effect of arousal on perivascular CSF-ISF exchange and interstitial solute clearance, appeared to be in part regulated by cortical noradrenergic tone, as local pharmacological blockade of noradrenergic receptors restored waking extracellular volume fraction, perivascular CSF influx and interstitial solute clearance to levels observed during natural sleep or anesthesia. These findings suggest that the processes of CSF circulation, including its exchange with the interstitial compartment along perivascular pathways, may be under dynamic physiological regulation. In agreeance with this hypothesis, recent work has indicated that some transporters that interact with CSF solute concentrations, such as P-glycoprotein may exhibit diurnal variations in activity (Kervezee et al., 2014). While the 'glymphatic' hypothesis as it is currently articulated remains controversial, it provides a potentially powerful framework through which to understand the interrelationship between CSF circulation, interstitial solute clearance, and vascular and neural physiology in supporting physiological brain function.

Astrocytes and the perivascular endfoot domain

Astrocytes are the most abundant cell type in the brain and serve a wide range of functions in maintaining brain homeostasis. Astrocytes form a syncytium across the brain, with non-overlapping spherical domains, 50-60 μm in diameter, that are connected to each other via gap junctions (Bushong et al., 2002). Each astrocyte exhibits a star-like morphology with several processes contacting vasculature, synapses and other glial cells (Figure 1.2a). These processes are incredibly complex, with a surface area of 60,000-80,000 μm^2 (Kettenmann and Verkhratsky, 2011). These processes are compartmentalized and exhibit unique Ca^{2+} dynamic allowing for signaling, despite being an electrically non-excitable cell type (Bindocci et al., 2017). Via these compartments, astrocytes perform a wide range of homeostatic functions including the uptake and recycling of neurotransmitters like GABA and glutamate, maintenance of ionic gradients and extracellular pH, and trafficking of nutrients and metabolites.

Astrocytes also contribute to the brain's immune response to a range of pathologies including chronic conditions like neurodegenerative disease and acute injuries such as TBI and infection. Upon exposure to brain insults, astrocytes will alter their morphology and transcriptional profile to become 'reactive'.

Ca^{2+} signaling in astrocytes

Ca^{2+} is the most well-characterized secondary signaling messenger in astrocytes, though other potential signaling pathways such 3′,5′-cyclic adenosine monophosphate (cAMP) dependent signaling, also contribute. Astrocytes invoke a wide range of sources to trigger Ca^{2+} activity, which allows for spatially and temporally distinct Ca^{2+} events. Ca^{2+}flux into the cell can originate from the extracellular compartment, or from internally sequestered Ca^{2+} stores in the endoplasmic reticulum and mitochondria. External Ca^{2+} flux is driven by many pathways, including ionotropic receptors, transient receptor potential (TRP) channels, and voltage-gated Ca^{2+} channels and sodium-calcium exchangers (NCX). Internal release is thought to occur primarily via inositol-3-phosphate (IP_3) receptors in the endoplasmic reticulum.

Ionotropic receptors including N-methyl-d-aspartate (NMDA) and ATP-gated P2X(1/5) receptors have been described in astrocytes and are thought to be involved in facilitating astrocytic response to synaptic activity (Palygin et al., 2010). Similarly, voltage-gated Ca^{2+} channels are expressed in astrocytes and potentially activated in response to depolarization of astrocytes in response to K^+ influx. However, expression of voltage-gated Ca^{2+} channels is relatively low in the healthy brain, though it has been reported that expression is elevated in pathogenic states including mouse models of amyloid β accumulation (Willis et al., 2010; Zhang et al., 2014). Mechanical perturbations represent another intriguing mechanism of Ca^{2+} influx via TRP channels, which respond to changes in the extracellular environment. At their endfoot processes, astrocytes contact the brain vasculature. Here TRP channels can respond to vasomotion-triggered pressure changes, osmotic changes due to fluid movement, and even temperature changes as a result of metabolic activity and pathological conditions involving neuroinflammation (Kim et al., 2015; Wang et al., 2014).

Profiling astrocytic Ca^{2+}signaling becomes even more nuanced and complicated due to Ca^{2+} triggered release of intracellular Ca^{2+} stores via IP_3 receptors. The contribution of IP_3 receptors to Ca^{2+} flux can be modulated by the local expression of IP_3 (Semyanov, 2019). This is in turn regulated by phospholipase C, which is activated by a wide range of astrocytic G_q protein receptors including α1 adrenergic receptors, P2Y receptors, mGluR1/5 and the muscarinic receptor mAchR1α (De Pittà et al., 2019; Kastritsis et al., 1992; Porter-Stransky et al., 2019).

Both these intracellular and extracellular mechanisms of Ca^{2+} release can be dynamically modulated to promote or inhibit Ca^{2+} signaling in a spatiotemporally defined manner. How these mechanisms drive coordinated propagation of Ca^{2+} waves both on the level of individual astrocytes as well as across the astrocytic syncytium remains a topic of active investigation.

Astrocyte heterogeneity and reactive astrogliosis

Among neurons, several different subpopulations have been identified morphologically, molecularly and functionally. In contrast, astrocytes have classically been thought of as a homogenous cell type apart from differences in grey matter (protoplasmic) and white matter (fibrous) astrocytes (Andriezen, 1893). To identify mature astrocytes histologically, a small set of markers have been identified: the intermediate filament protein GFAP and more recently aldehyde dehydrogenase 1 family, member L1 (Aldh1L1) (Cahoy et al., 2008; Pixley and de Vellis, 1984). However, it has long been known that labeling of astrocytes with these or any known markers is highly heterogenous across brain regions and following state changes such as injury or disease. In fact, elevated levels of GFAP is the defining histopathological hallmark of reactive astrogliosis (discussed below). Together, this suggests that there are distinct transcriptional and proteomic populations of astrocytes, though isolating unique markers for these populations has proven challenging. Recent advances in single cell RNA sequencing technology has allowed for clustering based identification of subpopulations of mouse astrocytes and regional differences in gene expression (Boisvert et al., 2018; Zeisel et al., 2018), though further studies are needed to identify functional and structural characteristics associated with these subpopulations. Further complicating the study of

astrocytes is abundant species differences between astrocytes and astrocyte-like cells in different model organisms. The most striking of these is the differences between rodent and human astrocytes, with human astrocytes exhibiting three fold larger volumes and up to ten times more processes than astrocytes in mice or rats (Oberheim et al., 2009).

Reactive gliosis is a process by which astrocyte undergo a change in gene expression, morphology and function, in response to changes in the brain environment. This was initially described by Rudolf Virchow, as the formation of thick fibrillary scarring surrounding a spinal lesion in a man with limb paralysis (Virchow, 1855). Since the late 1970's, the primary histological marker of reactive astrogliosis has been elevated expression levels of GFAP, a protein also found abundantly in healthy astrocytes (Eng et al., 1971). Since these initial studies and several studies associating reactive gliosis with various disease states, our understanding of this state has hardly expanded. The functional impact and degree of change associated with conversion to a reactive state is unclear, as are the mechanisms responsible for driving the conversion. To add further confusion, both protective and damaging phenotypes have been associated with the reactive state.

Recent transcriptomic work has articulated two subclasses of reactive astrocytes. A1 astrocytes are induced by microglia-secreted factors (including Il-1α, TNF α, and C1q) and promote death of neighboring neurons and oligodendrocytes. A2 astrocytes secrete neurotrophic factors (Liddelow et al., 2017). It has been reported that A1 astrocytes are associated with a variety of human neurodegenerative diseases including AD, MS, PD and Huntington's disease. Whether the gene expression changes associated with these reactive states contribute to the progression of neurodegenerative diseases or are simply concomitant, remains to be seen.

Compartmentalization of astrocytes

Astrocytic branching is incredibly complex and numerous. So much so, that functionally imaging the fine processes in the spongiform domains in vivo and in 3 dimensions, remains a challenging endeavor reliant on technical advances (Audrey et al., 2019; Bindocci et al., 2017). Study of astrocytic morphology has revealed three subcellular domains in addition to the soma: the perivascular endfoot domain as well as two sub-classifications of processes in the spongiform domain: flat, organelle-free

'leaflets', and 'branchlets' that contain endoplasmic reticulum and mitochondria, allowing for Ca^{2+} signaling via intracellular Ca^{2+} stores (Figure 1.2a) (Semyanov, 2019).

Contact between astrocytic processes and dendritic spines occurs with both branchlets and leaflets, suggesting that Ca^{2+} signals can propagate/diffuse at least locally without release of internal Ca^{2+} stores, though the mechanism of this remain unclear. The presence of leaflets is advantageous as it allows for abundant surface area at which glutamate uptake can occur. Interestingly, both leaflets and branchlets are thought to undergo morphological remodeling in response to both physiological or pathological stimuli and state changes, including AD (Rodriguez et al., 2009). These morphological changes can alter functions including Ca^{2+} signaling and glutamate reuptake (Henneberger et al., 2019; Wu et al., 2019). Even so, spontaneous activity occurs across astrocytes that is heterogenous not only between sub-compartments, but even within individual processes. Further studies are needed to clarify the relationship between astrocyte structure and observed Ca^{2+} transients, particularly in the spongiform domain, due to the need for both high temporal and spatial resolution.

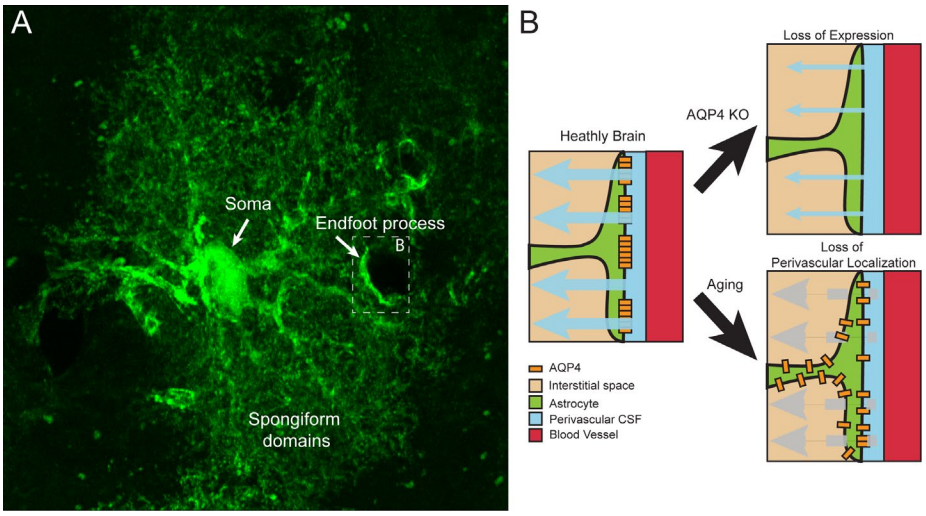

Figure 1.2. Astrocyte morphology and the astrocytic endfoot process.
(A) Astrocytes exhibit a highly branched 'star' like morphology. In addition to processes that contact neurons and other glia cells in the spongiform domains, astrocytes possess a specialized process that abuts the vasculature in the brain. (B) Endfeet are enriched with high expression levels of AQP4 in the healthy brain, which contributes to flux of solutes and fluid across this compartment. Disruption of AQP4 by genetic deletion dramatically reduces this exchange. The impact of loss of perivascular AQP4 localization, without a loss of total expression as seen in the aging brain, has not yet been demonstrated.

The endfoot domain

One of the unique processes that astrocytes extend is the endfoot domain (Figure 1.2). These are processes that interact with blood vessels and almost entirely ensheath the vasculature of the brain, from the penetrating vessels at the brain surface, all the way to the capillary bed (Mathiisen et al., 2010). Up to 99% of the abluminal face of blood vessels is thought to be contacted by endfeet (McCaslin et al., 2011). Endfeet processes play several roles in facilitating neurovascular interactions. Endfeet have been shown to play a role in facilitating vascular dilation in response to neural activity and in the regulation of cerebral blood flow (Kim et al., 2015; Mishra et al., 2016). Endfeet facilitate the trafficking of nutrients between neurons and vasculature and managing brain glucose utilization and distribution (Belanger et al., 2011). Beyond these interactions fundamental processes associated with this domain include maintenance of blood-brain-barrier integrity, facilitation of brain edema response, and regulation of extracellular space and composition. Underlying these functions are properties such as highly distinct spontaneous Ca^{2+} waves, even between endfeet in contact with the same blood vessel, and local translation of mRNA (Bindocci et al., 2017; Boulay et al., 2017). While many physiological functions are associated with endfeet processes, the cellular properties facilitating these functions remain largely unarticulated. Known protein elements of endfeet are limited to a few membrane proteins (Kir4.1, Connexin-43, TRPV4), a scaffolding complex (dystrophin associated complex) and the water channel AQP4.

Aquaporin-4

History and biophysical properties

The most well-established component of the astrocytic endfoot is the water channel AQP4. Originally identified due to its exceptionally high expression levels in the brain, AQP4 is a water specific channel that is highly enriched in astrocytes, with low levels of expression in ependymal cells lining the ventricles (Frigeri et al., 1995). The robust perivascular localization of AQP4 was first identified by immunogold labeling of AQP4 in electron micrographs (Nielsen et al., 1997). Two decades earlier, the endfoot

domain had been shown to possess large assemblies of proteins in the membrane called ‘orthogonal arrays’, identified by freeze fracture electron microscopy, though the protein constituents of these arrays were unknown (Dermietzel, 1973). Shortly after its discovery, AQP4 was identified as the culprit responsible for these arrays, as genetic deletion of AQP4 null mice eliminates their formation (Verbavatz et al., 1997). These studies lead to elevated interest in the physiological significance of AQP4 and these array formations at the endfoot compartment and their significance at the blood-brain interface.

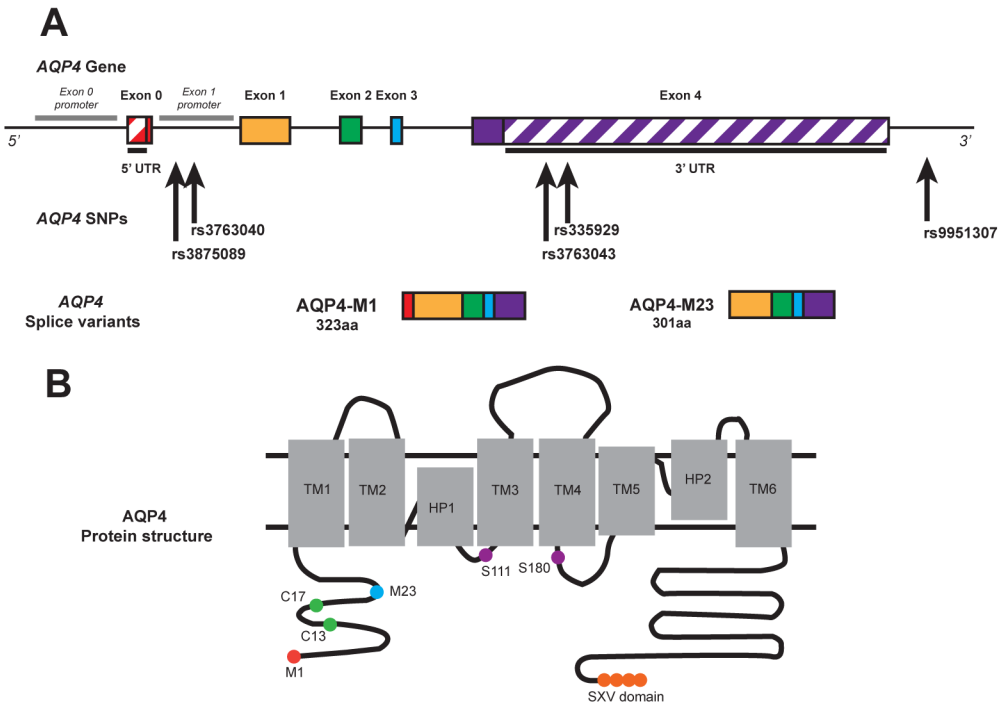

Figure 1.3: Schematic representation of AQP4 gene and protein structure.
(A) AQP4 consists of five exons (shown as solid colored rectangles) and can be translated into two different isoforms. AQP4-M1 consists of exons 0–4 and is 323 amino acids long. The AQP4-M23 isoform consists of exons 1–4 and is 301 amino acids long. When APQ4 is translated into the AQP4-M23 isoform, the subsequent protein organizes into crystalline arrays that localize to astrocyte endfeet that ensheathe the cerebral vasculature. (B) AQP4 protein has 6 transmembrane domains with two connecting loops that form hemipore domains. Several regulatory elements have been identified including methionine start sites for the M1 (orange) and M23 (blue) isoforms. Cysteine residues that serve as palmytoylation sites (green) and identified phosphylation sites at serines (purple) have been indicated. The SXV sequence that interacts with PDZ domains is indicated in orange. Adapted from the figure generated for Burfiend et al. 2017.

Biophysical studies have revealed that AQP4 has six transmembrane domains with 5 connecting loops (Figure 1.3b). This organization possesses three main features responsible for the water selectivity of the channel. First, two of the connecting loops serve as hemipores containing Asn-Pro-Ala (NPA) motifs that converge to cause the formation of a narrow (2.8 Å) pore, that prevents many molecules larger than water from passing through (Walz et al., 2009). Additionally, this narrow pore contains an arginine selectivity filter (Arg216), preventing the passing of protonated molecules and cations. Finally, positively charged dipoles in the filter form an electrostatic field that reorients water molecules as they pass though the pore. As the water is reoriented, it forms transient hydrogen bonds with the amide groups of the Asn residue, preventing the flow of protons (Tani et al., 2009). The smallest functional organization of AQP4 in the plasma membrane are tetrameric units. The central pore generated by these tetramers has been implicated as a potential transporter of gas (Musa-Aziz et al., 2009; Thrane et al., 2013). The physiological significance of this transport remains unclear.

Isoforms

While several AQP4 isoforms have been described in mammals, AQP4-M1(M1) and AQP4-M23 (M23) have been identified as the most abundant isoforms observed in humans, though M23 expression is thought to be 3-fold greater than M1 (Lu et al., 1996; Neely et al., 1999). These isoforms are transcribed by the same gene, with two different initiation sites. Several single nucleotide polymorphisms (SNPs) have been identified within the AQP4 gene, mostly targeted to the 3' untranslated region, that have been linked to cognitive deficits and AD (Burfeind et al., 2017; Rainey-Smith et al., 2018). Differentiating the two isoforms is one additional exon specific to M1 (five total exons) relative to M23 (four total exons) that encodes an additional 22 amino acids found on the NH_2 terminus (Figure 1.3). These additional residues strikingly inhibit the M1 isoform from assembling into orthogonal arrays, as demonstrated in Chinese Hamster Ovary (CHO) cells, suggesting that the orthogonal arrays identified at the astrocytic endfoot domain are largely composed of the M23 isoform (Verkman et al., 2011). This difference in capacity for array formation is thought to derive from two palmitoylation sites (cysteine 13 and 17) found on the M1-specific NH_2 terminal residues, that restore array

formation when mutated to alanines (Suzuki et al. 2008). Whether these isoform properties are observed in vivo remains to be determined. Similarly unclear is the physiological significance of these arrays, which are densely expressed at the endfoot (500-600/μm^2, Wolburg et al. 2009). Wide-ranging functions of these arrays have been articulated including facilitation of fluid reabsorption, macromolecule clearance, gas exchange, and even adhesion, but to date these functions in vivo remain to be adequately defined.

Perivascular localization

Formation of large membrane arrays is inadequate to explain the perivascular localization of AQP4. In other cell types a tight junction boundary is sufficient to maintain subcellular distribution of membrane arrays due to limited diffusion. In astrocytes, anchoring of AQP4 has been shown to be facilitated by the dystrophin-associated complex (DAC), a macromolecular scaffolding complex comprised of α-syntrophin, α-dystrobrevin, dystrophin, α-dystroglycan and β-dystroglycan. AQP4 directly interacts with the complex via a PDZ domain of α-syntrophin, that binds to the SXV-sequence found on the COOH terminus of both the M1 and M23 AQP4 isoforms. Genetic deletion of each of these DAC proteins have been associated with a loss of perivascular AQP4 localization and general disruption of the endfoot compartment (Dalloz et al., 2003; Enger et al., 2012; Lien et al., 2012; Neely et al., 2001; Noell et al., 2011). Additionally, extracellular scaffolding elements including laminin and agrin interact with the DAC via α-dystroglycan, and disruption of this interaction can also impact AQP4 expression and localization (Noel et al., 2009; Noell et al., 2009).

Short term regulation of water flux through AQP4 has been reported, though few gating mechanisms have been described and remain poorly characterized. Phosphorylation of Ser180 is linked to inhibition of water flux through AQP4 (Han et al., 1998), while phosphorylation of Ser111 has been linked to activation (Gunnarson et al., 2005). However, follow up studies targeting these residues have not been able to identify conformational changes associated with these modifications and whether closing of AQP4 channels can occur remains to be demonstrated (Assentoft et al., 2013; Mitsuma et al., 2010). Conversely, several studies suggest that AQP4 function may be modulated by

altering subcellular distribution. In the acute setting, activation of vasopressin 1 receptors (V1R) results in internalization of AQP4 in *Xenopus* oocytes (Moeller et al., 2009). Activation of V1R leads to internalization of AQP4 via PKC dependent phosphorylation of Ser 180 of AQP4. In contrast, PKA dependent phosphorylation of serine 276 has been associated with translocation of AQP4 into the plasma membrane of cultured primary cortical astrocytes (Kitchen et al., 2015). Several other signaling cascades have also been implicated in the trafficking of AQP4 and other aquaporins including calmodulin-mediated Ca^{2+} signaling, Vasopressin 2 receptor signaling, and AKAP220 mediated actin rearrangement (Kishore et al., 1996; Kitchen et al., 2015; Whiting et al., 2016).

Chronic modulation of AQP4 localization of the endfoot compartment is associated with several pathological conditions in the brain. The most well-established of these is following transient ischemia (Frydenlund et al., 2006). Following occlusion of the middle cerebral artery, AQP4 localization to the endfoot was lost, without a concomitant loss of localization of α-syntrophin, suggesting that his rearrangement was not purely a result of broader disruption of the DAC and broad endfoot integrity. Other pathogenic conditions exhibiting a loss of AQP4 perivascular localization include epilepsy (Eid et al., 2005), TBI (Ren et al., 2013), and AD (Yang et al., 2011; Zeppenfeld et al., 2017). Loss of localization is also observed more broadly in the context of aging (Kress et al., 2014) and in reactive astrocytes (Wolburg et al., 2011). The mechanisms driving this loss of localization in pathogenic and chronic conditions have not yet been articulated.

CSF-ISF exchange in neurological disease

Alzheimer's Disease

AD, the most common cause of dementia, is a neurodegenerative disease characterized histopathologically by the formation of extracellular senile plaques composed primarily of amyloid β and intracellular neurofibrillary tangles (NFTs) comprised of hyperphosphorylated tau. According to the dominant 'Amyloid Cascade Hypothesis of AD', increasing levels of interstitial amyloid β species impair synaptic function, promoting tau aggregation and NFT formation and resulting in

neurodegeneration (Hardy and Selkoe, 2002; Karran et al., 2011). AD pathology is associated with pronounced neuroinflammation, including reactive astrogliosis (Rogers et al., 2002). CSF dynamics have also been found to change in the aging brain (Albeck et al., 1998; Pfefferbaum et al., 1994). While both AD-associated neuroinflammation and changes in CSF dynamics have been regarded as distinct contributors to the development of AD within the aging brain, recent studies suggest that these events may interact with one another during the onset of AD.

Amyloid β is formed from the amyloid protein precursor (APP) following successive cleavages by β- and γ-secretases to form the pro-fibrillary amyloid $\beta_{1\text{-}42}$ that is a key component of senile plaques and the more soluble amyloid $\beta_{1\text{-}40}$ that deposits in the walls of leptomeningeal and cerebral arteries in the condition cerebral amyloid angiopathy (CAA) (Attems et al., 2011). Amyloid β is produced in the brain during synaptic activity, and in the healthy young brain is rapidly eliminated by cellular uptake into microglia and astrocytes, efflux across the BBB via solute transporters including P-glycoprotein (PGP) and low density lipoprotein receptor-related protein 1 (LRP-1), and clearance along perivascular compartments (Bell et al., 2009; Cirrito et al., 2005; Iliff et al., 2013a; Kress et al., 2014; Paresce et al., 1996; Wyss-Coray et al., 2003; Xie et al., 2013). During waking hours, when CSF-ISF exchange and amyloid β clearance are markedly reduced, interstitial and CSF levels of amyloid β increase in mice and humans, respectively (Kang et al., 2009; Xie et al., 2013). Then with the onset of sleep, when perivascular CSF-ISF exchange is active and interstitial amyloid β clearance is more rapid, interstitial amyloid β levels decline.

In the aging brain, BBB amyloid β efflux pathways are impaired, including the down-regulation of PGP and LRP-1, resulting in slowed interstitial amyloid β clearance that may contribute to amyloid β aggregation and subsequent neurodegeneration (Deane et al., 2009). Amyloid β efflux transporter expression within the CP, however, increases in the aging brain, suggesting a potential compensatory role for the CP and blood-CSF-barrier (BCSFB) in the elimination of amyloid β from the ventricular CSF and associated ISF (Pascale et al., 2011). CSF secretion by the CPs slows with age and with the onset of AD and the deposition of amyloid β within the CP (Masseguin et al., 2005; Silverberg et

al., 2001), reducing the rate of CSF turnover and the efficacy of amyloid β clearance with the bulk reabsorption of CSF via arachnoid villi and along cranial nerve sheaths.

Impairment of glymphatic pathway function, including perivascular CSF-ISF exchange and the clearance of interstitial amyloid β, is similarly a feature of the aging brain (Kress et al., 2014). Whether slowing of perivascular CSF flux through the aging brain is in part the result of reduced CSF secretion by the CP is unclear. Experimentally impairing CSF secretion by administration of the carbonic anhydrase inhibitor acetazolamide, slows CSF-ISF exchange, suggesting that reduced CSF secretion at the CP may contribute to impaired glymphatic pathway function in the aging brain (Plog et al., 2015). As previously mentioned, perivascular AQP4 localization is also markedly reduced in the aging brain and is significantly associated with slowing of perivascular CSF influx into the brain parenchyma (Kress et al., 2014). Whether loss of perivascular AQP4 localization promotes amyloid β aggregation in the aging brain has not yet been formally evaluated. Yet the ability of amyloid β deposits, either in the form of senile plaques or in the form of CAA, to cause mis-localization of AQP4 suggests the presence of a feed-forward pathogenic cycle, with reactive astrogliosis impairing glymphatic pathway function and amyloid β clearance, promoting amyloid β deposition, which in turn causes further neuroinflammation and glymphatic pathway dysfunction. It is worth noting however that a recent study found that deletion of AQP4 reduced the density of GFAP-positive processes surrounding plaque formations in a mouse model of amyloid β deposition (Smith et al., 2019). The authors propose that this reflects the role that AQP4 plays in structural remodeling of reactive astrocytes.

NFTs are a second histopathological feature associated with AD. Tau is a microtubule associated protein that in healthy cells is involved in stabilization of microtubules and is localized to neuronal axons. Under physiological conditions, phosphorylation is important for modulation of tau binding to microtubules and tau is the target of several kinases, including cdk5, PKA, and CaMKII among others (Billingsley and Kincaid, 1997). NFTs occur when tau becomes abnormally phosphorylated, dissociates from microtubules, relocates to the somato-dendritic compartments of the cell, and forms tangles. Whether aging or disease-related changes in CSF circulation or glymphatic pathway function promote NFT formation in AD remains speculative. Recent

studies utilizing in vivo microdialysis in mice suggests that tau is released into the interstitium of the healthy young brain during synaptic activity (Yamada et al., 2014). Other recent studies suggest that tau aggregates can pass from cell to cell through the extracellular compartment, seeding aggregate formation in neighboring cells in a 'prion-like' manner (Holmes and Diamond, 2014). These findings provide a powerful mechanistic explanation for the classical neuroanatomical spread of neurodegenerative diseases characterized by the mis-accumulation of protein aggregates, including AD. Moreover, they suggest the intriguing possibility that age- and disease-associated changes in processes that determine the dynamics of macromolecular movement within and clearance from the brain interstitium, including CSF circulation and glymphatic pathway function, may be intimately involved in the spread of protein aggregates along neuroanatomical pathways.

Another clinical condition frequently associated with AD that may be affected by changes in CSF circulation is CAA. As described above, the widely accepted model of CAA pathogenesis proposed by Weller and Carare posits that under physiological conditions amyloid $\beta_{1\text{-}40}$ is cleared along perivascular spaces surrounding penetrating and leptomeningeal arteries in a direction opposite to that of blood flow, while the impairment amyloid $\beta_{1\text{-}40}$ clearance along these routes leads to the deposition of amyloid $\beta_{1\text{-}40}$ within the walls of cerebral arteries (Weller et al., 2009) in CAA. This direction of flow in the perivascular space is in opposition to the recent studies done by the Nedergaard lab. One possible explanation for these discrepancies is that fluid and solutes move both outward and inward along different glial-vascular elements within the perivascular space, with amyloid β efflux occurring along the cerebral arterial basement membrane and subarachnoid CSF influx occurring through a space immediately bounded by astrocyte endfeet (Figure 1.1B). A second possibility is that fluid and solute movement can occur in both directions depending on physiological or pathophysiological context, and that these differences are revealed under the different experimental conditions in these studies. Currently, the basis of these discrepancies remains unclear.

The recent observations of Iliff, Nedergaard and colleagues showing CSF tracer circulation into the brain along penetrating cerebral arteries suggest that amyloid β-laden CSF from the subarachnoid space may in fact be re-circulating into and through the brain

along perivascular pathways. Under physiological conditions, with intact BBB amyloid β efflux mechanisms, this recirculating amyloid β would be readily eliminated. However, in the aging or injured brain in which endogenous mechanisms of BBB amyloid β efflux are impaired, recirculation along perivascular spaces may promote amyloid β deposition within the arterial wall. This model may explain the pattern of amyloid β deposition seen in post mortem studies, including the finding that amyloid β deposition is greatest in pial arteries and decreases in deeper layers of the cortex.

Parkinson's Disease and synucleinopathies

The second most common neurodegenerative disease is Parkinson's disease (PD), a progressive motor disorder, characterized histopathologically by the occurrence of intracellular inclusions of insoluble α-synuclein. The occurrence of these inclusions, called Lewy bodies, is the defining characteristic of a broader class of neurodegenerative diseases called 'synucleinopathies', which includes PD, multiple system atrophy and dementia with Lewy bodies, among several more. Interestingly several of these demonstrate a progressive distribution of aggregates across neuroanatomical regions that seems to correlate with clinical severity of the disease.

α-Synuclein is a small (14 kD) protein found predominantly in pre-synaptic neuronal terminals. While the exact function is unknown, it is thought that it contributes to the machinery necessary for exocytotic release of synaptic vesicles (Burre et al., 2014). α-Synuclein also interacts with other cellular compartments which may also contribute to the pathology observed in PD and other synucleinopathies (Burbulla et al., 2017). Interestingly, it has been proposed that the oligomeric species of α-synuclein may have a physiological role in promoting the formation of the SNARE complex at the synapse (Burre et al., 2014). The oligomeric form of α-synuclein is thought to serve as a precursor to the insoluble aggregates observed in PD and may serve as a template for a 'prion-like' seeding of further aggregate formation, as discussed below. It is possible that these physiologically relevant forms of the protein may be responsible for triggering Lewy body formation.

Like amyloid β and tau for AD, a stereotyped, progressive neuroanatomical distribution of α-synuclein is observed in PD (Braak et al., 2003). Classically, this

distribution was attributed to selective vulnerability of brain regions and cell types within those regions to α-synuclein aggregation. However, recent studies suggest intercellular trafficking of pathological α-synuclein 'templates' the formation of new aggregates in the downstream cell. The strongest evidence supporting this mechanism is derived from the occurrence of α-synuclein aggregation in healthy dopaminergic neurons transplanted into PD patients (Li et al., 2008a). Since this time, building evidence in rodent models supports a role for intercellular transmission of α-synuclein in Lewy body formation and synucleinopathy progression (Luk et al., 2012a; Luk et al., 2012b; Recasens et al., 2014; Volpicelli-Daley et al., 2011). These studies have demonstrated that various isoforms of fibrillary α-synuclein are capable of triggering the propagation of aggregates in both murine and primate models. There remains however, abundant evidence of other factors influencing α-synuclein aggregation, including environmental factors, TBI, and the microbiome. Relative contributions of these various factors remain to determined.

Studies involving the contribution of CSF-ISF exchange to α-synuclein distribution and clearance are few. Several studies have investigated CSF abundance of α-synuclein as a biomarker for disease progression in PD and other synucleinopathies. While high variability has been reported, meta-analysis studies suggest a decrease in CSF synuclein in PD (Eusebi et al., 2017). Consistent with this, a recent study using a transgenic mouse model of α-synuclein aggregation found that blocking CSF drainage from the cranium via ligation of the deep cervical lymph nodes, exacerbated α-synuclein accumulation and impaired CSF-ISF exchange (Zou et al., 2019). Furthermore, the authors demonstrated that in this mouse model perivascular AQP4 localization was reduced. Interestingly, PD patients also show sleep disruptions (Schreiner et al., 2019). Together these results highlight intriguing associations between CSF-ISF exchange and the progressive nature of synculeinopathies.

Neurovascular Disease: Stroke, TBI and Subarachnoid Hemorrhage

Brain injury, including ischemic and traumatic injury (TBI), are two key contributors to human death and disability and are associated with substantial disruption of CSF circulation, which in turn, may promote secondary injury and impede recovery of surviving tissue. The CP may be directly damaged by either ischemic or traumatic injury,

leading to the breakdown of the BCSFB and the accumulation of fluid within the cranium (Sharma et al., 2006). Compounding these effects, debris mobilized within the CSF from the ischemic or traumatic lesion may interrupt CSF flow and block CSF reabsorption sites, leading to a dangerous increase in intracranial pressure that can result in further tissue ischemia and ultimately brain herniation (Johanson et al., 2011). Breakdown of the BCSFB following ischemic or traumatic brain injury may also increase its permeability to leukocyte trafficking, promoting immune cell infiltration into the injured brain (Carlos et al., 1997).

Beyond the acute and subacute effects of ischemic or traumatic brain injury, these conditions are also associated with the development of dementia, including vascular dementia and Alzheimer's disease, in the years following injury (Smith et al., 2013; Vinters et al., 2000). In addition to regional ischemic infarcts, small ischemic lesions, including microinfarcts and lacunar infarcts, are key contributors to the development of vascular dementia (Haglund et al., 2006). Similarly, although moderate-to-severe TBI is most widely reported to be associated with an increase in AD risk, exposure to even a single episode of mild TBI (or concussion) may be sufficient to confer vulnerability to the development of early onset dementia (Guo et al., 2000; Nordstrom et al., 2014; Plassman et al., 2000). Recently published studies suggest that the association between TBI, including mild TBI, and ischemic injury, including relatively small microvascular lesions, may exert widespread and long-lasting effects upon glymphatic pathway function, rendering the injured brain vulnerable to protein mis-aggregation and neurodegeneration.

In a mouse model of moderate-to-severe TBI, perivascular AQP4 localization was lost in reactive astrocytes throughout the cortex for at least 28 days post-injury (Ren et al., 2013). In the same model, a subsequent study reported that impairment of perivascular AQP4 localization after TBI is associated with persistently impaired glymphatic function, slowing perivascular CSF influx into the brain and the clearance of ISF solutes from the brain (Iliff et al., 2014). Importantly, when CSF-ISF exchange was reduced by genetic deletion of the *Aqp4* gene, levels of phosphorylated tau in the post-traumatic cortex increased and neurocognitive function worsened 28 days post-injury, suggesting that chronic impairment of glymphatic function after TBI may promote

protein mis-aggregation and neurodegeneration in the post-traumatic brain. Although glymphatic function has not yet been evaluated in an experimental model of mild TBI, perivascular AQP4 localization was lost to a similar extent after mild TBI as for moderate-to-severe TBI, suggesting that similar processes may be at work (Ren et al., 2013).

Similar results are observed in experimental models of cerebral ischemia. In a mouse model of focal cerebral ischemia, the influx of intracisternally-injected MRI contrast agent was evaluated. During the acute ischemic period, glymphatic pathway function was impaired in the ipsilateral cortex, while 24 hours after ischemia after re-canalization of the occluded artery had occurred, CSF tracer influx returned to baseline values (Gaberel et al., 2014). In another mouse model of transient cerebral ischemia, Badaut and colleagues reported that AQP4 expression was increased while perivascular AQP4 localization was reduced 48 hours after ischemic injury (Hirt et al., 2009; Ribeiro Mde et al., 2006). In a third model of diffuse cerebral microinfarcts, Wang et al. reported that microscopic vascular lesions were associated with wide fields of reactive astrogliosis, with persistently reactive astrocytes exhibiting reduced perivascular AQP4 localization for up to 28 days after injury (Wang et al., 2012). These findings suggest that in the chronic phase after ischemic injury, persistent loss of perivascular AQP4 localization in reactive astrocytes may impair glymphatic pathway function and the associated clearance of harmful interstitial solutes such as amyloid β, promoting neurodegeneration in the post-ischemic brain.

Traumatic and ischemic brain injury share many common pathological features, such as BBB disruption, cerebral edema, and the development of neuroinflammation including the induction of reactive astrogliosis. As observed in the aging and AD brain, loss of perivascular AQP4 localization appears to be a general feature of reactive astrocytes in the post-traumatic and post-ischemic brain (Fukuda et al., 2012; Lu et al., 2011; Ren et al., 2013). Based upon these findings, Iliff, Nedergaard and colleagues have proposed that persistent reactive astrogliosis in the injured brain chronically impairs glymphatic pathway function, promoting protein mis-aggregation and neurodegeneration, and perhaps providing the basis for the association between ischemic and traumatic brain injury and the development of dementia later in life.

In the setting of subarachnoid hemorrhage (SAH), blood entering the subarachnoid CSF compartment causes a direct increase in ICP. Changes in CSF circulation, including the occurrence of hydrocephalus is secondary to the blockage of CSF efflux routes such as the arachnoid villi by fibrin clots and other blood components (Black et al., 1985). Studies in experimental animal models of SAH in monkeys, cats, and mice suggest that intrathecal anti-coagulation or fibrinolysis can restore CSF outflow resistance to normal levels and restore CSF flow through the subarachnoid space (Blasberg et al., 1981; Brinker et al., 1991; Siler et al., 2014). In two studies carried out in mice, perivascular CSF influx into the brain was reduced after induction of experimental subarachnoid hemorrhage. In both cases, glymphatic function was at least partially restored with the intrathecal administration of the fibrinolytic tissue-type plasminogen activator (tPA) (Gaberel et al., 2014; Siler et al., 2014). Siler et al. reported that improvement of perivascular CSF circulation with intrathecal tPA was associated with both reduced ICP and improved cortical blood flow 24 hours after hemorrhage, suggesting that impairment of glymphatic function after SAH may contribute to secondary injury progression in this neurovascular condition.

Neuroinflammatory diseases

In addition to neurodegenerative diseases and brain injury, another class of neurological disorders afflicting the CNS that is closely tied to CSF function are neuroinflammatory disorders. The most common and most extensively studied of these is multiple sclerosis (MS). MS is characterized by loss of oligodendrocyte myelination of CNS neurons which is thought to result from the autoimmune destruction of these cells.

One of the key determinants to CNS autoimmune disease progression is access of peripheral immune cells to their CNS targets. Within the cerebral vasculature, infiltration of peripheral immune cells is restricted by the BBB. Interestingly, in the rodent experimental autoimmune encephalomyelitis (EAE) model of MS, clinical indicators of disease progression are only observed when immune cells leave perivascular spaces surrounding post-capillary venules to reach the wider brain parenchyma, suggesting that both the glial limitans and the perivascular astroglial ensheathment of the cerebral vasculature function to restrict immune access to the CNS (Bartholomaus et al., 2009;

Lucchinetti et al., 2011). In addition, CNS endothelial cells constitutively express CXCL12 which binds CXCR4 expressing T-cells and prevents their exit from perivascular and leptomeningeal locations during immune surveillance (McCandless et al., 2008; McCandless et al., 2006).

In the healthy brain, the BCSFB at the CP serves as an entry point of peripheral immune cells into the CSF. From here, peripheral immune cells appear to circulate through perivascular, leptomeningeal and ventricular CSF compartments, but do not penetrate into the brain parenchyma. From these locations, it is widely believed that these peripheral immune cells conduct immune surveillance of the brain (Engelhardt and Ransohoff, 2012). In MS, the CP is suggested to provide the route utilized by auto-aggressive T-cells to gain access to the brain parenchyma. This process includes the breach of the BCSFB by T-Cells, permitting access to the ventricular CSF compartment. The mechanisms governing this process are still under investigation, however some evidence suggests that CCR6 T-helper cells may mediate the crossing of the BCSFB via the CCL20 ligand, which is expressed by CP epithelial cells (Reboldi et al., 2009).

CSF biomarkers have become important for the diagnosis of subsets of autoimmune disorders, a role that will likely increase with further research. The CNS demyelinating autoimmune disorder neuromyelitis optica (NMO), which was for a long time considered a variant of MS, is characterized by transverse myelitis and optic neuritis which are also seen in other autoimmune disorders, which leads to difficulty in distinguishing between this and other diseases. Recently, however, it was discovered that patients with NMO test positive for AQP4 auto-antibodies while MS patients do not (Lennon et al., 2005; Lennon et al., 2004; Reboldi et al., 2009; Roemer et al., 2007). This discovery permitted the differentiation of these conditions from one another and turned attention towards the CSF for identification of other biomarkers distinguishing the two diseases.

This discovery of AQP4-targeting auto-antibodies in NMO poses an interesting question regarding the role of CSF circulation in autoimmune disorders. One can imagine that if auto-antibodies target and inhibit AQP4 in astrocytes, then CSF-ISF exchange may also be disrupted. In addition, in an EAE model of MS, although antibodies targeting AQP4 have not been identified, a loss of perivascular AQP4 localization is observed

(Wolburg-Buchholz et al., 2009). Thus, impairment of AQP4 function, either by targeting by autoantibodies in NMO or by its mis-localization in MS, may lead to further consequences including accumulation of neurotoxic solutes in the parenchyma and progression of neurodegeneration. Further investigation is necessary to clarify the effects of changes in AQP4 function in the development of NMO and MS.

Rationale

As described above, several questions remain unanswered with regards to CSF-ISF circulation, the role that astrocytic endfeet and perivascular AQP4 localization play in these processes, and the significance that impairments of this biology have for neurodegenerative disease progression. In the following chapters, I first elaborate on the deficits in CSF-ISF exchange resulting from disruption of the DAC complex, and the impact that has for the propagation of α-synuclein. Next, I investigate the capacity to modulate AQP4 perivascular localization in vivo using a virus mediated approach, and the consequences this modulation has for CSF-ISF exchange. In the third and fourth chapters, I will describe work done to identify novel elements of the astrocytic endfoot domain, generated from publicly available RNA sequencing (RNAseq) datasets. Finally, I will discuss the conclusion of my studies, as well as future directions in which this research could be taken.

Chapter 2: Deletion of α-syntrophin slows CSF-ISF exchange and promotes α-synuclein aggregate propagation in mice

Matthew J Simon[1,2], Alexandra B Pincus[2], Allison J Schaser[3,4], Vivek K Unni[3,4], Jeffrey J Iliff[1,5] *

[1]Department of Anesthesiology and Perioperative Medicine, [2]Neuroscience Graduate Program, [3]Jungers Center for Neuroscience Research, [4]Department of Neurology, [5]Knight Cardiovascular Institute; Oregon Health & Science University, Portland, OR, USA.

Foreword

This chapter reflects data generated and submitted as a manuscript to Journal of Experimental Medicine. Portions of the data generated in this chapter were created in collaboration with Dr. Vivek Unni and a postdoctoral researcher in his lab (Allison Schaser). Much of the data surrounding α-synuclein propagation was initiated and preliminarily described by Alexandra Pincus, a rotating graduate student. Drs. Schaser and Unni performed the PFF injections as described in Figures 6a. Alexandra Pincus collected the images used for analysis of PFF distribution seen in Figure 6b-c as well as the CSF extraction and ELISA data seen in Figure 6d. Dr. Martin Pike was instrumental to establishing the DCE-MRI imaging paradigm as seen in Appendix A and collecting those data. The rest of the data collection, analysis, figure preparation was performed by me. Drs. Iliff, Unni, Schaser and Alexandra Pincus all reviewed and edited the manuscript.

Abstract

Synucleinopathies are a class of neurodegenerative diseases defined by the aggregation of misfolded α-synuclein. Recent evidence suggests misfolded α-synuclein spreads between cells, seeding new aggregate formation, yet the mechanisms driving intercellular propagation remain unclear. The glymphatic pathway contributes to clearance of brain solutes and is thought to depend on perivascular localization of the astrocytic water channel aquaporin-4 (AQP4). We hypothesized that loss of perivascular AQP4 disrupts glymphatic exchange and exacerbates α-synuclein propagation. Here, we model loss of perivascular AQP4 localization in mice by genetic deletion of the adapter protein α-syntrophin (SNTA1). We find that loss of SNTA1 slows solute exchange into subcortical brain structures including hippocampus and striatum. Congruently, we show that efflux of solutes from the brain is slowed by SNTA1 deletion, and instead these solutes accumulate in deep brain structures. Finally, we demonstrate that SNTA1 gene deletion exacerbates brain-wide α-synuclein aggregation following intracortical inoculation with fibrillary α-synuclein. Our results support a role for the glymphatic pathway in prevention of aggregate propagation.

Introduction

Accumulation of soluble proteins into insoluble aggregates is a defining pathological feature common to a broad range of neurodegenerative diseases including Alzheimer's disease (AD), Huntington's disease (HD), amyotrophic lateral sclerosis (ALS) and Parkinson's disease (PD). Mounting evidence suggests intercellular transmission of these aggregates contributes to the stereotyped progressive neuroanatomical spread of pathology that parallels the clinical progression of several neurodegenerative diseases (Guo and Lee, 2014; Jucker and Walker, 2013). This propagation is perhaps most well established among the synucleinopathies, a family of neurodegenerative diseases which includes PD and dementia with Lewy bodies (DLB), and is typified by the age-associated appearance of α-synuclein inclusions in either neuronal or glial cell bodies (Angot et al., 2010). While cell-cell transmission of α-synuclein aggregates has been demonstrated across several model systems (Li et al.,

2008a; Luk et al., 2012a; Shimozawa et al., 2017; Volpicelli-Daley et al., 2011), and is modulated by the isoform of aggregated α-synuclein (Bousset et al., 2013; Luk et al., 2012b; Peng et al., 2018; Samuel et al., 2016), whether or not host physiology within the brain environment alters the dynamics of this propagation remains unknown.

Several mechanisms have been proposed to govern intercellular aggregate transmission, including synaptic transmission, extracellular vesicle release and release by damaged or dead cells (Valdinocci et al., 2017), however the relative contributions of each to total α-synuclein aggregate propagation is unclear. Common among each of these is the obligatory transit of aggregates, either freely floating or enclosed within a vesicle, through the brain interstitium (i.e. extracellular space). The recent characterization of the "glymphatic" pathway, a brain-wide network of perivascular spaces that regulates the clearance of interstitial proteins including amyloid β (Iliff et al., 2012) and tau (Iliff et al., 2014) through the exchange of cerebrospinal fluid (CSF) and interstitial fluid (ISF) (Iliff et al., 2013a; Iliff et al., 2012; Simon and Iliff, 2016), represents one mechanism that may modulate the dynamics of α-synuclein aggregate propagation. Impairment of glymphatic exchange is observed in the aging (Kress et al., 2014) and post-traumatic brain (Iliff et al., 2014), two states representing risk factors for PD (Gardner et al., 2015; Goldman et al., 2006; Jafari et al., 2013). Thus, impairment of glymphatic function due to aging or following brain injury may promote the process of α-synuclein aggregate propagation.

Perivascular CSF-ISF exchange is dependent upon the astroglial water channel aquaporin-4 (AQP4), which localizes to perivascular astrocytic endfeet ensheathing the brain vasculature (Iliff et al., 2012; Mestre et al., 2018a) (Appendix A). In mice, deletion of *Aqp4* slows perivascular CSF-ISF exchange and accelerates amyloid β and tau aggregate formation (Iliff et al., 2014; Xu et al., 2015), while impairment of glymphatic function in aging (Kress et al., 2014), TBI (Iliff et al., 2014; Ren et al., 2013) and ischemic injury (Wang et al., 2017; Wang et al., 2012) are each associated with the loss of perivascular AQP4 localization. In human subjects loss of perivascular AQP4 localization is associated with AD status and pathology (Zeppenfeld et al., 2017). However, whether loss of perivascular AQP4 localization impairs glymphatic function has not been directly evaluated.

In the present study we use a transgenic mouse model to determine if loss of perivascular AQP4 localization impairs brain CSF-ISF exchange. We then investigate whether impairment of glymphatic function alters the exchange of α-synuclein between the ISF and CSF compartments. Lastly, we test if impairment of glymphatic function accelerates propagation of α-synuclein aggregates in a seeding/propagation model.

Results

Perivascular CSF-ISF exchange is impaired in the Snta1$^{-/-}$ mouse

α-Syntrophin (SNTA1) is an adapter protein that couples AQP4 to the capillary basal lamina via its binding to the dystrophin-associated complex, a macromolecular scaffolding complex found in astrocytic endfeet (Adams et al., 2000; Nagelhus and Ottersen, 2013). To directly assess the role of perivascular AQP4 localization in CSF-ISF exchange, we utilized the α-syntrophin (*Snta1*$^{-/-}$) knockout mouse line, which expresses normal levels of AQP4 yet is reported to lack perivascular AQP4 localization. As previously demonstrated using electron microscopy (Amiry-Moghaddam et al., 2003; Neely et al., 2001), we observed by immunofluorescence that *Snta1*$^{-/-}$ mice lack perivascular AQP4 localization yet overall AQP4 immunoreactivity remains largely unchanged (Figure 2.1a). We further investigated which vessel types exhibit altered perivascular localization in the *Snta1*$^{-/-}$ mice by evaluating localization at capillaries (~5μm diameter), large vessels (~25μm diameter), and the glia limitans (Figure2.1b-d). Semi-quantitative analysis by immunoblot shows loss of SNTA1 expression in *Snta1*$^{-/-}$ mice (Figure 2.1e, n = 4 per group, P = 0.029), while expression of AQP4 remains unchanged between *Snta1*$^{-/-}$ and wild type mice (Figure 2.1f).

Prior studies demonstrated that loss of perivascular AQP4 localization is correlated with glymphatic pathway impairment (Iliff et al., 2014; Kress et al., 2014; Wang et al., 2017). To evaluate glymphatic function, CSF tracer influx into brain tissue was measured using whole-slice fluorescence microscopy following intracisternal tracer infusion in both wild type and *Snta1*$^{-/-}$ mice (Figure 2.2a). CSF tracers of different molecular weights distribute into and through the brain parenchyma along different pathways (Bedussi et al., 2015; Iliff et al., 2012). As shown in wild type animals in

Figure 2.2b-c, small molecular weight tracers (10 kD dextran), enter superficial brain structures across the glial limitans at the pial surface and enter deeper brain structures along perivascular spaces surrounding penetrating arteries. Intermediate molecular weight tracers (70 kD dextrans), cross the pial surface much less readily, but enter both superficial and deep brain structures along perivascular spaces surrounding penetrating arteries to exchange throughout the interstitial compartment. Large molecular weight tracers (2000 kD dextrans), do not cross the pial surface but enter the brain along perivascular spaces. Unlike smaller tracers, 2000 kD dextrans do not appreciably cross from the perivascular compartment into the wider neuropil.

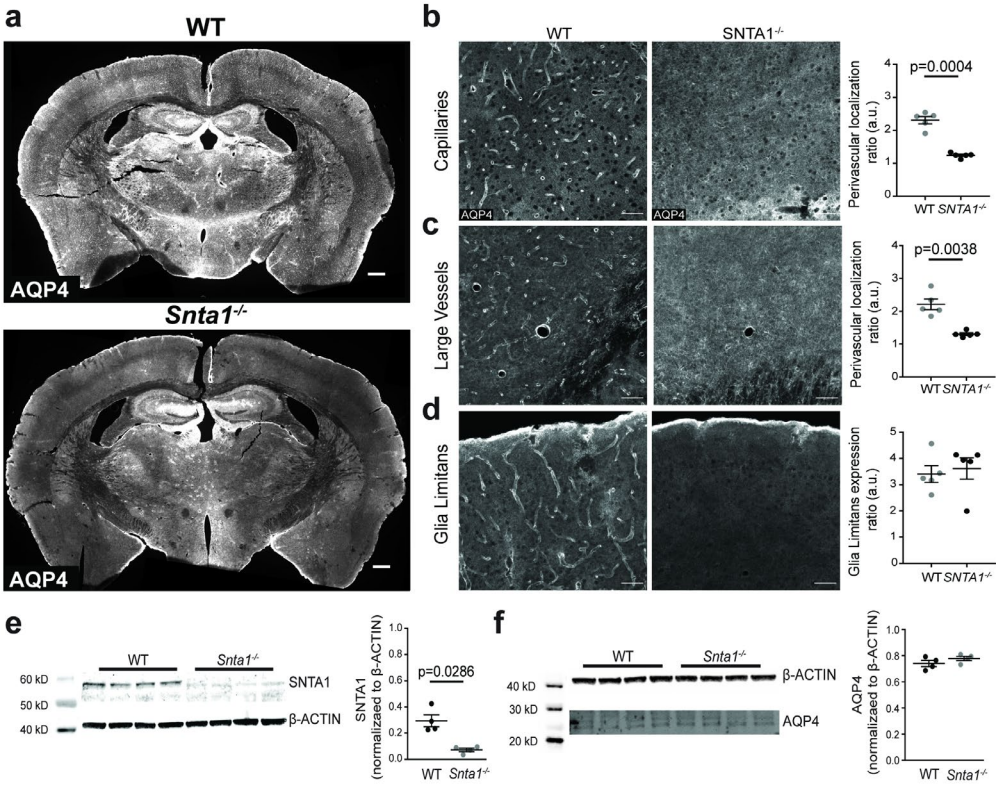

Figure 2.1: α-syntrophin deletion eliminates perivascular localization of AQP4 but maintains AQP4 protein expression.

(a) Full-brain immunofluorescence labeling of AQP4 reveals the robust loss of perivascular localization in Snta1-/- mice. Scale bars = 500 µm. (b-d) perivascular localization was characterized at capillaries (b), large vessels (c) and the glia limitans (d), revealing loss of AQP4 localization at capillaries and large vessels of Snta1-/- mice. Scale bars = 50 µm (n=5 animals / group, Mann-Whitney U test). (e-f) Western blot quantification confirms the loss of α-syntrophin expression in Snta1-/- mice (e) but maintained expression of AQP4 (f).

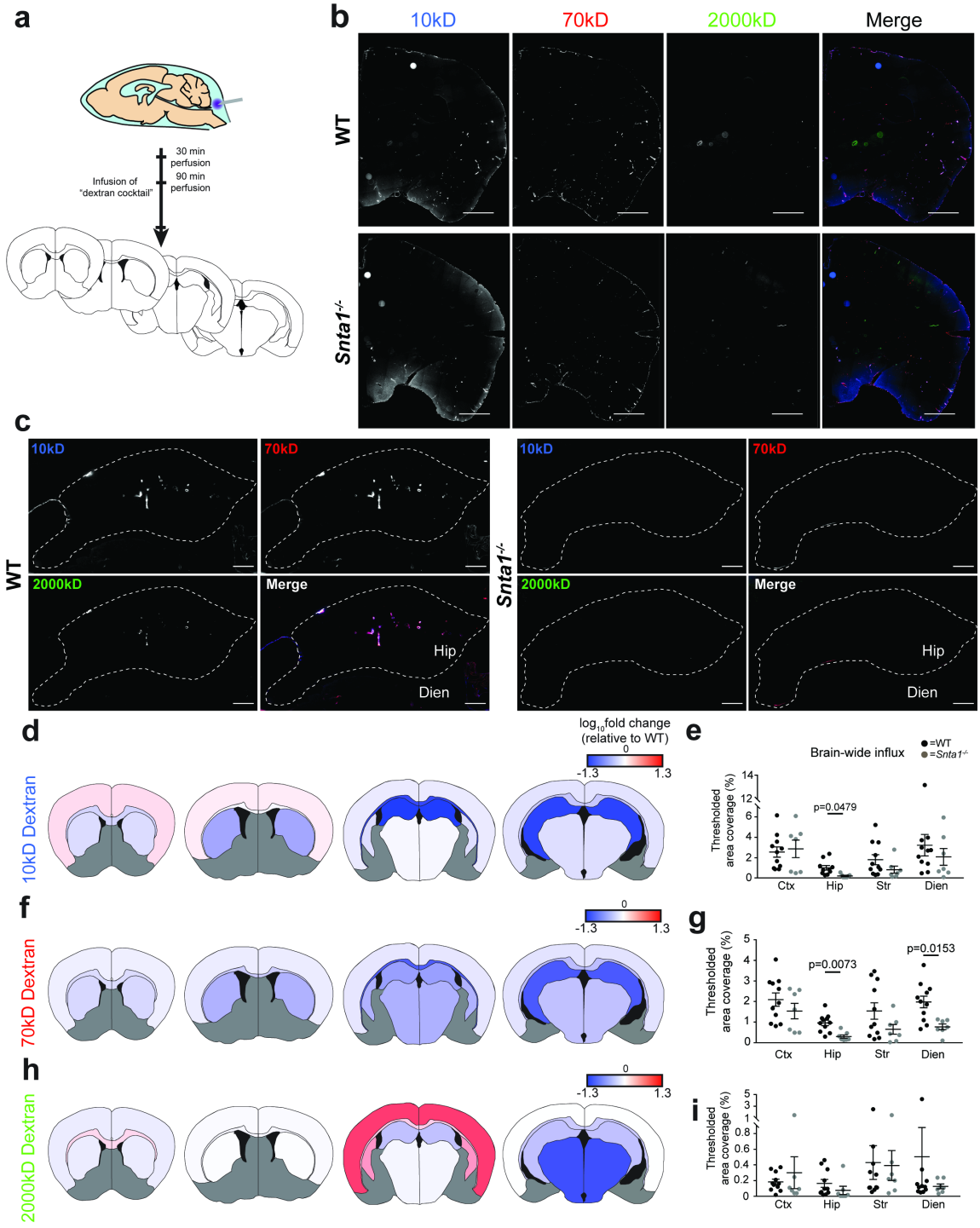

Figure 2.2: Deletion of α-syntrophin slows CSF tracer influx into the brain.

(a) Schematic representation of CSF influx studies. (b) Representative confocal images of dextran distribution within the brain 90 min post-injection. Dextrans 10kD (far left), 70kD (center left), 2000kD dextrans (center right) are all shown along with a composite image at right (n = 7-11 animals/group). Scale bars = 1000 µm. (c) Confocal imaging of tracer presence in the hippocampus demonstrates sub-regional genotype differences and size dependent distribution away from the perivascular space. Scale bars = 250 µm. (d,f,h) Heat map representations of regional dextran influx differences between wild type and Snta1-/- mice at 90 minutes post infusion for 10 kD (d), 70 kD (f) and 2000 kD (h) dextrans. Differences shown as a log10 transformation of the regional area coverage as determined by thresholding, normalized to wild type animals. Grey regions were not evaluated. (e,g,i) Integrated regional area coverage across all 4 sections evaluated for the 10 kD (e), 70 kD (g) and 2000 kD (i) dextrans in cortex (Ctx), hippocampus (Hip), striatum (Str) and the diencephalon (Dien). Adjusted P values provided for regions in which statistically significant associations were observed (Multiple t-tests with Holm-Sidak correction, n = 7-11/group). Black bars represent the mean ± S.E.M.

To define the effect of *Snta1* gene deletion on CSF influx along these different pathways, a cocktail of three fluorescent tracers of various sizes (Cascade Blue-conjugated 10 kD dextran (CB-10kD), Texas Red-conjugated 70 kD dextran (TR-70kD), and FITC-conjugated 2000 kD dextran (FITC-2000kD)) was infused into the cisterna magna of 10-16 week-old mice anesthetized with ketamine/xylazine (0.10 mg/g, 0.01 mg/g ip, respectively). Animals were perfused 30 and 90 minutes post-infusion and tracer distribution was imaged by whole-slice fluorescence imaging. Tracer influx was observed along the vasculature and proximal to the pial surface (Figure 2.2b-c). Tracer distribution was evaluated as a proxy for CSF influx. To measure tracer distribution, a thresholded area coverage of tracer in the cortex (CTX), hippocampus (HIP), striatum (STR) and the diencephalon (DIEN) was measured and integrated across four coronal sections per animal located at 1.0, 0, -1.5 and -2.5 mm relative to bregma.

At 90 min post-injection, penetration of CB-10kD was reduced in deep brain structures of *Snta1*$^{-/-}$ compared to wild type mice, as depicted in the heat maps from each coronal slice (Figure 2.2d). This effect was significant in the HIP, integrated across all four coronal sections (Figure 2.2e, $P_{adj} = 0.048$, n = 7-11 per group). TR-70KD penetration at 90 min was reduced in the HIP and DIEN (Figure 2.2f-g, $P_{adj} = 0.007$, 0.015, respectively), while reductions in the CTX and STR did not reach statistical

significance. Penetration of FITC-2000kD did not differ between *Snta1*$^{-/-}$ and wild type animals (Figure 2.2h-i). Consistent with dynamic contrast-enhanced MRI experiments, no effect of *Snta1* gene deletion was observed for any tracer at 30 min post-injection (Supplementary Figure 2.1, Appendix A), suggesting that the CSF-ISF exchange phenotype of the *Snta1*$^{-/-}$ mice is muted relative to that observed for global *Aqp4* gene knockout (Iliff et al., 2012; Mestre et al., 2018a) (Appendix A). It is also noteworthy that cortical CSF tracer influx was not altered in any setting. Recent evidence suggests that diffusion of small molecules occurs across the pia mater and glial limitans (Bedussi et al., 2015; Iliff et al., 2012). Qualitative assessment of cortical regions and brain surface images suggests that in *Snta1*$^{-/-}$ mice diffusion of 10kD and 70kD dextrans across the pial surface of the brain may be enhanced compared to wild type animals (Figure 2.2b-c, Supplemental Figures 2.1-2.2). It is possible that this effect masked the impact of *Snta1* gene deletion on perivascular tracer distribution observed in deeper brain structures.

Snta1 gene deletion slows interstitial solute efflux

To define the effect that loss of perivascular AQP4 localization has on interstitial solute efflux, we evaluated the distribution of 10 kD dextrans following intraparenchymal injection in *Snta1*$^{-/-}$ and wild type mice. Tracer was infused into motor cortex and allowed to distribute for 120 min prior to fixation and whole-slice fluorescence microscopy. Distribution was defined by area coverage of tracer fluorescence within CTX, HIP, STR and DIEN integrated across five coronal slices per animal (1, 0, -1.5, -2.5 and -3.5 mm relative to bregma, Figure 2.3a). Following intracortical injection, CB-10KD distributed through the CTX, and into the subcortical regions HIP, STR and DIEN (Figure 2.3b). When compared to wild type mice, tracer levels in deep structures such as STR, HIP, and DIEN remained elevated in *Snta1*$^{-/-}$ mice at 120 min after injection. CB-10KD fluorescence integrated across all slices exhibited a trend towards globally elevated levels in *Snta1*$^{-/-}$ relative to wild type animals (Figure 2.3c, e, P=0.067) and significantly increased levels in the STR (Figure 2.3d, Padj = 0.003, n = 12-15 per group). A trend towards increased levels in the DIEN was also observed (Padj = 0.108).

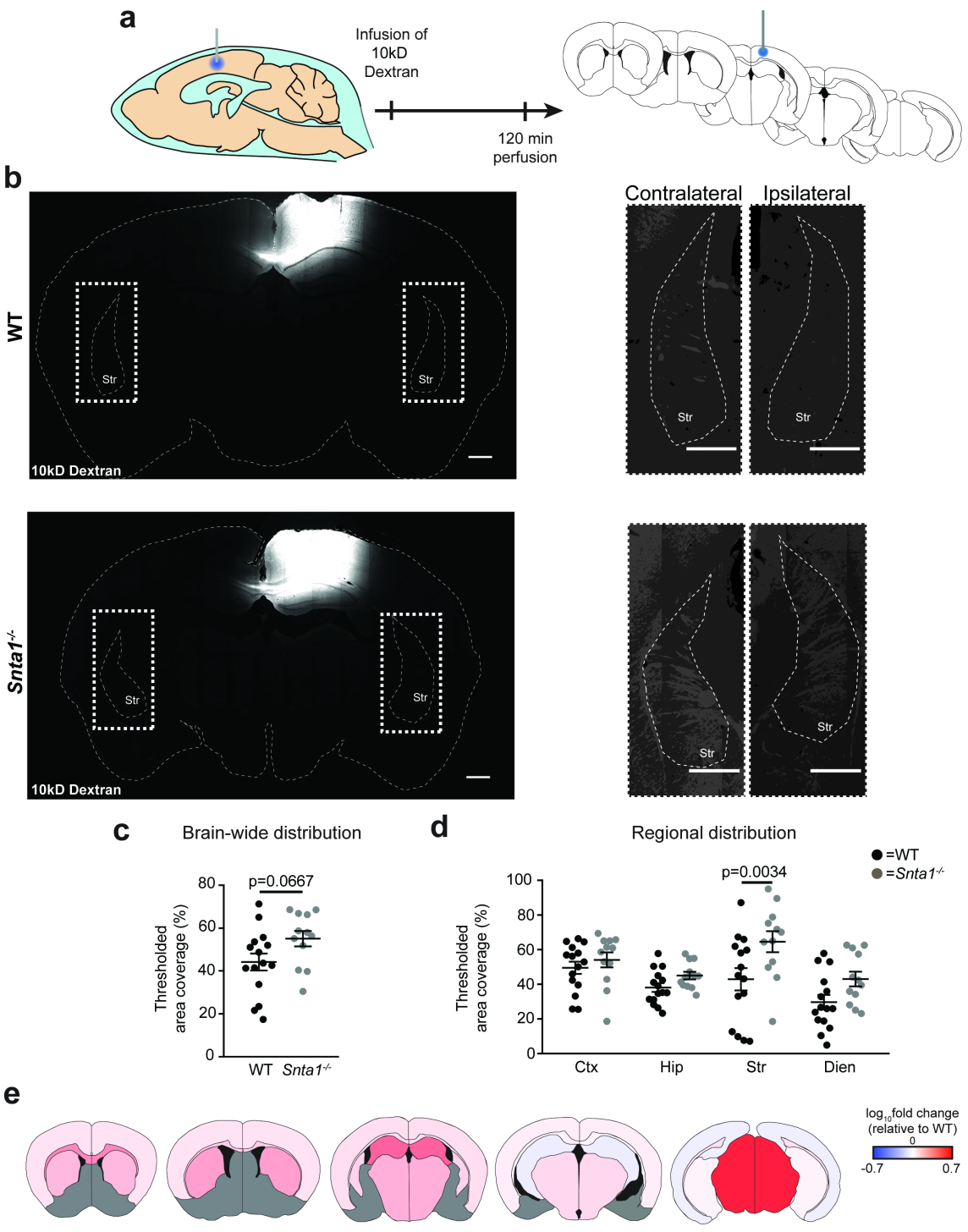

Figure 2.3: Interstitial solute efflux is slowed in *Snta1*$^{-/-}$ *mice.*

(a) Schematic representation of inert dextran efflux studies. Sections at right indicate the coronal sections at which distribution was evaluated. (b) Representative images demonstrating brain-wide tracer distribution 120 minutes post injection Scale bar = 500 µm. Insets at right contain higher magnification images of striatum with scaled fluorescence. Scale bar = 500 µm. (c) Threshold-based assessment of dextran distribution across 5 sections suggests a trend towards elevated dextran levels in *Snta1*$^{-/-}$ mice (P = 0.0667, Mann-Whitney U test, n = 12-15/group). (d) Regional dextran influx was evaluated in CTX, HIP, STR and DIEN regions (P_{adj}=0.0034, Multiple t-tests with Holm-Sidak correction, n = 12-15/group). (e) Heat map characterization of regional 10kD dextran distribution differences between wild type and *Snta1*$^{-/-}$ mice at 120 minutes post cortical infusion integrated across all five sections. Differences shown as a $\log_{10}$ transformation of thresholded area coverage, normalized to wild type animals. Grey regions were not evaluated. For all plots, black bars represent the mean ± S.E.M.

Snta1$^{-/-}$ *mice exhibit altered soluble α-synuclein dynamics*

In addition to exogenous tracers, the glymphatic pathway also contributes to clearance of endogenous compounds and proteins, including small molecules such as lactate (Lundgaard et al., 2017) and pathogenic peptides such as amyloid β and tau (Iliff et al., 2014; Iliff et al., 2012; Peng et al., 2016; Xu et al., 2015). We evaluated whether α-synuclein is cleared from the brain along perivascular pathways. Intrastriatal infusions of fluorescently tagged α-synuclein were performed in mice, then fixed 30 min later. Immunofluorescence demonstrated preferential accumulation of fluorescently tagged α-synuclein along perivascular compartments, labeled with DiD (injected iv prior to perfusion) and AQP4 (Figure 2.4a). To assess α-synuclein efflux dependence upon perivascular AQP4 localization, fluorescently tagged α-synuclein distribution was evaluated 120 min after intracortical injection in wild type and Snta1$^{-/-}$ mice (Figure 2.4b-c). Like the inert 10 kD dextran, α-synuclein levels integrated across all regions were greater in the Snta1$^{-/-}$ compared to wild type mice (Figure 2.4d, P=0.040; n = 12-13 per group). This change was driven primarily by elevated α-synuclein in the HIP (Figure 2.4e-f, Padj = 0.015) and in the DIEN (Padj = 0.106) of Snta1$^{-/-}$ compared to wild type mice.

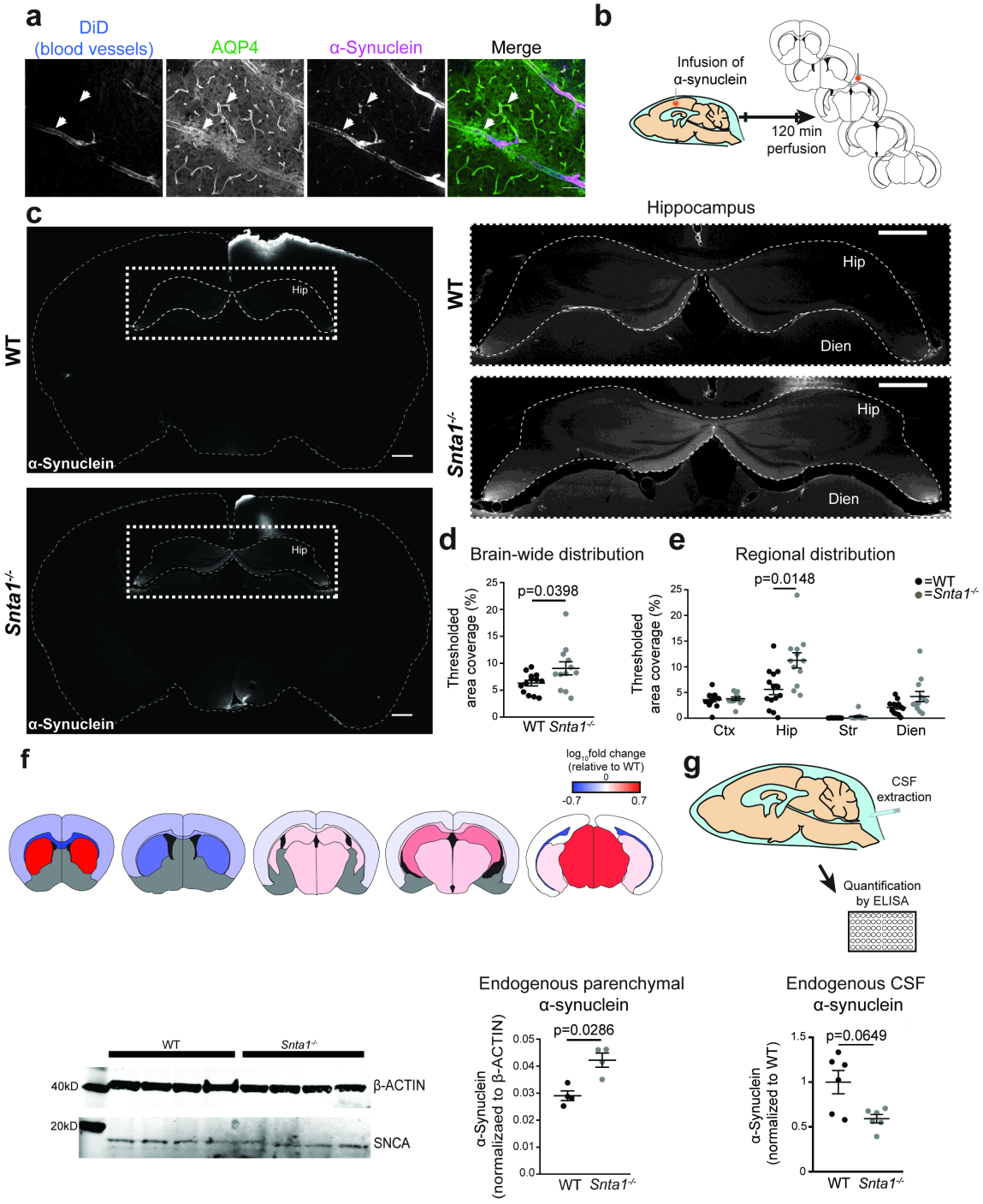

Figure 2.4: Interstitial α-synuclein clearance is impaired in *Snta1*$^{-/-}$ mice.

(a) 30 minutes following intraparenchymal injection of soluble α-synuclein (magenta) in wild type mice, preferential accumulation is observed along the perivascular space of both capillaries and arterioles (arrows). Vessels labeled by vascular infusion of the dye DiD (blue), outer boundary of perivascular space identified by AQP4 immunofluorescence (green). (b) Schematic representation of α-synuclein efflux studies following motor cortex infusion. The five sections at which distribution was evaluated are at right. (c) Representative images demonstrating α-synuclein distribution 120 minutes post injection Scale bar = 500 µm. Insets at right contain higher magnification images of HIP (outlined) with linearly scaled fluorescence. Scale bar = 500 µm. (d) Total area coverage by α-synuclein integrated across all five sections 120 minutes after injection ($P = 0.0398$, Mann-Whitney U test, n=12-15/group) (e) Sub-regional α-synuclein area coverage assessment for CTX, HIP, STR and DIEN. Statistically significant differences are observed in hippocampus (Padj = 0.0148, multiple t-tests with Holm-Sidak correction, n=12-15/group) (f) Heat map characterization of regional α-synuclein distribution differences between wild type and *Snta1*$^{-/-}$ mice at 120 minutes after cortical injection. Differences shown as a log10 transformation of thresholded area coverage, normalized to wild type animals. Grey regions were not evaluated. (g) ELISA-based quantification of homeostatic CSF α-synuclein concentrations following CSF extraction (top) ($P = 0.0649$, Mann-Whitney U test, n = 6/group). Raw α-synuclein concentrations are normalized to the mean wild type CSF α-synuclein concentration. Western blot analysis of total brain homogenate (left) ($P= 0.0286$, Mann-Whitney U test, n= 4/group). For all plots, black bars represent the mean ± S.E.M.

Although the 10kD dextran tracer and α-synuclein (14kD) are of similar molecular weight and exhibit a similar pattern of increased retention in subcortical brain structures of *Snta1*$^{-/-}$ compared to wild type mice, differences in regional distribution (compare Figure 2.3d-e to Figure 2.4e-f) suggest protein interactions within the neuropil may modulate the transport kinetics of these solutes. To evaluate this, we assessed the interaction of both α-synuclein and the CB-10KD with cellular structures within 1 mm^2 of the motor cortex injection site (Supplemental Figure 2.3a). Across both wild type and *Snta1*$^{-/-}$ mice, 10 kD accumulated markedly more in cell bodies (Supplemental Figure 2.3b, $P<0.0001$) and along blood vessels (Supplemental Figure 2.3c, $P<0.0001$) compared to α-synuclein. These findings suggest that differences in cellular uptake or retention within the perivascular compartment may underlie subtle differences in distribution between CB-10KD and α-synuclein following intraparenchymal injection.

To assess the impact that impairment in perivascular CSF-ISF exchange has on endogenous α-synuclein dynamics, we measured α-synuclein levels in the CSF of wild

type and *Snta1*$^{-/-}$ mice by enzyme-linked immunosorbent assays (ELISA). Consistent with retention of interstitial solutes including α-synuclein (Figures 2.3-2.4), CSF α-synuclein levels were 41% greater in wild type (450 ± 58.4 pg/ml) compared to *Snta1*$^{-/-}$ mice (266 ± 21.29 pg/ml) (Figure 2.4g, P = 0.065, n = 5-6 per group).

Exacerbated α-synuclein aggregation in Snta1$^{-/-}$ *mice*

Prior studies have demonstrated that *Aqp4* gene deletion accelerates amyloid β aggregate formation (Xu et al., 2015) and increases phosphorylated tau levels after experimental traumatic brain injury (Iliff et al., 2014). To evaluate whether loss of perivascular AQP4 localization and impaired perivascular CSF-ISF exchange exacerbates pathogenic α-synuclein aggregation and propagation, we utilized a mouse model of synucleinopathy propagation involving a single intracortical inoculation with synthetic α-synuclein pre-formed fibrils (PFFs, Figure 2.5a) (Luk et al., 2012a). Consistent with the initial description of this model, four months following injection of PFFs into the motor cortex of wild type mice, widespread phosphorylated α-synuclein (P-syn) immunoreactivity was detectable in ipsilateral CTX and HIP as well as more distal areas including the contralateral CTX, HIP and STR (Figure 2.5b). Following PFF infusion, the general anatomical distribution of P-syn immunoreactivity did not differ between wild type and *Snta1*$^{-/-}$ mice. However, the number of aggregates was markedly increased in *Snta1*$^{-/-}$compared to wild type mice (Figure 2.5b-c, P = 0.008, n = 5 per group). This increase was greatest in the CTX (P_{adj} = 0.109), but was also observed across the STR, HIP and DIEN (P_{adj} = 0.200). CSF α-synuclein was also evaluated by ELISA in these animals immediately prior to sacrifice. In agreement with the baseline CSF α-synuclein differences reported above (Figure 2.4g), we observed that CSF levels of α-synuclein were 32% lower in *Snta1*$^{-/-}$ mice (1826 ± 329 pg/ml) than in wild type animals (2685 ± 245 pg/ml) 4 months after PFF injection (Figure 2.5d, P = 0.064, n = 4-5 per group). When CSF α-synuclein levels were plotted against parenchymal P-syn immunoreactivity for the wild type (n = 5) and *Snta1*$^{-/-}$ mice (n = 4; due to failed CSF sampling in one animal), a strong significant negative association was observed (Figure 2.5e, P = 0.005, R^2 = 0.706), with lower CSF α-synuclein levels corresponding to greater P-syn immunoreactivity across all animals.

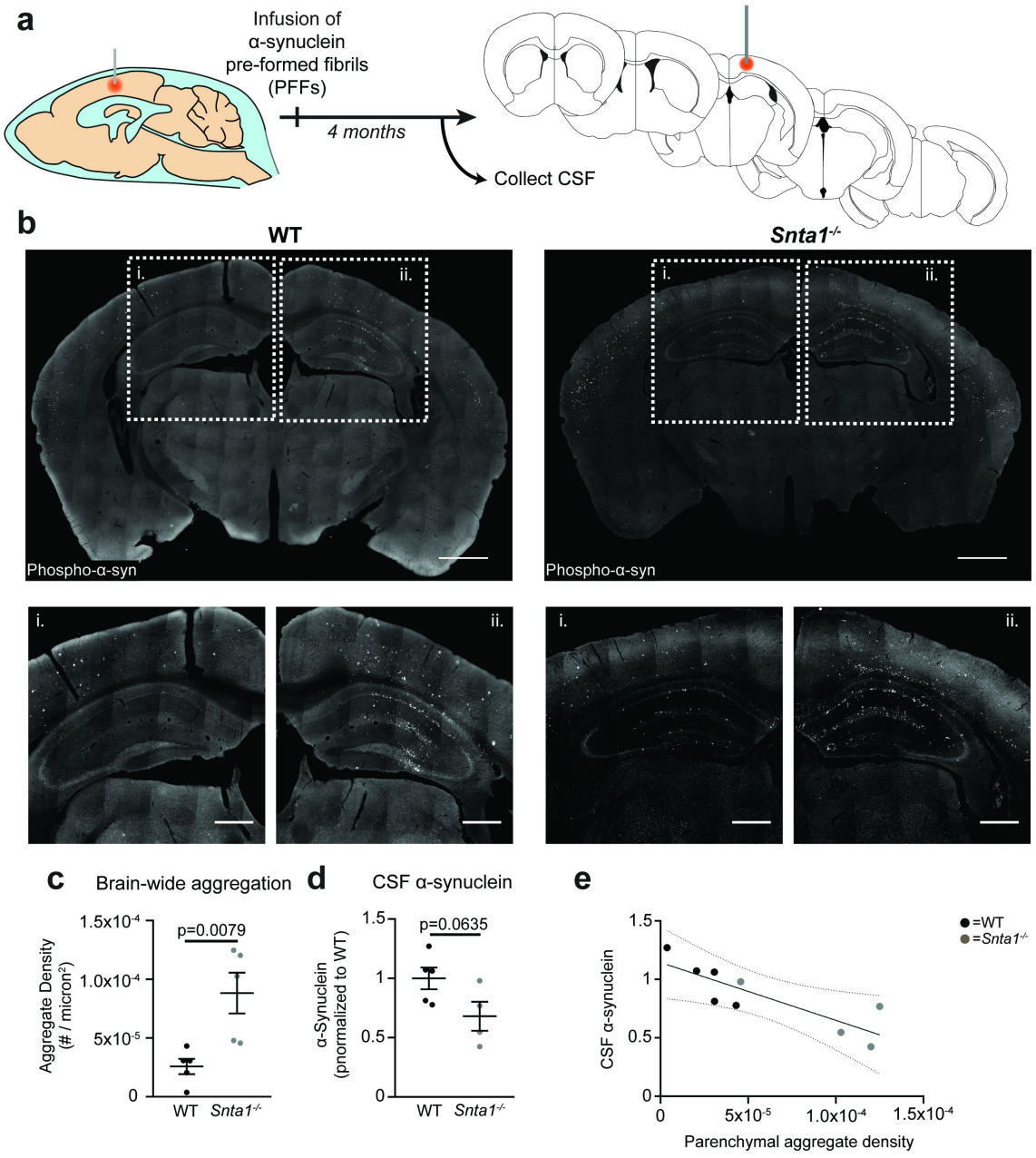

Figure 2.5: Insoluble α-synuclein aggregation is exacerbated in *Snta1*$^{-/-}$ mice following inoculation with PFFs.

(a) Schematic depiction of α-synuclein propagation studies following motor cortex injection of pre-formed fibrils (PFFs). The five coronal sections at which phospho-α-synuclein aggregate burden was evaluated 4 months following injection of PFFs at shown at right. Orange circle represents the site of infusion. (b) Representative images illustrating phospho-α-synuclein distribution in wild type and *Snta1*$^{-/-}$ mice. Scale bar = 1000 μm. Higher magnification images of contralateral (i) and ipsilateral (ii) cortex and hippocampus illustrate abundant aggregation in both regions. Scale bar = 200 μm. (c) Quantification of aggregate density determined by integration of phospho-α-synuclein aggregate counts across five sections reveals elevated global aggregate density in *Snta1*$^{-/-}$ mice (P = 0.0079, Mann-Whitney U test, n=5/group). (d) ELISA-based quantification of CSF α-synuclein concentrations 4 months following PFF injection, normalized to mean wild type values (P=0.0635, Mann-Whitney U test. n = 4-5/group). (e) Plotting aggregate density against CSF α-synuclein levels in individual animals reveals a linear negative association between these values across genotype. (P = 0.005, R-squared = 0.7063, Linear regression, n = 4-5/group). For all plots, black bars represent the mean ± S.E.M.

It has been proposed that pathological aggregate propagation occurs trans-synaptically, transmitting aggregates along synaptically-linked neural circuits. Two alternative possibilities are that aggregate propagation occurs non-specifically between anatomically neighboring cells or regions, or along permissive anatomical routes such as perivascular spaces or within the CSF compartment. To begin to address the contribution of these alternative mechanisms, we sought to compare P-syn immunoreactivity distribution to the known distribution of first order synaptic connections from the motor cortex where PFFs were infused in the present study. We accomplished this using raw tomographic images from the Allen Brain Institute Cell Connectivity Atlas, in which projections from 300 different brain regions were defined by 3D volumetric tract tracing (2011; Oh et al., 2014). Within this database, there are 8 replicate motor cortex injections in C57Bl6J mice with associated 3D tract tracing (one of which is shown in Figure 2.6a). The projection patterns from all 8 replicates were overlaid on an anatomical reference for each of the five coronal slice coordinates utilized for the ISF tracer studies (Figure 2.3-2.4) and P-syn aggregate study (Figure 2.5) above. The summed projections are shown in Figure 2.6b and reflect an inclusive view of all first order retrograde projections from the motor cortex site of PFF injections in the present study. Figure 2.6c-d show the P-syn distribution patterns 4 months after PFF injection. There is notable overlap between the

first order retrograde projections and P-syn immunoreactivity, including in the anterior cortex and posterior thalamic nuclei (Figure 2.6c-d, arrows). However, there are also notable discrepancies. For example, the motor cortex extends many projections bilaterally into the striatum. In wild type mice, very few P-syn-positive puncta were evident in STR 4 months following PFF injection (Figure 2.6c-d, open arrowheads). Conversely, there do not appear to be any first order retrograde projections from motor cortex to the hippocampal formation, and few within the posterior cortical regions. P-syn immunoreactivity was readily seen bilaterally throughout the posterior cortex and hippocampus (Figure 2.6c & f, solid arrowheads). The distribution pattern of P-syn immunoreactivity across the CTX, STR, HIP and DIEN of wild type mice 4 months after motor cortex PFF injection are shown in Figure 2.6g. The differences in P-syn immunoreactivity between *Snta1*$^{-/-}$ and wild type mice are shown on the heat maps in Figure 2.6h. *Snta1* gene knockout increased P-Syn immunoreactivity throughout the mouse brain, with changes being most evident in the striatum, and the posterior cortex and hippocampus.

Immunofluorescence revealed that as previously reported (Luk et al., 2012a), P-syn co-localized with the neuronal marker NeuN (Supplemental Figure 2.4a). Both diffuse P-syn immunoreactivity and dense inclusion bodies were detected in neurons. Unexpectedly, P-syn also co-localized with markers of astrocytes (GFAP) and microglia (Iba1), which do not express high levels of endogenous α-synuclein (Zhang et al., 2014; Zhang et al., 2016) (Supplemental Figure 2.4a-b).

Discussion

Though experimental studies support the role of intercellular propagation of protein aggregates in the pathology of several neurodegenerative conditions such as AD, PD, HD, ALS and DLB (Desplats et al., 2009; Iba et al., 2013; Jeon et al., 2016; Nonaka et al., 2013; Stohr et al., 2012), whether host features influence the rate of aggregate propagation remains unknown. Here we define the effect that loss of perivascular AQP4 localization has on perivascular CSF-ISF exchange and evaluate whether impairment of glymphatic function promotes α-synuclein aggregate propagation. We find that *Snta1*$^{-/-}$ mice, which lack perivascular AQP4 localization, also exhibit impaired glymphatic function, even when overall AQP4 expression remains unchanged. Further, we

demonstrate that loss of perivascular AQP4 localization slows interstitial α-synuclein clearance and reduces CSF α-synuclein levels. Lastly, we show that these changes accelerate propagation of P-syn in a mouse model of α-synuclein aggregation. Based on these findings, we propose that loss of perivascular AQP4 localization slows glymphatic function and promotes propagation of α-synuclein aggregation.

Recent histological studies demonstrate that changes in perivascular AQP4 localization and expression are associated with neurodegenerative disease and brain injury in both murine models and human subjects (Hadjihambi et al., 2018; Hoshi et al., 2017; Wilcock et al., 2009; Yang et al., 2011). Our own data suggest that loss of perivascular AQP4 localization in the aging (Kress et al., 2014), post-ischemic (Wang et al., 2017; Wang et al., 2012), and post-traumatic (Iliff et al., 2014; Ren et al., 2013) brain are associated with impaired glymphatic pathway function. In human post mortem frontal cortex, we observed that loss of perivascular localization predicts AD status and is associated with amyloid β and neurofibrillary pathology (Zeppenfeld et al., 2017). These correlative studies do not, however, resolve whether loss of perivascular AQP4 localization directly impairs glymphatic function or simply reflect age- or injury-dependent changes in glial function, such as reactive astrogliosis.

In a similar manner, studies that have implicated AQP4 in glymphatic pathway function have relied upon global *Aqp4* knockout lines (Iliff et al., 2012; Xu et al., 2015). These approaches are limited in that they do not recapitulate the AQP4 phenotype of the aging and injured brain (in which AQP4 expression increases, while perivascular AQP4 localization is lost), and they do not account for the possible contribution of developmental changes in brain water homeostasis resulting from *Aqp4* gene deletion that may confound findings (Vindedal et al., 2016; Yao et al., 2008). Furthermore, a recent study by Smith et al. failed to recapitulate the impairment in CSF tracer influx in *Aqp4*$^{-/-}$ mice (Smith et al., 2017), though a subsequent study using four distinct *Aqp4*$^{-/-}$ lines in the hands of four different research groups, reasserted that perivascular CSF-ISF exchange is impaired with deletion of the *Aqp4* gene (Mestre et al., 2018a) (Appendix A). By evaluating perivascular CSF-ISF exchange in *Snta1*$^{-/-}$ mice, we sought to address these concerns of previous studies.

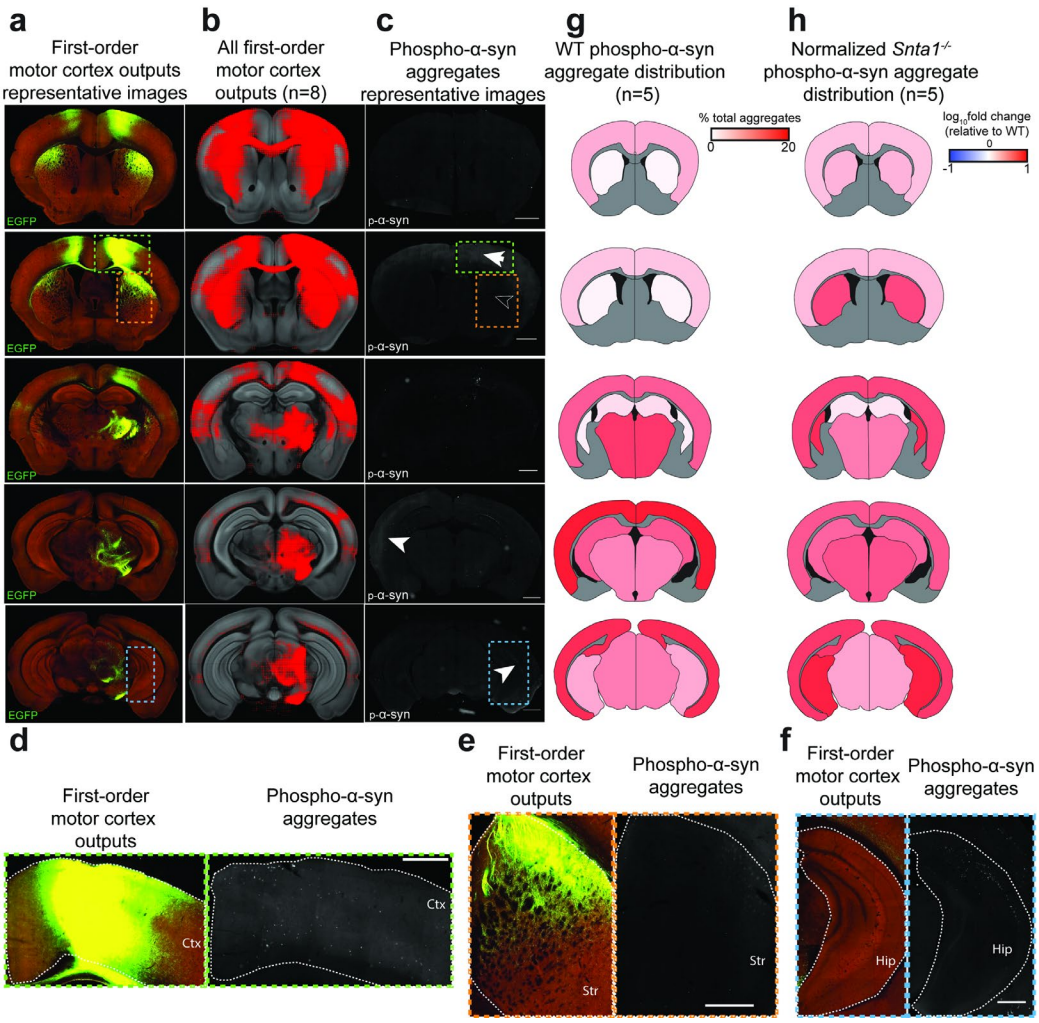

Figure 2.6: α-Synuclein aggregate spread diverges from first-order synaptic projections. (a-b) projections from motor cortex as mapped by rAAV expression of GFP in the Allen Connectivity Atlas are demonstrated for a single injection (a) and summed across all injections (b, n=8). (c) Distribution of phosphorylated α-synuclein aggregates are represented in a single replicate. Regions of overlap between first order inputs and aggregates are labeled with arrows. Unfilled arrowheads indicate regions with first order synaptic projections but sparse aggregate formation. Filled arrowheads label regions with abundant aggregation but few synaptic inputs. Scale bar = 1000 µm. (d,e,f) Higher magnification examples of the arrows (d), unfilled arrowheads (e), and filled arrowheads (f) respectively, along with synaptic projections labeled in an equivalent section. Scale bars in d,f = 200 µm. Scale bars in e = 100 µm. (g) The average percentage of aggregates in each of the subregions at each of the sections is demonstrated as a heatmap. Measured regions CTX, HIP, STR and DIEN (n = 5). (h) The regions where *Snta1* deletion has the greatest impact on aggregate formation are shown as a relative change in aggregate density per region, normalized to wild type aggregate densities (n = 5/group).

The disruption of both CSF tracer influx and interstitial solute efflux in the Snta1$^{-/-}$ model provides corroborating evidence for the role of perivascular AQP4 in facilitation of glymphatic function. However, while loss of perivascular AQP4 localization is the only described CNS phenotype of the *Snta1*$^{-/-}$ line, we cannot rule out the possibility that deletion of *Snta1* disrupts localization or function of a presently unknown perivascular endfoot element that contributes to perivascular CSF-ISF exchange. Indeed, recent transcriptomic profiling studies from mice and human brain tissue have identified several potential perivascular endfoot elements whose expression predict dementia status and P-tau levels in the aging human brain (Boulay et al., 2017; Simon et al., 2017; Simon et al., 2018). However, whether SNTA1 expression regulates the localization or function of these or any other putative endfoot elements is not yet known.

The impairments in perivascular CSF-ISF exchange described in the present study are more modest than those observed in *Aqp4*$^{-/-}$ mice (Iliff et al., 2014; Iliff et al., 2012; Mestre et al., 2018a; Plog et al., 2015) (Appendix A). For example, differences in CSF tracer distribution between wild type and *Snta1*$^{-/-}$ were evident 90 min, but not 30 min following intracisternal injection whereas differences between *Aqp4*$^{-/-}$ and wild type mice are readily observed at the 30 min time point. If AQP4 supports perivascular CSF-ISF exchange, then it is not surprising that a genetic model lacking localization exhibits a muted phenotype relative to a global knockout. We also observed regional, rather than global changes in CSF-ISF influx in the *Snta1* knockout line. We noted that in *Snta1*$^{-/-}$ mice, both 10 kD and 70 kD tracer penetration across the glial limitans at the pial surface appeared to be increased relative to wild type animals. Such trans-pial tracer exchange does not appreciably influence tracer distribution in deeper brain structures where perivascular tracer distribution plays a greater role. Thus, the increase in trans-pial tracer movement may have masked changes in perivascular tracer distribution in the cortex of *Snta1*$^{-/-}$ mice that were evident in deeper structures. These findings argue for a more comprehensive evaluation of CSF-ISF exchange, with careful attention paid to exchange dynamics across different CSF-ISF interfaces, including the ependymal boundary, the glial limitans, and perivascular spaces surrounding penetrating blood vessels. Importantly, the use of different molecular weight tracers, which exhibit differing

transport behaviors at these different interfaces, provide a useful tool to distinguish these effects.

The hypothesis of pathogenic aggregate seeding and propagation in neurodegenerative disease is gaining substantial experimental validation, particularly for synucleinopathies, yet critics of this hypothesis contend that trans-synaptic spread of aggregates does not account for the pathology observed in post-mortem tissue of patients with synucleinopathies (Surmeier et al., 2017). Our results are in part consistent with this criticism, as first order retrograde projections from primary motor cortex do not overlap with the regions most abundantly populated by P-syn immunoreactivity following PFF inoculation. It is important to note however, that our analysis focused exclusively on first order retrograde projections. The contribution of multi-synaptic or anterograde transport were not evaluated. It is possible that spread along these synaptic pathways could account for the discrepancies observed. Even so, the exacerbation of aggregate formation in Snta1$^{-/-}$ mice supports a role for glymphatic CSF-ISF exchange in facilitating the propagation process. It is possible that when α-synuclein aggregates are released into the extracellular space (by synaptic release, release by damaged or dying cells, etc.), the glymphatic system plays a role in facilitating their clearance out of the brain. As a result, impairment of glymphatic function may promote uptake of pathogenic aggregates by neighboring cells. An alternative possibility is that the glymphatic system is critical for regulating endogenous α-synuclein concentrations and disruption of this pathway promotes aggregation by shifting α-synuclein levels above the critical concentration needed for fibrillization (van Raaij et al., 2008). The marked changes in distribution of interstitial dextrans and fluorescently-labeled α-synuclein, in addition to reduced α-synuclein levels measured in the CSF of *Snta1*$^{-/-}$ mice support this explanation.

Several open questions remain regarding the fundamental mechanism of glymphatic pathway function and impairment, and their role in the pathogenesis of synucleinopathies such as DLB or PD. It is currently unclear precisely how perivascular AQP4 supports macroscopic CSF-ISF exchange across the brain structure, and the contribution that AQP4 expression at the glial limitans may make to these dynamics. The discrepancy between experimental observations carried out in *Aqp4*$^{-/-}$ (Iliff et al., 2014; Iliff et al., 2012; Mestre et al., 2018a; Plog et al., 2015) (Appendix A), and now *Snta1*$^{-/-}$

mice and microscopic (cellular) scale modeling studies (Asgari et al., 2015; Nicholson and Hrabetova, 2017) suggests that key gaps in the present understanding of these systems and their dynamics persist and await further exploration. Despite these persistent questions, our data suggests that the perivascular astrocytic endfoot domain, and AQP4 play a vital role in facilitating the influx and efflux of proteins in the brain and that disruption of this system contributes to the accelerated aggregation of pathogenic proteins such as α-synuclein. These results clarify basic mechanisms of protein transport at perivascular spaces and provide clinically relevant insight into age-dependent mechanisms of α-synuclein clearance and aggregation.

Methods

Materials and Antibodies

10kD Cascade Blue-labeled dextran (ThermoFisher D1976), 70kD Texas Red-labeled dextran (ThermoFisher D1864) and 2000kD FITC-labeled dextran (ThermoFisher (D7137) were dissolved in saline at maximum solubility concentrations as listed by the manufacturer. Aliquots of the "Dextran cocktail" were made using equal parts of each of the three tracers and were frozen at -20° C until used. Soluble α-synuclein (Anaspec, AS-55457) was used at the stock concentration of 1 mg/ml. Mouse wild type sequence preformed-fibrils (PFFs) were generated and prepared as previously described (Luk et al., 2012a; Osterberg et al., 2015). Primary antibodies included rabbit anti-AQP4 (1:500, Millipore AB3594), rabbit anti-α-syntrophin (1:500, Signalway Antibody 22845), mouse anti-β-actin (1:1000, Novus NB600-501), mouse anti-α-synuclein (1:100, ThermoFisher 32-8100), rabbit anti-phospho-α-synuclein (1:500, Abcam ab51253), mouse anti-GFAP (1:300, Millipore MAB360), mouse anti-NeuN (1:100, Millipore MAB377) and goat anti-Iba1 (1:200, Novus Biologicals NB100-1028). All secondary antibodies for immunofluorescence were generated in donkey, were conjugated to either Alexafluor-488, Alexafluor 594, or Alexafluor 647, used at a concentration of 1:500 and were ordered from ThermoFisher. Secondary antibodies for western blot included donkey anti-mouse IgG 680RD (Licor 925-68072) and donkey anti-rabbit IgG 800CW (Licor 925-32213). Hoescht 33342 (1:5000, ThermoFisher H3570) was used to label cell nuclei. CSF

quantification of mouse α-synuclein was performed with a commercially available ELISA detection kit (Biomatik EKU07561).

Animals

Homozygous *Snta1*$^{-/-}$ mice were generated by Dr. Stanley Froehner (Adams et al., 2000) and were obtained from Jackson Laboratories (stock no. 012940). Mice were maintained on a C57Bl6/J background and were homozygously bred. Animals were used between 10-16 weeks of age for all experiments. Age-matched C57Bl6/J mice obtained from Jackson Laboratories were used for wild-type controls. All mice were cared for by the Oregon Health & Science Department of Comparative Medicine in an Association for Assessment and Accreditation of Laboratory Animal Care (AALAC) accredited vivarium. All experiments were performed in accordance with state and federal guidelines and all experimental protocols were approved by the institutional animal care and use committee (IACUC). Power analysis was performed either using pilot experiments or literature review to estimate animal counts for each experiment. Power analyses were run to detect significance levels of $p \leq 0.05$, with a power of 80% and effect size of 50%.

Immunofluorescence

All tissue slices were generated by 20um sectioning on a cryostat. Free-floating immunofluorescence was performed on 20um sections for all acute time-frame experiments. For PFF experiments immunofluorescence was performed on slide mounted sections. For both free-floating and slide mounted sections, tissue was incubated overnight at 4° C on a rocker with blocking solution (.3% Triton-100, 5% normal donkey serum, 2% bovine serum albumin (BSA) in phosphate buffered saline (PBS)). Both primary antibody and secondary antibodies were diluted in blocking solution and incubations were performed overnight at 4° C on a rocker. Hoescht staining was applied for 10 minutes during the final set of washes to label nuclei. Floating sections were then positioned directly onto coverslips with a paintbrush. All samples were mounted with Fluoromount-G mounting media (Southern Biotech 0100-01) or homemade Mowiol 4-88.

Protein isolation and Western blot

Whole brain tissue lysates were generated by dounce homogenization in RIPA buffer (ThermoFisher 89900) with added protease inhibitor cocktail (Sigma-Aldrich 11836170001). Samples were spun at 2000g for 10min at 4° C to remove cellular debris then frozen at -80° C. Protein concentration was quantified by Pierce BCA protein assays (ThermoFisher 23225). Western blots were run on NuPage 4-12% Bis-tris gels. 50ug of protein were combined with LDS sample buffer and run on the gel for 90 minutes at 200mV on ice at 4° C. Protein transfer was done using Immobilon-FL membranes and was run at 30mV for 60 minutes at 4° C. Primary and secondary antibodies were applied over the course of 3 hours using the Invitrogen iBind Flex system. Bands were imaged using a Licor Odyssey CLx fluorescence gel imaging system. Values for each sample were generated by averaging across two independent blots. Abundance was determined by measuring the abundance relative to the loading control band (β-ACTIN).

Anesthesia

For all acute time-course experiments, anesthesia was briefly induced under isoflurane (2-4%), then maintained under ketamine/xylazine (KX) anesthesia for the duration of the experiment (0.10 mg/g ketamine, 0.01 mg/g xylazine, i.p.). For chronic experiments (e.g. PFF-injections), mice were induced and maintained under isoflurane anesthesia. During all surgeries, mouse body temperature was maintained by heating pads and overhead heating lamps. For long surgeries, (90-120 minutes) mice were given intraperitoneal saline approximately halfway through the surgical procedure to minimize dehydration.

Cisterna magna infusion

Prior to surgery, a 30-gauge needle tip inserted into PE-10 tubing was connected to a 10ul Hamilton syringe (Hamilton 80001). The syringe was then backfilled with saline, as well as the dextran cocktail and placed in a syringe pump. KX-anesthetized mice were head-fixed in a stereotaxic frame and fur was cleaned from the neck of the animal with Nair. An incision was made along midline from the bregma suture of the

skull to the subcutaneous fat of the back, exposing three muscular layers in the neck. The exposed muscle was then cut along midline to the point at which it attaches to the external occipital protuberance of the skull, and then laterally along this junction. All three muscular layers were reflected away to expose the transparent atlanto-occipital membrane (AOM) covering the cisterna magna. The surface of the AOM was swabbed to clear any blood/fibrous tissue remaining, and the mouthpiece of the stereotax was tilted slightly downward to maximize the size of the cisterna magna compartment. The needle tip was then inserted through the AOM and into the cisterna magna at a low angle to avoid puncturing the brainstem/cerebellum. To assure correct needle placement, visual confirmation was made that the AOM contacted the needle directly below the needle bevel and that the needle bevel was completely visible, then it was glued in place using VetBond. The syringe pump was used to drive the dextran cocktail into the cisterna magna at a rate of 500nl/min over 10 min for a total infusion volume of 5 ul. Adequate clearance of the AOM surface allows for visualization of dextran distribution into the CSF compartment. Mice were excluded from analysis if the needle slid out of the cisterna magna prior to gluing (resulting in CSF drainage) or if the needle was placed too deeply and tracer dispersion into the CSF could not be observed (suggesting the needle-tip was in the brain tissue). Based on these criteria, two animals were excluded in the 90-minute influx study, one from each genotype (Figure 2). Animals were monitored throughout the duration of the experiments to maintain anesthesia levels by toe pinch and observation of whisker movement and respiratory rate. When necessary, KX was re-administered intraperitoneally at approximately 1/3 the initial dose following animal recovery from the initial dose. Upon completion of the experiment, brain tissue was fixed with 4% paraformaldehyde (PFA) via transcardiac perfusion under anesthesia. Brains surfaces were imaged immediately (allowing for validation of successful infusion), and then brains were post-fixed overnight, followed by a second night in 30% sucrose before being frozen in OCT and stored at -80° C until sectioned.

Intraparenchymal injections

Intracortical injections (Fig 2-4) targeted the motor cortex (1, -1.5, .3). Intrastriatal injections (Fig 3A) targeted caudate putamen (2.8, -0.5, 3.5). Anesthetized

mice were head-fixed in a stereotaxic frame. Fur was cleared from the skin above the skull using Nair or an electric razor. An incision was made along midline to expose the skull and connective tissue was removed with a cotton-tipped applicator. A sterotax-mounted dremel was used to create a small burr-hole at the medial/lateral and anterior/posterior bregma coordinates. The dremel was replaced with a 10ul Hamilton syringe outfitted with a 32g needle (Hamilton 80014) that was loaded into a syringe pump and backfilled with either a 10kD dextran + α-synuclein cocktail or PFFs. For the 10kD dextran + α-synuclein cocktail experiments, the needle tip was lowered slowly into the brain through the burr hole to the injection coordinate. The needle was left in place for 5 minutes, then infusions were performed at a rate of 50nl/min for 20 minutes for a final volume of 1ul to minimize pressure-driven bulk flow of tracer. For PFF injections, the needle was lowered to .6mm of the dorsal/ventral bregma coordinates, left in place for 1 minute, then raised to the .3mm depth of the dorsal/ventral bregma coordinates prior to the start of infusion. PFFs were infused at a rate of 200nl/min for 12.5 minutes for a final volume of 2.5ul. The needle was then left in the brain for 3 minutes to prevent reflux of PFFs up the needle tract, then extracted and the skin was sutured over the injection site. For both experiments, the needle was left in place and anesthesia depth was monitored and adjusted as necessary (as described above) over the course of the experimental time frame (120 minutes). Upon completion of experiments, transcardiac PFA perfusion was performed under anesthesia. For the intrastriatal injections, a solution of the lipophilic dye DiD was perfused prior to PFA to label large blood vessels as previously described (Fig 3A) (Li et al., 2008b). For the PFF dataset, CSF was extracted immediately prior to perfusion (see below). Brains surfaces were imaged to confirm successful infusion and minimal recirculation of tracer via the CSF (indicating the needle tip was in the CSF or ventricle) when fluorescent tracers were infused. Brains were post-fixed overnight in PFA, followed by an overnight incubation in 30% sucrose to cryo-protect the tissue. Brains were then frozen in OCT and stored at -80° C until sectioning.

CSF collection and ELISA assays

Both the homeostatic and post-PFF CSF α-synuclein levels were quantified using a commercially available enzyme-linked immunosorbent assays (ELISA). CSF was

collected in a similar manner to CSF infusion experiments. A 30g needle was attached to PE-10 tubing and connected it to a Hamilton syringe in a syringe pump (no backfill). The AOM was exposed in isoflurane (1-3%) anesthetized mice as described above and the needle was inserted into the cisterna magna. The syringe pump was then run in reverse at a speed of .5ul/min until the AOM had completely collapsed around the needle tip (after approximately 7-8ul had been collected. Animals were excluded if obvious leakage of CSF occurred during needle placement, if blood was detected in the sample (as observed by eye before and/or after centrifugation of the CSF), or enough CSF was not collected for at minimum two replicates. Based on these criteria, one mouse was excluded in the PFF CSF analysis (Figure 5) and nine mice were excluded in the endogenous CSF expression study (Figure 4). ELISA assay was performed according to manufacturer instructions. Due to limited sample quantity and low anticipated protein abundance, two technical replicates were run per sample.

Confocal and widefield imaging

Full-brain imaging was performed using an automated, slide-scanning confocal microscope (Zeiss AxioScan.Z1). Images were acquired using a 20X 0.8 PlanApo objective. High-magnification images were acquired using an inverted laser-scanning confocal microscope equipped with an AiryScan super-resolution detector (Zeiss LSM 880 with Fast Airyscan). Images were collected using either a 63X 1.4 Plan Apo objective or a 20X Plan Apo objective. Based on the semi-quantitative nature of the analysis, all images were acquired to minimize signal outside of the dynamic range of the detector. Brain surface images were acquired using a Zeiss AxioImager upright microscope equipped with a 5x 0.16 PlanApo objective.

Image and statistical analysis

All image analysis was performed using FIJI software (Schindelin et al., 2012). All statistical analysis was performed using Graphpad Prism 7, except for the Levene's test, which was performed using R (data not shown). Linear adjustments to minimum and maximum histogram values were made to many of the images presented in the

manuscript to improve clarity, however all image analysis was performed on images as acquired, or uniformly size-scaled images (due to computer memory limitations). Due to the automated acquisition of large-scale images, a small percentage (1-2 images across all datasets) exhibited poor focusing and were thus excluded from further analysis. Analyses requiring subjective distinctions (region of interest (ROI) generation, cell counts, threshold identification) were performed in a blinded, manual fashion. During the ROI generation process, ventricles as well as obvious imaging artifacts were excluded from regional and total brain ROIs. FIJI scripts were generated to automate all image measurements once ROIs and/or thresholds were established. Area coverage was calculated using a threshold-based approach. Briefly, a uniform threshold was established prior to analysis that most accurately captured "real" fluorescent signal for any given tracer or immunolabel. A percentage of the total ROI covered by the threshold generated ROI was then calculated. For the PFF dataset, due to intermittent tissue drying artifacts, thresholds were adjusted to best reflect P-syn derived signal in a blinded fashion. To most accurately capture the punctate nature of the aggregates, an additional analysis using the "analyze particles" function in FIJI was used to generate an aggregate count. All plots in the figures are presented with bars representing mean ± S.E.M. Mann-Whitney U tests were used to compare all datasets with only 2 values as many exhibited non-parametric distributions. For subregional analyses, a Levene's test revealed largely heterogenous variability values between subregions with regard to tracer influx (data not shown). As a result, multiple t-tests were used for all regional analyses rather than ANOVAs. These t-tests were corrected for multiple comparisons using the Holm-Sidak method. All statistical tests are also listed in the text and figure legends.

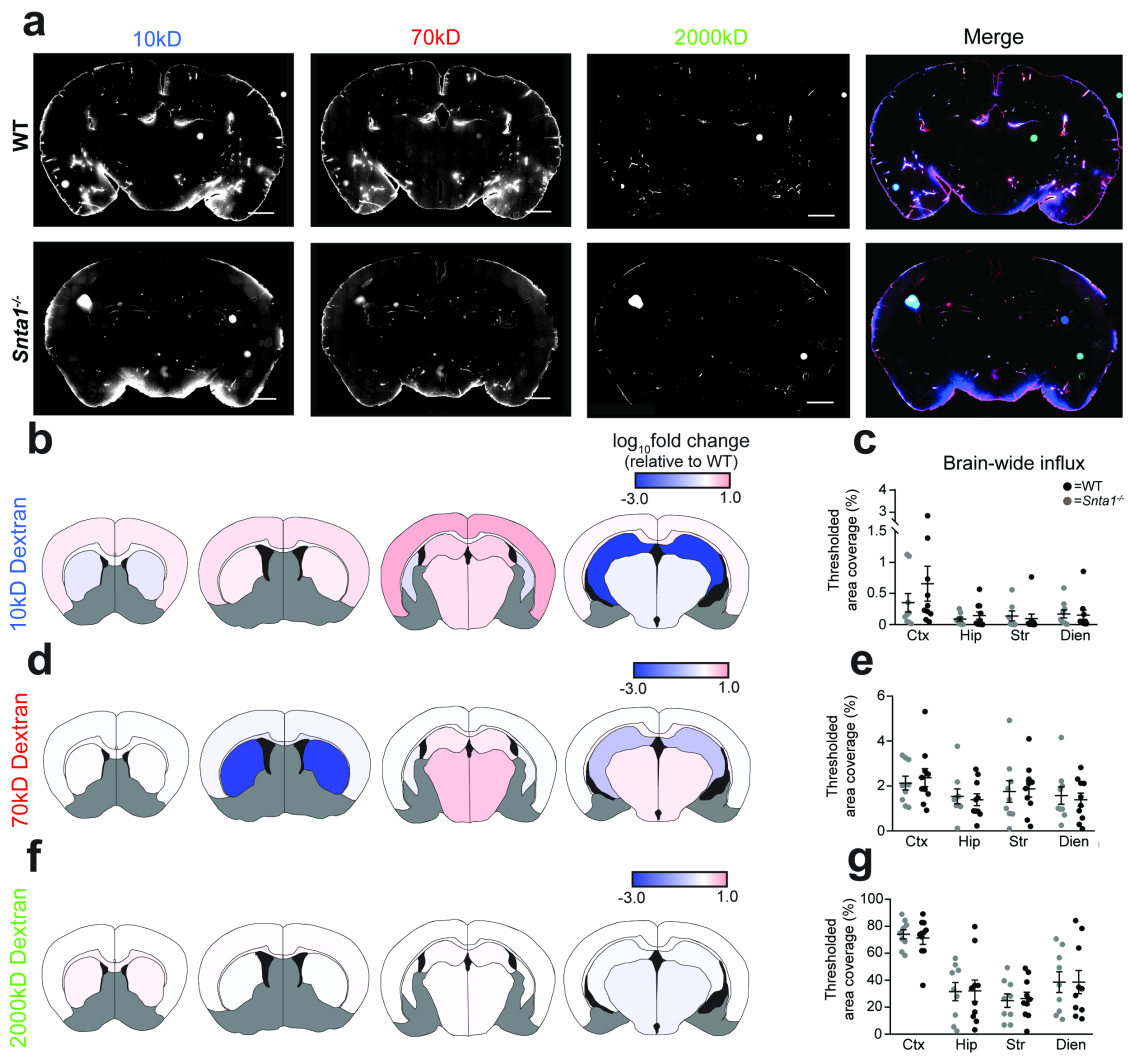

Supplemental Figure 2.1: CSF tracer influx 30 min post-injection.

(**a**) CSF tracer infusion evaluated at 30 minutes post-injection. Representative images shown for each dextran size with composite image at right. Scale bars = 1000 µm. (**b**,**d**,**f**) Heat map characterization of regional dextran influx differences between wild type and *Snta1*$^{-/-}$ mice at 30 minutes post infusion integrated across all 4 sections for 10 kD (**b**), 70 kD (**d**), and 2000 kD (**f**) dextrans respectively. Differences shown as a $\log_{10}$ transformation of area coverage, normalized to wild type animals. Grey regions were not evaluated. (**c**,**e**,**g**) Integrated regional area coverage across all 4 sections was determined for cortex (Ctx), hippocampus (Hip), striatum (Str) and the diencephalon (Dien). No significant differences were observed in any region for any dextran size (multiple t tests with Holm-Sidak correction, n = 8-9 animals/group). For all plots, black bars represent the mean ± S.E.M.

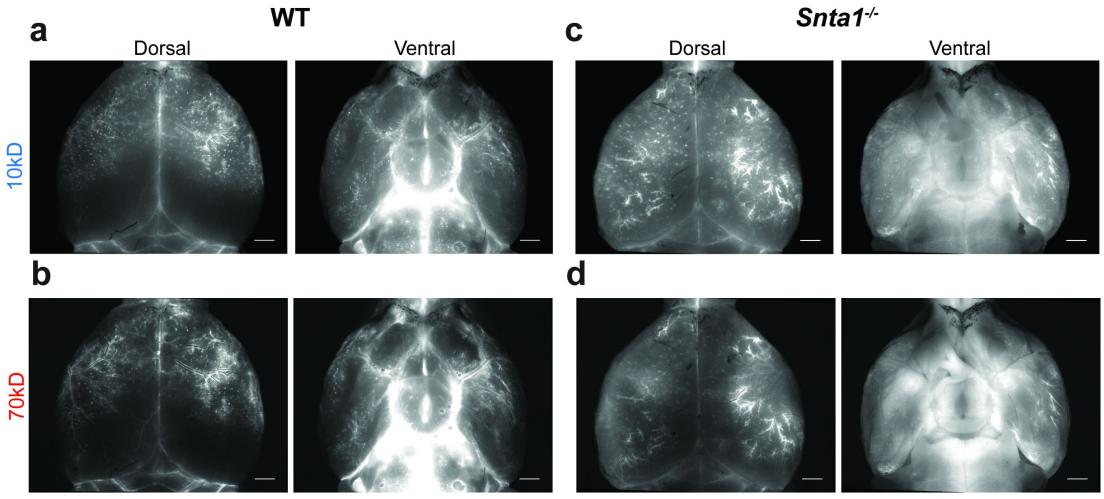

Supplemental Figure 2.2: Size dependent distribution of tracers at the brain surface 90 minutes after injection into the CSF.

Brain surface images of dextrans 90 minutes following cisterna magna infusion in both wild type (**a-b**) and *Snta1*$^{-/-}$ mice (**c-d**). Surface images reveal wider surface distribution of smaller (**a,c**, 10 kD) and medium sized dextrans (**b,d**, 70 kD) in *Snta1*$^{-/-}$ mice relative to wild type animals. Scale bar = 1000 µm.

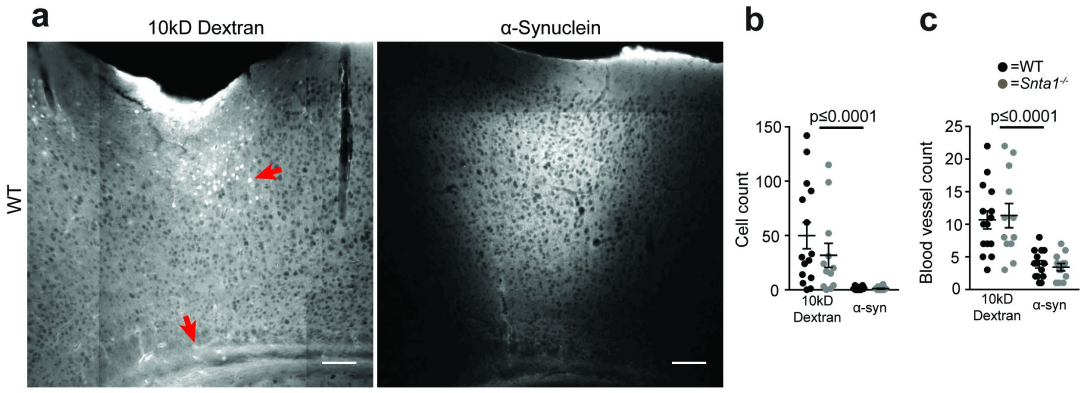

Supplemental Figure 2.3: Inert dextrans accumulate in cells and along blood vessels more abundantly than α-synuclein.

(a) Images of 10 kD dextran (left) and α-synuclein (right) distribution proximal to the injection site reveal greater cellular and perivascular accumulation of 10 kD dextran, than of α-synuclein (red arrows). (b) Quantification of cells exhibiting accumulation of either the 10 kD dextran or α-synuclein immediately adjacent to the injection site indicates significantly fewer cells containing α-synuclein than 10 kD dextran ($P \leq 0.0001$, Mann-Whitney U test, n = 12-14). Scale bar = 100 µm. (c) Quantification of blood vessels exhibiting perivascular accumulation of either the 10 kD dextran or α-synuclein immediately adjacent to the injection site ($P \leq 0.0001$, Mann-Whitney U test, n = 12-14).

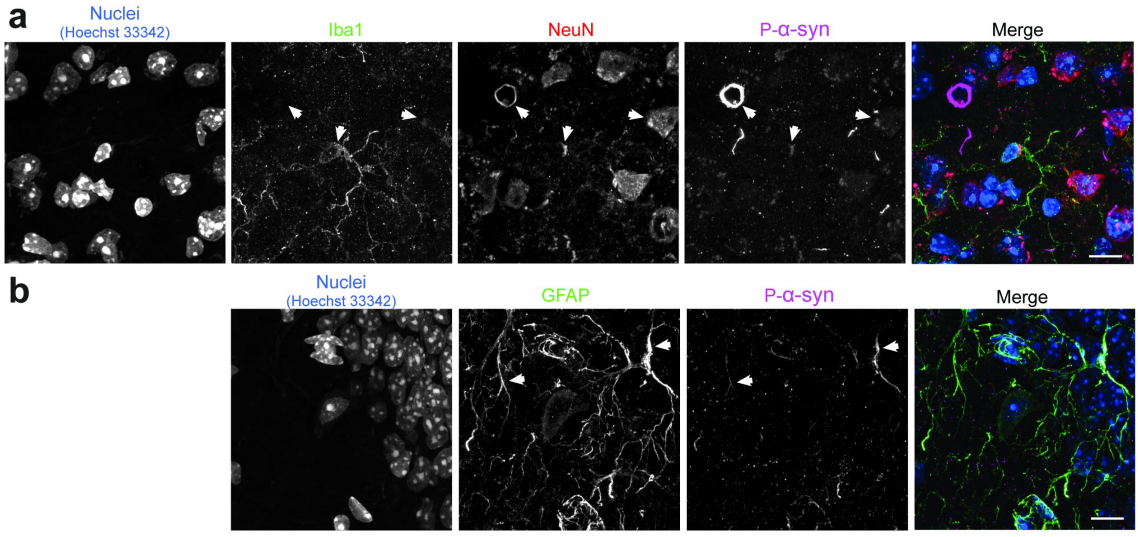

Supplemental Figure 2.4: Cell types exhibiting α-synuclein aggregate formation following PFF injection.

(A) Immunofluorescence imaging of phospho-α-synuclein (magenta) with cell type markers for microglia (Iba1, green) and neurons (NeuN, red) reveal colocalization with both cell types, though more abundantly with neurons. (B) Immunofluorescence imaging of phospho-α-synuclein an astrocytic marker (GFAP, green) reveals colocalization. Arrows indicate sites of co-localization as well as phospho-α-synuclein exhibiting various morphologies (neuritic, glial and somatic inclusions as well as diffuse). Merged images at left. Scale bar = 10µm.

Chapter 3: Overexpression of AQP4-M1 alters perivascular localization at capillaries but does not impact CSF-ISF exchange in mice

Matthew J Simon[1,2], Jesica Reemmer[3], Marie Wang[1], Zhongya Wang[3], Detlev Boison[3], Jeffrey Iliff[1,4*]

[1]Department of Anesthesiology and Perioperative Medicine, Oregon Health & Science University, Portland, OR, USA.

[2]Neuroscience Graduate Program, Oregon Health & Science University, Portland, OR, USA.

[3]Robert Stone Dow Neurobiology Laboratories, Legacy Research Institute, Portland, OR, USA.

[4]Knight Cardiovascular Institute, Oregon Health & Science University, Portland, OR, USA.

Foreword

This chapter reflects data generated and submitted as a manuscript to the journal Glia. Viruses utilized in the chapter were generated in collaboration with Dr. Detlev Boison at Legacy Research Institute and two members of his lab Jesica Reemmer, Dr. Zhongya Wang. Typically, viral constructs were generated by me, amplified by maxiprep to allow for large scale production, then handed to the Boison lab for packaging and purification. The input of Dr. Zhongya Wang was critical for designing and developing viral constructs. Dr. Marie Wang performed the ELISA quantification of amyloid β seen in Figure 2. The rest of the data collection, analysis, figure and manuscript preparation was performed by me.

Abstract

The perivascular localization of aquaporin-4 (AQP4) has been recently shown to play a role in regulating glymphatic exchange, and to be disrupted in the aging brain. The mechanisms by which perivascular localization is regulated in vivo have not yet been defined. In vitro studies suggest that differential expression of two AQP4 isoforms: M1 and M23, may contribute to perivascular localization, with the M1 isoform exhibiting dramatically reduced localization. We hypothesized that overexpression of the M1 isoform would be sufficient to modulate AQP4 perivascular localization in vivo and subsequently, modulate glymphatic exchange. Using a virus mediated delivery approach, we demonstrate that while overexpression of AQP4-M1 does reduces global localization at the capillary level, it does not alter localization along larger vessel, and has no impact of CSF-ISF exchange. Furthermore, we demonstrate that overexpressed M23 exhibits no effect on perivascular localization of AQP4 or glymphatic exchange. Finally, we demonstrate that the overexpressed M1 and M23 isoforms differentially target the endfoot compartment, validating associations presented in culture models, in vivo. Our results further our understanding of the endfoot compartment and mechanisms that govern AQP4 subcellular distribution.

Introduction

Aquaporin-4 (AQP4) is a highly expressed water channel exhibiting enriched expression in astrocytes. Specifically, it exhibits abundant expression levels at the astrocytic endfoot, a subcellular domain adjacent to brain vasculature. This unique localization profile has implicated AQP4 as a regulator of brain fluid homeostasis, playing a role in physiological processes including neurovascular coupling, and in facilitating pathophysiological responses to brain insults, including edema. In more chronic brain pathologies, a loss of the extreme perivascular localization of AQP4 has been observed. Recent studies have demonstrated this phenomenon in the context of stroke, Alzheimer's disease (AD), Parkinson's disease (PD) and aging. What remain unclear is the mechanisms that regulate AQP4 localization in the healthy brain, and the loss of localization observed in disease states.

Regulators of AQP4 localization have been largely studied in cultured astrocytes. From these studies, a wide range of mechanisms have been described that contribute to the membrane distribution of AQP4. Acutely, AQP4 can be trafficked into and out of the membrane in a PKA dependent manner in response to osmolarity changes (Kitchen et al., 2015). PKC-dependent internalization of AQP4 has been reported in response to vasopressin receptor 1 activation (Moeller et al., 2009). Still more mechanisms of rapid trafficking have been described for other aquaporins, particularly for AQP2 in the collecting ducts of the kidney where AKAP220-dependent rearrangement of the actin cytoskeleton impacts membrane insertion (Whiting et al., 2016). Genetic deletion of elements of the dystrophin associated complex (DAC) including the adapter protein α-syntrophin and dystrophin, also result in a loss of AQP4 localization and a disruption of the entire endfoot domain (Dalloz et al., 2003; Enger et al., 2012; Lien et al., 2012; Neely et al., 2001; Noell et al., 2011). A third intriguing mechanism of perivascular localization is alternative isoform expression. AQP4 abundantly expresses two isoforms as well as, to a lesser degree several additional isoforms. The most abundantly expressed in humans: AQP4-M1 and AQP4-M23 differ by 22 amino acids uniquely expressed by the AQP4-M1 variant on the N-terminus of protein. Intriguingly, overexpression of each variant on a non-endogenously expressing background exhibits a strikingly unique membrane distribution, with the M1 variant diffuse across the cell membrane and the M23 clustering into large lipid rafts previously defined as orthogonal arrays (Verkman et al., 2011). These arrays are also observed at the endfoot domain (Dermietzel, 1973) and are assumed to be linked to expression of the M23 isoform (Neely et al., 1999), however isoforms mediated regulation of AQP4 localization *in vivo* has not been explicitly studied.

Recently AQP4 has gained renewed interest as a regulator of waste clearance facilitated by the exchange of cerebrospinal fluid (CSF) and interstitial fluid (ISF) at the boundary between perivascular spaces of large caliber blood vessels and the broader brain parenchyma. This is a process known as CSF-ISF exchange, recently re-popularized as the ‘glymphatic pathway’. Genetic deletion of AQP4 has been shown to dramatically reduce solute trafficking in these compartments. Aging and several neurodegenerative states have also been associated with impairments in this exchange pathway including aging, AD, and traumatic brain injury. Recently, we demonstrated that

a loss of perivascular AQP4 localization is sufficient to impair CSF-ISF exchange and exacerbate propagation of fibrillary α-synuclein (Chapter 2). These studies have raised questions regarding perivascular AQP4 localization as a targetable regulator of CSF-ISF impairments in aging and neurodegenerative disease.

In the present study, we investigate differential AQP4 isoform expression as a regulator of perivascular localization in vivo. We then investigate the potential for virally-mediated gene therapy targeting AQP4 isoform expression as a regulator of both perivascular AQP4 localization and CSF-ISF exchange. Lastly, we expand on the targeting of the AAV-PHP.B virus serotype and evaluate it as a tool for modulating gene expression in the study of interactions between astrocytes and the brain vasculature.

Results

GFP-tagged AQP4 isoforms demonstrate differential membrane localization in vitro and in vivo

The two most abundant AQP4 isoforms: AQP4-M1 (M1) and AQP4-M23 (M23) exhibit divergent membrane localization profiles when overexpressed in AQP4 deficient astrocytes (Furman et al., 2003). As cultured astrocytes do not fully mimic the complexity of astrocytes in vivo, we first sought to determine if this effect could be recapitulated when overexpressed on an endogenous background in vitro. To achieve this, expression of c-terminus GFP-tagged versions of either the M1 (M1-GFP) or M23 (M23-GFP) isoform was driven in cultured primary astrocytes using AAV virus with an astrocyte specific promoter (AAV8-GfaABC1D) (Supplementary Figure 3.1a-b). Consistent with previous literature, overexpression of M23-GFP resulted in a 3-fold increase in the ratio of large volume membrane clusters ($\geq 2\mu m^2$) to small volume clusters ($\leq 1\ \mu m^2$) relative to overexpression of M1-GFP (Supplementary Figure 3.1c-e). Next, we sought to determine if volume cluster size reflected perivascular localization of AQP4 *in vivo*. Using the same viral overexpression system coupled with 2-photon microscopy, perivascular localization of overexpressed, GFP-tagged AQP4 was evaluated relative to an intravascular tracer (70kD texas red conjugated dextran) *in vivo*. Overexpressed M23-GFP exhibited 19% greater perivascular localization than overexpressed M1-GFP

(Supplementary Figure 3.1f & h). Qualitative assessment of GFP expression in fixed tissue demonstrated that the tendency for larger volume protein clusters to form with M23-GFP relative to M1-GFP is seen *in vivo* as it has been described in cultured astrocytes (Supplementary Figure 3.1g) (Crane et al., 2008).

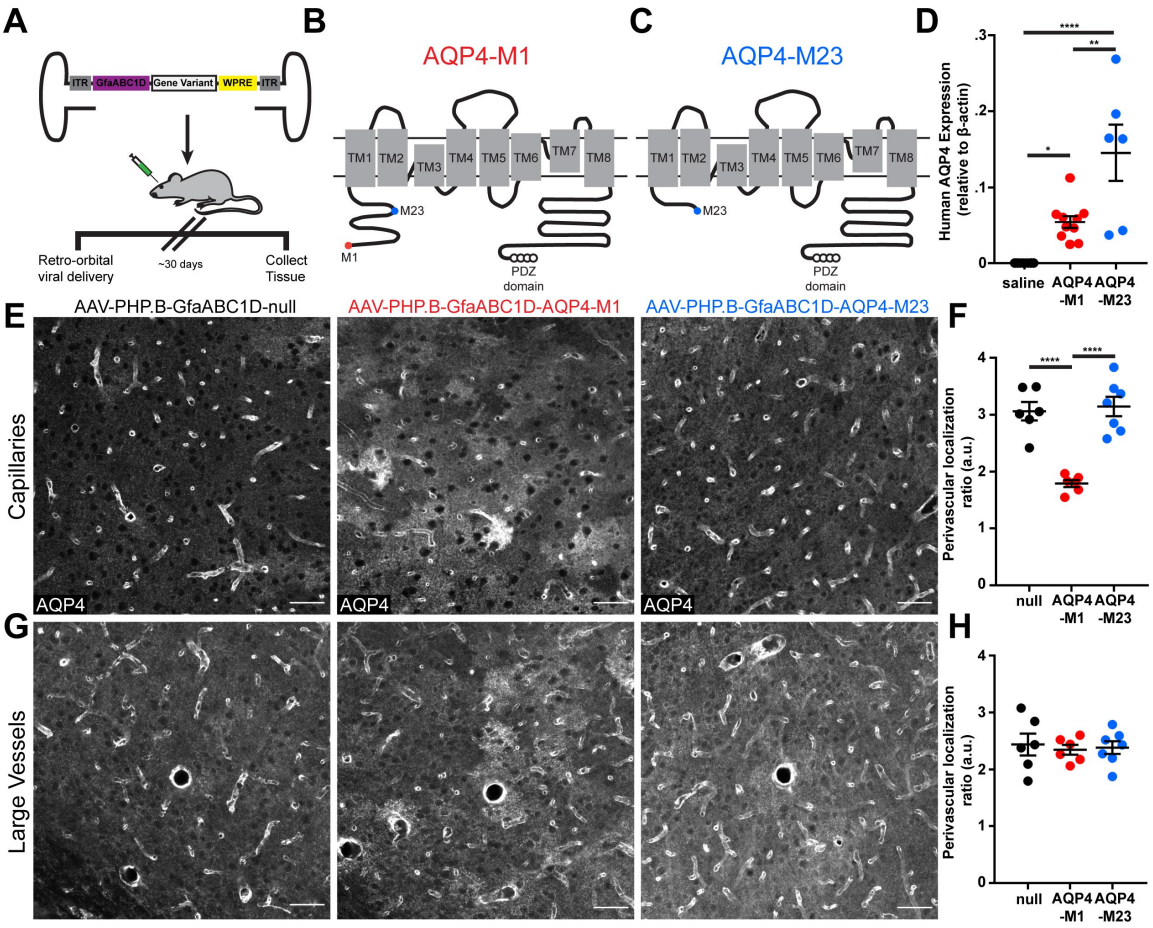

Figure 3.1: Overexpression of AQP4-M1 reduces perivascular localization at capillaries Schematic of the viral construct used to drive global, astrocyte specific expression of AQP4 constructs (AAV.PHP.B-GfaABC1D). (B-C) Protein constructs driven by the M1 (B) and M23 (C) viral constructs. (D) rt-PCR quantification of human AQP4 expression following delivery of the virus (N=6-7/group, One-way ANOVA). (E-F) Quantification of perivascular localization at the capillary level (F), with representative images of capillary level distribution (E, Scale bars = 50 µm) (N=5-7/group, One-way ANOVA). (G-H) Representative images (G, Scale bars = 50 µm) and quantification (H) of localization at large vessels. For all plots, black bars represent the mean ± S.E.M.

AQP4-M1 overexpression reduce capillary perivascular localization in vivo

Due to concerns regarding GFP's impact on AQP4 trafficking and localization, we further assessed the ability of overexpressing untagged AQP4 to alter perivascular localization. Global overexpression of human AQP4 isoforms was driven by retroorbital injection of an AAV variant that efficiently crosses the blood-brain barrier, and exhibits a high trophism for astrocytes, coupled with an astrocyte specific promoter (AAV-PHP.B-GfaABC1D) (Deverman et al., 2016). We evaluated perivascular localization of AQP4 in cortex and hippocampus of young mice, following 30 days of inoculation with AQP4 overexpression viruses (Figure 3.1a-c). Abundant expression of human AQP4 was confirmed with quantitative PCR (Figure 3.1d). In cortex, overexpression of AQP4-M1 resulted in a 42% reduction in perivascular localization at the capillary level, while M23 overexpression had no effect (Figure 3.1e-f, $p<0.001$, One-way ANOVA)). At the level of large vessels, viral overexpression of either isoform had no impact on perivascular localization (Figure 3.1g-h). These findings were also observed in hippocampus (data not shown). Together, these results suggest that overexpression of AQP4-M1 impacts perivascular localization *in vivo*, at the capillary level specifically.

Overexpression of untagged AQP4-M1 has no effect on CSF-ISF exchange or amyloid-β homeostasis

Next, we sought to measure whether loss of localization of perivascular localization at the capillary level was sufficient to alter global CSF-ISF exchange. To assess this, 10kD and 70kD detrains were infused into CSF. 90 minutes later, the tissue was perfusion-fixed and parenchymal tracer influx was evaluated by imaging five coronal sections across the cerebrum (1, 0, -1.5, -2.5 and -3.5 mm relative to bregma). Overexpression of either M1 or M23 had no effect on tracer influx compared to mice treated with null virus for either the 10kD or 70kD dextrans (Figure 3.2). This was observed both globally, and upon assessment of tracer influx into subregions including cortex, hippocampus, striatum, and the diencephalon (Figure 3.2b-c).

Loss of perivascular localization has also been linked to Alzheimer's pathology and amyloid β burden (Zeppenfeld et al., 2017). Furthermore, impairment of the

glymphatic pathway has previously implicated in exacerbation of amyloid β (Aβ) pathology and aggregate formation (Iliff et al., 2012; Xu et al., 2015). To determine if loss of capillary perivascular AQP4 localization impacts Aβ clearance, we assessed if overexpression of either AQP4 isoform would alter Aβ burden in a mouse model of Aβ aggregation (Tg2576) (Hsiao et al., 1996). Tg2576 mice were injected with either null, M1, or M23 overexpression viruses at 3 months of age. At 6 months of age, brains were saline perfused, and collected for histology and enzyme-linked immune absorbance assay quantification (ELISA) of Aβ in the brain parenchyma. At 6 months of age, only sparse plaques were detected in any of the 3 groups, suggesting that viral treatment did not accelerate plaque formation (data not shown). Furthermore, ELISA based quantification of total $A\beta_{1\text{-}40}$ and $A\beta_{1\text{-}42}$ exhibited no differences between mice overexpressing either AQP4 isoform and null treated controls (Figure 3.2d-e). Interestingly, a negative association between perivascular localization at large vessels and $A\beta_{1\text{-}42}$ was observed, independent of viral treatment (Figure 3e). These data suggest that AQP4 isoform expression has no effect on baseline CSF-ISF exchange or Aβ homeostasis.

Overexpression of AQP4-M23 has no effect on perivascular localization or CSF-ISF exchange in aged mice

It has been reported that perivascular localization of AQP4 is lost in the aging brain and that this is accompanied by an age-dependent decrease in CSF-ISF exchange (Kress et al., 2014). Though overexpression of AQP4-M23 has no effect on perivascular localization in young mice, the increased perivascular localization observed during GFP-tagged experiments raised the possibility that it may rescue perivascular localization in the context of the aging brain. To assess this possibility, M23 overexpression was driven virally beginning at one year of age. After 50 days, perivascular localization and CSF-ISF exchange was evaluated as described above. M23 overexpression did not demonstrate any impact on perivascular localization at either the capillary or large vessel level relative to null injected controls (Figure 3.3a). Furthermore, no increase in CSF-ISF exchange was detected (Figure 3.3b). Based on these data we concluded that overexpression of AQP4-M23 is insufficient to rescue age dependent reductions in perivascular AQP4 localization and CSF-ISF exchange.

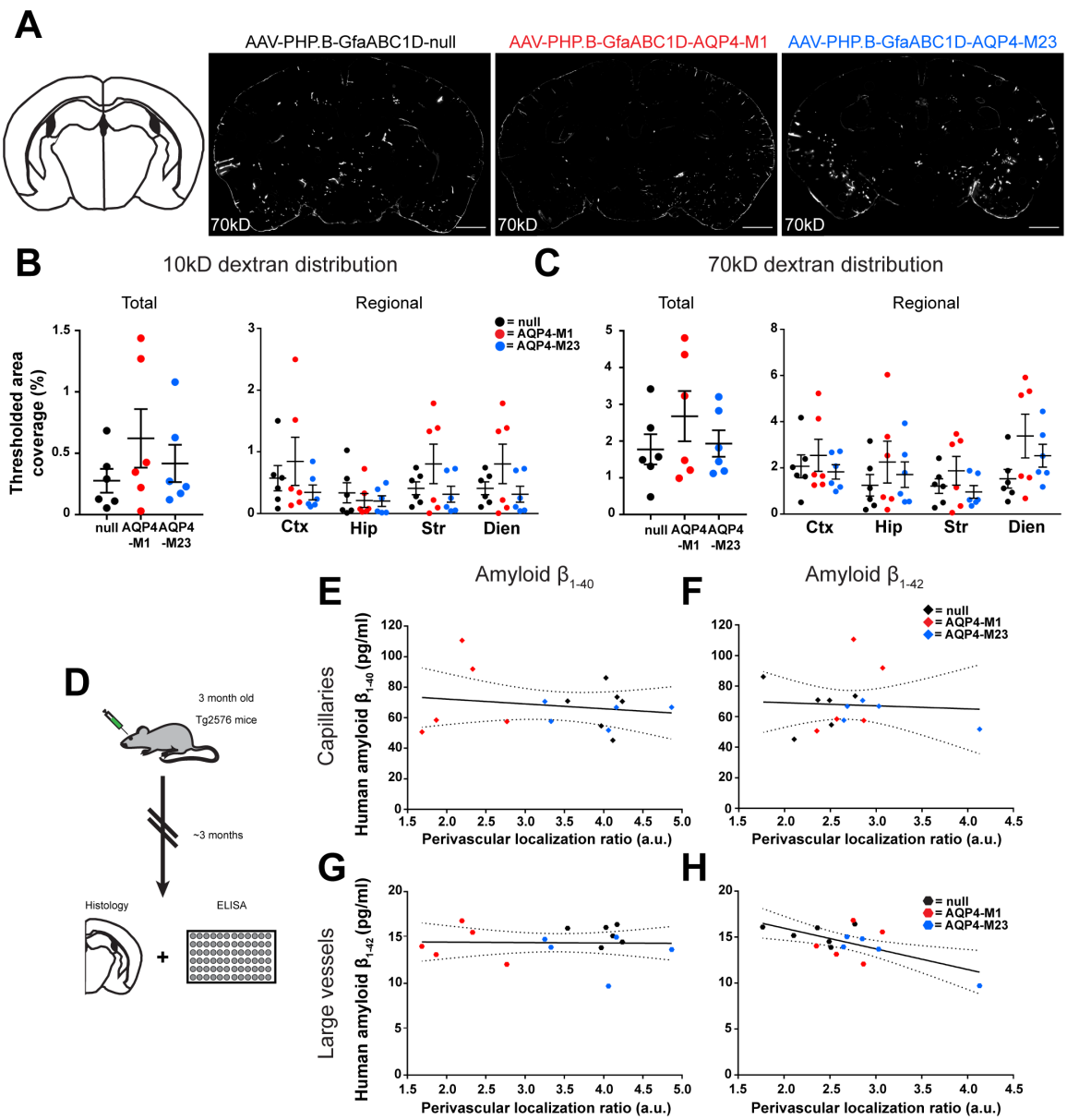

Figure 3.2: Overexpression of AQP4 isoforms has no effect on CSF-ISF exchange or amyloid β accumulation.

(A) Representative images of CSF-ISF exchange in wild-type mice 1 month following virus treatment (Scale bar = 500 µm). (B-C) Quantification of integrated tracer distribution in each region assessed for 10kD dextrans (B, N=6/group), or 70kD dextrans (C). (D) Schematic representation of viral treatment in Tg2576 mice followed by assessment of plaque formation and soluble amyloid β levels. (E-H) Perivascular localization was quantified at capillaries (E,G) and large vessels (F,H), and correlated with total amyloid β burden (N=5/group).

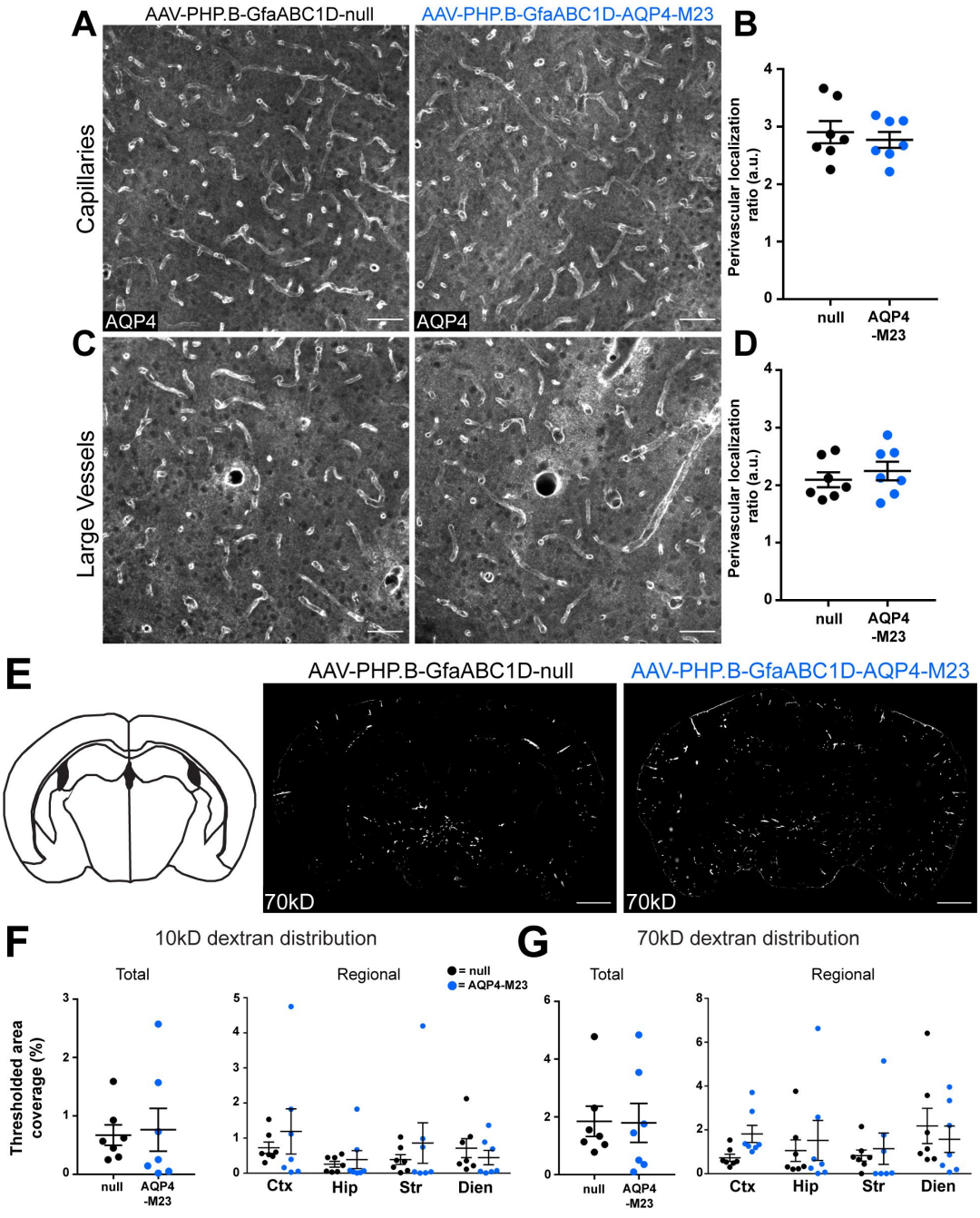

Figure 3.3: Overexpressed AQP4-M23 does not alter perivascular localization or CSF-ISF exchange in aged mice.

(A-D) Images depicting perivascular localization in aged mice following viral transduction of either M23 or a null-vector control, along with quantification of localization at right (Scale bars = 50 µm, N=7/group). (E) Representative images of CSF-ISF exchange in aged animals after treatment with control or M23 virus. (F-G) Sub-regional quantification of distribution revealed no differences for either 10kD (F) or 70kD dextrans (G). Scale bars = 50 µm.

Overexpression of PDZ deficient AQP4 does not impact CSF-ISF exchange

We previously demonstrated a complete loss of perivascular localization impairs CSF-ISF exchange (Chapter 2, Appendix A) (Mestre et al., 2018a) (Appendix A). This effect was identified using a transgenic mouse model lacking expression of the adapter protein α-syntrophin (*Snta1*$^{-/-}$) which anchors AQP4 at the endfoot domain via a PDZ-domain. We hypothesized that overexpressing PDZ-deficient AQP4 would recapitulate the *Snta1*$^{-/-}$ phenotype. PDZ deficient variants of both isoforms (M1Δ6 and M23Δ6, respectively) were generated based on previously culture studies (Crane et al., 2008). Regardless of isoform, overexpression of PDZ deficient AQP4 reduced perivascular localization at capillaries by around 30% (Figure 3.4a-d). Surprisingly, PDZ deficient AQP4 overexpression had no effect on large vessel perivascular localization (Figure 3.4e-f). This result is divergent from the phenotype in *Snta1*$^{-/-}$ mice. Evaluation of CSF-ISF tracer exchange revealed no differences at 90 minutes, regardless of tracer size (Figure 3.4g-i). We concluded that virus mediated loss of localization does not recapitulate the perivascular localization loss or CSF-ISF exchange deficits observed in genetic models.

AQP4-M23 preferentially targets the endfoot domain relative to AQP4-M1

Several possible explanations exist for the incongruent impact of α-syntrophin deletion and overexpression of PDZ-deficient AQP4 on large vessel perivascular localization. These include factors such as preferential targeting of capillary-adjacent astrocytes, relative to large-vessel adjacent astrocytes by AAV-PHP.B, or deficits in membrane insertion of overexpressed AQP4. To address these possibilities and investigate the biodistribution of our PHP.B-GfaAB1D virus, we used a P2A site to co-express AQP4 isoforms tagged with a hemagglutinin (HA) tag on the second external loop of the protein, as well as eGFP (PHP.B-GfaABC1D-AQP4-M1HA-P2A-eGFP referred to as M1-HA and PHP.B-GfaABC1D-AQP4-M23HA-P2A-eGFP referred to as M23-HA). The second extracellular loop HA-tag was added to assess subcellular distribution of overexpressed AQP4 relative to endogenous AQP4 with minimal interference relative to other, larger protein tags (ex: GFP) . The P2A-eGFP allowed for detection of transduced astrocytes and mapping of subcellular compartments.

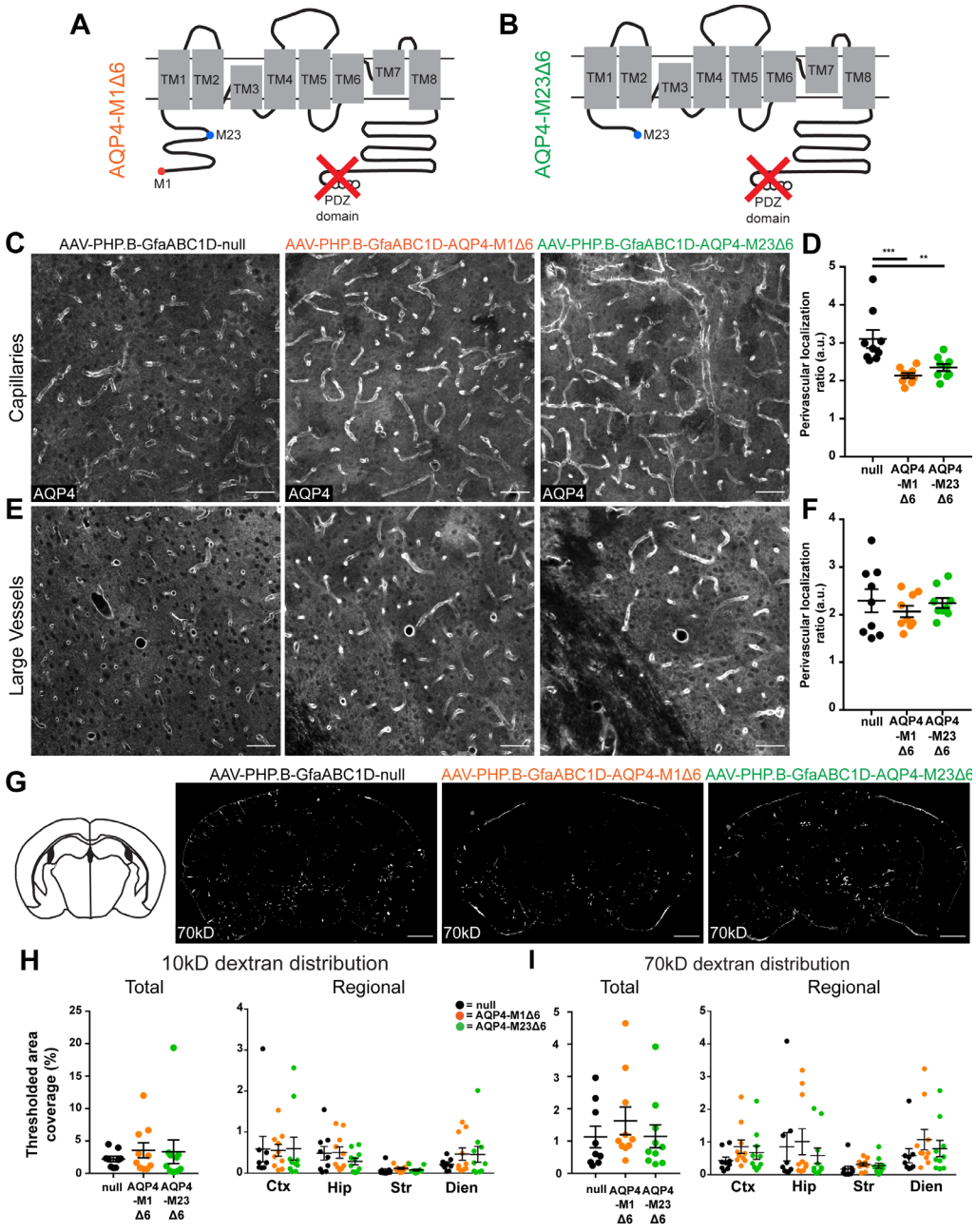

Figure 3.4: Overexpression of PDZ deficient AQP4 reduces localization at capillaries but has no effect on CSF-ISF exchange.

(A-B) Schematic representations of M1Δ6 (A) and M23Δ6 (B) constructs that lack the SXV sequence to bind PDZ domains. (C-F) Perivascular localization of AQP4 following viral treatment. At capillaries, both the M1Δ6 and M23Δ6 viruses impair localization Scale bars = 50 µm. (D, N=8-9/group, One-way ANOVA). At large vessels no effect is seen (E-F). (G) Representative images of CSF-ISF exchange following treatment with M1Δ6 and M23Δ6. (H-I) Distribution of both 10kD (H) and 70kD (I) dextrans are unaffected by M1Δ6 or M23Δ6 overexpression (N=9-10/group). Scale bars = 500 µm.

We first analyzed if any subpopulations of astrocytes in cortex or hippocampus demonstrated enriched targeting by the PHP.B-GfaABC1D virus. GFP expression was evaluated for enrichment proximal to large vessels or within capillary beds. Transduction of large vessel-adjacent and capillary-adjacent astrocytes was observed as well as at the glia limitans for both M1 and M23 viruses (Figure 3.5a-b). Quantification of the ratio of capillary adjacent astrocytes to large vessel adjacent astrocytes revealed a 2.24-fold higher transduction of capillary astrocytes across viruses (Figure 3.5c). This may be obscured however by the relative abundance of capillary-adjacent astrocytes to large-vessel adjacent astrocytes. These results suggest that there is no obvious targeting of astrocyte subpopulations by the PHP.B-GfaABC1D virus.

Next, we investigated the subcellular distribution of both endogenous and exogenous AQP4 in cells overexpressing HA-tagged AQP4. To assess this, super resolution images of individual astrocytes exhibiting triple labeling of HA-tagged AQP4, global AQP4 and a GFP cell-fill were acquired. We assessed distribution of overexpressed AQP4 to the perivascular compartment by measuring mean intensity at the endfoot (defined by global AQP4 labeling), relative to mean intensity across the astrocyte (defined by GFP cell fill). Interestingly, we found that in cells overexpressing M1, the perivascular enrichment ratio was 0.98, while cells expressing M23 exhibited a perivascular enrichment of 1.32 (Figure 3.5d-e, $P = 0.0148$, n=8 cells/virus). Based on these results we conclude that AQP4 isoforms differentially localize to the endfoot compartment, consistent with hypotheses presented based on *in vitro* localization.

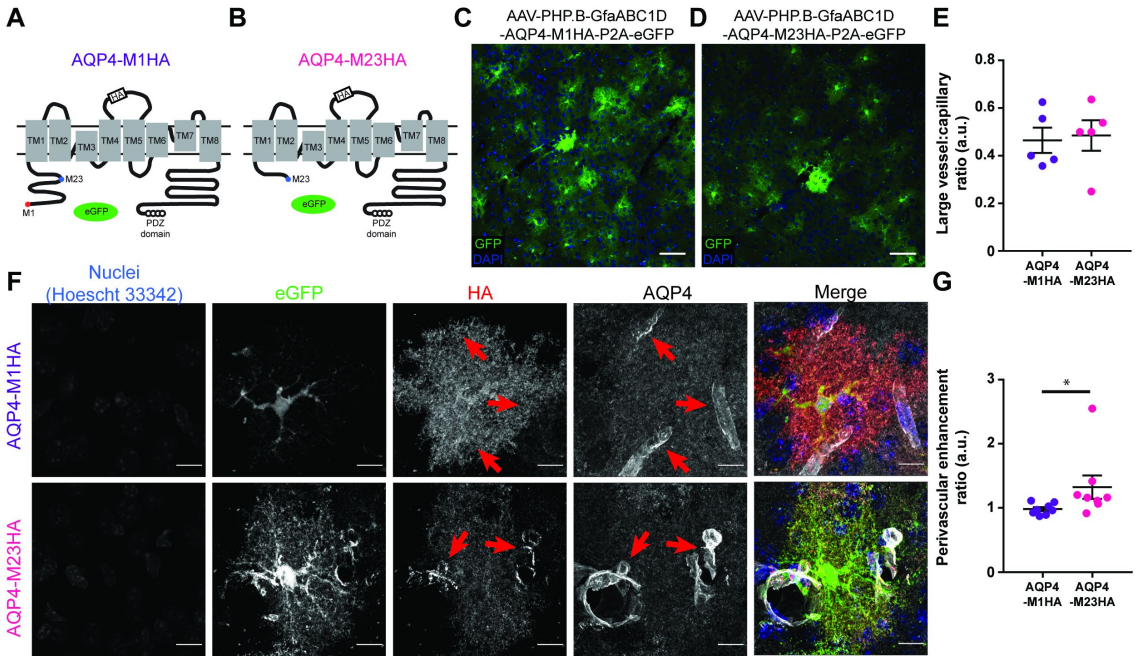

Figure 3.5: Biodistribution of overexpressed AQP4 constructs.
(A-B) Schematic representations of the proteins expressed by vectors designed to test biodistribution. For both M1HA and M23HA, HA tags were inserted in the second extracellular loops, while a P2A site was utilized to allow for co-expression with GFP. (C-E) Assessment of transduced cell distribution revealed substantial transduction at both capillary-adjacent and large vessel-adjacent astrocytes, with substantially greater transduction at capillaries (Scale bars = 50 µm. N=5/group, Mann-Whitney U test). (F-G) Representative images of subcellular AQP distribution for both M1HA and M23HA. Overexpressed AQP4 (HA) was assessed relative to cell architecture (GFP) and total AQP4 (AQP4), revealing a greater perivascular affinity in M23HA overexpressing cells (Scale bars = 2 µm, N=8 cells from 3 animals/group, P = 0.0148, Mann-Whitney U test).

Discussion

Differential isoform expression has long been hypothesized to contribute to the robust perivascular localization of AQP4 seen in astrocytes. Much of this work has stemmed from in vitro studies suggesting that the M23 isoform is responsible for the orthogonal arrays observed at the endfoot compartment, however little evidence of this relationship has been demonstrated *in vivo*. Here, we provide evidence in mice that the AQP4 M1 isoform does not localize to the endfoot compartment when overexpressed, while the M23 isoform does, consistent with previous isoform localization studies *in*

vitro. We also demonstrate that using an AAV mediated gene therapy approach we can globally modulate localization of AQP4 by overexpressing the M1 isoform at the level of capillaries, but not at large vessels. Finally, we demonstrate that modulation of AQP4 at the capillary level is insufficient to impact CSF-ISF exchange. Based on these findings we suggest that AQP4 isoforms contribute to the regulation of perivascular AQP4 localization, but simple overexpression is not a viable therapeutic avenue for targeting CSF-ISF exchange deficits. The expression and localization of AQP4 has been shown to be widely impacted across several brain disease and injury states, including several neurodegenerative diseases such as AD, PD and brain aging (Hoshi et al., 2017; Kress et al., 2014; Zeppenfeld et al., 2017). We have additionally demonstrated that a loss of AQP4 localization without any change in expression as seen in mice lacking expression of the adapter protein α-syntrophin, is sufficient to impair CSF-ISF exchange and alter the propagation kinetics of α-synuclein (Chapter 2). These studies have generated two major questions. 1: what is the mechanism regulating localization in the aging and diseased brain? 2: can therapeutic modulation of AQP4 localization alter CSF-ISF exchange and clearance in pathogenic states?

Here we found that, consistent with *in vitro* studies, the M1 and M23 isoforms of AQP4 exhibit unique subcellular localization profiles *in vivo*. Additionally, we demonstrate that simple overexpression of the AQP4-M1 isoform can alter localization. This is also consistent with previous reports that suggest that palmitoylation sites specific to the NH_2 terminus of the M1 isoform are responsible for the inability of the isoform to assemble into orthogonal arrays, and consequently, localize to the endfoot (Suzuki et al., 2008). Further supporting this is the loss of localization observed in both isoforms when the PDZ domain was deleted, suggesting that the loss of localization seen in the M1 isoform is in fact a result of the isoform difference and not driven by an epiphenomenon of overexpression. These results suggest that AQP4 isoforms likely contribute to perivascular localization *in vivo* at least at the capillary level.

The second major question we had was whether simple, virally driven overexpression of AQP4 isoforms is sufficient to modulate localization and CSF-ISF exchange in the context of pathogenic states. Consistently, we observed that overexpression of AQP4 is insufficient to modulate localization in the context of aging or

in a mouse model of amyloid β deposition. Furthermore, overexpression in these contexts has no functional consequence, either on CSF influx, or on pathogenic processes such as accumulation of amyloid β. Several potential reasons exist for the failure of this method to modulate function or pathology. One possibility is that while isoform expression contributes to establishing perivascular localization, other mechanisms such as AQP4 internalization, or disruption of scaffolding proteins, are responsible for the loss of localization in pathogenic contexts. Wolburg and colleagues reported that reactive astrocytes exhibit a loss of perivascular AQP4 localization, a phenotype associated with aging and brain insult (Wolburg et al., 2011). Numerous studies have demonstrated that in reactive states, astrocytes exhibit wide ranging alterations in Ca^{2+} signaling and structural changes, that may be associated with non-isoform mechanisms of AQP4 subcellular distribution such as PKC and PKA signaling and cytoskeletal rearrangements. Further characterization of changes to the endfoot domain in reactive astrogliosis will help to determine other factors regulating localization in these states.

A second intriguing possibility is that the much of the function of perivascular AQP4 localization in facilitating CSF-ISF exchange, is executed at large vessels rather than at capillaries. The distance along the vascular tree at which perivascular flow is observed remains a topic of active investigation (Abbott et al., 2018). Additionally, age-dependent loss of localization observed in mice occurs at large vessels and not at capillaries (Kress et al., 2014). In our own studies, disruption of perivascular localization at both large vessels and capillaries was sufficient to alter CSF-ISF exchange (chapter 2), while disruption at capillaries alone was not (Figure 3.2). Interestingly, here we also found that perivascular localization at large vessels was the only significant predictor of $A\beta_{1\text{-}42}$ levels in Tg2576 mice, and this effect was independent of viral treatment (Figure 3.2e). These results together suggest that the pool of AQP4 along large vessels may be primarily responsible for facilitating CSF-ISF-exchange, perhaps reflecting disparities between the capacity for bulk flow in the perivascular compartment of Virchow-robin spaces, relative to the perivascular space along capillaries. Here we found that while our virus-based gene therapy approach did target astrocytes along all vessel types, there was an enrichment observed in capillary adjacent astrocytes (Figure 3.5). The development of tools to more specifically modulate AQP4 expression in astrocytes along large vessels

will help to tease apart the contributions of large and small vessel-adjacent astrocytes in basic CSF-ISF exchange physiology and in the context of brain pathology.

Recently, two independent groups have found that AQP4 exhibits an exceptionally high rate of translation readthrough, resulting in the common occurrence of a novel isoform AQP4-X (otherwise known as AQP4-ex) (De Bellis et al., 2017; Sapkota et al., 2019). This variant has been shown to exhibit robust perivascular localization and is significantly less upregulated in response to reactive astrogliosis than global AQP4 levels (Sapkota et al., 2019). While here we investigated the role of the most abundant AQP4 isoforms, the role that the AQP4-X isoform plays in CSF-ISF exchange and in disease pathogenesis remains an important, unanswered question.

It is important to note that all the experiments performed in this study were done on a wild-type background, meaning that endogenous AQP4 expression might be modulating the trafficking and distribution of overexpressed AQP4. This was done to allow for assessment of overexpression as a therapeutic avenue for modulation of CSF-ISF exchange deficits. It is possible that if performed on a non-endogenously expressing background, AQP4 isoform behavior would be modified, however, the consistency between *in vitro* studies, our GFP tagged AQP4 studies (Figure 3.1) and the HA-tagged studies (Figure 3.5), suggest that hypothesized relationships between AQP4-M23 and the perivascular pool of AQP4 are in fact observed *in vivo* and that these relationships can be observed with a wide range of protein-tagging approaches. It is also worth noting that while the PHP.B virus drove abundant, global expression, the incomplete transduction of cells, particularly along large vessels may catastrophically inhibit function of a brain-wide system such as CSF-ISF exchange and contribute to the lack of exchange deficits.

The results of our study have provided an important in vivo validation of the role that AQP4 M1 and M23 isoforms play in regulating perivascular localization. Additionally, they have demonstrated that localization can be modulated by gene therapy in vivo. Perhaps most importantly, these data have exposed several gaps in our understanding of astrocytic endfoot physiology along the vascular tree and in pathogenic contexts. These questions await the development of a more comprehensive profiling of the endfoot compartment and better tools for targeting astrocyte subtypes and subcellular compartments in vivo.

Methods

Materials and antibodies

10kD Cascade Blue-conjugated dextran (ThermoFisher D1976) and 70kD Texas Red-conjugated dextran (ThermoFisher D1864) were dissolved in saline. Aliquots of a 1:1 combined mixture of the dextrans were made and frozen at -20° C until used. 70kD Texas Red-conjugated dextran was also used as an intravascular tracer for in vivo 2-photon experiments. Taqman assays used to measure gene expression include human AQP4 pan-isoform (Hs0024342_m1, Life Technologies) and mouse β-actin (Mm00607939_s1, Life Technologies). Primary antibodies included rabbit anti-AQP4 (1:500, Millipore AB3594), and mouse anti-β amyloid (1:200, Novus Biologicals NBP2-13075). All secondary antibodies were generated in donkey, and conjugated to either Alexafluor-488, Alexafluor 594, or Alexafluor 647. All secondary antibodies for immunofluorescence were used at a concentration of 1:500 and were ordered from ThermoFisher. Hoescht 33342 (1:5000, ThermoFisher H3570) was used to label cell nuclei. Human AQP4 used in viral studies was derived from a human AQP4 cDNA plasmid (Sino HG15306-G). Parent plasmid used for viral constructs was generated and deposited to Addgene by Bryan Roth (Addgene plasmid #50478; http://n2t.net/addgene:50478 ; RRID:Addgene_50478). HA-tagged AQP4 viruses were generated by Vector Biolabs. Quantification of amyloid-β was performed using commercially available ELISA detection kits for amyloid-$\beta_{1\text{-}40}$ or amyloid-$\beta_{1\text{-}42}$ (Fisher Scientific KHB3481 and KHB3441 respectively).

Animals

Homozygous B6;SJL-Tg(APPSWE)2576Kha mice were generated by Dr. Karen Hsiao (Hsiao et al., 1996) and were obtained from Taconic (stock no. 1349), before being crossed onto and maintained on a C57Bl6/J background. Animals were used between 10-16 weeks of age for all experiments in your animals. Aged animal experiments were performed in mice around 59-60 weeks of age. C57Bl6/J mice obtained from Jackson Laboratories were used for all other viral experiments. All mice were cared for by the

Oregon Health & Science Department of Comparative Medicine in an Association for Assessment and Accreditation of Laboratory Animal Care (AALAC) accredited vivarium. All experiments were performed in accordance with state and federal guidelines and all experimental protocols were approved by the institutional animal care and use committee (IACUC). Power analysis was performed either using pilot experiments or literature review to estimate animal counts for each experiment. Power analyses were run to detect significance levels of $p \leq 0.05$, with a power of 80% and effect size of 50%.

Virus production

Recombinant AAV expression plasmids were generated by adapting the parent pAAV-GfaABC1D plasmid (Roth lab, Addgene plasmid #50478) AAV constructs contained 3′ woodchuck hepatitis virus posttranscriptional regulatory element (WPRE) to promote gene expression and stability of intronless RNA (Martin et al., 2002). Recombinant AAV8 and PHP.B were packaged in cultures of HEK 293T cells. Approximately 1.5×10^7 293T cells were seeded into 150 cm dishes in complete DMEM supplemented with 10% fetal bovine serum, 1 mM MEM sodium pyruvate, 0.1 mM MEM nonessential amino acids solution, and 0.05% Penicillin-Streptomycin (5,000 units/mL). At 24 h media was changed to culture media containing 5% FBS and cells were transfected three separate plasmids: 1) Adeno helper plasmid (pFΔ6), 2) AAV helper encoding the Rep 2 and Cap 8 sequences for serotype 8 (pAR8) (Broekman et al., 2006) and 3) the recombinant AQP4 plasmids described above. After culturing cells for 48 h at 37° C, 5% CO_2, cells were harvested and pelleted by centrifugation. The pellet was resuspended in 10 mM Tris, pH 8.0 and chilled on ice. Cells were lysed by repeated freeze-thaw cycles followed by treatment with 50 U benzonase (Novagen, CA) and 0.5% sodium deoxycholate for 30 min at 37° C. Virus was purified by density gradient centrifugation in iodixanol (Zolotukhin et al., 1999). Two buffer exchanges with ACSF were performed. The purified virus was then concentrated in ACSF by centrifugation in Amicon Ultra-15 Centrifugal Filter Units. The final preparation was sterile filtered through a syringe filter. Viral titers were determined by quantitative RT-PCR using primers specific to the WPRE sequence.

Primary astrocyte culture

Primary astrocyte cultures were generated using a serum-containing-media based approach derived from classic astrocyte culture preparation protocol, rather than an immunopanning-based approach (McCarthy and de Vellis, 1980). Briefly, cortical homogenates were collected on ice from neonatal pups aged P2-P5. Astrocytes were purified over the course of several centrifugation and filtering steps. Astrocyte solutions were plated at an initial density of ~100,000 cells/cm^2 in a 75 cm^2 flask, grown to ~60% confluency prior to plating on Poly-D-Lysine (PDL) coated coverslips. While on glass coverslips, viral treatments were administered in 10% FBS-containing media over the course of several days prior to imaging experiments.

Thin skull surgery and intravital 2-photon microscopy

Viral constructs were delivered via intraparenchymal injection approximately 4 weeks prior to imaging experiments. On the day of imaging, a thin-skull preparation was performed above motor cortex. Briefly, mice were anesthetized under isoflurane and head-fixed in a three-point stereotax. Skin was deflected to expose the skull, then a 10% ferric chloride solution was used to dry the skull and allow for removal of overlying tissues. A head plate was then fixed on the skull with superglue, centered over right motor cortex. A microtorque drill was used to gently thin the skull down through the diploe, across a 3mm diameter region. During this process, saline was intermittently applied to the surface of the skull to minimize heat damage at the surface of the brain. A dental microblade was then used to further thin the skull to a uniform thickness of under 50um and a glass coverslip was superglued in place over the thinned skull.

To image the vasculature, a BBB-impermeable Texas red conjugated 70kD dextran was injected into the vascular system via the right retroorbital sinus. Mice were then slowly transitioned to KX anesthesia over the course of 15 minutes and moved in the stereotaxic frame to a Zeiss LSM 7MP multiphoton microscope equipped with dual channel binary GaAsP (BiG) detectors and a Coherent Technologies Chameleon titanium-sapphire femtosecond pulsed laser source. 1024x1024 pixel images were acquired.

Real-time PCR

Total RNA was extracted from brain homogenate using a mirVana Paris RNA purification kit. A cDNA library was then constructed using a high-capacity reverse-transcription kit (Applied Biosystems). Taqman assyas were then performed using a thermal cycler according to manufacturer recommendations.

Cisterna magna tracer infusions

Tracer infusions were performed at previously described (chapter 2). Briefly, a 30g needle tip, was connected to a 10ul Hamilton syringe (Hamilton 80001) by PE-10 tubing. The line was filled with saline and tracer cocktails were backfilled immediately prior to injections. Mice were lightly anesthetized with isoflurane to minimize stress, then ketamine-xylazine (KX) anesthesia was administered peritoneally. Mice were head-fixed in a stereotax and the skin of the neck was exposed with Nair. An incision was made along the midline of neck muscular layers and the tissue was deflected to expose the atlanto-occipital membrane covering the cisterna magna. The needle was inserted into the cisterna magna compartment, until the bottom of the bevel had passed through the AOM, then VetBond was used to secure the needle in place. A syringe pump was used to drive tracer into the cisterna magna at a rate of 500nl/min, for 8 minutes, resulting in the infusion of 4ul total. Successful injection was confirmed immediately, by visualization of tracer pulsation within the cisterna magna, and after tissue collection by observing tracer long perivascular spaces. Mice were maintained under KX anesthesia for the duration of the 90-minute experiments, with peritoneally redosing administered as necessary. Depth of anesthesia was monitored by pedal reflex throughout the course of the experiment. Body temperature was maintained between 36-38C using a heating pad and lamp. Upon experiment completion, brain tissue was fixed with transcardiac perfusion of 4% PFA. Brain surfaces were imaged immediately following the experiment using a fluorescence dissection scope (Zeiss AxioImager upright microscope). Brains were then post-fixed in 4% PFA overnight, followed by cryopreservation in 30% sucrose overnight, prior to freezing in OCT and stored at -80C until sectioning.

Tissue preparation and confocal imaging

Brain were serially sectioned at a thickness of 30um using a cryostat for all datasets, with the exception of HA-tagged experiments which were collected at a thickness of 20um. All immunofluorescence staining was performed on free floating sections. Sections were incubated on a rocker for 4-12 hours in blocking solution (.3% Triton-100, 5% normal donkey serum, 2% bovine serum albumin (BSA) in phosphate buffered saline (PBS) at room temperature. Primary and secondary antibodies were diluted in blocking solution and were incubated with the sections on a rocker overnight at 4C. When used, Hoescht staining was performed for 10 minutes during the last round of washing. Tissue sections were mounted directly onto coverslips with a paintbrush and mounted with Fluoromount-G mounting media for all experiments with the exception of the HA-tagged experiments for which Prolong-gold mounting media was used.

Full brain images were acquired using an automated, slide-scanning confocal microscopy (Zeiss AxioScan.Z1). Images were acquired with a 20X 0.8 PlanApo objective. High magnification images were acquired using a laser scanning confocal microscope, equipped with an AiryScan super-resolution detector (Zeiss LSM880 with Fast Airyscan). Here, images were acquired at 63X (1.4 PlanApo objective) or 20X (PlanApo objective). To maximize the uniformity of quantifications across images, all laser intensities were selected to minimize signal outside of the dynamic range of the detector across all samples imaged.

Image and statistical analysis

All image analysis was performed using FIJI (Schindelin et al., 2012) and IMARIS software. All statistical analysis was performed using Graphpad Prism 7. Uniform, linear adjustments to pixel intensities have been applied to images in figures, but all analyses were run on images as acquired, or uniformly size-scaled images (due to computational memory constraints). Imaris was used to render three-dimensional GFP volumes in cultured cells. All other analyses including total brain and sub-regional brain tracer influx, and perivascular AQP4 localization were quantified in FIJI, consistent with previous descriptions (chapter 2). Briefly, identification of subjective values including

ROIs and uniform threshold selection were performed in a blinded, manual fashion. After these values were selected, custom scripts were generated to automate analysis. One-way ANOVAs were utilized to statistical differences in studies involving two or more groups. For comparisons of two groups, Mann-Whitney U tests were used. All plots in figures are presented with mean and S.E.M. Due to the use of automated image acquisition software, occasionally a small percentage of images would exhibit poor focusing and were subsequently excluded from analysis (1-2 images/dataset). In these situations, integrated density was calculated across the remain sections.

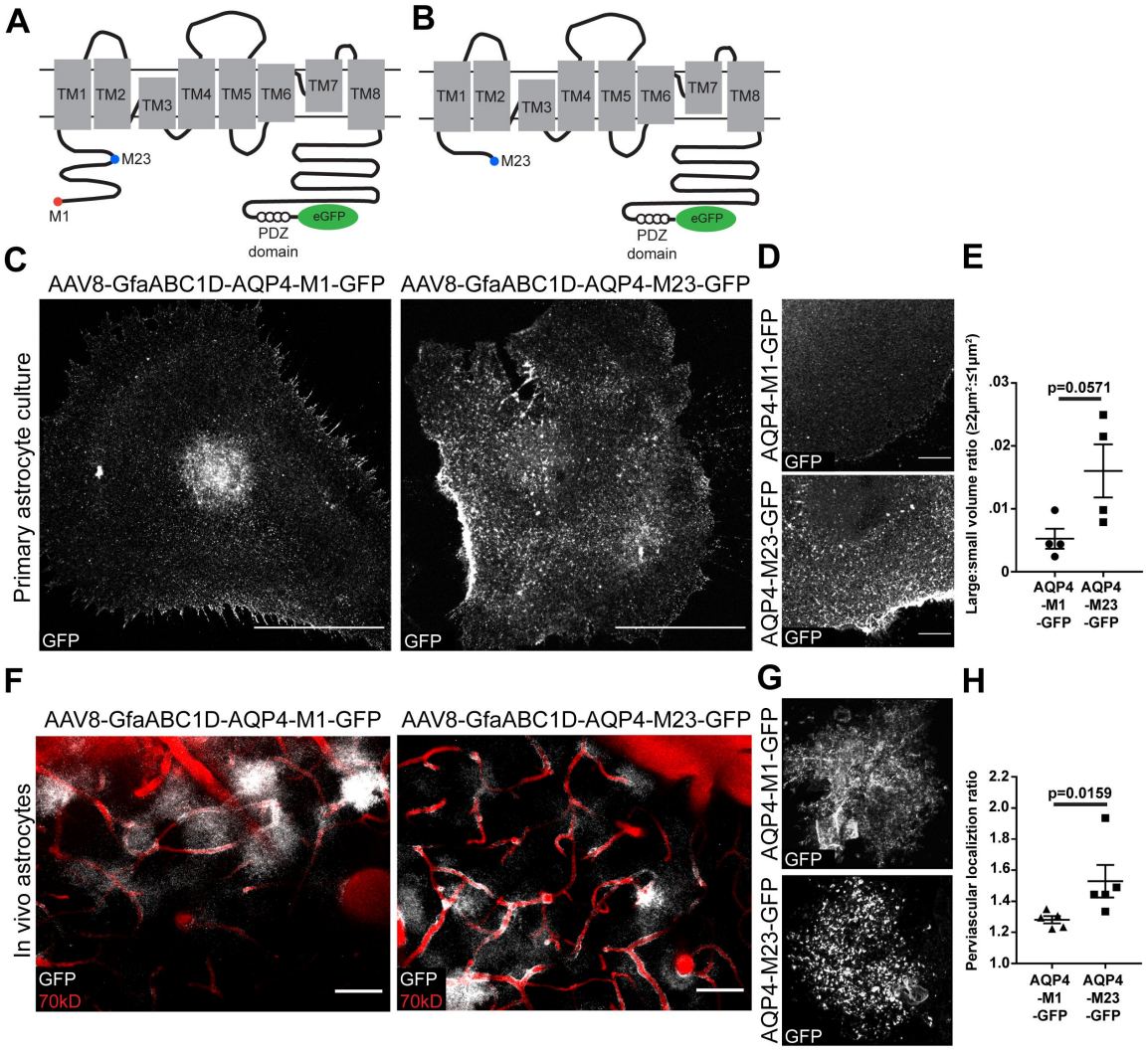

Supplementary Figure 3.1: GFP-tagged AQP4-M23 exhibits greater perivascular localization that GFP-tagged AQP4-M1

(A-B) Schematic representations of the GFP-tagged AQP4 constructs. (C-E) In primary astrocyte cultures, GFP-tagged AQP4-M23 exhibits larger volume protein clustering than AQP4-M1 across the membrane of the cell (Scale bar= 5 µm, 1 µm, N=4/group, Mann-Whitney U test) (F) Assessment of perivascular localization of GFP-tagged constructs in vivo was performed using intravital 2-photon imaging. Blood vessels are labeled by Texas-red conjugated 70kD dextran introduced intravenously. (H) GFP-tagged M23 exhibits greated perivascular localization than GFP-tagged M1 (N=5/group, Scale bars = 25 µm). (G) Fixed tissue imaging of overexpressed GFP-tagged AQP4 demonstrates a similar protein clustering profile to clustering observed in cultured astrocytes.

Chapter 4: A transcriptome-based assessment of the astrocytic dystrophin associated complex in the developing human brain

Matthew J. Simon[1], Charles Murchison[2], Jeffrey J. Iliff[3,4] *

[1]Neuroscience Graduate Program, [2]Department of Neurology, [3]Department of Anesthesiology and Perioperative Medicine, [4]Knight Cardiovascular Research Institute. Oregon Health & Science University, Portland, OR, USA.

Foreword

This chapter reflects analyses of publicly available datasets submitted as a manuscript to the Journal of Neuroscience Research. Datasets utilized in this manuscript were primarily generated and sourced from the Allen Brain Institute. Chad Murchison played a critical role in confirming the validity of bioinformatic approaches utilized and suggesting and implementing appropriate statistical analyses. The rest of the data aggregation, analysis, figure and manuscript preparation was performed by me.

Abstract

Astrocytes play a critical role in regulating the interface between the cerebral vasculature and neurons within the central nervous system. In this space, a specialized structure called the perivascular astrocytic endfoot ensheathes the entirety of the vasculature and mediates signaling between endothelial cells, pericytes and neurons. This structure has been implicated as a critical element of the glymphatic pathway and changes in protein expression profiles in this cellular domain are linked to Alzheimer's disease pathology. Despite this, relatively little is known about how this specialized structure develops, and what protein elements are found at the glial-vascular interface. Here we use human transcriptome data from males and females across several developmental stages and brain regions to characterize the gene expression profile of the dystrophin associated complex (DAC), a known structural component of the astrocytic endfoot that supports perivascular localization of the astroglial water channel aquaporin-4 (AQP4). Transcriptomic profiling is also used to define genes exhibiting parallel expression profiles to DAC elements, generating a pool of candidate gene products, including several genes encoding transporters that may contribute to the physiological function of the perivascular astrocytic endfoot domain.

Introduction

Astrocytes contribute to several physiological functions that involve distribution or transport of water, ions and other solutes including neuromodulation, waste clearance, maintenance of the blood brain barrier (BBB), and regulation of metabolic and ionic homeostasis (Broux et al., 2015; Erdo et al., 2016; Hertz et al., 2014; Hladky and Barrand, 2016; Langer et al., 2017; Longden et al., 2016; Stokum et al., 2015; Tritsch and Bergles, 2007). Deriving their name from their star-like appearance, the unique morphology of astrocytes promotes their role in these functions. This includes the non-overlapping, but gap-junction connected astrocytic syncytium which supports movement of ions, nutrients and water throughout brain tissue (Bennett et al., 2003; Nedergaard et al., 2003). Another distinct feature of astrocytes is the perivascular endfoot domain which completely ensheathes the brain microcirculation (Mathiisen et al., 2010; McCaslin et al.,

2011). This structure represents a secondary barrier, restricting the movement of cells and macromolecules from the abluminal face of the BBB into the wider parenchyma (Agrawal et al., 2006; Engelhardt and Coisne, 2011). Though these anatomical features are well defined, little is known regarding the molecular composition of perivascular astroglial endfeet nor the biophysical basis of their function. Here we utilize a human developmental transcriptomic database to gain insight into the developmental timing of endfoot protein expression. Furthermore, gene network analysis is used to identify novel gene products that may be involved in perivascular endfoot function.

Developmentally, astrogliogenesis occurs over a wide time frame, beginning during embryonic stages but continuing on into early childhood (Reemst et al., 2016; Skoff, 1990). Demonstrated in a number of model systems, ensheathment of the vasculature by perivascular endfoot processes is not believed to occur until after the BBB has formed (Ben-Zvi et al., 2014; Daneman et al., 2010; Nakamura et al., 2012; Sauvageot and Stiles, 2002; Sohet et al., 2015; Tien et al., 2012; Wu et al., 2016). However, secreted factors from astrocytes are critical to maintenance of the integrity of the BBB (Blanchette and Daneman, 2015). Astrogliogenesis has not been well studied in the human brain and the timing of astrocytic ensheathment relative to BBB formation is unknown. This has important implications for understanding both BBB maintenance and biological processes taking place across the perivascular space, including nutrient delivery, waste clearance and immune surveillance (Abbott, 2004; Bakker et al., 2016; Williams et al., 2001).

Perivascular astrocytic endfoot processes have long been associated with dense macromolecular arrays comprised of the astroglial water channel aquaporin-4 (AQP4), which is primarily localized to these perivascular structures (Dermietzel, 1973; Nielsen et al., 1997; Rash et al., 1998; Verbavatz et al., 1997). Yet the physiological relevance of these formations is still not well understood. One possible function is in the recently described “glymphatic” system, a perivascular network that supports interstitial solute clearance through a process that is dependent upon astroglial water transport (Iliff et al., 2012; Xie et al., 2013). Along this pathway, cerebrospinal fluid (CSF) and interstitial fluid (ISF) exchange across the perivascular astrocytic endfoot in an AQP4-dependent manner (Iliff et al., 2014; Iliff et al., 2012). While the dense AQP4 arrays provide a low-

resistance path for water diffusion, it remains unclear what cellular processes facilitate the rapid exchange of solutes along the perivascular compartment.

A critical component of the perivascular astrocytic endfoot domain is the dystrophin associated complex (DAC). This multi-protein scaffolding complex maintains endfoot stability by intracellular interactions with astrocytic cytoskeletal components and binding extracellularly with elements of the basal lamina including laminin and agrin (Boulay et al., 2015; Lunde et al., 2015). Known protein constituents of the DAC include dystroglycan, dystrophin, dystrobrevin and α-syntrophin. The perivascular localization of AQP4 is maintained through its association with the DAC, as elimination of several DAC components including dystrophin and α-syntrophin, or their extracellular binding partners such as agrin, disrupt perivascular AQP4 localization and endfoot integrity (Bragg et al., 2006; Bragg et al., 2010; Derouiche et al., 2012; Nico et al., 2003; Noell et al., 2007; Noell et al., 2011). In the present study, we first characterize the developmental profile of DAC component expression throughout different human brain regions in order to define the temporal profile of astrocytic endfoot development. Expanding upon this analysis, an unbiased bioinformatics approach is used to identify candidate genes exhibiting similar regional and developmental expression profiles to genes of the DAC complex. These genes encode products that may contribute to perivascular endfoot function.

Results

DAC genes are highly expressed in astrocytes

To examine the transcriptome profile of the astrocytic endfoot, we first defined a set of "candidate endfoot genes" encoding proteins established as elements of the DAC in perivascular endfeet. This included 5 genes: *SNTA1* (alpha-syntrophin)*, DTNA* (dystrobrevin)*, DMD* (dystrophin)*, DAG1* (dystroglycan) as well as *AQP4* (Figure 4.1a). Genes encoding DAC proteins were chosen based on their function as a scaffolding complex and integral role for endfoot stability (Bragg et al., 2006; Bragg et al., 2010; Nico et al., 2003; Noell et al., 2007; Noell et al., 2011). AQP4 interacts with the DAC, contributes to neurovascular and glymphatic pathway functions of the endfoot and is thought to mediate cell adhesion (Hiroaki et al., 2006; Iliff et al., 2012; Sun et al., 2016).

The developmental transcriptome data used here, was collected by regional microdissection of tissue, with no cell type specificity. To ensure that information derived from these data is applicable to astrocytic endfeet and not influenced by multiple cell types, cell type expression of the selected DAC genes was characterized. FACs sorting-derived, single cell transcriptome data from the mouse brain obtained from the Barres Brain RNA-seq Database was used (Zhang et al., 2014). The results demonstrate abundant expression of all 5 genes in astrocytes, with specific astroglial expression relative to other major brain cell types including neurons, microglia, endothelial cells and oligodendrocytes, except for *Snta1* which is present in both astrocytes and microglia (Figure 4.1b). We also evaluated the relative abundance of DAC-associated genes. *Aqp4, Dag1* and *Dtna* demonstrate elevated FPKM values relative to a constitutively stable gene (*Gapdh*) while *Dmd* and *Snta1* expression is lower. Together, these results suggest that the selected candidate genes are significantly expressed in astrocytes.

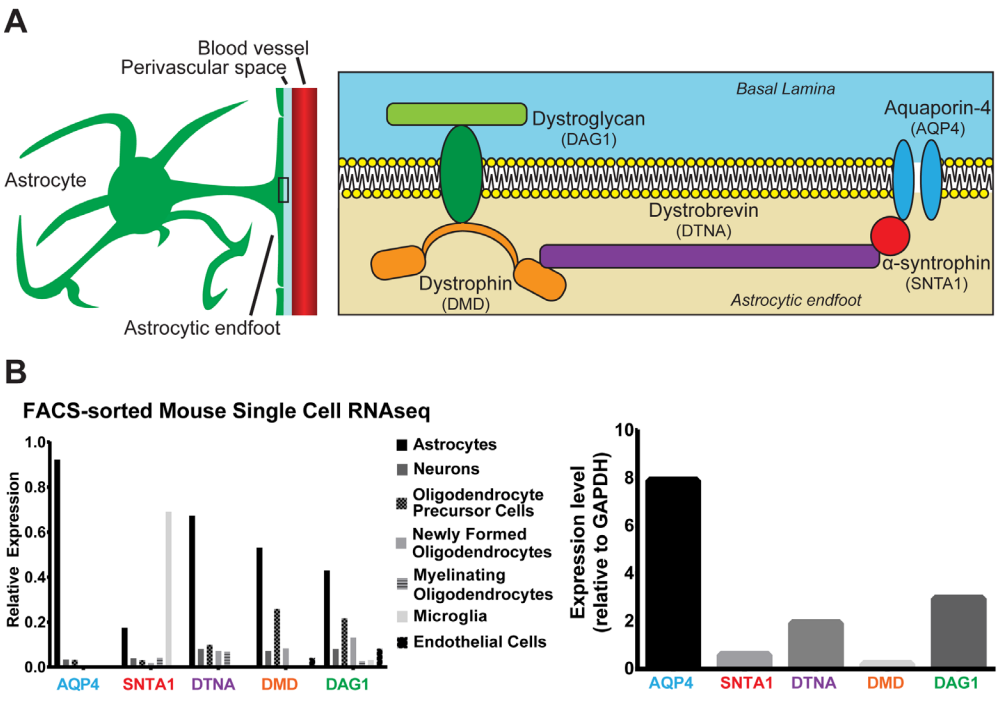

Figure 4.1: Cell type expression profile of DAC proteins.
(A) Schematic of known components of the dystrophin associated complex, and a primary binding partner: AQP4. (B) Percentage of total expression of DAC proteins in each cell type as measured by the Barres Brain RNA-seq Database (left), as well as a quantification of total expression relative to a control gene (*Gapdh*, right).

DAC genes demonstrate two temporally distinct expression profiles

To characterize temporal expression patterns through development, mean transcript expression of endfoot gene products was quantified across prenatal and postnatal time points through adulthood. To assure that changes seen do not purely reflect changes in overall astroglial expression, DAC gene expression was compared to the general astrocytic gene *S100β*. Quantification of mean gene expression level at each time point reveal that the endfoot gene products stratify into two groups (Figure 4.2a-e). Expression of *AQP4*, *DTNA* and *SNTA1* demonstrate increased expression beginning at the "Late Prenatal" stage, while *DAG1* and *DMD* maintain a consistent expression level throughout development (Figure 4.2d-e). Interestingly, when compared to *S100β*, both DAC profiles were independent (Figure 4.2f). Though the *AQP4*, *DTNA* and *SNTA1* share a similar expression profile in later developmental stages, expression of these DAC genes increases robustly during late prenatal stages while *S100β* does not increase until "Early Infancy" (Figure 4.2g). These data suggest that the genes comprising the DAC are not entirely transcriptionally linked and instead, reflect two distinct profiles.

WGCNA reveals clustered expression of DAC genes

Prompted by the two temporally distinct DAC gene groupings, we next probed the transcriptome database for novel candidate genes that might be transcriptionally linked to the DAC proteins. To cluster DAC expression patterns into broader gene expression groups within each brain region, weighted correlated network analysis (WGCNA) was performed to generate an unbiased, biologically motivated hierarchical clustering of genes across developmental age (Figure 4.3). These clusters were probed for expression of the candidate endfoot proteins. For all brain regions examined, only two did not result in any 'endfoot enriched' clusters, or a cluster containing at least two of the five DAC proteins: amgydaloid complex and cerebellar cortex (Table 4.1). In the 14 of 16 regions that demonstrated endfoot gene clustering, *AQP4* expression was present in all of the "endfoot enriched" clusters. *DTNA* and *SNTA1* were in 11 of the 14 "endfoot enriched" clusters. These results are indicative of highly correlated expression of three of the candidate DAC genes, *AQP4, DTNA* and *SNTA1*, across most brain regions.

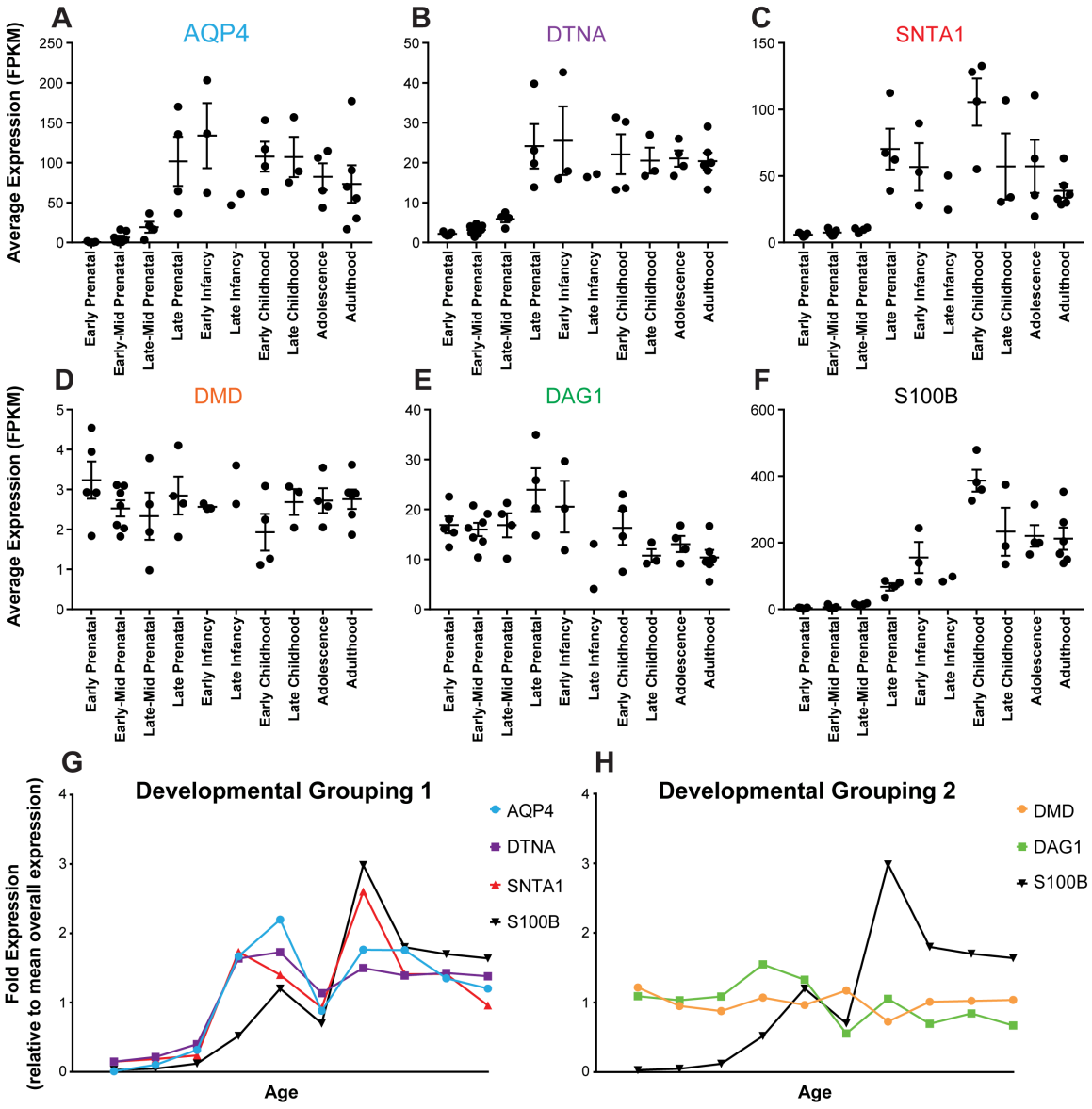

Figure 4.2: Temporal expression profile of DAC proteins during human development. (**A-F**) Mean normalized RNA-seq FPKM values with standard error for DAC genes at ten developmental stages. Statistical analyses available in Supplemental Table 1, One-way ANOVA, Multiple comparisons. (**G**) Mean expression of genes at each developmental stage relative to total sample mean values. DAC candidate genes have been grouped based on similar developmental timing profiles. This clusters *AQP4*, *DTNA*, and *SNTA1* together (left), and *DMD* and *DAG1* together (right). Both are compared to the astrocytic gene *S100β*.

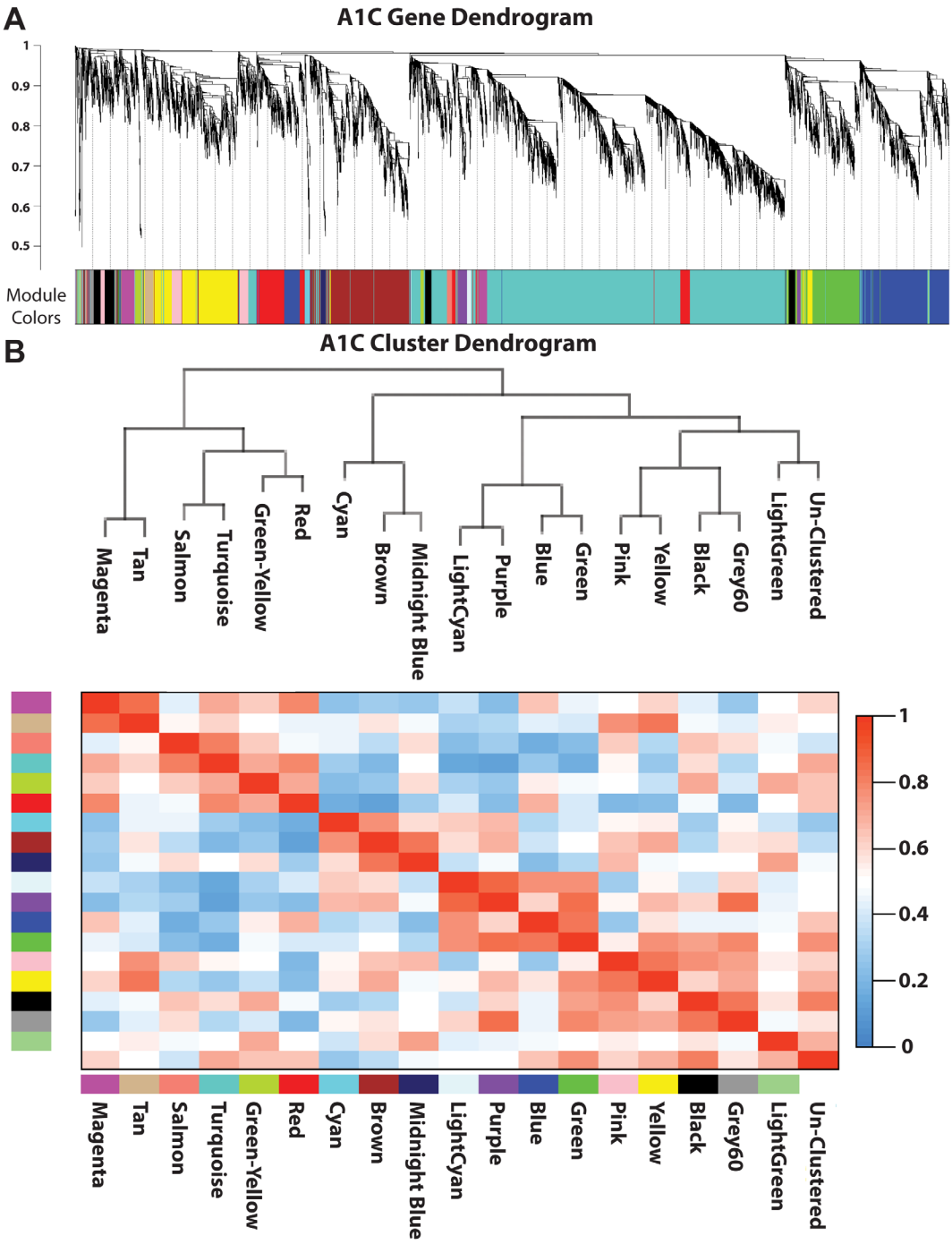

Figure 4.3: Example WGCNA results for primary auditory cortex.

(**A**) Relationship between each gene in the A1C RNA-seq transcriptome. Hierarchical branching of genes is described by the dendrogram (top) while the colors correspond to the cluster each gene was assigned (bottom). (**B**) Relatedness between clusters generated by WGCNA analysis. Dendrogram demonstrating the relatedness between the clustered modules (top), while the correlation between any two dendrograms is represented by the heat map (bottom).

Although they did not consistently cluster with the other DAC candidate genes, we sought to determine if *DMD* and *DAG1* display co-clustering as suggested by their temporal expression profiles. Thresholding used in the initial WGCNA eliminated *DMD* from analysis due to low expression across samples (Figure 4.1b), so a second WGCNA with a lower inclusion threshold was performed (data not shown). In this analysis, *DMD* did not demonstrate co-clustering with other candidate endfoot genes in any of the 16 regions. *DAG1* clustered with the other candidate genes in 4 of the 16 regions. With this reduced threshold all three remaining candidate genes (*AQP4, DTNA* and *SNTA1*) clustered together in 9 of the 16 regions, and at least 2 of the 3 clustered together in 14 of the 16 regions investigated. These data support the co-clustering of the original WGCNA and suggest that *DMD* and *DAG1*, are not linked transcriptionally.

Identification of candidate genes transcriptionally linked to DAC- genes

Utilizing the gene pools generated by the WGCNA, we next aimed to identify candidate genes that may be co-expressed with DAC genes. An "endfoot enriched" cluster gene list was collected for all 14 regions that exhibited co-clustering of candidate genes. Only genes that had a significant Pearson's correlation coefficient with either *AQP4* or *DTNA* in 13 of the 14 brain regions were analyzed further. To ensure selection of astrocytic genes, *SNTA1* was excluded from this filtering step due to microglial expression (Figure 4.1a), as were *DMD* or *DAG1* due to lack of co-clustering with other DAC genes. These highly conservative criteria were utilized to offset the heterogeneity in the available data set. A list of 41 genes was generated (Supplementary Table 4.1) with similar expression patterns to *AQP4* and *DTNA* across nearly all brain regions and timepoints. A literature review suggests that 8 of these gene products (*GJA1, SLC1A2, GJB6, S1PR1, TIMP3, SLC1A3, CYBRD1* and *SLC4A4*) have previously been implicated at the astrocytic endfoot or brain perivascular space, while the remaining genes encode novel candidate proteins (Supplementary Table 4.1). These data support the role of the previously defined proteins at the perivascular endfoot. The full list represents a transcriptionally linked unit that may contribute functionally at the endfoot domain.

Region	*Region Abbreviation*	*Included Genes*	*Number of Modules*	*"Endfoot" Module*	*Genes in "Endfoot" module*	*"Candidate endfoot gene" in module*
Primary auditory cortex	A1C	8321	19	Brown	902	AQP4, DTNA, SNTA1
Amygdaloid complex	AMY	8537	20	-	-	-
Cerebellar cortex	CBC	8514	26	-	-	-
Dorsolateral prefrontal Cortex	DFC	8689	23	Green	544	AQP4, DTNA, SNTA1
Hippocampus	HIP	8639	19	Cyan	119	AQP4, DTNA
Posteroventral (inferior) parietal cortex	IPC	8300	21	Yellow	697	AQP4, DTNA, SNTA1
Inferolateral temporal cortex	ITC	8437	23	Green	465	AQP4, DTNA
Primary motor cortex	M1C	8551	16	Yellow	982	AQP4, DTNA, SNTA1, DAG1
Mediodorsal nucleus of thalamus	MD	7968	19	Green	700	AQP4, SNTA1, DAG1
Anterior (rostral) cingulate cortex	MFC	8447	19	Red	542	AQP4, DTNA, SNTA1
Orbital frontal cortex	OFC	8402	18	Black	416	AQP4, DTNA, SNTA1
Primary somatosensory cortex	S1C	8568	17	Yellow	921	AQP4, SNTA1
Posterior (caudal) superior temporal cortex	STC	8580	21	Green	613	AQP4, SNTA1
Striatum	STR	8620	27	Pink	388	AQP4, DTNA
Primary visual cortex	V1C	8472	19	Yellow	841	AQP4, DTNA, SNTA1
Ventrolateral prefrontal cortex	VFC	8621	24	Yellow	588	AQP4, DTNA, SNTA1

Table 4.1 WGCNA-based Clustering of DAC proteins across 16 brain regions. Summary of the clustering resulting from WGCNA of gene expression in each brain region. The cluster which contained the greatest number of candidate DAC genes is listed along with the genes that were associated with it.

Characterization of novel DAC candidate genes

To gain insight into what role the DAC-associated candidate genes play in endfoot biology, the known functions and properties of the proteins they encode were

analyzed by gene ontology (GO) annotations for molecular function (mf), cellular components (cc) and biological function (bf) in the genes identified as highly co-expressing with DAC genes (data not shown). In the set of identified highly-DAC correlated genes, enrichment for membrane proteins, and connexin complex proteins was detected (p = <.0001). Analysis of associated molecular functions indicate significant enrichment for a ionic and molecular transporter functions, with 11 genes identified as transporters (Table 4.2, p = <.0001). Based on the CellWhere database and a literature review, the 11 genes were classified into the cellular components where the encoded proteins localize (Figure 4.5). We also sought to characterize the developmental profile of the identified genes. All 11 of the genes undergo a increase in expression beginning at late prenatal stages, concurrent with *AQP4*, *DTNA* and *SNTA1* profiles (Figure 4.4).

Molecular Function (MF)	***Gene Ontology (GO) identifier***	***P-Value***	***Number of Genes***	***Genes***
sodium ion transmembrane transporter activity	GO:0015081	8.03E-06	5	ATP1A2, ATP1B2, SLC1A2, SLC1A3, SLC4A4
transmembrane transporter activity	GO:0022857	2.59E-05	10	ATP1A2, ATP1B2, GJA1, FXYD1, SLC1A2, SLC1A3, SLC4A4, SLC25A18, SFXN5, SLC39A12
transporter activity	GO:0005215	3.9606E-05	11	ATP1A2, ATP1B2, GJA1, FXYD1, SLC1A2, SLC1A3, SLC4A4, SLC25A18, SFXN5, SLC39A12, MLC1
ion transmembrane transporter activity	GO:0015075	4.25941E-05	9	ATP1A2, ATP1B2, GJA1, FXYD1, SLC1A2, SLC1A3, SLC4A4, SFXN5, SLC39A12
substrate-specific transporter activity	GO:0022892	5.49191E-05	10	ATP1A2, ATP1B2, GJA1, FXYD1, SLC1A2, SLC1A3, SLC4A4, SFXN5, SLC39A12, MLC1
substrate-specific transmembrane transporter activity	GO:0022891	8.06906E-05	9	ATP1A2, ATP1B2, GJA1, FXYD1, SLC1A2, SLC1A3, SLC4A4, SFXN5, SLC39A12
active transmembrane transporter activity	GO:0022804	8.27759E-05	6	ATP1A2, ATP1B2, SLC1A2, SLC1A3, SLC4A4, SLC25A18

Table 4.2: Molecular functions associated with WGCNA-derived candidate genes
Molecular functions identified by GO analysis as enriched within the list of genes highly correlated to the DAC candidate genes (P<.00001). All functions are related to transporter functions and produced a list of 11 total genes.

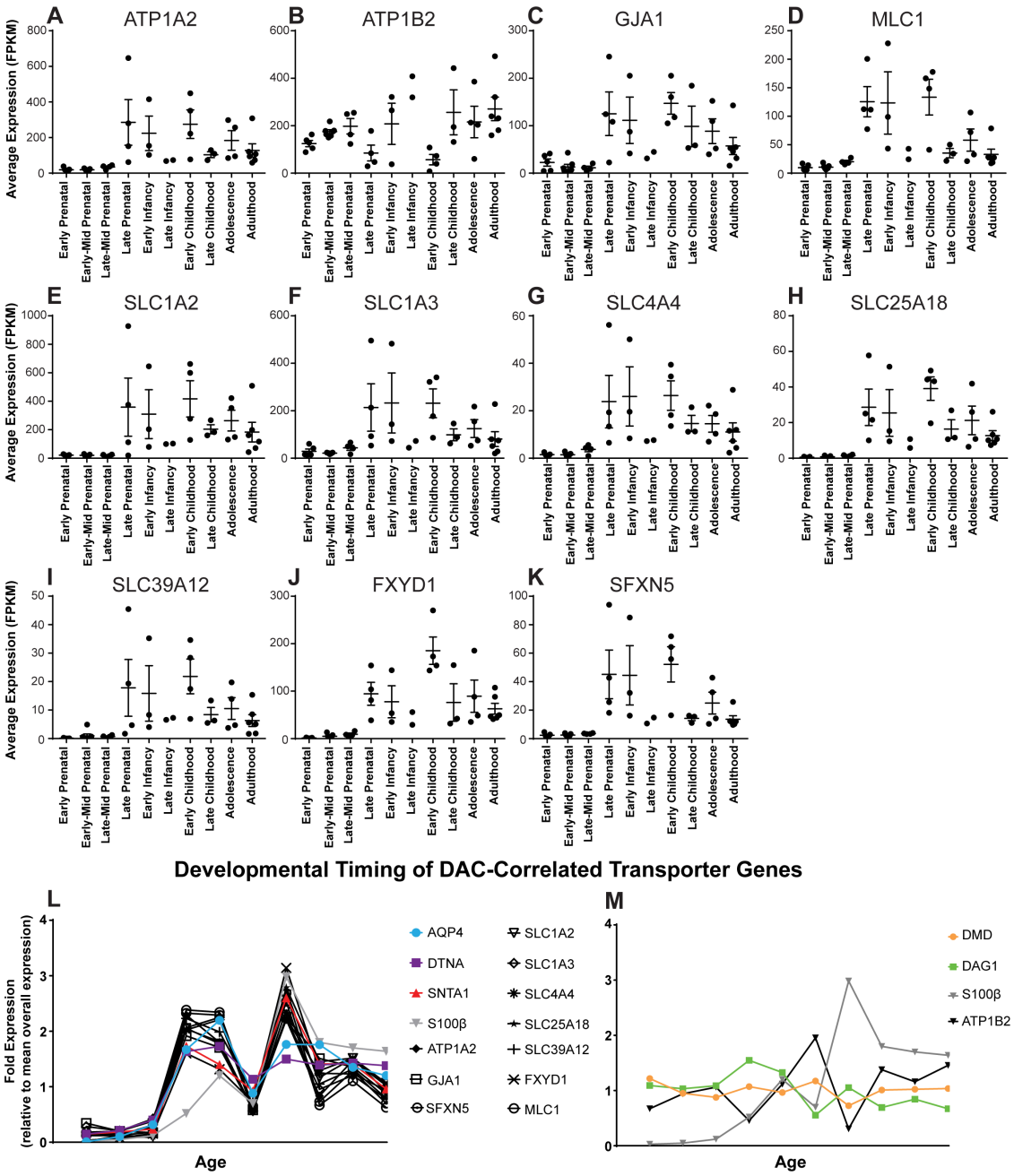

Figure 4.4: Developmental profile of WGCNA-derived candidate transporter genes. (**A-K**) Temporal expression profile of the candidate transporter genes identified by WGCNA. Mean FPKM values with standard error from each individual are represented for each time point. Statistical analyses available in Supplemental Table 1, One-way ANOVA, Multiple comparisons. (**L-M**) Mean expression of WGCNA-derived candidate genes at each developmental stage relative to total sample mean values. Expression of similarly grouped probe genes *AQP4*, *DTNA*, and *SNTA1*, as well as the generic astrocyte gene *S100β* are overlaid to demonstrate temporal similarities.

Discussion

In the present study, the developmental expression profile of genes encoding proteins that contribute to perivascular astroglial endfoot function in the human brain was investigated. We first defined the transcriptional expression profile of DAC components and the water channel AQP4, which encode proteins known to localize to perivascular astrocytic endfeet and contribute to neurovascular unit function. Using the unbiased gene clustering technique WGCNA, we observed that DAC components, including most prominently AQP4, DTNA and SNTA1 clustered in terms of their expression profiles across brain regions and throughout development. Based on these clusters, we defined genes associated with DAC elements and *AQP4* throughout the course of human brain development. The genes identified by this analysis encode both proteins previously reported at the endfoot domain, as well as entirely novel candidate proteins. Our results suggest that components of the astrocytic endfoot complex may undergo concurrent upregulation during development. Furthermore, in addition to the water channel AQP4, components of the DAC may interact with, and be transcriptionally linked to a number of ion and solute transporters.

Temporal analysis of DAC gene expression revealed two distinct profiles within the complex. While *DMD* and *DAG1* demonstrate a consistent level of expression across development and aging, expression of the other three components (*AQP4*, *DTNA* and *SNTA1*) undergo significant age-linked fluctuation. These data suggest that the DAC complex is not transcriptionally linked as a whole, but rather suggests that it is regulated through two or more transcriptional modules. *DMD* and *DAG1* have been suggested to directly interact with cytoskeletal and extracellular matrix components respectively (Gesemann et al., 1998; Michalak and Opas, 1997; Szabo et al., 2004). These proteins may represent the “core” of the DAC complex that facilitate the membrane localization properties of the complex. Complementary to this, *SNTA1* and *DTNA* express multiple protein binding domains (Constantin, 2014) and may serve as interchangeable scaffolding components of the DAC that link the core to functional units such as signaling and transporter proteins. Further investigation is necessary to determine whether the apparent

transcriptional co-regulation of DAC proteins facilitates functional subdomains of the complex.

AQP4, *DTNA* and *SNTA1* demonstrate a significant elevation in expression beginning at late prenatal stages (25-39 post-conception weeks) and a slow decline in expression beginning after early childhood (19 months-5 years of age). This rise and fall in expression exhibits key differences from expression of the general astrocytic protein *S100β*. Specifically, AQP4, DTNA, and SNTA1 gene expression diverge from *S100β* expression both in late prenatal development and in the aging brain. This suggests that development and maintenance of the perivascular endfoot and the distribution of signaling molecules relevant to BBB maintenance and neuronal maturation may be distinct from the general process of astrogliogenesis. The late embryonic timing of DAC gene expression observed in our study is consistent with reported findings in mammalian model systems and supports the prevailing hypothesis that astrocytes do not contribute to angiogenesis and BBB formation in humans but are likely involved in secretion of factors that maintain BBB integrity (Blanchette and Daneman, 2015). Furthermore, the CSF has been implicated as a distribution route for developmentally important trophic factors and may contribute to neuronal plasticity and circuit formation that is abundant during this period. (Chau et al., 2015; Gato et al., 2014; Lehtinen et al., 2011).

With its unique location at the neurovascular interface, the endfoot is also critical to generation and maintenance of fluid and ionic homeostasis in the brain. Previous research in rats proposes that total water content in the brain decreases postnatally and similarly the total brain amount of key ions Na^+, K^+, and Cl^- all decline during early postnatal weeks (Erecinska et al., 2005; Vernadakis and Woodbury, 1962). Consistent with this, regulation of the extracellular space of the brain is greatest during this period. Measurement of the extracellular volume fraction in developing rats demonstrates the most robust changes occur during early postnatal stages (Lehmenkuhler et al., 1993; Sykova, 2005; Vorisek and Sykova, 1997). Accordingly, several DAC proteins found at the astrocytic endfoot, including AQP4, have been shown to markedly increase expression during the first two weeks of postnatal development in rodents, suggesting a role for these proteins regulating developmental chances in extracellular volume and ion homeostasis (Lunde et al., 2015; Wen et al., 1999). This notion is supported by the

observation of increased total brain water with *Aqp4* gene deletion (Nagelhus and Ottersen, 2013).The data collected in this study demonstrate a slight difference in timing, with the greatest increase of expression of DAC-associated proteins occurring during late embryonic stages. This difference is likely a reflection of inter-species differences in developmental timing, and suggests a similar role of these proteins in maintaining osmotic homeostasis in humans as has been shown in rodents (Clancy et al., 2001). The decline in expression of these proteins with aging has implications for our understanding of fluid and solute movement systems in the pathophysiology of the aging brain.

The data from this study suggest that connexin members of the gap junction complex *GJA1* (encoding connexin 43) and *GJB6* (encoding connexin 30) may be co-regulated at the gene expression level with a subset of DAC-associated genes. These gap junction proteins are astrocyte specific and play a role in maintenance of the interconnectivity of the astrocytic syncytium (Giaume et al., 2010). Interestingly, GJA1 has been suggested to functionally couple endfeet domains. Fenestrations resulting from inter-endfoot process gaps along with gap junction coupling between endfeet may contribute to macromolecular transport in this space. While the initial characterization of glymphatic function suggested that arterial pulsation drives convective movement of CSF through the brain interstitial space (Iliff et al., 2012; Iliff et al., 2013b), more recent computational modeling studies have suggested that these forces may be insufficient to drive bulk flow through these spaces under physiological conditions (Jin et al., 2016; Smith et al., 2015). Most recently, intracellular flow and dispersion models have been elaborated as potential alternative pathways to explain the rapid exchange of solutes between the CSF and the ISF along perivascular pathways (Asgari et al., 2015; Asgari et al., 2016). Together these illustrate the need for a more thorough understanding of the constituents of the astrocytic endfoot that may contribute to fluid and solute movement across this domain. Development of an understanding of how homeostasis is maintained at the neurovascular unit has important implications for a wide range of pathophysiological conditions including cerebral edema and cerebral amyloid angiopathy (Thrane et al., 2014; Thrane et al., 2015; Wilcock et al., 2009).Our data support the notion that connexins may be a critical component for movement of large solutes and macromolecules in the context of glymphatic function.

Molecular and ionic transporters were highly represented within the identified candidate genes. In addition to the connexin genes, 4 other genes with described roles in ion or molecule transport were identified: *SLC1A2*, *SLC1A3*, *SLC4A4*, and *CYBRD1*. The glymphatic system is a solute clearance pathway that is based on CSF movement into and through the interstitial space of the brain (Iliff et al., 2012; Nedergaard, 2013), yet the cellular mechanism of this system which drives the water and solute movement along these pathways remains a contentious question. Here we identified genes that encode solute transporters and show congruent age-dependent expression with AQP4. These genes may provide important new insight into perivascular astroglial water and solute transport particularly in the context of glymphatic pathway function. SLC4A4 encodes a sodium bicarbonate co-transporter that may contribute to generation of the ionic gradients necessary for fluid movement across the endfoot. In addition to these ion transporters, several genes were identified with unknown functions at the endfoot domain. PRODH and GLUD1 have been previously described components of mitochondria and TIMP3 is thought to be involved with regulation of localization. With further investigation, these proteins may provide insight into the functional architecture at the astrocytic endfoot critical for neurovascular regulations and glymphatic mediated clearance (Figure. 4.5).

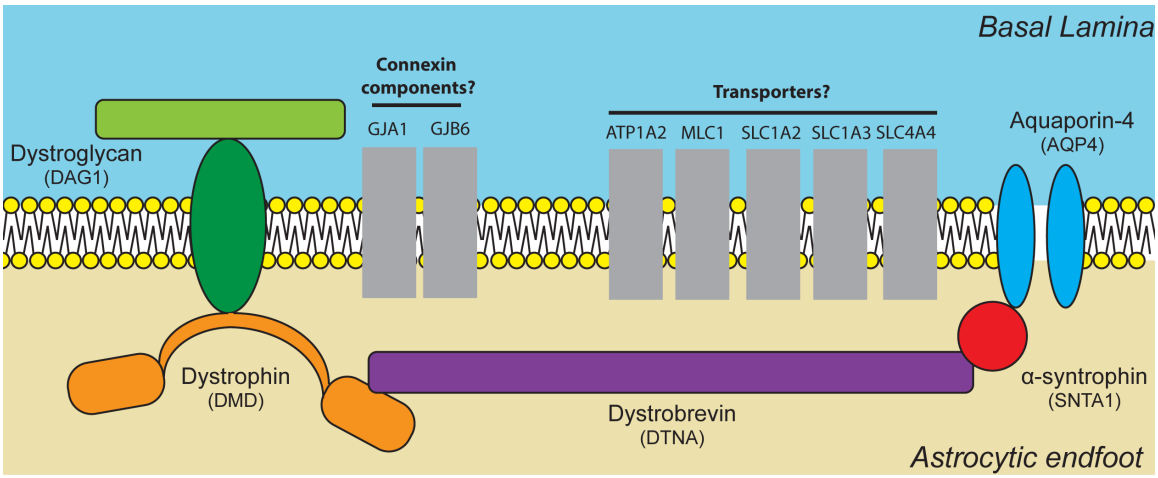

Figure 4.5: Proposed schematic of DAC interactions with transporters at the end foot. Diagram representing possible interaction between gene products encoded by the candidate genes identified by WGCNA. All gene products illustrated have been previously reported to have a role at the astrocytic endfoot domain. Genes are clustered by established functional roles. Proteins are represented in grey as further biochemical and histological validation is necessary to confirm endfoot localization and interactions.

There are several limitations to our study. Primary among these is the data set upon which our analysis was performed as many of the time points had small sample sizes. This is demonstrated by the "Late Infancy" developmental stage, from which only two samples were available. Furthermore, many of these did not have adequate coverage between genders. As previously noted, an additional drawback for our characterization is the RNA-seq data utilized was not astrocyte specific and instead encompasses genes expressed in all brain cell types. To diminish these effects and generate a conservative candidate gene list, strict inclusion criterion was utilized. However, this itself alters the interpretation of our data. This is exemplified by interrogation of the gene expression profile of angiotensinogen (*AGT*), a secreted factor produced by astrocytes known to regulate tight junctions at the BBB (Wosik et al., 2007) and Megalencephalic leukoencephalopathy with subcortical cysts 1 (*MLC1*) a transporter previously demonstrated to interact with the DAC (Boor et al., 2007). Both meet all inclusion criteria but clustered with the subset of DAC genes in 12/14 regions and 11/14 regions respectively, rather than the cutoff of 13/14 (Supplemental Table 2). These data illustrate that additional information may be extracted from this dataset based on what inclusion criteria are defined, but conversely that despite the unbiased nature of the clustering approach, inherit biases exist in how subsequent inclusion criteria are established. Finally, it is important to note that analysis was limited to assessment of transcriptional expression, with no experimental validation of protein localization. Associated gene expression does not necessitate co-localization at the astrocytic endfoot. Despite this, 8 of the 12 endfoot correlated genes identified encode proteins previously described at the endfoot domain. Though experimental validation is necessary, these findings support the concept of a transcriptionally linked endfoot unit.

In this study, our data has defined a transcriptionally linked DAC-associated unit, along with new candidate genes for this region. If confirmed by biochemical studies, these proteins represent novel targets for understanding and therapeutically treating impaired waste clearance in the aging brain.

Methods

Data sources

All data was collected from publicly available data repositories generated and curated by the Allen Brain Institute, or the Barres lab at Stanford.

Allen Brain Institute Developing Human Brain database

The data used for analysis came from the Allen Brain Institute Developing Human Brain Database (McCaslin et al., 2011; Miller et al., 2014). This data contained RNA-seq based transcriptome data from 42 individuals ranging in ages from 7 post-conception weeks to 40 years. Sex of the individuals was balanced approximately evenly (19 females, 23 males). RNA-seq data was collected from 16 brain regions within each individual with over 20,000 genes read from each region, with the exception of tissue collected at the earliest prenatal stage (8-9 post-conception weeks) at which larger regional dissections were made (10 total regions). Detailed description of tissue collection and processing is available in the documentation associated with the database (http://help.brain-map.org//display/devhumanbrain/Documentation). Data was downloaded on October 24th 2016. Entrez IDs (as provided by Allen Brain Institute) were used for protein identification and subsequent analysis.

Weighted Correlation Network Analysis

Weighted Correlation Network Analysis (WGCNA) was implemented using the WGCNA package in R (http://www.genetics.ucla.edu/labs/horvath/CoexpressionNetwork/, RRID: SCR_003302) (Langfelder and Horvath, 2008; Langfelder and Horvath, 2012). Due to the lack of full male and female datasets for multiple ages, a single network correlation network was constructed for each brain region of which there were 16 in total. Initial filtering was applied prior to the analysis to eliminate spurious genes that had fragments per kilobase per million (FPKM) values of less than 10 in 90% or more of total reads. This resulted in approximately 8000 genes per brain region. For the second, less-conservative WGCNA,

this threshold was adjusted to FPKM values of less than 3 in 95% or more of total reads. Following standard practices, soft-thresholding was used to establish a connection weight between each gene pair across gender and age within each brain region (Zhang and Horvath, 2005). Using this soft-thresholding power, a topographical overlap matrix was generated and a dendrogram relating gene expression was derived. Leveraging the developed dendrogram, gene modules were generated using hierarchical clustering.

Cluster-based analysis

The gene modules in which DAC genes were most highly expressed were extracted from each brain region's WGCNA-based clusters. Of the 16 brain regions, 2 (amygdaloid complex and cerebellar cortex) did not demonstrate clustering of DAC genes and were excluded from further consideration. Genes with astrocyte specific expression were extracted by thresholding out genes with less than 50% of total expression derived from astrocytes. Cell type expression values were derived from a separate cell-type RNA-seq transcriptome database which resulted in 50-100 astrocytic genes per cluster (Zhang et al., 2014). Drawing on the consistent joint clustering of DAC genes, Pearson's correlation coefficient was used to identify additional genes highly co-expressed with DAC complex genes across subjects. First, a gene was only considered as co-expressing with DAC after a conservative correlation of $r>0.65$ ($p<1e^{-5}$) was observed with at least 2 of the DAC genes. Next, genes were only selected that demonstrated this significant correlation to the DAC genes *AQP4*, *DTNA*, *SNTA1* or *DAG1* in at least 11 of 14 brain regions.

Gene-Ontology Analysis

To explore protein functions overrepresented in the "endfoot enriched" modules, gene ontology analysis was used. Gene ontology was performed using the limma package in R (http://bioinf.wehi.edu.au/limma/, RRID: SCR_010943) (Ritchie et al., 2015). Only human pathway information was probed, with a false discovery rate cutoff of 0.05. Genes with a p-value for over-representation of $p<0.001$ were reported.

Subcellular localization mapping

Localization and associated functions of identified proteins was determined through literature review and the CellWhere database (http://cellwhere-myo.rhcloud.com/) (Zhu et al., 2015). The UniProt and Gene ontology functions were used to assess cell localization.

Gene	*Gene Name*	*Reference*
S1PR1	sphingosine-1-phosphate receptor 1	*(Nishimura et al. 2010)*
TIMP3	TIMP metallopeptidase inhibitor 3	*(Manousopoulou et al. 2016)*
SLC4A4	solute carrier family 4 (sodium bicarbonate cotransporter), member 4	*(Majumdar et al. 2008)*
CYBRD1	cytochrome b reductase 1	*(Loke et al. 2013)*
SLC1A2	solute carrier family 1 (glial high affinity glutamate transporter), member 2	*(Langer et al. 2016; Schreiner et al. 2014)*
SLC1A3	solute carrier family 1 (glial high affinity glutamate transporter), member 3	*(Langer et al. 2016; Schreiner et al. 2014*
GJA1	gap junction protein, alpha 1, 43kDa	*Boulay et al. 2015; Simard et al. 2003*
GJB6	gap junction protein, beta 6, 30kDa	*(Boulay et al. 2015; Nagy et al. 1999)*
AGT	Angiotensinogen (serpin peptidase inhibitor, clade A, member 8)	*(Wosik et al. 2007)*
ATP1B2	ATPase, Na+/K+ transporting, beta 2 polypeptide	*(Brignone et al. 2011)*
AXL	AXL receptor tyrosine kinase	*(Miner et al. 2015)*
NDRG2	NDRG family member 2	*(Flugge et al. 2014)*
MLC1	Megalencephalic leukoencephalopathy with subcortical cysts 1	*(Boor et al. 2007)*
PPAP2B	phosphatidic acid phosphatase type 2B	-
PRODH	proline dehydrogenase (oxidase) 2	-
GLUD1	glutamate dehydrogenase 1	-
CPE	cytoplasmic polyadenylation element binding protein 3	-
CLDN10	Claudin 10	-
AK4	adenylate kinase 4	-
PPP1R3C	Protein phosphatase 1, regulatory (inhibitor) subunit 3C	-
DIO2	Deiodinase, iodothyronine, type II	-
SLC39A12	Solute carrier family 39 (zinc transporter), member 12	-
SLC25A18	Solute carrier family 25 (mitochondrial carrier), member 18	-
F3	Coagulation factor III (thromboplastin, tissue factor)	-
TST	Thiosulfate sulfurtransferase (rhodanese)	-
HTRA1	HtrA serine peptidase 1	-
ATP1A2	ATPase, Na+/K+ transporting, alpha 2 (+) polypeptide	-
TRIL	TLR4 interactor with leucine rich repeats	-
NTSR2	Neurotensin receptor 2	-
BAALC	Brain and acute leukemia, cytoplasmic	-
PBXIP1	Pre-B-cell leukemia homeobox interacting protein 1	-
LRIG1	Leucine-rich repeats and immunoglobulin-like domains 1	-
RANBP3L	RAN binding protein 3-like	-
ACSBG1	Acyl-CoA synthetase bubblegum family member 1	-
AMOT	Angiomotin	-
SFXN5	Sideroflexin 5	-
FXYD1	FXYD domain containing ion transport regulator 1 (phospholemman)	-
ACSS1	Acyl-CoA synthetase short-chain family member 1	-
CLU	Clusterin	-
SLC9A3R1	Solute carrier family 9 (sodium/hydrogen exchanger), member 3 regulator 1	-
FAM69C	Family With Sequence Similarity 69 Member C, C18orf51	-

Supplementary Table 4.1: Genes highly correlated to expression of DAC genes. The list of 41 genes derived from the correlation analysis of genes in the "endfoot associated" WGCNA clusters across brain regions, with any published literature regarding their known localization to the astrocytic endfoot domain. Genes in the gray section have been previously described to encode gene products found at the endfoot domain, while those in white have not been validated.

Chapter 5: Transcriptional network analysis of human astrocytic endfoot genes reveals region-specific associations with dementia status and tau pathology

Matthew J. Simon[1,2], Marie X. Wang[1], Charles F. Murchison[3], Natalie E. Roese[1], Erin L. Boespflug[3], Randall L. Woltjer[4], Jeffrey J. Iliff[1,5] *

[1]Department of Anesthesiology and Perioperative Medicine, [2]Neuroscience Graduate Program, [3]Department of Neurology, [4]Department of Pathology, [5]Knight Cardiovascular Institute; Oregon Health & Science University, Portland, OR, USA.

Foreword

This chapter reflects analyses of publicly available datasets submitted as a manuscript to Scientific Reports. Datasets utilized in this manuscript were primarily generated and sourced from the Allen Brain Institute. As with the data in chapter 4, Chad Murchison was fundamental to selecting and implementing appropriate statistical analyses. Marie Wang and Natalie Roese contributed to the collection of western blot data seen in Figure 6. The rest of the data aggregation, analysis, figure and manuscript preparation was performed by me. All authors contributed to the editing of the manuscript.

Abstract

The deposition of misfolded proteins, including amyloid beta plaques and neurofibrillary tangles is the histopathological hallmark of Alzheimer's disease (AD). The glymphatic system, a brain-wide network of perivascular pathways that supports interstitial solute clearance, is dependent upon expression of the perivascular astroglial water channel aquaporin-4 (AQP4). Impairment of glymphatic function in the aging rodent brain is associated with reduced perivascular AQP4 localization, and in human subjects, reduced perivascular AQP4 localization is associated with AD diagnosis and pathology. Using human transcriptomic data, we demonstrate that expression of perivascular astroglial gene products dystroglycan (*DAG1*), dystrobrevin (*DTNA*) and alpha-syntrophin (*SNTA1*), are associated with dementia status and phosphorylated tau (P-tau) levels in temporal cortex. Gene correlation analysis reveals altered expression of a cluster of potential astrocytic endfoot components in human subjects with dementia, with increased expression associated with temporal cortical P-tau levels. The association between these gene products, including *DTNA* and megalencephalic leukoencephalopathy with subcortical cysts 1 (*MLC1*) with AD status was confirmed in a second human RNA dataset and in human autopsy tissue by Western blot. This suggests changes in the astroglial endfoot domain may underlie vulnerability to protein aggregation in AD.

Introduction

Aggregation of mis-folded proteins is a central hallmark of numerous neurodegenerative diseases. For example, Alzheimer's disease (AD) is characterized histopathologically by the presence of extracellular plaques made up of amyloid β (Aβ) and intracellular neurofibrillary tangles (NFTs) comprised of hyperphosphorylated versions of the microtubule-associated protein tau (Serrano-Pozo et al., 2011). Aβ, an extracellular peptide released through the sequential cleavage of the transmembrane amyloid precursor protein (APP), is produced within the brain throughout life in response to synaptic activity (Cirrito et al., 2008). Radiotracer studies carried out in human subjects demonstrate that the slowing of Aβ clearance, rather than an increase in the rate of Aβ production, occurs in both the aging and AD brain (Mawuenyega et al., 2010;

Patterson et al., 2015). It remains unknown, however, what cellular and molecular changes in the aging and AD brain slow Aβ clearance and render it vulnerable to Aβ plaque formation.

The basis for tau aggregation in NFTs remains similarly unclear. Recent experimental studies suggest that tau aggregates propagate in a prion-like manner through the extracellular compartment between neighboring or synaptically connected neurons, potentially accounting for the stereotyped neuroanatomical progression of neurofibrillary pathology throughout the course of AD (Guo and Lee, 2011; Liu et al., 2012). In vivo microdialysis experiments in mice demonstrate that tau is released into the interstitium of the healthy young brain in response to excitatory synaptic activity (Yamada et al., 2014). Whether changes in the dynamics of extracellular tau underlie the development of NFTs in the aging and AD brain likewise remains unclear.

The glymphatic system is a brain-wide network of perivascular pathways that facilitates the exchange of interstitial and cerebrospinal fluid (CSF), supporting the clearance of Aβ and tau from the brain interstitium. Glymphatic function, including Aβ clearance, is dependent upon the expression of the astroglial water channel aquaporin-4 (AQP4) that is localized primarily to perivascular astrocytic endfeet ensheathing the cerebral vasculature (Iliff et al., 2012). *Aqp4* gene deletion in mice slows Aβ clearance (Iliff et al., 2012) and promotes Aβ plaque formation in a mouse model of AD (Xu et al., 2015), and exacerbates pathological tau phosphorylation in an experimental model of traumatic brain injury (Iliff et al., 2014). In the aging and post-traumatic rodent brain, impairment of glymphatic function is associated with the loss of perivascular AQP4 localization (Iliff et al., 2014; Kress et al., 2014).

Glymphatic function has been visualized clinically only on a limited basis (Eide and Ringstad, 2015; Ringstad et al., 2017), but a recent study in human post-mortem tissue demonstrated that loss of perivascular AQP4 localization is associated with AD status, and with both Aβ plaque burden and neurofibrillary pathology (Zeppenfeld et al., 2017). In the present study, we use human transcriptomic data from aged cognitively-intact and demented subjects to demonstrate that changes in the expression of components of the dystrophin-associated complex (DAC), the multi-protein complex that anchors AQP4 to the astrocytic perivascular endfoot, are associated with dementia status

and tau pathology in the human cortex. Using Weighted correlation network analysis (WGCNA), we identify 11 astrocytic genes with gene expression profiles similar to DAC genes and *AQP4* in the aging brain, and whose expression levels predict dementia status and and temporal cortical tau pathology. Lastly, we confirm the associations between the newly identified genes and AD pathology at both the gene expression and protein levels in independent human AD cohorts. These findings suggest that changes in perivascular astroglial function may be one factor contributing to the development of AD pathology.

Results

To evaluate the relationship between perivascular astroglial gene expression and AD pathology in the aging and AD brain, we utilized publicly available data from the Allen Brain Institute Aging, Dementia and TBI study. Demographic data on study subjects is provided in Table 1. The study included RNA sequencing (RNAseq) and clinical data from 57 subjects that remained free from dementia through the course of the community-based Adult Changes in Thought (ACT) study and 50 subjects with a clinical diagnosis of dementia. Of these, 22 met NINDS-ARDA Alzheimer's criteria for 'Probable AD', 21 met criteria for 'Possible AD' and 7 were 'Unlikely AD' (including 3 cases with clinical diagnosis of vascular dementia). Ages were well matched between Non-Dementia and Dementia groups and expected differences in gender makeup (more women among Demented vs. Non-Demented subjects), APOε4 allele carrier status (more APOε4 allele carriers among Demented subjects) and educational attainment (lower levels of educational attainment among Demented subjects) were observed. As anticipated, Aβ plaque burden and NFT severity, measured by the Consortium to Establish a Registry for Alzheimer's disease (CERAD) score and Braak stage, respectively, were greater among Dementia versus Non-Dementia subjects.

AQP4 expression is associated with amyloid β burden in parietal cortex

RNAseq-based profiling of the transcriptome was performed in the tissue from temporal (TCX) and parietal cortex (PCX), hippocampus (HIP) and frontal white matter (FWM). Two techniques measured Aβ burden and tau pathology in each region:

immunohistochemistry (6E10 and AT8 antibodies, respectively) and quantitative $A\beta_{1-40}$, $A\beta_{1-42}$, pTau-181 (P-tau) and total tau Luminex assays.

Prior work from our group demonstrated that changes in AQP4 protein expression and localization are associated with Aβ and progression of tau pathology(Iliff et al., 2014; Zeppenfeld et al., 2017). Based on this, we evaluated the relationship between *AQP4* gene expression and dementia status. Controlling for age, gender, APOε4 and traumatic brain injury status, there was a trend towards greater *AQP4* expression in the HIP of individuals with dementia ($t=1.895$, $p_{adj}=0.087$), and no statistically significant differences in gene expression across any of the four brain regions (Figure 5.1a). We next assessed if transcript level expression of *AQP4* is associated with Aβ and tau pathology. Consistent with previous findings, a significant positive association between *AQP4* expression and $A\beta_{1-42}$ concentration ($t=2.238$, $p_{adj}=0.028$) was observed in the PCX (Figure 5.1b, Table 5.2). *AQP4* expression was not significantly associated with markers of tau pathology in any region (Figure 5.1c).

	n	Males (%)	APOε4 carriers (%)	Education	CERAD	Braak Stage
Non-Dementia	57	36 (63.2)	7 (12.3)	15 (12.5, 16)	1 (1, 2)	3 (2, 4)
77 – 89 yrs	31	24 (77.4)	4 (12.9)	16 (14, 17)	1 (1, 1)	3 (1, 3)
90+ yrs	26	12 (46.2)	3 (11.5)	14 (12, 16)	1 (1, 2)	3 (2, 4.25)
Dementia	50	27 (54.0)	13 (26.0)	13 (12, 16)	**2 (0.75, 3)***	**4 (3, 6)*****
77 – 89 yrs	26	13 (50.0)	8 (30.8)	**12.5 (12, 16)***	1.5 (0, 3)	**4 (2, 6)****
90+ yrs	24	14 (58.3)	5 (20.8)	13.5 (12, 15.75)	**2.5 (1.25, 3)***	**5 (3.25, 5.75)****

Table 5.1: Subject Demographic Data

*P<0.05, **P<0.01, ***P<0.001 vs. corresponding Non-Dementia group. Statistical associations determined by Mann-Whitney *U* test. Education, CERAD Score, Braak Stage include median (1st and 3rd quartile) values.

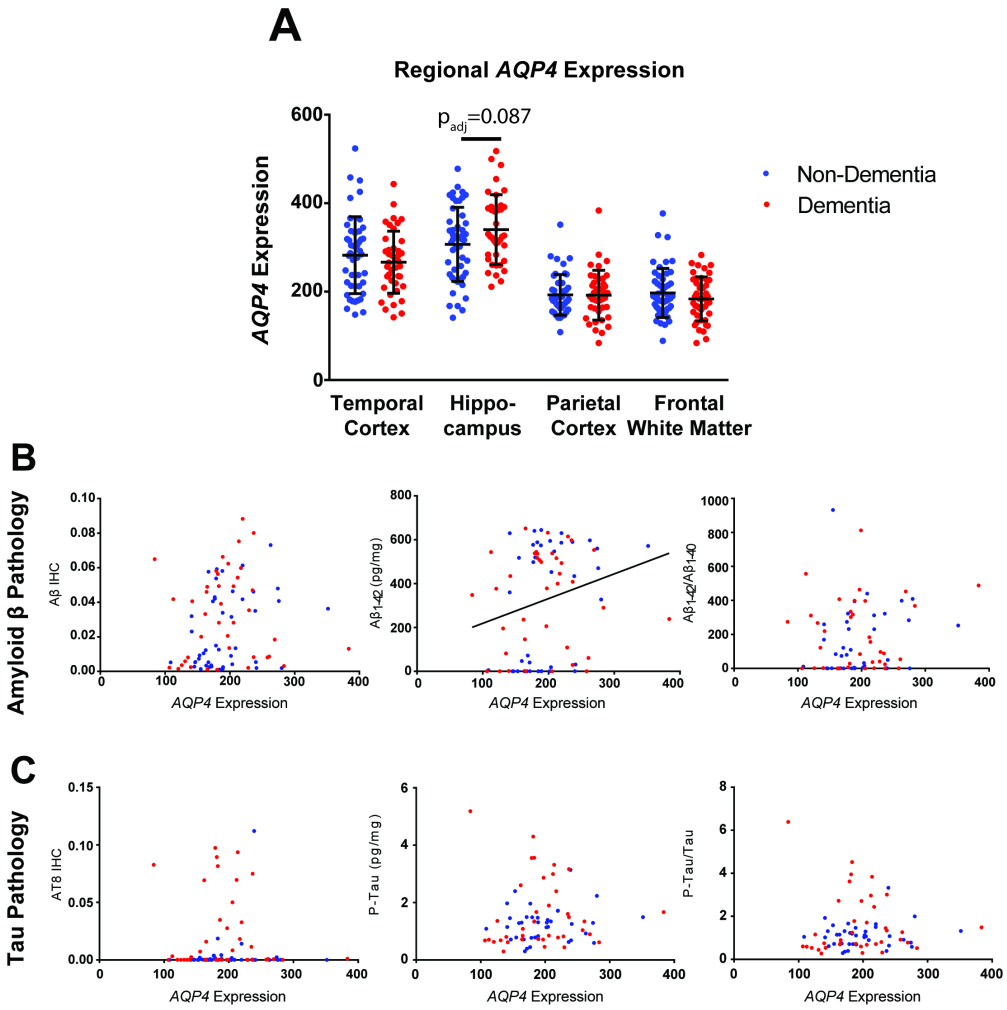

Figure 5.1: Elevated *AQP4* gene expression is associated with parietal cortical Aβ. (A) Expression levels of *AQP4* were quantified across 4 brain regions, TCX, HIP, PCX, and FWM, in subjects with (blue, n=57) and without (red, n=50) dementia. Hippocampus demonstrates a trend towards elevated AQP4 in demented subjects (logistic regression, t = -0.947, p_{adj}= 0.087). (B) Significant associations between *AQP4* expression with $A\beta_{1\text{-}42}$ levels (center, OLS regression, t=3.29, p_{adj}=0.028), were detected in PCX. (C) No significant association between *AQP4* expression and markers of tau pathology were detected in PCX. The bars in figures A represent the mean ± the standard deviation (S.D.). The line in figure B, center represents the least squares (ordinary) fit for all data points that show a significant statistical association.

		AQP4	*DAG1*	*DMD*	*DTNA*	*SNTA1*
TCX	**Aβ IHC**	0.525	-0.747	0.181	0.569	-0.150
	$A\beta_{1-40}$ (pg/mg)	1.598	0.515	-0.316	*2.277 (0.025, 0.051)*	**2.579 (0.011, 0.034)**
	$A\beta_{1-42}$ (pg/mg)	0.811	-0.125	-1.247	1.138	0.106
	$A\beta_{1-42}$ /$A\beta_{1-40}$	0.222	-0.727	-1.144	-0.002	-1.480
	AT8 IHC	0.527	-0.005	0.435	-0.109	-0.681
	P-Tau (ng/mg)	1.897	**3.290 (0.001, 0.010)**	-0.317	1.971	**2.380 (0.019, 0.038)**
	P-Tau/Tau_{total}	1.603	**2.953 (0.004, 0.023)**	-0.295	1.870	1.948
HIP	**Aβ IHC**	-0.090	1.182	-1.525	0.523	0.072
	$A\beta_{1-40}$ (pg/mg)	-0.287	0.062	1.273	-0.014	0.612
	$A\beta_{1-42}$ (pg/mg)	-0.013	0.373	-1.503	0.778	1.804
	$A\beta_{1-42}$ /$A\beta_{1-40}$	0.079	0.383	-2.067	0.847	1.746
	AT8 IHC	0.643	1.392	-1.198	0.665	-0.171
	P-Tau (ng/mg)	0.883	0.669	0.253	0.857	-0.753
	P-Tau/Tau_{total}	1.005	0.520	0.031	0.855	-0.753
PCX	**Aβ IHC**	1.742	0.113	0.606	-0.288	0.864
	$A\beta_{1-40}$ (pg/mg)	1.446	-1.028	1.579	0.534	-0.339
	$A\beta_{1-42}$ (pg/mg)	**2.238 (0.002, 0.028)**	-1.281	-0.314	2.021	-1.340
	$A\beta_{1-42}$ /$A\beta_{1-40}$	1.268	-0.597	-1.519	1.744	-1.177
	AT8 IHC	0.725	-0.005	-0.884	-0.209	-0.299
	P-Tau (ng/mg)	0.907	1.574	-0.121	-0.803	0.495
	P-Tau/Tau_{total}	0.683	1.498	-0.115	-0.729	0.477
FWM	**Aβ IHC**	0.553	0.033	0.149	1.169	0.695
	$A\beta_{1-40}$ (pg/mg)	-0.323	-0.516	-0.368	-0.373	0.434
	$A\beta_{1-42}$ (pg/mg)	-0.097	-1.175	-0.448	0.231	-0.561
	$A\beta_{1-42}$ /$A\beta_{1-40}$	0.061	-0.972	-0.251	0.406	-0.820
	AT8 IHC	-0.358	0.148	0.052	0.067	1.521
	P-Tau (ng/mg)	0.568	1.859	-0.127	*-2.194 (0.031, 0.061)*	0.545
	P-Tau/Tau_{total}	0.555	1.856	-0.110	-1.802	0.684

Table 5.2. Association of AQP4 and DAC gene expression with Alzheimer's pathology *t*-statistics for the association from Ordinary Least Squares (OLS) regression corrected for age, APOε4 status and TBI history. *P_{adj}<0.05 encoded in bold. Italics indicate outcomes that were statistically significant prior to, but not after false discovery rate and multiple comparison correction. Values in parenthesis represent the unadjusted (left) and adjusted (right) P-values. Positive t statistics represent a positive association between gene expression and pathology outcomes, while negative statistics represent an inverse association between gene expression and pathology.

Astrocytic dystrophin-associated complex components are associated with temporal tau pathology

AQP4 is anchored at the perivascular astrocytic endfoot by the DAC, comprised of dystrophin (*DMD*), dystroglycan (*DAG1*), dystrobrevin (*DTNA*) and α-syntrophin (*SNTA1*) (Figure 5.2a). We evaluated whether hippocampal expression of the four DAC

genes share a similar relationship with dementia status and AD pathology as *AQP4*. While *SNTA1* expression did not differ between dementia statuses (Figure 5.2b, t=1.437, p_{adj}=0.226), both *DTNA* and *DAG1* expression in the HIP were significantly increased among subjects with dementia (Figure 5.2c-d, t=2.731, 2.632; p_{adj} =0.009, 0.013; respectively). In contrast, *DMD* expression was significantly reduced in the HIP of demented subjects (Figure 5.2e, t=2.632, p_{adj}=0.013). No changes in the expression of *AQP4* (Figure 5.1a) nor any of the 4 DAC genes (Figure 5.2b-e) in the TCX, PCX or FWM significantly predicted dementia status.

Assessment of the relationship between different DAC gene expression and AD pathology revealed no significant associations with markers of Aβ or phosphorylated tau within the PCX, HIP or FWM (Table 5.2)**.** However, within the TCX, increased *SNTA1* expression was associated with increased levels of $A\beta_{1\text{-}40}$ (t=2.579, p_{adj} =0.034). Strikingly, higher expression of *SNTA1* and *DAG1* were both significantly associated with elevated P-tau levels (Figure 5.2 f & h, t=3.290, 2.380; p_{adj}=0.010, 0.039; respectively). *DNTA* and *DMD* did not demonstrate these associations (Figure 5.2 g & i). While these results support the role of AQP4 as a regulator of Aβ dynamics, they further suggest that other elements of the astroglial perivascular endfoot processes may contribute to the development of tau pathology within the TCX.

Unbiased identification of candidate genes that may encode elements of the astrocytic endfoot

We next sought to identify candidate genes that may encode proteins involved in perivascular astrocytic endfoot function. To achieve this, we identified genes with similar expression profiles to the ‘established endfoot genes’ including *AQP4* and the DAC component genes. We first confirmed the astrocyte specificity of *AQP4* and DAC gene expression within the brain using two independent single-cell RNAseq datasets: the Allen Brain Institute Cell Types dataset and the Brain RNAseq database (Science, 2015; Zhang et al., 2016). Except for *DMD*, greater than 50% of total gene expression was derived from astrocytes for the established DAC genes (*SNTA1, DAG1, DTNA*) and *AQP4*.

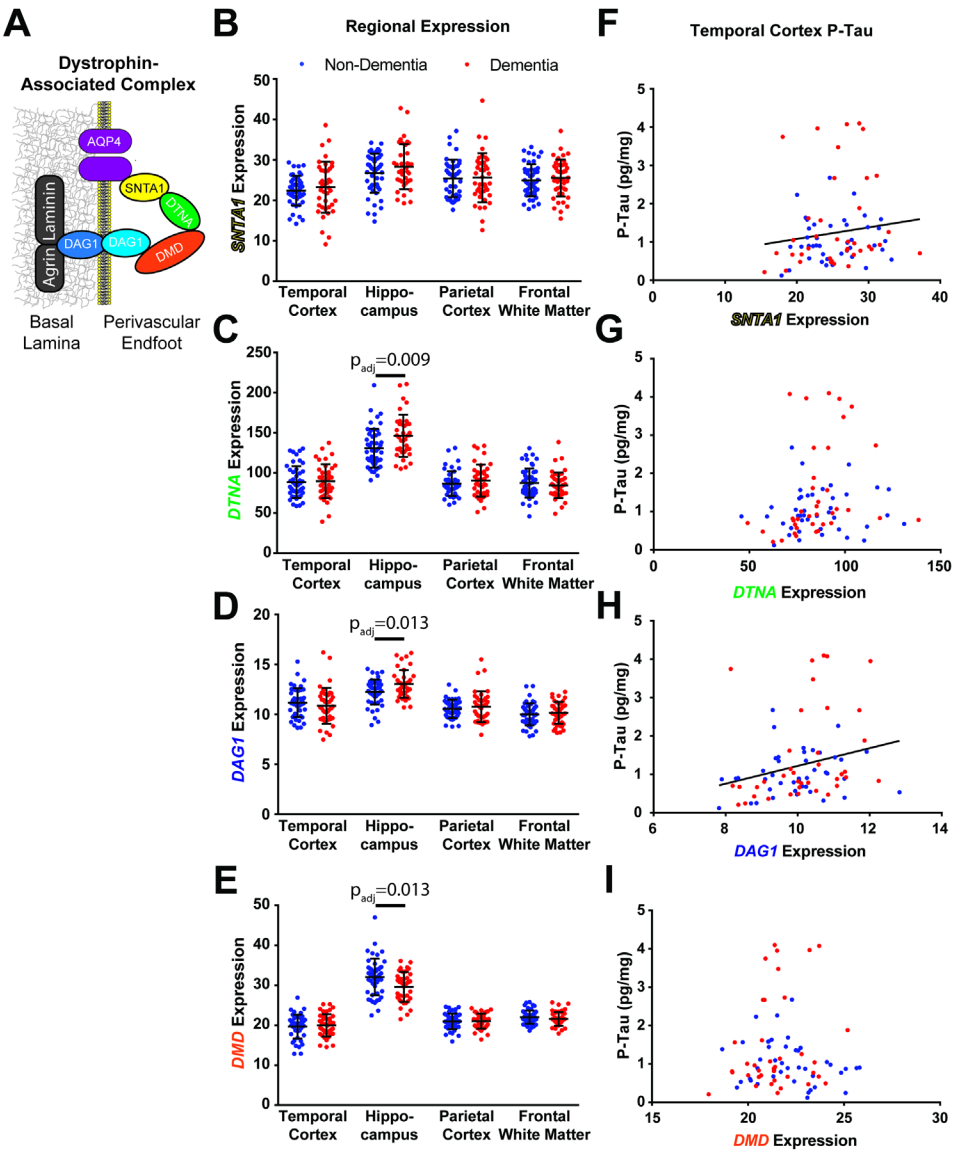

Figure 5.2: DAC gene expression associations with dementia and temporal cortical P-tau. (A) Schematic of the DAC at the astrocytic endfoot. Known components include aquaporin-4 (AQP4), α-syntrophin (SNTA1), dystrobrevin (DTNA), dystrophin (DMD) and dystroglycan (DAG1). (B-E) Expression of the 4 DAC components across the 4 brain regions. *DTNA* and *DAG1* are elevated in the HIP of demented subjects (t=2.731, 2.632; p_{adj}=0.009, 0.013), while *DMD* expression is reduced (t=-2.615, p_{adj}=0.013). (F-I) Association of DAC gene expression with TCX P-tau. *SNTA* and *DAG1* are associated with tau pathology regardless of dementia status (t=2.380, 3.29; p_{adj}=0.038, 0.010; respectively). The bars in B-E represent the mean ± standard deviation. Lines in F, H represent the least squares (ordinary) fit for all data. Statistical associations between gene expression and dementia status assessed using logistic regression. Statistical associations between gene expression and pathology were evaluated using OLS regression.

To identify novel endfoot candidate genes, we utilized the unbiased, biologically motivated hierarchical clustering method of WGCNA to identify similar human RNAseq expression profiles to the established endfoot genes. WGCNA was performed for each of the 4 brain regions: PCX, TCX, HIP and FWM. All regions except FWM demonstrated co-clustering of the established endfoot genes, and the cluster(s) that contained the greatest number of the endfoot established genes were defined as the "endfoot enriched cluster(s)" (Figure 5.3a).

Upon generation of a single WGCNA network for all subjects, 340 genes sorted in the endfoot-enriched cluster in at least one of the 3 gray matter regions (Figure 5.3b). 143 of these genes appeared in the endfoot-enriched cluster in more than one region. After applying a stringent gene expression correlation-based thresholding process and filtering out genes that are not predominantly expressed in astrocytes, 11 genes were identified within these clusters that had highly robust correlations with established endfoot genes, and demonstrate enriched expression in astrocytes across multiple brain regions (Figure 5.3c). To determine the most connected genes within modules, intramodular connectivity was assessed for all genes within the end foot enriched clusters. In all three regions the novel genes were hub genes within the endfoot-enriched clusters (Figure 5.3a). Generation of a consensus network across dementia status resulted in less robust clustering of novel genes into the endfoot-enriched module when comparing across brain regions. In HIP, all candidate genes again clustered in the endfoot-enriched module, while in TCX 8 of the 11 genes co-clustered with *SNTA1* and in PCX, there were no consistent clustering patterns among novel genes.

Literature review revealed that three of these 11 candidate genes (*MLC1*, *NDRG2* and *SLC1A*) are previously reported components of the perivascular astrocytic end foot . Though the present WGNCA was carried out based on 3 brain regions from aged subjects (minimum 77 years), we previously identified 9 of these 11 genes as possible endfoot genes based upon a similar WGCNA analysis of RNAseq data from human brain samples at various developmental time points (Simon et al., 2017). These 11 gene endfoot candidates thus represent a novel pool of potential regulators of perivascular astrocytic function across aging and disease states.

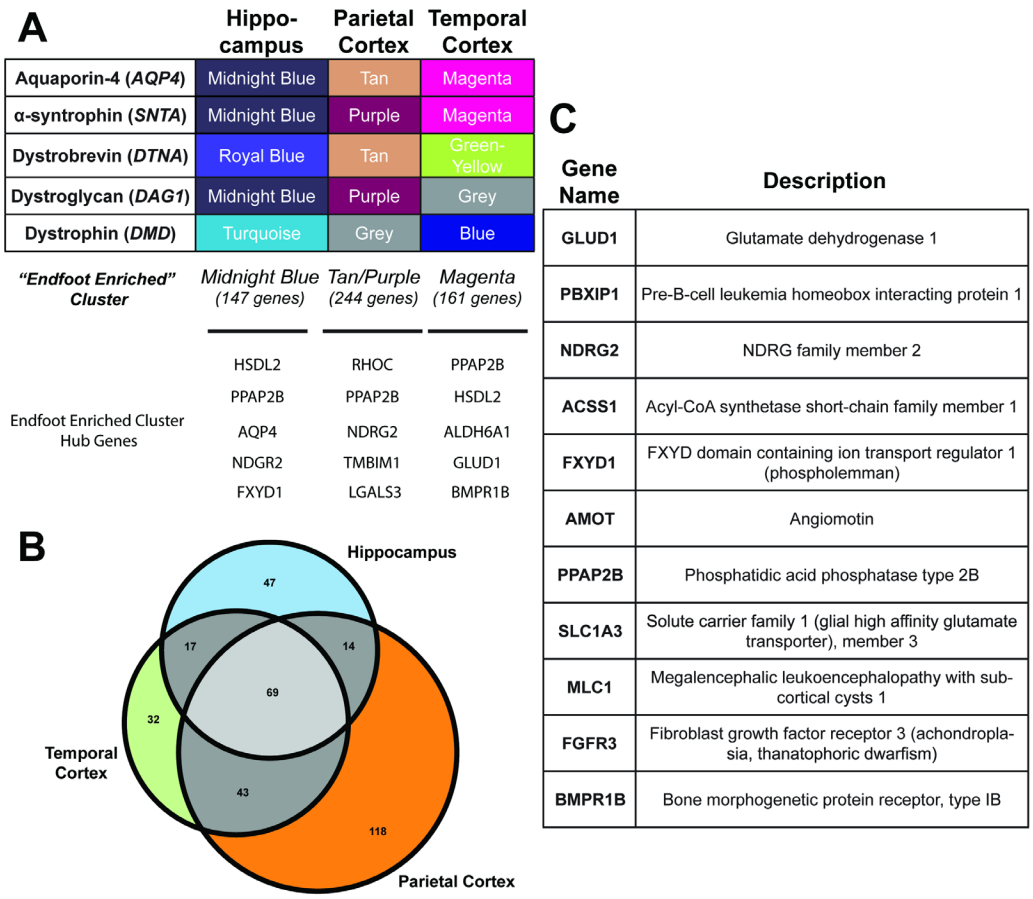

Figure 5.3: Identification of novel endfoot gene candidates by Weighted Correlation Network Analysis (WGCNA).
(A) Cluster in which each of the five established endfoot genes assembled for each region. The cluster containing the greatest number of established endfoot genes was defined as the "endfoot enriched" cluster (bottom). Hub genes for each cluster are also identified. (B) Gene expression overlap for the "endfoot enriched" cluster across gray matter regions. (C) Consensus endfoot candidate genes identified by thresholding for astrocyte specificity (≥50% total expression), co-clustering with DAC genes across multiple brain regions, and high Pearson's correlation with DAC genes.

Expression of novel endfoot candidate genes is significantly associated with dementia status and tau pathology

Like the established DAC genes *AQP4, DTNA, DAG1* and *DMD,* expression of several endfoot candidate genes differed between non-demented and demented subjects (Figure 5.4a-k). *AMOT* (Figure 5.4a, t=2.606, p_{adj}=0.014) and *MLC1* (Figure 5.4g,

t=2.512, p_{adj}=0.018) expression in HIP was significantly greater in demented than non-demented subjects, while *BMPR1B* (Figure 5.4c, t=2.073, p_{adj}=0.057) exhibited a similar trend that did not remain significant after correction for multiple comparisons. Within TCX, expression of *GLUD1* (Figure 5.4f, t=-2.255, p_{adj}=0.036) and *NDRG2* (Figure 5.4h, t=-2.120, p_{adj}=0.048) were significantly lower in demented versus non-demented subjects. A similar trend was observed for both *PPAP2B* (Figure 5.4j, t=-1.986, p_{adj}=0.070) and *SLC1A3* (Figure 5.4k, t=-2.048, p_{adj}=0.061) in the TCX, although these effects did not survive correction for multiple comparisons.

Pathological analysis revealed a striking association between these endfoot candidate genes and temporal tau pathology. 8 out of 11 genes (*ACSS1, AMOT, BMPR1B, FGFR3, FXYD1, GLUD1, MLC1,* and *PPAP2B)* were associated with increasing P-Tau levels within the TCX (Table 5.3). These associations were unique to the genes identified and not seen between P-tau and the endfoot enriched module eigengene. Only *NDGR2* and *SLC1A3* did not demonstrate any association with tau pathology. As seen in Table 5.3, significant associations between increasing gene expression and increasing P-Tau were observed in PCX (*FGFR3*) and FWM (*AMOT, FGFR3*). Interestingly, in PCX, associations between tau pathology and the endfoot enriched cluster eigengene were observed, suggesting other genes may also be of interest that were eliminated based on thresholding criteria. There were also significant positive associations between increasing TCX expression of *FXYD1, MLC1* and *PBXIP1*, and $A\beta_{1\text{-}40}$ levels. These findings suggest that these endfoot candidate genes, like the DAC elements, may play an important role in the development of P-tau aggregation.

Validation of protein level expression changes for a subset of novel gene candidates

The Allen Aging, Dementia and TBI cohort was generated to assess age-related changes in brain gene expression and neuropathology while directly controlling for the effects of TBI, but not AD. Additionally, this dataset does not include protein expression data for AQP4, DAC gene products or the candidate endfoot proteins. To address these issues, we sought to validate the identified associations in two independent AD cohorts, both at the gene and protein expression levels. We selected four genes from the pool of

known and novel candidate endfoot genes: *AQP4*, *DTNA*, *MLC1* and *FXYD1*. *AQP4* was selected due to its established role in Aβ dynamics(Iliff et al., 2012; Xu et al., 2015) and associations with AD status and pathology (Zeppenfeld et al., 2017). From the DAC complex, we selected *DTNA* based on the robust associations with dementia status and P-tau pathology. *MLC1* and *FXYD1* were chosen from the larger pool of novel gene candidates based on the associations identified with dementia status and tau pathology. Like *DTNA,* hippocampal *MLC1* expression robustly predicts dementia status while TCX expression is strongly associated with P-tau levels. In contrast, *FXYD1* expression does not predict dementia status, but is strongly associated with temporal cortical P-tau levels.

We first validated the observed gene expression changes in the Hisayama Study Microarray Dataset, an independently generated AD gene expression cohort. This dataset contains microarray data from 47 non-AD and 32 AD subjects ranging in age from 54 to 105 years of age. Samples were collected from three different grey matter regions including HIP, frontal cortex (FCX) and TCX. Gender distributions within each group were approximately even, however there is a significant difference in median age between AD (median=91 years, Interquartile range (IQR)=7 years) and non-AD subjects (median=80 years, IQR=9 years). This dataset did not distinguish between healthy controls and controls with non-AD forms of dementia.

Evaluation of this microarray data revealed strikingly consistent associations with the Allen Aging, Dementia, and TBI dataset for each of the four genes (*AQP4, DTNA, MLC1, FXYD1*; Figure 5.4, Table 5.4). In FCX, no significant associations are observed for any of the four genes. In HIP, both *AQP4* (Figure 5.5a; z=2.85, p=0.012) and *DTNA* (Figure 5.5b; z=2.35, p=0.033) show significantly elevated expression among AD subjects. Although *MLC1* expression was generally higher in AD compared to non-AD HIP, this effect was not significant (Figure 5.5c; z=1.78, p=0.075). Hippocampal *FXYD1* expression was not significantly different between AD and non-AD subjects. In TCX *AQP4* (Figure 5.5a; z=2.32, p=0.02)*, DTNA* (Figure 5.5b; z=2.16, p=0.031), and *FXYD1* (Figure 5.5d; z=2.39, p=0.017) all show significant increases in expression in AD subjects, while *MLC1* demonstrates only a trend towards increased expression among AD subjects (Figure 5.5c, z=1.82, p=0.069).

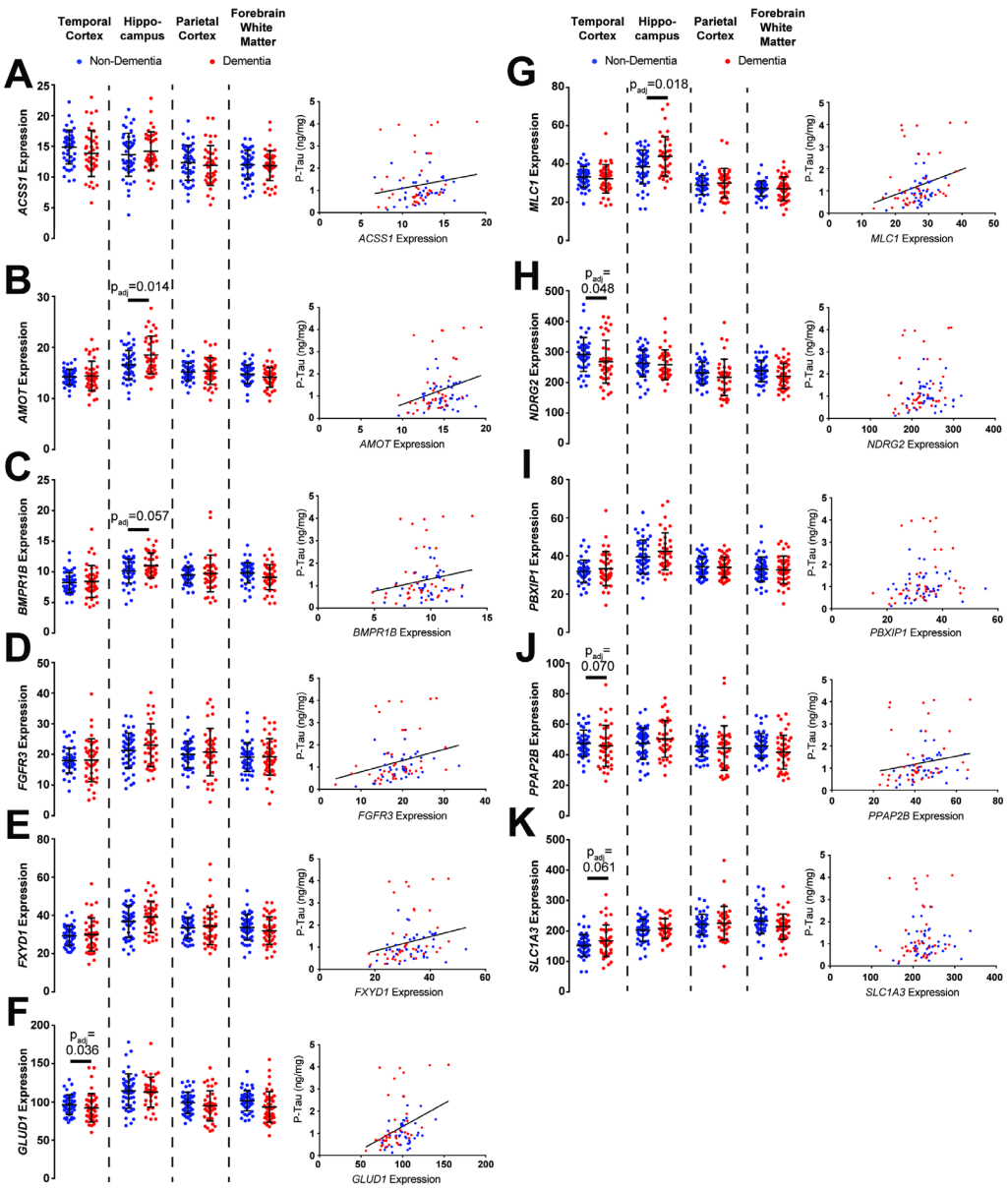

Figure 5.4: Candidate gene expression associations with TCX tau and dementia.
For each gene (A-K, left), expression is quantified in cognitively intact subjects (blue, n= 57) and subjects with dementia (red, n=50). HIP gene expression was increased in demented subjects for *AMOT* (B, t= 2.606, p= 0.014), and *MLC1* (G, t= 2.512, p=0.018), while reduced expression of *GLUD1* (F, t= -2.255, p= 0.036) and *NDRG2* (H, t= -2.120, p=0.048) was observed in TCX. All candidate genes except *NDRG2*, *PBXIP1* and *SLCA1A3* exhibited associations with P-tau levels (right). Bars in A-K, left represent the mean ± the standard deviation. Lines in A-K, right represent the least squares fit for plots that show significant statistical associations. Associations between gene expression and dementia status assessed using logistic regression. Associations between gene expression and pathology evaluated using OLS regression.

		ACSS1	*AMOT*	*BMPR1B*	*FGFR3*	*FXYD1*	*GLUD1*	*MLC1*	*NDRG2*	*PBXIP1*	*PPAP2B*	*SLC1A3*
TCX	**Aβ IHC**	0.301	0.810	-0.727	0.158	-0.217	1.234	0.069	-1.037	0.032	-0.593	-0.965
	$A\beta_{1-40}$ (pg/mg)	0.902	*2.260 (0.026, 0.051)*	*2.187 (0.031, 0.061)*	1.312	**2.719 (0.008, 0.015)**	2.118	**2.719 (0.008, 0.015)**	0.760	**3.493 (0.001, 0.001)**	1.656	1.338
	$A\beta_{1-42}$ (pg/mg)	-0.599	0.615	0.039	-1.409	-0.224	-0.351	-1.384	-1.121	0.685	-0.112	-0.423
	$A\beta_{1-42}$ /$A\beta_{1-40}$	-1.310	-0.816	-1.199	**-2.471 (0.015, 0.030)**	-1.873	-1.534	**-3.031 (0.003, 0.006)**	-1.718	-1.441	-1.190	-0.890
	AT8 IHC	0.364	1.078	-0.081	0.199	1.141	0.597	0.931	-1.285	1.843	-0.229	-0.464
	P-Tau (ng/mg)	**2.573 (0.012, 0.023)**	**3.549 (0.001, 0.001)**	**2.498 (0.014, 0.027)**	**4.196 (<0.001, <0.001)**	**3.383 (0.001, 0.002)**	**3.986 (<0.001, <0.001)**	**4.115 (<0.001, <0.001)**	1.990	**2.463 (0.016, 0.031)**	**2.856 (0.005, 0.010)**	1.217
	P-Tau /Tau_{tot}	*2.462 (0.016, 0.031)*	**3.397 (0.001, 0.002)**	2.080	**3.868 (<0.001, <0.001)**	**3.154 (0.002, 0.004)**	**3.467 (0.001, 0.001)**	**4.020 (<0.001, <0.001)**	1.637	*2.159 (0.033, 0.065)*	**2.390 (0.019, 0.037)**	0.953
HIP	**Aβ IHC**	0.300	1.314	0.892	1.052	-0.818	-0.588	0.492	-0.284	-0.312	-0.188	-0.522
	$A\beta_{1-40}$ (pg/mg)	0.401	0.438	-0.370	-0.103	-0.149	-0.593	-0.202	-0.400	-0.076	0.171	-1.559
	$A\beta_{1-42}$ (pg/mg)	0.381	0.463	0.067	-0.206	-0.319	-1.256	0.035	0.043	1.522	0.705	0.097
	$A\beta_{1-42}$ /$A\beta_{1-40}$	0.282	0.358	0.192	-0.189	-0.296	-1.163	0.103	0.176	1.676	0.706	0.603
	AT8 IHC	-0.717	0.306	0.115	-0.592	-1.820	-1.838	-1.218	-2.600	0.238	-1.258	0.069
	P-Tau (ng/mg)	-0.301	0.726	1.999	-0.387	-0.098	0.380	-0.814	-0.692	0.512	1.046	0.263
	P-Tau /Tau_{tot}	-0.229	0.693	*2.157 (0.034, 0.066)*	-0.527	-0.077	0.423	-0.902	-0.714	0.576	1.250	0.322
PCX	**Aβ IHC**	1.302	0.706	0.454	1.121	0.537	1.056	0.919	0.413	0.651	0.906	-1.086
	$A\beta_{1-40}$ (pg/mg)	0.009	0.317	-0.075	-0.171	-0.349	1.038	-0.033	-0.568	-0.316	-0.043	-1.340
	$A\beta_{1-42}$ (pg/mg)	-1.709	0.076	0.386	-1.229	-0.046	0.100	-1.050	-1.117	-0.099	0.055	0.358
	$A\beta_{1-42}$ /$A\beta_{1-40}$	-1.843	-0.155	0.470	-1.186	0.211	-0.664	-1.101	-0.766	0.130	0.091	1.390
	AT8 IHC	-0.987	0.393	-0.550	-0.352	-0.250	-0.766	-0.201	**-2.671 (0.021, 0.041)**	-0.092	-1.107	-1.079
	P-Tau (ng/mg)	0.749	2.113	0.916	**2.735 (0.020, 0.015)**	2.033	2.069	**2.376 (0.001, 0.038)**	-0.429	0.075	1.049	-1.249
	P-Tau /Tau_{tot}	0.612	*2.128 (0.036, 0.071)*	0.738	**2.641 (0.028, 0.019)**	1.836	1.788	*2.233 (0.001, 0.054)*	-0.583	0.043	0.866	-1.318
FWM	**Aβ IHC**	-0.037	0.279	1.153	0.613	1.267	0.488	0.431	0.256	1.637	1.226	**3.086 (0.003, 0.005)**
	$A\beta_{1-40}$ (pg/mg)	0.889	1.656	0.314	1.597	1.230	1.013	0.793	0.047	0.245	0.525	0.274
	$A\beta_{1-42}$ (pg/mg)	-0.360	0.211	-0.931	-1.093	-0.643	-0.458	-1.565	-1.122	-0.286	-0.560	-0.079
	$A\beta_{1-42}$ /$A\beta_{1-40}$	-0.898	-0.684	-1.156	*-2.040 (0.044, 0.087)*	-1.330	-1.088	-2.125	-1.263	-0.422	-0.885	-0.213
	AT8 IHC	-1.281	-0.155	-1.210	-0.168	-0.162	-1.279	-0.127	-1.910	0.008	-1.362	-0.432
	P-Tau (ng/mg)	0.440	*2.291 (0.024, 0.047)*	0.292	**4.015 (<0.001, <0.001)**	1.045	1.937	0.803	-0.812	0.307	1.765	-0.726
	P-Tau /Tau_{tot}	0.290	**2.566 (0.012, 0.023)**	0.399	**4.239 (<0.001, <0.001)**	1.202	1.947	1.050	-0.968	0.420	1.666	-0.628

Table 5.3: Association of novel gene products with Alzheimer's pathology

t-statistics for the association from Ordinary Least Squares (OLS) regression corrected for age, APOε4 status and TBI history. *P_{adj}<0.05 encoded in bold. Italics indicate outcomes that were statistically significant prior to, but not after false discovery rate and multiple comparison correction. Values in parenthesis represent the unadjusted (left) and adjusted (right) P-values. Positive t statistics represent a positive association between gene expression and pathology outcomes, while negative statistics represent an inverse association between gene expression and pathology.

Study	Region	Gene/Protein	Coefficient	z-stat	p-value
Gene Expression (Hisayama Study)	Frontal Cortex	***AQP4***	1.092	1.08	0.28
		DTNA	1.633	1.13	0.26
		MLC1	0.777	0.53	0.59
		FXYD1	1.905	1.23	0.22
	Temporal Cortex	***AQP4***	6.34	2.32	**0.02**
		DTNA	5.014	2.16	**0.031**
		MLC1	5.298	1.82	*0.069*
		FXYD1	6.058	2.39	**0.017**
	Hippocampus	***AQP4***	5.472	2.85	**0.012**
		DTNA	4.312	2.35	**0.033**
		MLC1	15.68	1.78	*0.075*
		FXYD1	1.249	0.88	0.377
Protein Expression (Oregon Brain Bank)	Frontal Cortex	**AQP4**	-1.535	-0.94	0.35
		DTNA	0.064	0.33	0.74
		MLC1	0.406	0.22	0.83
		FXYD1	0.981	0.87	0.38
	Hippocampus	**AQP4**	0.281	0.17	0.864
		DTNA	2.932	2.16	**0.031**
		MLC1	9.25	2.25	**0.025**
		FXYD1	1.961	1.66	*0.096*
Hippocampal Protein Expression vs. Pathology (Oregon Brain Bank)	Neuritic Plaques	**AQP4**	0.684	0.38	0.705
		DTNA	2.708	2.04	**0.042**
		MLC1	0.253	0.15	0.88
		FXYD1	1.815	1.8	*0.073*
	Braak Staging	**AQP4**	0.544	0.51	0.612
		DTNA	2.732	2.01	**0.048**
		MLC1	9.688	2.21	**0.027**
		FXYD1	1.143	1.54	0.12
	Cerebral Amyloid Angiopathy	**AQP4**	-1.939	-0.56	0.575
		DTNA	2.591	1.86	*0.063*
		MLC1	-1.478	-0.51	0.61
		FXYD1	0.885	0.81	0.42

Table 5.4: Associations of gene expression and protein expression with Alzheimer's diagnosis and pathology in independently generated AD cohorts.
Correlation coefficients, z-statistics and p-values for the uncorrected logistic regression between gene/protein expression and AD diagnosis (top two groups) or AD pathologies (bottom group). P<0.05 labeled in bold. italics indicates statistical trends (P<.1). Positive z statistics represent a positive association between gene expression and pathology or diagnosis, while negative statistics represent an inverse association.

To determine if gene expression changes are indicative of protein expression levels, we evaluated AQP4, DTNA, MLC1 and FXYD1 expression by Western blot in fresh-frozen grey matter tissue. Samples were obtained from two brain regions: HIP and FCX. Subjects were selected based on the absence of clino-pathological diagnosis of vascular or mixed dementia, hippocampal sclerosis, Lewy body dementia, Parkinson's disease, tumor, or other non-AD pathologies, to best define the relationship with AD specifically. The resulting case series consisted of 35 FCX samples: 15 non-AD subjects and 20 AD subjects; and 27 HIP samples: 12 non-AD subjects and 15 AD subjects. Subject gender was roughly even (43% male among non-AD; 46% male among AD subjects). There were significant differences in the age distribution between AD subjects (median-=84.9 years, IQR=10.0 years) and Non-AD subjects (median= 96 years, IQR =

5.6 years), which is likely attributable to the exclusion of subjects with vascular or mixed dementia. No associations between protein expression and dementia status were observed in FCX (Figure 5.6, Table 4). Within HIP, significantly increased expression levels were observed in AD subjects for both DTNA (Figure 5.6b, z=2.16, p=0.031) and MLC1 (Figure 5.6c, z=2.25, p=0.025), while only a trend was observed towards increased FXYD1 expression subjects with AD diagnosis (Figure 5.6d, z=1.66, p=0.096). AQP4 did not demonstrate any significant association with AD diagnosis (Figure 5.6a).

Next, we assessed associations between protein expression changes, in HIP, and pathological indicators of protein aggregation: Braak stage, neuritic plaque burden, and cerebral amyloid angiopathy. Neuritic plaque burden was associated with elevated HIP DTNA expression (Table 5.4, z=2.04, p=0.042). HIP DTNA and MLC1 expression were associated with Braak stage (Table 5.4; z=2.01, p=0.048; z=2.21, p=0.027; respectively).

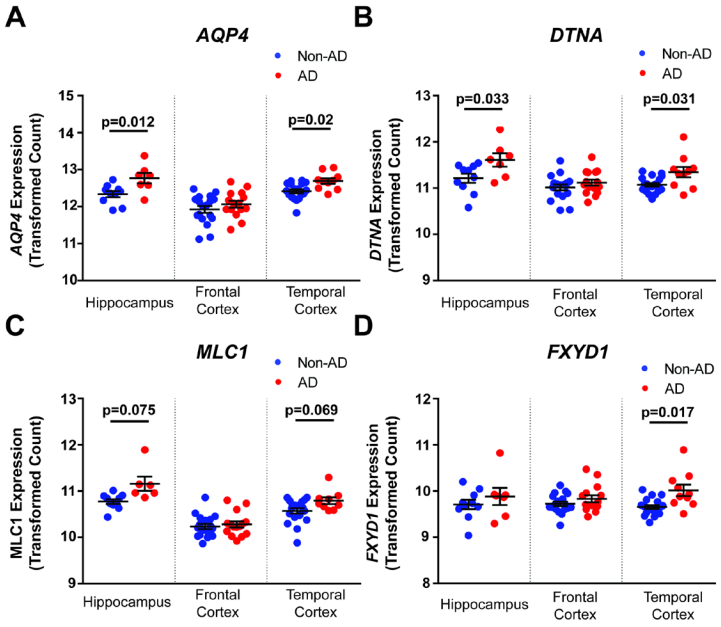

Figure 5.5: Validation of gene expression changes in the Hisayama microarray dataset. Association between gene expression and dementia evaluated in an independently generated AD cohort for *AQP4*, *DTNA*, *MLC1*, and *FXYD1*. (A-D). In HIP, elevated expression of *AQP4* (p= 0.012) and *DTNA* (p= 0.033) predict dementia status (red, n=7) compared to healthy individuals (blue, n=10). In TCX, *AQP4* (p= 0.02), *DTNA* (p= 0.031) and *FXYD1* (p= 0.017) significantly predict dementia status (red, n=10) compared to healthy subjects (blue, n=19). Associations calculated with logistic regression. Bars in A-D represent the mean ± S.E.M. Statistical information found in Table 4.

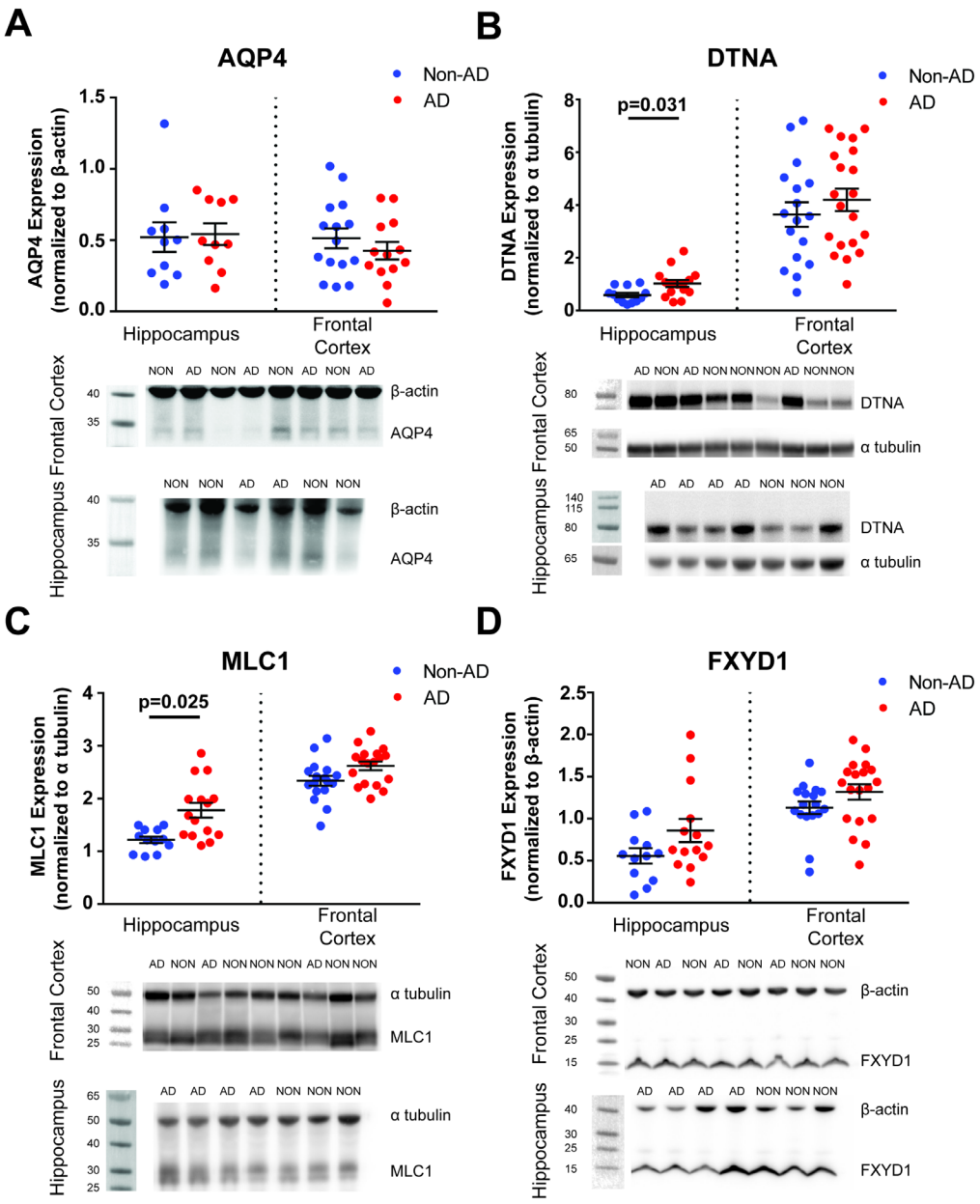

Figure 5.6: Assessment of the association between protein expression and AD status. Protein expression and associations with AD status for AQP4, DTNA, MLC1, and FXYD1. Expression changes measured in HIP ($n_{dementia}$= 10-15, $n_{non\text{-}dementia}$=10-12) and FCX ($n_{dementia}$= 13-20, $n_{non\text{-}dementia}$=15-17). For each gene, plots describe associations with AD status in each brain region (A-D). In HIP, elevated expression of DTNA (p= 0.031) and MLC1 (p= 0.025) significantly predict dementia status Statistical associations calculated with logistic regression. The bars in A-D represent the mean ± the S.E.M. Complete statistical information found in Table 4. Representative blots have been cropped for clarity. Dotted lines represent the boundary between cropped images. All blots were processed in parallel across subjects.

Discussion

In the present study, we utilized publicly available transcriptomic datasets to generate an unbiased, large-scale assessment of gene expression to evaluate potential associations between expression of perivascular astroglial endfoot components, dementia status and AD pathology in human brain tissue. This approach revealed that variation in several known genes encoding structural elements of the astroglial endfoot domain are associated with dementia status. Unexpectedly, differences in expression of these genes was also associated with P-tau pathology in TCX. WGCNA-based clustering approaches revealed several genes that may represent novel elements of the astrocytic endfoot domain. These candidate genes also exhibit associations with TCX P-tau pathology, and in many cases, hippocampal expression of these genes predicted dementia status. Finally, we validated these findings at the transcript and protein level in two independent AD cohorts, demonstrating that expression of the DAC protein DTNA (dystrobrevin) and the candidate endfoot protein MLC1 (megalencepalic leukoencephalopathy with subcortical cysts 1) predicts AD status and are associated with cortical tau pathology.

The perivascular astroglial water channel AQP4 supports perivascular CSF-interstitial fluid exchange, as deletion of the *Aqp4* gene in mice slows CSF influx into the brain parenchyma and the clearance of solutes, including Aβ, from the brain parenchyma(Iliff et al., 2012). Impairment of glymphatic function in the aging and post-traumatic rodent brain is associated with increased AQP4 expression and loss of perivascular AQP4 localization (Iliff et al., 2014; Kress et al., 2014; Zhao et al., 2017). In human post-mortem tissue, increasing AQP4 expression and loss of perivascular localization is associated with AD status, Aβ plaque burden and NFT pathology (Zeppenfeld et al., 2017). Yet the cellular and molecular underpinnings of glymphatic pathway function beyond AQP4 have not yet been defined. Beyond the glymphatic system, the astrocytic endfoot contributes to physiological processes such as fluid homeostasis, neurovascular coupling and brain metabolism. Under pathological conditions it also plays a critical role the formation and resolution to cerebral edema in response to brain injury (Nagelhus and Ottersen, 2013). Identification of novel elements

of the perivascular endfoot domain that contribute to these processes may provide new insight into the pathogenesis and potential treatment of neurodegenerative or neurovascular disorders. The present observation that increased *AQP4* expression was associated with increased Aβ levels in the parietal cortex is consistent with prior studies of glymphatic function demonstrating a role of AQP4 in Aβ clearance and deposition (Iliff et al., 2012; Kress et al., 2014; Xu et al., 2015). Similarly, the observed association between increasing *AQP4* expression in the HIP and dementia status is consistent with our prior finding that increased AQP4 expression and loss of perivascular localization predicted AD status, and that naturally occurring single-nucleotide polymorphisms in the human *AQP4* gene are associated with altered rates of neurocognitive decline among subjects with AD (Burfeind et al., 2017; Zeppenfeld et al., 2017).

Transcriptomic analysis of *AQP4* and the perivascular astroglial DAC genes *SNTA1* (α-syntrophin)*, DTNA* (dystrobrevin)*, DAG1* (dystroglycan) and *DMD* (dystrophin) across both the human developing brain(Simon et al., 2017) and in the aging brain (present study) showed that *AQP4, DTNA* and *SNTA1* exhibit a common expression profile that is shared by a group of astroglial genes. These datasets showed striking overlap in expression profiles with nine novel candidates identified in the endfoot-enriched cluster in both datasets. Furthermore, about one third (13 of 41 in the developmental dataset, 3 of 11 in the present dataset) of these endfoot candidate gene products have previously been localized to the perivascular endfoot domain, For example, *MLC1* encodes a putative astroglial membrane transporter of unknown function that associates with AQP4 and other DAC proteins in the perivascular astrocytic end foot (Boor et al., 2007). In contrast, the distribution and function of many of the remaining gene products remains unknown. The clustering profile of *AQP4*, the DAC genes (excluding *DMD*), and these endfoot candidates is largely distinct from that of other common astrocytic genes such as *GFAP*, *S100β* and *ALDH1L1*, suggesting that these may represent a cluster of genes that contribute to perivascular astroglial function. Initial assessment of functions within this group by gene ontology analysis reveals enrichment for molecular functions including amino acid binding and transmembrane receptor protein kinase activity (data not shown).

Taking advantage of RNAseq datasets allowed for an unbiased screen for novel gene candidates, but importantly does not provide information on protein-level expression. Western blot data from an independent AD cohort suggests that at least for the subset of the gene products evaluated, the associations between gene expression, AD status and neurofibrillary pathology were faithfully recapitulated at the protein expression level. Furthermore, these results exhibit the same regional specificity, as expression of DTNA and MLC1 within HIP, but not the FCX, predicted AD status. It is important to note that this validation cohort was relatively small and did not include TCX tissue, the region exhibiting the most robust associations between P-tau pathology and gene expression data in the Allen Aging, Dementia and TBI study. Thus, a more complete assessment of protein level expression as well as histological evaluation of localization patterns for the identified genes is warranted. Localization data obtained for novel candidates will be of particular interest due to the established loss of AQP4 localization in pathological states without robust changes in overall expression.

The surprisingly strong associations between TCX DAC gene expression and local P-tau levels observed in all three datasets suggests that astroglial endfoot function may play a previously unrecognized role in the dynamics of NFT formation. This notion is supported by the observed association between changes in AQP4 expression and localization and Braak stage in human post-mortem tissue (Zeppenfeld et al., 2017)and by the increased P-tau levels observed in *Aqp4*$^{-/-}$ mice after experimental TBI (Iliff et al., 2014). The functional link between the astroglial endfoot, which has been associated with extracellular solute homeostasis, and the development of intracellular aggregates of tau, remains speculative. One possibility is that perivascular endfoot function may influence the inter-cellular spread of tau aggregates. The neuroanatomical progression of tau pathology through the course of AD reflected in the Braak staging system is now widely believed to result from the prion-like spread of misfolded tau between neighboring cells within neural networks (Liu et al., 2012). Such prion-like spread has been observed for several protein aggregates related to neurodegenerative disease, including tau and α–synuclein (Guo and Lee, 2014). In an experimental setting, tau aggregates isolated from human brains can seed NFT formation in the wild type mouse brain, which does not form native NFTs, leading to the propagation of NFTs

through neuroanatomically connected brain regions (Recasens et al., 2014). Implicit within this model, is that intracellular tau aggregates must be released into and taken up out of the extracellular compartment. Cellular release and uptake of tau aggregates has been observed both *in vitro* and *in vivo*, where release of monomeric tau into the brain interstitium in response to excitatory synaptic activity has been detected by microdialysis(Frost et al., 2009; Pooler et al., 2013; Yamada et al., 2014). By altering the uptake and clearance dynamics of tau or tau aggregates within the extracellular compartment, changes in perivascular endfoot function may influence pathological tau propagation.

Among the three datasets, a consistent association between gene expression in temporal cortex and P-tau levels was observed, but not with dementia status. One possible explanation is that these differences reflect the regional progression of AD pathology, specifically neurofibrillary tau tangle formation, with regard to clinical severity. TCX P-tau burden is associated with late-preclinical stages of AD while tau pathology is not seen in HIP until the latest stages of AD, when it manifests clinically. If changes in DAC gene expression represent a response to tau phosphorylation, these changes may occur in TCX prior to the HIP. The lack of associations in PCX and FCX may reflect the cellular properties of the region that render it highly vulnerability to tau formation. In contrast, hippocampal gene expression and clino-pathological dementia status are associated, but without consistent associations to Aβ or tau pathology. A second possibility is that in HIP, these changes in expression do not occur until late stages of disease progression when clinical diagnosis is a stronger indicator of disease progression than tau burden. Further investigation of the timing of glial responses to disease progression are needed to better resolve the source of these regional differences.

One caveat to the present study is the inability to distinguish astrocytic gene expression from expression in other cell types in the datasets utilized. Though we controlled for this to the best of our ability by cross-referencing with single-cell transcriptomic data, heterogeneity among astrocyte populations remains a major gap in our understanding of the associations between different astroglial genes and local pathological features, such as P-tau levels. It remains an open question as to the specific cell types or subpopulations in which the novel ‘endfoot candidate’ genes are expressed

in. Other factors including neuronal subtypes and density, vascular supply and blood-brain barrier function, as well as proximity to white matter, subarachnoid or ventricular CSF compartments, also likely contribute to the variability in associations between regional pathology and gene expression. This further supports the need for validation of the present study in a manner that assesses cell-type expression and localization.

The present study demonstrated a robust association between both established and candidate molecular components of the perivascular astrocytic endfoot and dementia status and markers of AD pathology. Importantly, these novel astroglial gene candidates were identified through a non-biased clustering approach based on two distinct human transcriptomic datasets and exhibited a striking and near-universal association with P-tau levels within the TCX, albeit all associations were identified using admittedly correlation-based approaches. While we propose these candidate endfoot components exert these effects via their putative role in glymphatic pathway function, this remains to be experimentally validated. The strong association with both dementia status and P-tau pathology in a large cohort of human subjects indicates that perivascular astrocytic endfoot function, and specifically the 15 gene products (*AQP4,* the DAC genes, and the 11 candidate endfoot genes) may represent novel regulators of tau aggregation and the propagation of tau pathology in the setting of AD.

Methods

Data Sources

Data presented in this manuscript was primarily sourced from publicly available datasets. Datasets from the Allen Brain Institute and the Hisayama Study were used. Additionally, tissue obtained from the Oregon Brain Bank was used.

Allen Brain Institute Aging, Dementia and TBI database

This publicly available dataset contains RNAseq–derived transcriptome data from 107 individuals aged 77 and older obtained from the Adult Change in Thought (ACT) cohort. RNAseq data were collected from up to 4 brain regions within each subject, with over 20,000 genes read from each region, totaling 377 independent samples. Detailed

description of tissue collection and processing is available in the database documentation (http://help.brain-map.org/display/aging/Documentation). Entrez IDs (as provided by Allen Brain Institute) were used for protein identification and subsequent analysis.

Hisayama Study gene array database

The microarray data from the Hisayama study is publicly available through the Pubmed GEO database (GDS4758) and includes HIP, FCX, and TCX data from 79 subjects ranging in age from 54 to 105 years of age. Details regarding subjects and sample collection is found on the "sample subsets" page of the database (https://www.ncbi.nlm.nih.gov/sites/GDSbrowser?acc=GDS4758#details). Inclusion in the AD group was based upon histopathological evaluation based on the Consortium to Establish a Registry for Alzheimer's Disease (CERAD) guidelines(Mirra et al., 1991) and Braak staging(Braak and Braak, 1995; Hokama et al., 2014). Importantly, this study did not distinguish between healthy control subjects and control subjects with vascular dementia or other mixed dementias. This is different than the control group distinction made in the Oregon Brain Bank Dataset (described below).

Oregon Brain Bank Dataset

Frontal cortex grey matter or hippocampal samples were obtained from 43 subjects in the Oregon Health & Science University Layton Aging and Alzheimer's Disease Center and associated postmortem tissue repository, or the Oregon Brain Bank. Volunteers signed written informed consent. All aged participants were community-dwelling individuals with no known neurological disease or with a clinical history of AD as established by neurologic evaluation in the Layton Aging and Alzheimer Disease Center in accordance with established consensus criteria. Brain autopsy was performed on all participants after consent was obtained from the next of kin and in accordance with Oregon Health and Science University guidelines (IRB 00001623). Brains in the Oregon Brain Bank underwent neuropathological evaluation for Aβ plaque density, neurofibrillary pathology, and vascular pathology based on CERAD guidelines (Mirra et al., 1991) and Braak staging (Braak and Braak, 1995).The cohort utilized in this study

was selected to minimize inclusion of individuals with secondary pathologies beyond clino-pathological diagnosis of AD, including vascular or mixed dementia, Lewy body dementia, and hippocampal sclerosis. Consequently the 'Non-AD' group includes both cognitively intact subjects and those with a clinical diagnosis of mild cognitive impairment.

Statistical analysis

All statistical analyses were performed using R 3.2 and 3.3 (Team, 2014).

Allen Aging, Dementia and TBI dataset: Logistic regression was utilized to assess the relationship between propensity for a diagnosis of dementia at death, formatted as a dichotomous factor, against mRNA expression of the genes of interest. Mann-Whitney U test was used to assess group wise differences in demographic information. When evaluating the association of gene expression to Alzheimer's pathology, ordinary least-squares (OLS) regression was used to model the CNS pathology levels as continuous outcomes. Model diagnostics revealed the pathology measures to exhibit a right-skew and inconsistent variance of the residuals, therefore logarithmic transforms were applied to the outcomes as necessary. All regression models controlled for age, APOε4 carrier status and a previous history of TBI. Age was framed as a continuous factor although set in 5-year increments across the dataset to account for reporting of age ranges over 95 years of age. APOε4 carrier status was a dichotomous variable to indicate the subject as a heterozygous or homozygous minor allele carrier and TBI was set as a dichotomous variable based on a reported history of brain injury. Gene expression was first correlated with pathology across the entire cohort with subsequent analysis directly contrasting the correlation based on dementia status by assessing the interaction between RNAseq and clinical dementia diagnosis.

Model fit and integrity were examined using a combination of formal fit criteria, including Cook's distance and the standardized difference of the betas, and visual inspection of the residual plots. Results were considered significant at $p<0.05$ after repeated comparison correction to account for the multiple response variables. Test statistics were set a priori to establish power at 80% with an α value of 0.05. False discovery correction was first used across the entire cohort of assessed models to allow

for only 5% of erroneous discoveries in the significant results. The significance of this selection set was then further adjusted using the more stringent Holm-Sidak family-wise error rate correction to correct for multiple comparisons with adjustments carried out separately by individual brain regions due to their inherent differences in biology. These adjusted P values were used to determine final model significance.

Hisayama gene array and Oregon Brain Bank datasets: Logistic regression was used to assess the relationship between a diagnosis of dementia at death against mRNA expression of the genes of interest. Logistic regression was again used to model the relationship between AD diagnosis and CNS pathology levels as the ranges are too truncated to be used as linearly continuous outcomes. "Pathological" states were defined as follows; Braak Stage ≥ 5, Neuritic Plaques ≥ 3, Cerebral amyloid angiopathy ≥ 3. In neither of these datasets were corrections made to account for the covariates. This was due to two features of these datasets. First, both datasets were chosen as validation cohorts and therefore have small sample sizes. Compared to the large discovery cohort, the small sample sizes in these validation datasets made correction for covariates impracticable. Second, both validation datasets were selected because they originated in AD-focused cohorts, allowing a more discreet assessment of associations between the expression of four discrete genes and their products with AD diagnoses or pathological indicators. Consequently, this resulted in substantial age gaps between AD and non-AD cohorts due to the well-established age dependency of the disease.

In contrast to the exploratory nature of the correlation network analysis, the validation cohorts were chosen to explicitly confirm the effects of four heavily implicated genes in particular: the known endfoot elements AQP4 and DTNA, and the WGCNA-identified candidates MLC1 and FXYD1. Furthermore, gene effects were compared within brain regions that had been observed to be biologically distinct with respect to pathology and RNAseq levels. Based on these a priori notions, multiple comparison adjustments were not performed with original p-values presented. Although this does lead to a reduction in the post-hoc power of these validation datasets, it is also able to highlight the sheer number of observed significant relationships across a variety of multiple experimental studies and frameworks.

Weighted Correlation Network Analysis (WGCNA

Weighted Correlation Network Analysis (WGCNA) was implemented using the WGCNA package in R (http://www.genetics.ucla.edu/labs/horvath/CoexpressionNetwork/, RRID: SCR_003302) (Langfelder and Horvath, 2008; Langfelder and Horvath, 2012). Four independent networks were generated from the dataset: single networks were constructed within the full, dementia-only, and non-dementia-only populations and a consensus network was generated across dementia status. Initial filtering was applied prior to each analysis to eliminate spurious genes that had fragments per kilobase per million (FPKM) values of less than 10 in 90% or more of total reads resulting in approximately 7,000 genes per brain region. Adjacency matrices for demented and non-demented populations were generated by calculating biweight midcorrelations for gene pairs. Soft thresholding was used to establish a connection weight between each gene pair within each brain region (Zhang and Horvath, 2005). Threshold values were between 4-7 for all analyses and were determined by manual assessment of scale-free topology after plotting. Next, a topographical overlap matrix (TOM) was generated to determine adjacency for gene pairs. Component-wise minimum of the single network TOMs were used to generate the dementia: non-dementia consensus TOM. Dissimilarity matrices were generated by subtracting the TOM values from 1. Using these values, hierarchical clustering defined modules based on highly interconnected expression profiles. In addition to TOM values, the parameters used from clustering included a minimum module size of 30 and an unsigned network. Eigengenes were calculated for each module to allow for evaluation of module expression with pathology data and hub gene identification. Hub genes were determined by calculating the correlation between each gene in a module and each module's calculated eigengene.

Cluster analysis

The gene modules in which DAC genes were most highly expressed were extracted from each brain region's WGCNA-based clusters. For this analysis, the clusters generated by the full, single network WGCNA was utilized as it resulted in smaller

cluster sizes, and generally greater intramodular connectivity for DAC genes than in the consensus network. Genes with robust astrocytic expression were extracted by thresholding out genes with less than 50% of total expression derived from astrocytes. Cell-type expression values were derived from a separate cell-type RNAseq transcriptome database (Zhang et al., 2016). Pearson correlation coefficient was used to identify genes highly coexpressed with DAC complex genes across subjects. A gene was only considered as coexpressing with DAC components after a conservative correlation of $r>.65$ ($p<1e25$) was observed with at least two of the DAC genes. These conservative thresholds on Pearson's correlation coefficient were selected according to the most stringent Bonferonni-based correction possible under this framework (50281 transcripts contrasted against 4 DAC members across 3 brain regions) and to indicate effect sizes that have traditionally been cited as notably powerful (Pearson's $r>0.6$ and Cohen's $d>1.5$). Genes were only selected that demonstrated significant correlation to AQP4 or the DAC genes in at least 2 of the 3 brain regions.

Western blot analysis

Human frontal cortex grey matter or hippocampus frozen tissue was homogenized by sonication in tissue homogenization buffer (62.5 mM Tris (pH 6.8), 10% glycerol, and 2% SDS) on ice. BCA assays were performed to determine the protein concentration (ThermoFisher Cat# 23225). Additional 0.1% bromophenol blue and 50 mM DTT were added to the sample after the BCA reaction and before the denaturation at 95°C for 5 minutes. Depending on the sensitivity of the antibodies, 50-100 µg of samples were loaded for electrophoresis. Gels were transferred using BioRad Trans-Blot® Turbo™ Transfer System and blots were detected using BioRad ChemiDoc™ Touch Imaging System. Primary antibody used in this study are: AQP4 (1:500, Millipore, Cat# AB3594), FXYD1 (1:500, Abcam, Cat# ab76597), MLC1 (1:1000, Abcam, Cat# ab186436) and DTNA (1:500, BD, Cat# BDB610766). Secondary antibodies were purchased from GE healthcare (1:1000). Band intensity was quantified using ImageJ. The ratio in chemiluminescent signal of the target band relative to the loading control band was measured and normalized to the reference sample on each gel. The average value of two batches were used for quantification.

Chapter 6: A discussion of key findings, considerations, and future directions

Key Findings

1. Disruption of α-syntrophin eliminates perivascular localization of AQP4.
2. α-Syntrophin deletion disrupts CSF-ISF exchange.
3. α-Syntrophin deletion does not phenocopy age-dependent loss of perivascular AQP4 localization.
4. α-Syntrophin deletion exacerbates propagation of α-synuclein aggregates.
5. Overexpression of the AQP4-M1 isoform reduces perivascular localization at capillaries but not large vessels.
6. Overexpression of AQP4-M23 is insufficient to rescue CSF-ISF exchange deficits in aged mice.
7. Numerous transporter proteins exhibit RNA expression profiles linked to the expression profile of the DAC complex throughout human development and disease states.
8. Candidate genes MLC1 and FXYD1 among others exhibit associations with AD and represent promising contributors to endfoot physiology.

Discussion

The glymphatics controversy

Since its initial description in 2012, the glymphatic hypothesis has garnered much attention and controversy. This has been primarily driven by a critique paper in 2017, that was focused on two discrete elements of the hypothesis: 1) the occurrence of interstitial bulk flow and 2) the dependence of perivascular CSF-ISF exchange upon the astroglial water channel aquaporin-4 (AQP4) (Smith et al., 2017). Since then, a collaborative response paper was published refuting the findings of Smith and colleagues (Mestre et

al., 2018a) (Appendix A). Below I will discuss where the controversy stands and how the work I have generated fits into the current body of literature in the field and the greater discussion occurring in the field.

Bulk flow and diffusion in the cerebrum

Solute movement in tissue occurs principally by two processes: diffusion, thermally driven movement of solutes down their concentration gradients; and bulk flow, solute motion resulting from the pressure-driven movement of its solvent. The rate of diffusion slows with increasing molecular size, while within certain limits the movement by bulk flow is independent of molecular size (Sykova and Nicholson, 2008).

The basis of the glymphatic system was derived from experiments focused on two exchange processes: CSF solute influx and ISF solute efflux. In vivo 2-photon microscopy and dynamic contrast-enhanced-MRI demonstrated that tracers injected into the CSF compartment move rapidly along perivascular spaces surrounding pial arteries and into the brain along perivascular spaces surrounding penetrating arteries (Iliff et al., 2013a; Iliff et al., 2012; Iliff et al., 2013b). In these experiments, the rate of CSF distribution along perivascular pathways did not differ across tracer sizes. In chapter two, the data provided in Figure 2 also exhibits size independent distribution of tracers along perivascular spaces, supporting the occurrence of bulk flow in these compartments. Whole-slice imaging following intraparenchymal injection of fluorescent tracers demonstrated that solute efflux occurs along white matter tracks and veins associated with ventricular and cisternal CSF compartments (Iliff et al., 2014; Iliff et al., 2012). Using a more quantitative approach, clearance rates of radiolabeled tracers did not differ between tracers 0.2kD and 10kD in size (Iliff et al., 2012). These findings suggested that brain CSF-ISF exchange involves bulk flow of solutes along perivascular compartments, linked to the efflux of interstitial solutes through interstitial bulk flow. The description of CSF influx is consistent with widely reported occurrences of bulk-flow dependent CSF movement in low-resistance compartments including the ventricles, cisterns, perivascular spaces and white matter (Ghersi-Egea et al., 1996; Mestre et al., 2018a; Rennels et al., 1985; Rosenberg et al., 1980) (Appendix A). The extent of bulk flow in

distal segments of the vasculature as well as the wider brain interstitium, remains a topic of active debate.

Based on elegant experiments using tracers (Patlak and Fenstermacher, 1975; Pizzo et al., 2018), real-time iontophoresis (RTI) (Nicholson et al., 1979) and fluorescence recovery after photobleaching (FRAP) (Smith et al., 2017), diffusion has been classically thought to dominate solute distribution in grey matter regions of the rodent brain. Though not explicitly described, size dependent distribution of CSF tracers away from perivascular compartments was also observed in the initial glymphatic report (Iliff et al., 2012). However, several experimental studies suggest interstitial solute distribution and efflux cannot be explained by diffusion alone. A seminal study by Cserr and colleagues demonstrated that intraparenchymally-injected solutes were cleared from the brain with size-independent kinetics (Cserr et al., 1981), a finding replicated by Iliff et al. (Iliff et al., 2012). Additionally, a comprehensive pharmacokinetic study reported the efflux kinetics of a wide range of solutes from the rat brain following striatal injection (Groothuis et al., 2007), demonstrating complex pattern of efflux, in which both diffusion and bulk flow were observed and relative contributions were dependent upon solute size, chemistry, and interactions with efflux transporters.

Recent computational modeling studies suggest that bulk flow in the brain interstitium is unlikely under physiological conditions due to the hydraulic resistance of this compartment (Asgari et al., 2016; Faghih and Sharp, 2018; Holter et al., 2017; Jin et al., 2016). What accounts for the discrepancy between these modeling studies and experimental studies suggesting a role for bulk flow? One possibility is that anatomical dimensions informing these models are derived from electron microscopy datasets where fixation processes distort observed structures of the extracellular space and glia from those that occur in vivo (Korogod et al., 2015; Tonnesen et al., 2018). Additionally, these models focus on the microscopic scale of small ensembles of vessels. In biological systems, perivascular CSF tracer distribution and interstitial solute efflux occur across a macroscopic scale, including different vessel types, CSF compartments, brain regions, and mixtures of gray and white matter; complexity and scale not accounted for in presently reported models of extracellular diffusion.

In many ways the data presented here supports that current understanding of bulk flow and diffusion in the cerebrum. We too, observed size independent movement of tracers along perivascular spaces across all cisterna-magna injection studies in both WT and *SNTA1*$^{-/-}$ mice (Chapters 2 and 3) and size-dependent movement of tracers within the broader brain parenchyma. This is mostly clearly demonstrated in chapter 2, figure 2. Our intraparenchymal studies (chapter 2, figures 3 & 4) demonstrate that both 10kd dextrans and α-synuclein clear along perivascular compartments. However, assessment of the sub-regional distribution of tracers revealed differences between the inert dextran and soluble α-synuclein, These differences are likely a reflection of cell-mediated trafficking of α-synuclein rather than differences in diffusion properties, due to the small size difference between the tracer (10kD) and the size of soluble α-synuclein (14kD).

Together, these results suggest that brain solute efflux is likely driven by both bulk flow and diffusion though their relative contributions remain undefined. A recent computational study used primary RTI data from several published studies estimated a theoretical interstitial bulk flow velocity of 50 μm/min (Ray et al., 2019). At such a low rate, it is likely that diffusion dominates distribution and efflux of small molecular weight interstitial solutes. For macromolecules however, which exhibit low rates of diffusion, even slow interstitial bulk flow may play a critical role in distribution and efflux. An additional possibility is that bulk flow may be restricted to permissive low-resistance pathways including perivascular spaces and white matter tracks, while diffusion accounts for solute movement between such pathways.

The role of AQP4 in perivascular CSF-ISF exchange

One novel element of the glymphatic system is the dependence of perivascular CSF-ISF exchange on the astroglial water channel AQP4 (Iliff et al., 2012). Iliff et al. reported CSF tracer influx and interstitial tracer efflux were both dramatically slowed in *Aqp4* knockout mice, a finding which Smith et al. could not replicate in a different *Aqp4* knockout mouse line (Smith et al., 2017). Subsequently, however, a study from a consortium of five labs confirmed *Aqp4* gene deletion impairs glymphatic CSF tracer influx and interstitial solute distribution and clearance using four different *Aqp4* knockout lines (Mestre et al., 2018a) (Appendix A). Several additional studies report that deletion

of *Aqp4* slows distribution and clearance of other interstitial solutes, including lactate (Lundgaard et al., 2017), tau (Iliff et al., 2014), ApoE (Achariyar et al., 2016) and adeno-associated viruses (Murlidharan et al., 2016).

It is likely that differences in anesthesia and other technical details underlie these discrepant findings. Groothius et al., as well as a recent study suggest a significant role for anesthetics in modulating both CSF influx and ISF efflux (Groothuis et al., 2007; Hablitz et al., 2019). Importantly, Hablitz et al. demonstrated that tribromoethanol (Avertin), reduced CSF influx to approximately half the magnitude seen when using ketamine-xylazine. Additional technical differences including injection rate and volume may contribute to the inconsistent results.

The biophysical role for AQP4 in facilitating CSF-ISF exchange remains unclear and the mechanism of solute movement into and out of the perivascular compartment, remain unresolved. Along arteries, directional, peristaltic flow of fluid along the perivascular space has been reported (Bedussi et al., 2018; Hadaczek et al., 2006b; Mestre et al., 2018c) and has been attributed to pulsation of the arterial wall. The pressure generated by these pulsations has been proposed to drive fluid across the endfeet due to the conservation of mass. As mentioned in chapter 1, AQP4 makes up a substantial fraction of the endfoot compartment, due to the density of orthogonal arrays in this space. Therefore, these channels may play a critical role in allowing displacement of fluid from the perivascular compartment, into the astrocyte syncytium and brain extracellular space in response to arterial pulsations. Disruption of AQP4 (by AQP4 knockout or loss of localization), may dramatically increase resistance to flow across this compartment and the subsequent exchange of fluid.

The studies presented in chapter 2 and appendix a, tangentially support a role for AQP4 in CSF-ISF exchange demonstrating that mice with disrupted perivascular AQP4 localization exhibit CSF-ISF exchange deficit. Perhaps more interestingly, the data collected in *SNTA1*$^{-/-}$ mice and presented in chapter 2, may provide some insight into the contributions of AQP4 to bulk flow and diffusion based solute movement. Most of the deficits observe in *SNTA1*$^{-/-}$ mice were restricted to deep brain structures, rather than in superficial regions such as cortex. This suggests that regions with greater access to CSF compartments (the glia limitans and large perivascular compartments of penetrating

vessels), may rely on diffusion-based movement of tracer, while deeper brain structures, with more restricted interfaces with the CSF compartments may depend on perivascular bulk flow mechanisms. Deletion of α-syntrophin preserves AQP4 expression, so diffusion-based mechanisms, not dependent on directional fluid flow, or response to pressure gradients would be unaffected, unlike AQP4 KO mice, that will exhibit deficits in all forms of fluid movement.

While there are several important technical considerations to be made when interpreting the data, the viral overexpression studies in chapter 3 may also provide interesting insight into the role of AQP4 in CSF-ISF exchange. We demonstrated that modulation of localization at the capillary level has no effect on CSF-ISF exchange. One interpretation of this result is that the CSF-ISF exchange occurs largely along large vessels. Consistent with our results in *SNTA1*$^{-/-}$ mice, this suggests that depending on the localization within the brain assessed, mechanisms of solute clearance may differ dramatically. These data, along with the broad inconsistencies observed in CSF-ISF exchange between various laboratories, illustrate the necessity for a higher resolution assessment of exchange both regionally, and at the level of individual vessel types.

Defining the landscape of the astrocytic endfoot domain

One of the greatest caveats associated with α-syntrophin deletion as a model for loss of perivascular AQP4 localization, is the high probability of concomitant disruption of other elements of the endfoot domain. Despite its possession of a PDZ domain, the potassium channel Kir4.1 is the only discrete protein (aside from AQP4) described to interact with α-syntrophin in astrocytes (Masaki et al., 2010). In fact, general description of the proteomic profile of the endfoot compartment remains sparse. This may in part stem from technical challenges in isolating subtypes of astrocytes, let alone subcellular domains. However, this remains an important topic of investigation, as a clearer understanding of the protein architecture at the endfoot would help to explain the mechanistic questions involving fluid and solute transport in this compartment. As mentioned above, water movement is known to follow osmotic gradients. This suggests that the presence of ion and protein transporters at the endfoot may help to explain the

driving forces for directional fluid movement between the extracellular space and perivascular spaces.

Despite using crude methodology, the transcriptome datasets we analyzed in chapters 4 & 5 suggests a strikingly conserved expression profiles between the few known components of the endfoot (DAC complex and AQP4), and several transporter protein candidates. Among these candidates, with the help of a post-doc in the lab (Marie Wang), we have begun to further characterize a subset, with promising preliminary studies, confirming the perivascular localization of MLC1 (appendix b). These results providing promising first steps towards further characterization of the endfoot compartment. Encouragingly, an independent group also reported enriched mRNA levels of MLC1 and other genes identified in our studies (including Slc1a2, Slc25a18 and Gja1) (Boulay et al., 2017). This is particularly interesting in light of recent evidence suggesting the occurrence of local translation in astrocytes and in response to stimulation (Sapkota et al., 2019).

How these newly identified candidates and any candidates identified in the future contribute to CSF-ISF exchange remains undetermined. An intriguing possibility is that local translation at the endfoot can modulate the protein pool in response to state changes or vascular derived signals, factors that have been previously implicated as regulators of CSF-ISF exchange, and may reflect the unique transcriptomic and spontaneous Ca^{2+} activity observed at the endfoot relative to other astrocytic compartments (Bindocci et al., 2017; Boulay et al., 2017; Iliff et al., 2013b; Xie et al., 2013).

State and activity dependent modulation of the endfoot domain.

Several state dependent changes have been linked to modulation both perivascular AQP4 localization and CSF-ISF exchange suggesting that there may be a role of non-cell autonomous factors regulating glymphatic exchange. Conversion of healthy astrocytes to a reactive state represents one change directly tied to several aging processes. Supporting a role for reactive astrocytes in modulation of CSF-ISF exchange, Liddelow and colleagues demonstrated that perivascular AQP4 localization is reduced in the mouse brain following LPS treatment, but that the loss in localization was blocked by triple knockout of neuroinflammation-linked genes thought to drive A1-type reactive

astrogliosis (Il-1α, TNF α, and C1q) (Liddelow et al., 2017). It is worth exploring whether the conversion of astrocytes to A1-reactive astrocytes in normal again is responsible for the loss of AQP4 localization observed in the aging brain, and if certain subpopulations of astrocytes exhibit selective vulnerability to this conversion (Clarke et al., 2018; Kress et al., 2014; Zeppenfeld et al., 2017).

Another state change commonly linked to CSF-ISF exchange is sleep. The abundance of CSF-influx in the brain has been revealed to be dramatically impacted by sleep-wake state (Xie et al., 2013). Alterations in sleep have also been frequently tied to pathological states and the interstitial concentration of a wide range of proteins show diurnal fluctuations (Holth et al., 2019; Lundgaard et al., 2017; Roh et al., 2012) Development of toolkits for more precisely scrutinizing and analyzing astrocyte cell types and subcellular domains will be critical for further protein candidate identification efforts and for interrogating state dependent changes.

Implications for neurodegenerative disease

Intercellular propagation of aggregated proteins is becoming increasingly linked to the progression of a wide range of neurodegenerative diseases (Walsh and Selkoe, 2016). Propagation and ‘seeding’ behavior has been linked to several common pathogenically aggregating proteins including amyloid β, tau, huntingtin, TDP-43 and α-synuclein (Desplats et al., 2009; Iba et al., 2015; Jeon et al., 2016; Nonaka et al., 2013; Stohr et al., 2012). Mechanisms of intercellular transmission of these proteins are particularly interesting, in part due to the intracellular pathology associated with many of the proteins with the notable exception of amyloid β. Proposed mechanisms of transmission include synaptic transmission, exosomes and release by dying cells. Ultimately, each of these mechanisms results in the release of aggregating proteins into the extracellular compartment, regardless of their origin, allowing for a putative role of CSF-ISF exchange in their clearance.

Increasing evidence suggests a role of CSF-ISF exchange in AD progression in humans. Of particular interest is the diurnal regulation of amyloid β in the brain and CSF and how it is linked to sleep-wake changes in CSF-ISF exchange (Xie et al., 2013). PET

studies indicate that sleep deprivation results in elevated levels of amyloid β (Shokri-Kojori et al., 2018), and slow wave sleep disruptions results in elevated levels of CSF amyloid β (Ju et al., 2017). Impairments of clearance via the CSF, ultimately resulting in elevated parenchymal levels of soluble amyloid β may allow for accelerated propagation of pathogenic species of the protein due to increased accessibility and concentration. This mechanism is intriguing as it could be conserved across proteins and diseases for which 'prion-like' seeding mechanisms have been implicated.

Our study in chapter 2 was among the first to characterize the role of CSF-ISF exchange in clearance of α-synuclein. Interestingly, biomarker studies have suggested that CSF levels of total α-synuclein tends to be lower in PD patients (Eusebi et al., 2017). Additionally, much like AD, sleep quality has been linked to clinical severity of PD (Schreiner et al., 2019). Our results suggest that impairment of CSF-ISF exchange may not only shift the homeostatic balance of soluble α-synuclein away from the CSF and into the brain, but also leads to increased formation of insoluble α-synuclein aggregates following injection of fibrillary species of the protein. Since completing this study, an independent group has also reported slowed α-synuclein clearance when glymphatic function is disrupted (Zou et al., 2019).

Clearly these studies warrant further investigation of the role of CSF-ISF exchange in α-synuclein clearance. Strong evidence exists supporting transsynaptic transmission of α-synuclein contributes to prion-like propagation (Danzer et al., 2011). The relative contribution of extracellular α-synuclein trafficking to global distribution awaits further characterization.

Redefining the glymphatic pathway

Iliff et al. originally described the glymphatic pathway as 'a brain-wide pathway for fluid transport in mice, which includes the para-arterial influx of subarachnoid CSF into the brain interstitium, followed by the clearance of ISF along large-caliber draining veins. Interstitial bulk flow between these influx and efflux pathways depends upon trans-astrocytic water movement…' (Iliff et al., 2012). Based on the addition of recently generated insights and a more comprehensive review of existing literature, we propose a critical appraisal of the initial description.

As outlined above substantial evidence exists to support 3 major elements of the glymphatic hypothesis: 1. Bulk flow occurs in low resistance compartments of the brain. 2. AQP4 facilitates exchange of solutes into and out of the ECS compartment. 3. Proteins and drugs are cleared from the interstitial space of the brain along perivascular spaces. Elements that remain unresolved include: 1. The relative contributions of bulk flow and diffusion to solute distribution in grey matter regions and 2. Physiological facilitators of fluid and solute transport at the perivascular compartment. Considering these data, we propose that the glymphatic system be reappraised simply as "A network of perivascular compartments, that allow for rapid trafficking of fluid and solutes in the brain, in an AQP4 dependent fashion".

Additional technical considerations

Anesthesia

As alluded to above, anesthesia has been demonstrated to play a significant role in modulating CSF-ISF exchange. This may reflect various modulations of cranial physiology observed in anesthetized states including intracranial pressure, blood-gas concentrations, respiratory rate and heart rate. For all studies, ketamine-xylazine anesthesia was used, however, animals were not ventilated nor were any of the values above measured. Replication of the studies presented in chapters 2 and 3 with mice with greater control/monitoring of these values (ex: intubation, arterial blood gas monitoring) would help to confirm the conclusions made are physiologically relevant and not epiphenomenon of experimental conditions.

Qualitative nature of fluorescence studies

While the fluorescence-based approaches utilized in chapters 2 and 3 allowed for relatively quick, easy assessments of CSF-ISF exchange, they do not allow for quantitative assessment of differences, due to the incomplete collection of tissue and difficulty measuring fluorescence without saturation. The variability observed in assessments of tracer distribution may be in part a result of these limitations, as well as subtle variability in physiological values as discussed above. Future follow-up

experiments would benefit from using more quantitative assessment approaches such as radiolabeled tracers, and fluorescence spectroscopy.

Future directions

The results from these studies have opened a wide-range of interesting topics for future investigation. I will focus on three.

CSF-ISF exchange at large and small vessels across the brain

The studies presented in chapters 2 and 3 suggested that there are likely differences in CSF-ISF not only between brain regions, but also along the vascular tree. Profiling the associations between CSF-ISF exchange and the size of the blood vessel at which they occur, could have substantial consequences for our understanding of CSF-ISF exchange, and help to resolve some of the discrepancies described by Smith and colleagues (Smith et al., 2017). Regional differences equally represent an important topic of investigation to more completely articulate bulk flow, or lack thereof, across the brain, and the brain structures associated with it (i.e. white matter tracts, etc.). Finally, developing approaches to modulate function at the specific compartments will be critical to developing causal relationships between specific anatomical features and CSF-ISF exchange. This could be achieved using directed evolution to develop viruses that can target specific cellular populations

Profiling of the endfoot compartment

Building evidence support a unique functional and proteomic profile at the endfoot compartment that likely plays a critical role in facilitating the state-dependent movement of fluid and solutes through the space. Further characterization of this domain remains an opportunity for impactful contribution to not only the study of CSF-ISF exchange, but also the role of the endfoot in general neurovascular functions. Rapidly developing tools in omics-based approaches should allow for characterization, pending the development of an effective biochemical approach for isolating this compartment.

Once profiled molecularly, endless opportunities exist for linking proteins to functional readouts including CSF-ISF exchange and Ca^{2+} signaling.

The role of CSF-ISF exchange in Parkinson's Disease

The studies presented in chapter 2 are the first indication that CSF-ISF exchange may contribute to α-synuclein, paving the way for a multitude of studies to better profile this relationship. Primary among these, is to repeat the PFF injection studies across several brain regions and in parallel with synaptic circuit tracing. This will be critical to determining the relative contributions of the various proposed transmission pathways. How this pathway and other intercellular transmission pathways are utilized across different α-synuclein and synucleinopathies also remains unclear. A third and very interesting question is whether other risk factors associated with these disease states, such as exposure to pesticides and heavy metals, might influence CSF-ISF exchange.

Summary

The astrocytic endfoot domain is a fascinating compartment positioned perfectly to operate as a master-regulator of neurovascular and neuro-CSF interactions. This is an anatomical space and biological topic just beginning to be studied and one that already appears to have substantial implications for our understanding of neurodegenerative diseases. Due to its function in clearance of aggregating proteins prior to pathogenic accumulation, approaches targeting this space have the potential to serve as therapeutic treatment options at early stages of disease progression. Studies focused on the regulation of AQP4 localization, represents a topic with the capacity to increase our understanding of both basic principles of brain physiology and targetable treatment options.

Appendix A: Aquaporin-4-dependent glymphatic solute transport in the rodent brain

Humberto Mestre[1*], Lauren M. Hablitz[1*], Anna L. B. Xavier[2*], Weixi Feng[3*], Wenyan Zou[3*], Tinglin Pu[3*], Hiromu Monai[4,5*], Giridhar Murlidharan[6*], Ruth M. Castellanos Rivera[6*], Matthew J. Simon[7*], Martin M. Pike[8*], Virginia Plá[1*], Ting Du[1*], Benjamin T. Kress[1*], Xiaowen Wang[4], Benjamin A Plog[1], Alexander S. Thrane[2,9] Iben Lundgaard[1,10,11], Yoichiro Abe[12], Masato Yasui[12], John H. Thomas[13], Ming Xiao[3#], Hajime Hirase[4,14#], Aravind Asokan[6,15#], Jeffrey J. Iliff[7,16#], Maiken Nedergaard[1, 2#]

[1]Center for Translational Neuromedicine, University of Rochester Medical Center, Rochester, NY, USA, [2]Center for Translational Neuromedicine, Faculty of Medical and Health Sciences, University of Copenhagen, Denmark, [3]Jiangsu Province Key Laboratory of Neurodegeneration, Center for Global Health, Nanjing Medical University, Nanjing, Jiangsu, P. R. China, [4]RIKEN Center for Brain Science, Wako, Saitama, Japan, [5]Ochanomizu University, Bunkyo-ku, Tokyo, Japan, [6]Gene Therapy Center, The University of North Carolina at Chapel Hill, Chapel Hill, North Carolina, USA, [7]Department of Anesthesiology and Perioperative Medicine, Oregon Health & Science University, Portland, OR, USA, [8]Advanced Imaging Research Center, Oregon Health & Science University, Oregon Health & Science University, Portland, OR, USA, [9]Department of Ophthalmology, Haukeland University Hospital, Bergen, Norway, [10]Department of Experimental Medical Science, Lund University, Lund, Sweden, [11]Wallenberg Center for Molecular Medicine, Lund University, Lund, Sweden, [12]Department of Pharmacology, School of Medicine, Keio University, Tokyo, Japan, [13]Department of Mechanical Engineering and Department of Physics & Astronomy, University of Rochester, Rochester, NY, USA, [14]Brain and Body System Science Institute, Saitama University, Sakura-ku, Saitama, Japan, [15]Surgery/Molecular Genetics & Microbiology, Duke University School of Medicine, Durham, North Carolina, USA. [16]Knight Cardiovascular Institute, Oregon Health & Science University, Portland, OR.

*Humberto Mestre, Lauren M. Hablitz, Anna L. R. Xavier, Weixi Feng, Wenyan Zou, Tinglin Pu, Hiromu Monai, Giridhar Murlidharan, Ruth M. Castellanos Rivera, Matthew J. Simon, Martin M. Pike, Virginia Plá, Ting Du, and Benjamin T. Kress contributed equally to this work.

Foreword

This work was generated and presented as an accepted manuscript in Elife. The work associated with OHSU in the text (Figure 6) was performed by myself. Martin Pike was instrumental to designing and performing dynamic contrast enhanced magnetic resonance imaging (DCE-MRI) experiments and designing an approach to perform the cisterna magna infusion in the bore of the 12T magnet. Work in the remaining figures was generated primarily by the other co-first authors of the manuscript (above).

Abstract

The glymphatic system is a brain-wide clearance pathway; its impairment contributes to the accumulation of amyloid-β. Influx of cerebrospinal fluid (CSF) depends upon the expression and perivascular localization of the astroglial water channel aquaporin-4(AQP4). Prompted by a recent failure to find an effect of *Aqp4* knock-out (KO) on CSF and interstitial fluid (ISF) tracer transport, five groups re-examined the importance of AQP4 in glymphatic transport. We concur that CSF influx is higher in wildtype mice than in four different *Aqp4* KO lines and in one line that lacks perivascular AQP4 (*Snta1* KO). Meta-analysis of all studies demonstrated a significant decrease in tracer transport in KO mice and rats compared to controls. Meta-regression indicated that anesthesia, age, and tracer delivery explain the opposing results. We also report that intrastriatal injections suppress glymphatic function. This validates the role of AQP4 in accordance with the glymphatic system and shows that invasive procedures should not be utilized.

Introduction

A brain-wide fluid transport pathway, known as the glymphatic system, supports the rapid exchange of cerebrospinal fluid (CSF) and interstitial fluid (ISF) along perivascular pathways (Iliff et al., 2012). The glymphatic system consists of three principal sequential anatomic segments: (i) CSF inflow along the perivascular spaces surrounding penetrating arteries, (ii) dispersion of CSF through the wider interstitium, and (iii) efflux of ISF along the large-caliber draining veins to re-enter the CSF within the ventricular and cisternal compartments (Jessen et al., 2015). Ultimately, interstitial solutes cleared to the CSF exit the brain through meningeal lymphatic vessels flanking the venous sinuses, along cranial and spinal nerve sheathes, and across the cribriform plate (Aspelund et al., 2015; Louveau et al., 2015). Astrocytic endfeet ensheath the cerebral vasculature, and the abundantly expressed astroglial water channel aquaporin-4 (AQP4) localizes primarily to the perivascular endfoot membrane domain abutting the basal lamina. As this anatomic arrangement provides a route for rapid water movement between the perivascular space and the glial syncytium, AQP4 has been proposed to

support perivascular fluid and solute movement along the glymphatic system (Nedergaard, 2013).

Several groups have independently shown that the astrocytic AQP4 is essential for fast glymphatic transport. Iliff et al. demonstrated a significant suppression of both perivascular CSF tracer influx and interstitial mannitol and amyloid-β (Aβ) clearance in *Aqp4* knockout (KO) mice (Iliff et al., 2012). Subsequent work demonstrated that *Aqp4* gene deletion exacerbated glymphatic pathway dysfunction after traumatic brain injury (TBI) and promoted the development of neurofibrillary pathology and neurodegeneration in the post-traumatic brain (Iliff et al., 2014). Plog et al. similarly found that *Aqp4* KO mice exhibit slowed transport of interstitial solutes to the blood after TBI, reflected by a significant reduction in plasma biomarkers of TBI, including GFAP, neuron-specific enolase, and S100β (Plog et al., 2015). Xu et al. reported that deletion of *Aqp4* exacerbated Aβ plaque accumulation and cerebral amyloid angiopathy in the APP/PS1 murine model of Alzheimer's disease (Xu et al., 2015). Achariyar et al. found significantly reduced distribution of FITC-ApoE3, ^{125}I-apoE2, ^{125}I-apoE3, ^{125}I-apoE4, as well as ^{14}C-inulin in *Aqp4* KO mice following tracer injection to the CSF(Achariyar et al., 2016). Lundgaard et al. reported that glymphatic clearance of lactate was reduced in *Aqp4* KO mice (Lundgaard et al., 2017). Finally, Murlidharan et al. demonstrated that *Aqp4* KO mice exhibit significantly impaired clearance of adeno-associated viruses (AAV) infused into the ventricles, and concluded that glymphatic transport profoundly affects various aspects of AAV gene transfer in the CNS (Murlidharan et al., 2016). A recent MRI study showed the AQP4 facilitator, TGN-073, potentiated the transport of interstitial fluid from the glia limitans externa to pericapillary Virchow-Robin space (Huber et al., 2018).

The critical role of AQP4 in supporting perivascular CSF-ISF exchange was recently questioned in a report by Smith et al. (Smith et al., 2017), in which the authors failed to detect any reduction in CSF tracer influx into the brain parenchyma of *Aqp4* KO mice compared to wild-type (WT) controls. Because a key element of the glymphatic hypothesis is the role of astroglial water transport in supporting perivascular CSF-ISF exchange, we consider it critical to re-examine the role of AQP4 in this process, with an

aim to resolve the discrepant reports. Using data generated from five independent laboratories, we have undertaken such a re-evaluation of the effects of *Aqp4* deletion on perivascular glymphatic exchange. Results of this analysis consistently confirm that *Aqp4* deletion impaired perivascular glymphatic flow relative to that in wild-type mice. Our conclusion is strengthened by the use of four independently generated *Aqp4* KO lines, including the line used by Smith et al. (Smith et al., 2017), as well as the α-syntrophin (*Snta1*) KO line, which lacks AQP4 perivascular localization despite normal expression levels (Amiry-Moghaddam et al., 2003).

Smith et al. (Smith et al., 2017) also questioned the existence of tissue bulk flow based injecting tracers of varying molecular sizes into cortex or striatum. We questioned this approach based on the prior finding that traumatic brain injury is linked to an immediated and sustained reduction in CSF influx (Iliff et al., 2014). As expected, our analysis showed that insertion of glass pipettes into the brain markedly reduced brain-wide CSF tracer influx. Thus, interstitial fluid transport should not be studied following invasive procedures in the brain.

Results

The study included data from five laboratories using four independently generated Aqp4 KO lines and one Snta1 KO mouse line (Figure A.1a-e) (Adams et al., 2000; Fan et al., 2005; Ikeshima-Kataoka et al., 2013; Ma et al., 1997; Thrane et al., 2011). Immunohistochemistry done in parallel with the glymphatic experiments verified that AQP4 was indeed deleted in all the Aqp4 KO mouse lines (Figure A.1a-c and e). In the Snta1 KO mice, immunofluorescence demonstrated that perivascular AQP4 polarization was absent in this line (Figure A.1d).

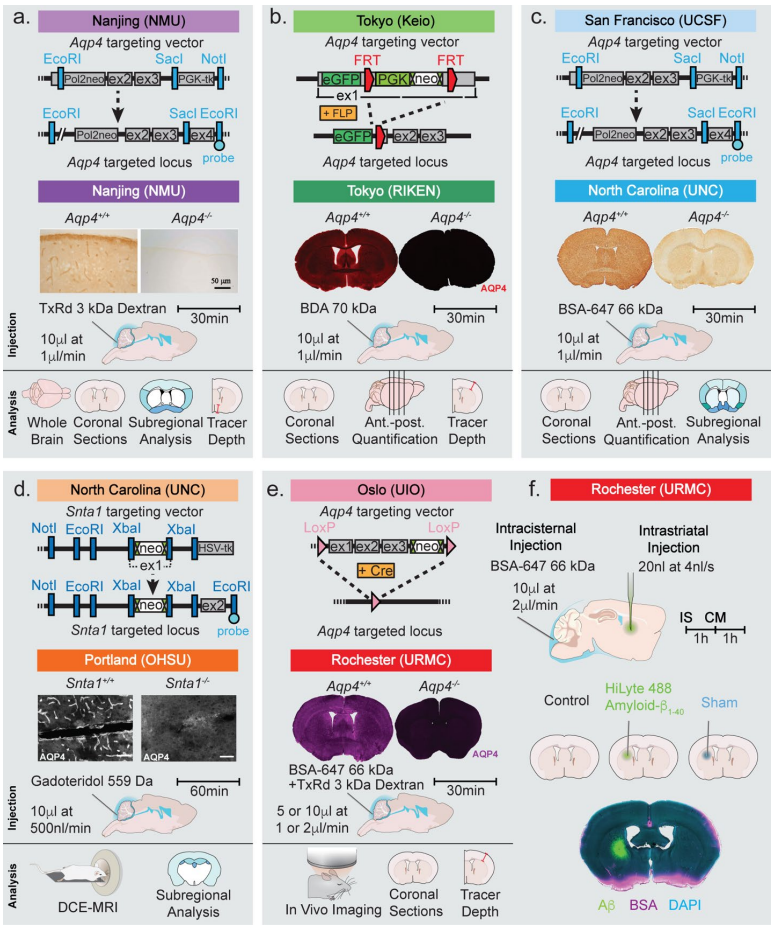

Figure A.1: Strategy used for generation of KO mice and the experimental design. Top row of each panel represents the institution where the line originated from and the strategy used to generate the four global Aqp4 KO mice and the Snta1 KO mice. Second row of each panel shows the five labs that collected data on glymphatic functions in the five transgenic mouse lines: (a) Nanjing Medical University (NMU), (b) RIKEN Center for Brain Science (RIKEN), (c) University of North Carolina (UNC), (d) Oregon Health & Science University (OHSU), (e) University of Rochester Medical Center (URMC). (a-e) Immunohistochemical analysis showing the lack of AQP4 expression in the global KOs and (d) lack of perivascular AQP4 localization in Snta1 KO compared to WT mice. Scale bar: 50 µm. (a-e) Third row displays the volume and rate used for the intracisterna magna (CM) injections for each experiment, the tracer used, and the experiment duration. Note that URMC collected two full data sets using an injection rate of either 1 or 2 µl/min. (a-e) The last row display the analyses strategy employed by each of the 5 research group in Figure A.2-6. (f) Additional experiments performed in Figure A.7 tested the effect of intrastriatal (IS) injection on global glymphatic function. TxRd, Texas Red; BDA, biotinylated dextran amine; BSA-647, bovine serum albumin-Alexa Fluor 647; DCE-MRI, dynamic contrast enhanced-magnetic resonance imaging.

NMU: Reduced influx of a fluorescent CSF tracer in Aqp4 KO mice

We injected the fluorescent tracer Texas Red-dextran (3 kD, TRd3) intracisternally, as previously described (Iliff et al., 2012). We first compared overall penetration of TRd3 into the dorsal and ventral surfaces of the whole-brain between WT and Aqp4 KO ($Aqp4^{-/-}$) mice using ex vivo near infrared fluorescence imaging. Quantification of the mean integrated optical density (MIOD) of TRd3 on the dorsal and ventral brain surface along anterior-posterior position of the bregma showed a significant reduction in Aqp4 KO mice compared with WT mice (Figure A.2a-c). Interestingly, CSF tracer entry into the ventral brain was higher than into the dorsal brain. We also compared penetration of TRd3 into the brain on the serial coronal forebrain slides (+1.7 to -0.7 mm from the bregma) between the two genotypes. The percentage area of whole-slice fluorescence was significantly reduced in Aqp4 KO mice compared to WT controls (Figure A.2d, f). Subregional quantification on the coronal section at the level of 0.5 mm anterior to the bregma showed that penetration of CSF tracer was high in the ventral and lateral brain surface of WT mice, but was comparable in the dorsal surface of the brain with Aqp4 KO mice (Figure A.2g-h), further supporting difference in brain regions of CSF tracer influx. Specifically, Aqp4 KO markedly impaired the influx of TR-d3 into both the perivascular space and the brain parenchyma in the hypothalamus, one of the brain regions with the highest expression of AQP4 (Nielsen et al., 1997) (Figure A.2e). Quantification of the intensity of TR-d3 as a function of the distance from the brain surface showed rapid decay of tracer with increasing distance from the ventral surface of the hypothalamus in Aqp4 KO mice. The tracer was almost undetectable at 500 μm below the brain surface in both the perivascular space and in the brain parenchyma in Aqp4 KO mice. By contrast, the TR-d3 fluorescence intensity remained at 90% of the pial surface intensity to a depth of 500 μm in the perivascular space as well as in the adjacent parenchyma in WT mice (Figure A.2i-j). Taken together, these results replicate the previous finding that AQP4 facilitates the transfer of intracisternally injected TR-d3 from the CSF into the parenchyma (Iliff et al., 2012).

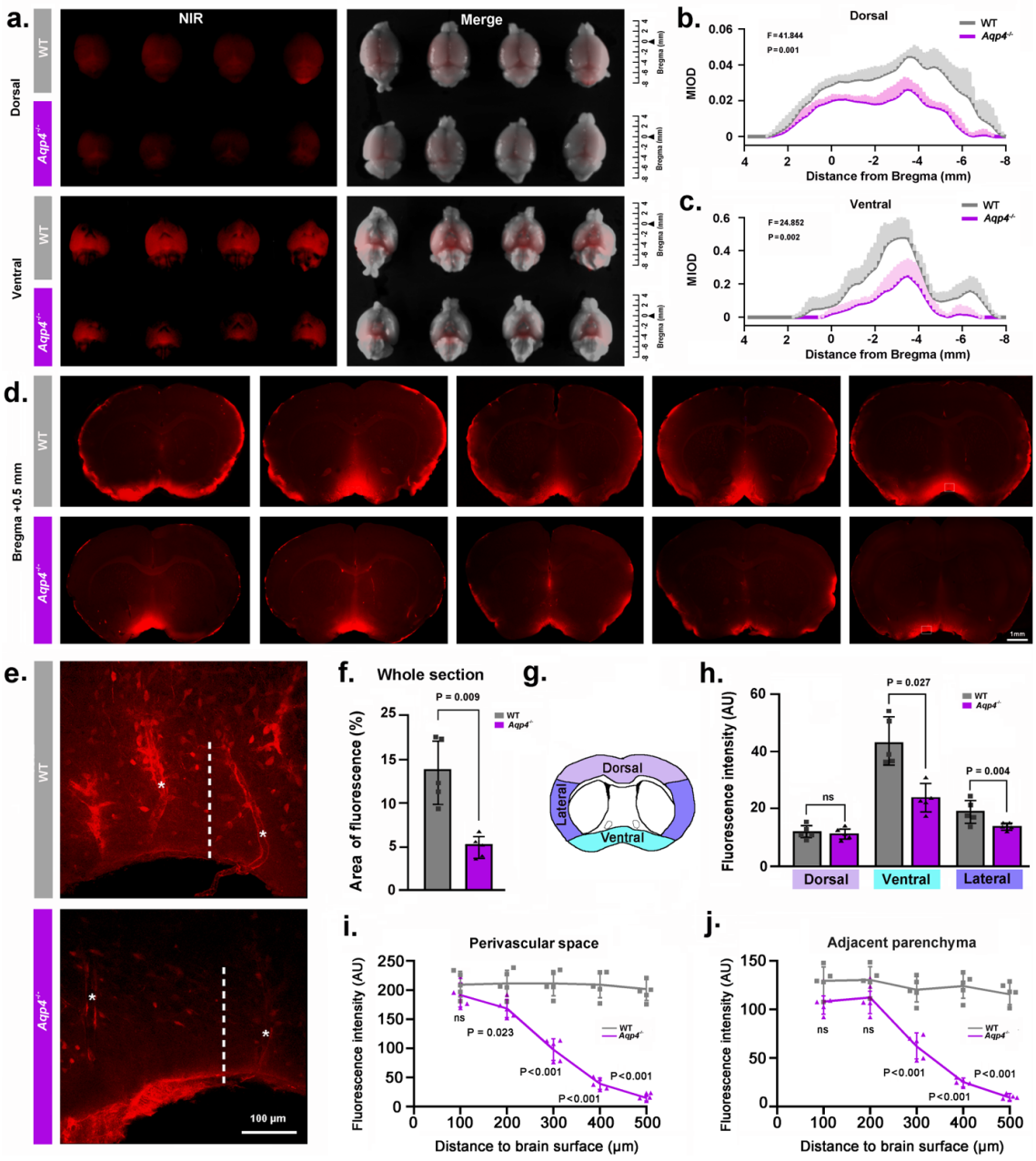

Figure A.2: NMU: Aqp4 gene deletion reduced the penetration of intracisternally injected tracer into the brain parenchyma.

Texas Red-conjugated dextran (TRd3, 3kD) was injected intracisternally into WT and *Aqp4* KO mice. Thirty minutes after injection, the anesthetized animals were perfusion fixed, and the fluorescence was evaluated ex vivo. (a) Representative near infrared (NIR) fluorescence images of the dorsal and ventral whole-brains of 4 mice per genotype. (b-c) Quantification of the mean integrated optical density (MIOD) of TRd3 on the dorsal (b) and ventral (c) brain surface of WT (grey) and *Aqp4* KO (purple) mice from 4.0 mm anterior to 8.0 mm posterior of the bregma. (d) Representative images of coronal brain sections at +0.5 mm from the bregma from 5 pairs of WT and *Aqp4* KO mice showing TRd3 distribution within the brain. (e) High magnification micrographs of the hypothalamus (lined area in d) showing the fluorescence intensity of TRd3 within the perivascular space (star) and adjacent brain parenchyma (dotted line) of WT mice and *Aqp4* KO mice, respectively. (f) Quantification of the percentage area of whole-slice fluorescence of the both genotypes for 6-8 forebrain sections (+1.7 to -0.7 mm from the bregma) of each mouse. (g) Diagram showing the subregional analysis of brain sections at the level of 0.5 mm anterior to the bregma. (h) Quantification of the mean fluorescence intensity (AU, arbitrary units) of TRd3 of the dorsal, ventral and lateral brain regions, respectively. (i-j) Quantification of the mean fluorescence intensity of TRd3 along the perivascular space and the interstitium adjacent to the vessels under the ventral surface of the hypothalamus of the both genotypes. Shades and error bars represent standard deviation. Data in Figure 2b and c were analyzed by repeated-measures ANOVA, N = 4 per group. Data in Figure 2f, h, i and j were analyzed by Student's t-test. P values shown are comparisons between WT and *Aqp4*$^{-/-}$. ns: not significant.

RIKEN: Histological enhancement of CSF tracer reveals compromised parenchymal tracer infiltration in Aqp4 KO mice

The RIKEN and Keio group used another strain of Aqp4 KO mice, in which the exon 1 of Aqp4 is replaced with eGFP. In this experiment, biotinylated dextran amine (BDA, 0.5%, 70 kDa) was injected under deep ketamine-xylazine (KX) anesthesia (Figure A.3a). Because Aqp4 KO mice express eGFP, we used Alexa 594-conjugated streptavidin (SA) to visualize BDA. This approach has an advantage that BDA signals are amplified by the histological processing and clearly distinguished from intrinsic fluorescence (i.e. before histological processing). As a result, BDA distribution appeared less extensive in the cortex of Aqp4 KO mice (Figure A.3b). Quantification of SA-enhanced BDA signals in the cortical parenchyma showed depth-dependent profiles that

decayed with cortical depth after the initial peak for both wild type and Aqp4 KO mice. Notably, BDA signals in the cortex of Aqp4 KO mice are of lower intensity and penetrated less into the parenchyma at an anterior-posterior position of bregma (Figure A.3c). Next, we examined if the compromised BDA penetration in Aqp4 KO mice is generally observed across the anterior-posterior extent of the cortex. Indeed, Figure A.3d shows that BDA distribution in Aqp4 KO cortex is broadly compromised. To evaluate the penetration depth of BDA, we calculated the depth at which the signal decays to the half-maximum intensity (Figure A.3d). The analysis showed that BDA penetration into the depth of cortex is significantly shallower in Aqp4 KO mice for a wide extent of the anterior-posterior axis.

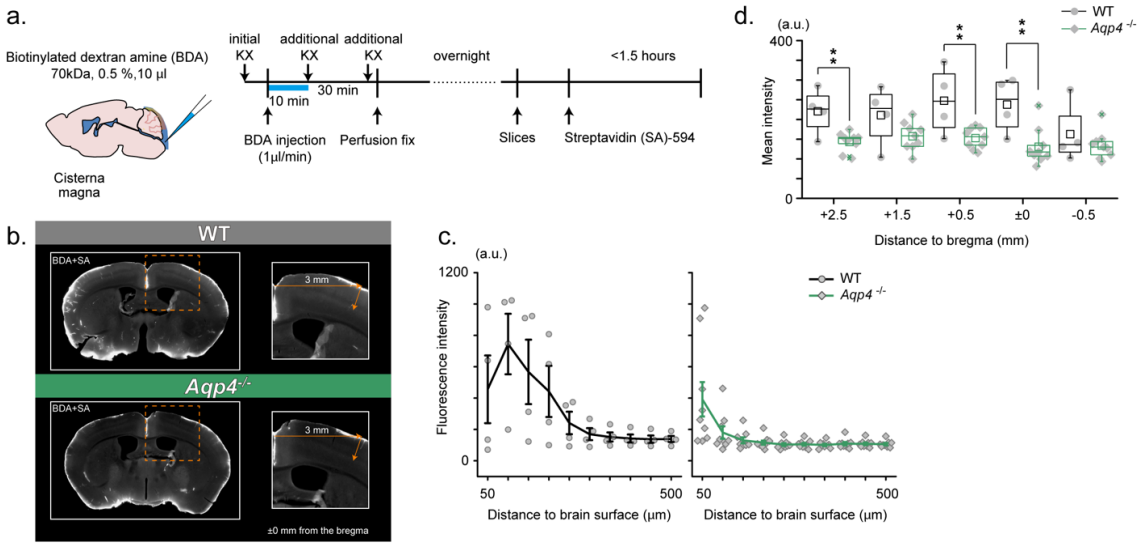

Figure A.3: RIKEN: Aqp4-/- mice display compromised CSF tracer infiltration under ketamine-xylazine anesthesia

(a). Schematic diagram for CM injection of BDA tracer (left) and experiment schedule (right). (b). Examples of SA-enhanced BDA distribution 30 min after CM injection. Slices at an anterior-posterior position of bregma are presented for WT (upper) and Aqp4-/- (lower) mice. Depth profile is calculated for the cortical position 3 mm lateral to the midline. (c) Mean depth profiles of SA-enhanced BDA signals for WT (black, N = 4) and Aqp4-/- (green, N = 9) mice. (d) Mean SA-enhanced BDA signal intensities (3 mm lateral to the midline, depths 0–800 µm) along anterior-posterior positions for WT (black) and Aqp4-/- (green) mice. Shades and error bars represent SEM. *p<0.05, **p<0.01, t-test.

UNC: CSF tracer influx is decreased in Aqp4 KO mice compared to background strain controls and wildtype mice.

We assessed the reproducibility of the experiments performed in Smith et al(Smith et al., 2017) by using the same Aqp4 KO mouse line but employing the original methodology reported by Iliff et al(Iliff et al., 2012). In order to determine if the background strains of the different Aqp4 KO lines have an effect on CSF inflow, we included both CD1 and C57BL/6 controls. We compared the intraparenchymal entry of Alexa Fluor 647-conjugated bovine serum albumin (66 kDa, BSA-647) delivered into cisterna magna of ketamine/xylazine-anesthetized mice. Thirty minutes after the injection, the brains were harvested, and tracer distribution evaluated in coronal sections as described previously(Iliff et al., 2012). Parenchymal distribution of tracer showed a significant reduction in Aqp4 KO mice compared with both CD1 mice (Aqp4+/+) and wildtype C57BL/6 (WT) mice (Figure A.4a-b). No significant difference in global tracer influx was seen between the two control groups. To evaluate if CSF influx was globally decreased or only limited to a particular brain region, we analyzed sections at different anterior-posterior coordinates as analyzed in Smith et al (Figure A.4c)(Smith et al., 2017). Differences in CSF influx between Aqp4 KO and controls was most notable in coronal sections anterior to bregma (Figure A.4d), perhaps reflecting that these sections include the cortical segment of the middle cerebral artery, a main site of CSF influx. Regional quantification showed that this difference was the result of decreased tracer penetration in the hypothalamus and areas of the basal forebrain (Figure A.4e-f). Interestingly, CSF tracer entry along the ventral and lateral cortex was highest in the WT compared to the Aqp4+/+ control (Figure A.4f) suggesting possible strain-dependent differences. We conclude that it is possible to replicate the original findings presented in Iliff et al. in the mouse line reported by Smith et al. when using similar methodology.

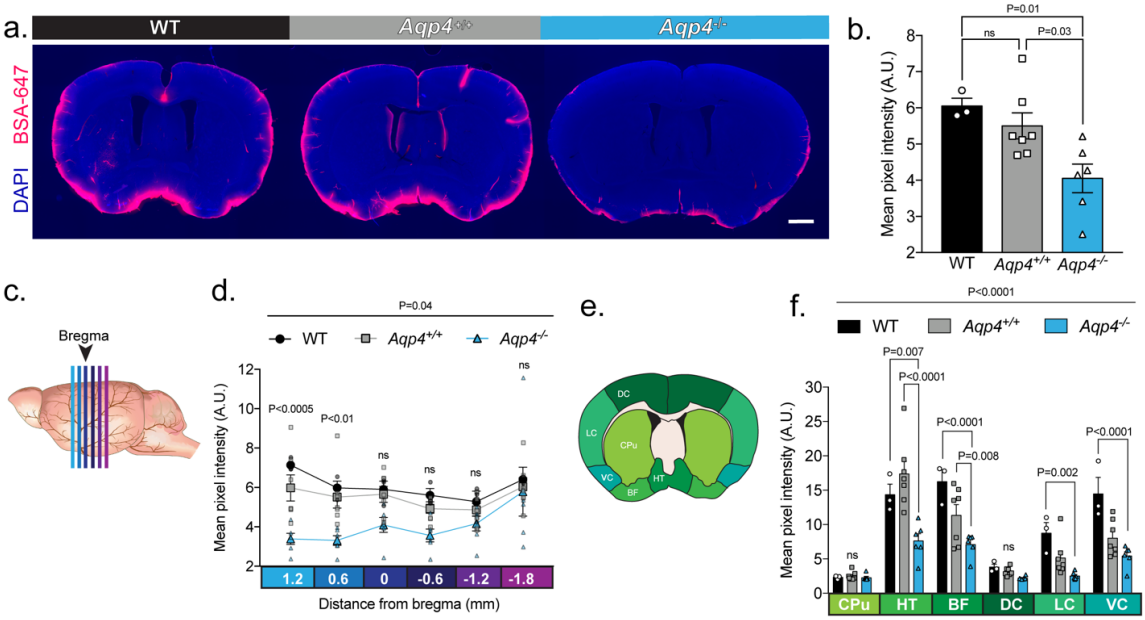

Figure A.4. UNC: CSF tracer influx is decreased in Aqp4 KO mice.
(a) Coronal sections from a C57BL/6 wildtype mouse (WT), CD1 background strain control (Aqp4+/+), and Aqp4 KO mice (Aqp4-/-) showing a fluorescent CSF tracer, BSA-647 and co-labeling with DAPI. Scale bar: 1mm (b) Mean pixel intensity in arbitrary units (A.U.) for six brain sections of each mouse for all three groups. n = 3 (WT), 7 (Aqp4+/+), 6 (Aqp4-/-). One-way ANOVA Tukey's multiple comparisons test, Interaction term: P = 0.0110, F = 6.512, ns: not significant. (c) Diagram showing the anterior-posterior range of the quantified coronal sections relative to bregma from (b). (d) Quantification of the slices shown in (c) +1.2 to -1.8 mm from bregma. Repeated measures two-way ANOVA with Tukey's multiple comparisons test, Interaction term: P = 0.038, F = 2.085, P values shown are comparisons of WT and Aqp4+/+ vs. Aqp4-/-. (e) Diagram depicting the ROIs included in the regional analysis of brain slices at +0.6 mm from bregma. CPu: caudoputamen; HT: hypothalamus; BF: basal forebrain; DC: dorsal cortex; LC: lateral cortex; VC: ventral cortex. (f) Mean pixel intensity of brain regions shown in (e) for coronal sections +0.6 mm from bregma. Repeated measures two-way ANOVA Tukey's multiple comparisons test, Interaction term: P < 0.0001, F = 8.109. Data is presented as mean ± SEM.

URMC: Cerebrospinal fluid entry to brain occurs along the glymphatic pathway and is facilitated by the presence of AQP4 water channels.

To evaluate the entry pathways of CSF to the brain we infused Alexa 647-conjugated bovine serum albumin (BSA) and a Texas Red 3 kDa dextran into the cisterna magna of anesthetized WT and *Aqp4* KO mice. In vivo transcranial optical imaging (Plog et al., 2018) of the far-red BSA-647 showed more CSF influx in the WT compared to the KO (Figure A.5a, b). Tracer evidently entered the brain parenchyma through a network of perivascular spaces of the large cerebral arteries on the pial surface. More tracer could be found on the dorsal cortical surface of WT mice compared to *Aqp4* KO mice. After 30 min, brains were extracted and immersion-fixed. The tracer distribution was quantified in coronal sections of both WT and *Aqp4* null mice. The KO mice had less influx for both the 3kDa dextran and the 66 kDa BSA compared to the WT (~32.7% and ~47.06%, respectively), despite the 22x difference in molecular weight (Figure A.5c-e). In a replicate experiment where the injection volume and injection rate was half of the previous, AQP4 deletion also reduced CSF entry through the glymphatic pathway by ~42.4% (Figure A.5f, g). The relative suppression of CSF tracer influx observed is comparable across previously reported findings, despite use of different tracer molecules and injection paradigms (Iliff et al., 2012). The depth of tracer penetration from the cortical surface was quantified using a similar approach to that reported in Smith et al (Figure A.5f, h)(Smith et al., 2017). Tracer penetration into brain was found to be ~2-fold higher in the WT than in the KO mice (Figure A.5i). To ensure that the mice were in fact knockouts, mice were genotyped using qPCR for both the *Aqp4* locus (Figure A.5j) and the excision sequence (Figure A.5k). The results confirmed that all mice were either homozygous for the *Aqp4* locus ($Aqp4^{+/+}$) or were homozygous knockouts ($Aqp4^{-/-}$) possessing no copies of exon 1-3 of the *Aqp4* gene.

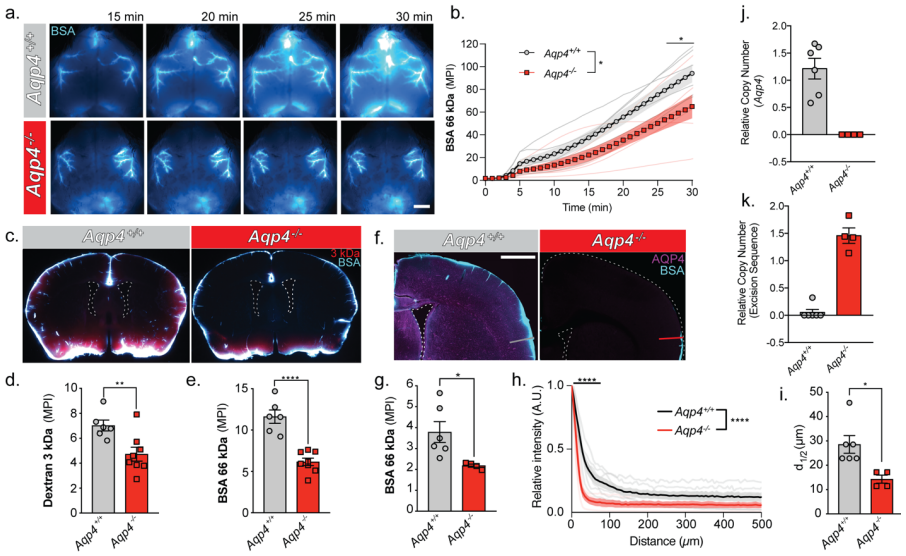

Figure A.5. URMC: Glymphatic influx of CSF tracer is facilitated by AQP4.
(a) Representative images from an in vivo transcranial optical imaging experiment of a WT control mice (Aqp4+/+) and Aqp4 KO (Aqp4-/-) mice starting at 15 min after intracisternal delivery of 10 µl (2 µl/min) of a 66 kDa fluorescent tracer, BSA-647. Scale bar: 2 mm. (b) Mean pixel intensity (MPI) of BSA-647 over a 30 min experiment, imaging was started at the beginning of the injection. Two-way repeated measures ANOVA with Sidak's multiple comparisons test, overall model *P=0.0329, multiple comparisons *P<0.05; n=6-7/group. (c) Coronal sections collected 30 min after intracisternal injection of two varying molecular size tracers, 3 kDa Texas Red dextran and BSA-647. Mean pixel intensity for a (d) 3 kDa dextran and (e) BSA from six coronal sections between +1.2 and -1.8 mm from bregma for each animal. Two-tailed unpaired t-test, **P=0.0097, ****P<0.0001; n=6-8/group. (f) Coronal section from an Aqp4+/+ mouse stained and imaged for AQP4 (magenta) and BSA-647 tracer (cyan). (g) Mean pixel intensity from a replicate experiment quantified the same as (e). Two-tailed unpaired t-test, *P=0.0335, n=4-6/group. (h) Mean tracer penetration depth profiles normalized to the fluorescence at the pial surface of a coronal section at bregma from the set of experiments displayed in (g). The line was placed orthogonal to the cortical surface at the most dorsal position where tracer could be found at the pial surface (f). Tracer depth in the WT mice was measured at the same position as the KO mouse. Two-way repeated measures ANOVA with Sidak's multiple comparisons test, overall model ****P<0.0001, multiple comparisons ****P<0.0001, n=4-6/group. (i) Cortical depth at which the fluorescence at the surface decreases by half for the profiles in (h). Two-tailed unpaired t-test, *P=0.0161, n=4-6/group. (j) Relative copy numbers of the Aqp4 gene locus and the excision sequence (k) showing successful deletion of Aqp4 exon 1-3. RCN was quantified by qPCR for mice used in (g). Data expressed as mean ± SEM.

OHSU: Reduced glymphatic CSF influx in Snta1 KO mice with loss of polarized expression of AQP4 in vascular endfeet of astrocytes

To assess the role of perivascular astrocytic localization of AQP4 in mediating CSF flux into the brain parenchyma, we utilized the *Snta1* KO mouse line. These mice lack expression of the adapter protein α-syntrophin, which links AQP4 to the dystrophin associated complex and is critical for maintenance of the perivascular localization of AQP4. Immunolabeling of AQP4 illustrates the loss of AQP4 perivascular localization in the *Snta1* KO mice (Figure A.6a, b). Higher magnification imaging reveals that, while perivascular localization is lost, widespread AQP4 expression is still detectable by immunofluorescence, consistent with a previous characterization of the mouse line (Figure A.6a, b insets (Neely et al., 2001)). We next sought to determine if parenchymal CSF influx kinetics are altered when perivascular AQP4 localization is lost. Here we used DCE-MRI to measure the influx of the contrast agent gadoteridol (Gad) into brain parenchyma after intracisternal injection. We performed serial T1-weighted imaging at 10-minute intervals following administration of the contrast agent (Figure A.6c-h). At 30 minutes after the start of the injection, elevated levels of Gad were detected in both WT mice and *Snta1* KO mice, particularly along the ventral surface of the brain (Figure A.6e-f), but by 60 minutes Gad signal within the parenchyma of *Snta1* KO mice was significantly reduced compared to wild type mice (Figure A.6g,h,n). Regional assessment revealed decreased signal in *Snta1* KO mice across brain regions, which was most pronounced in cortex and hippocampus compared to subcortical brain regions and within the ventricles (Figure A.5j-m). Taken together, these data illustrate a role for α-syntrophin in facilitating CSF-ISF exchange and, by extension, support the reported role of AQP4 in this process. Furthermore, these results suggest that the perivascular localization of AQP4 contributes to the kinetics of CSF influx into the brain parenchyma.

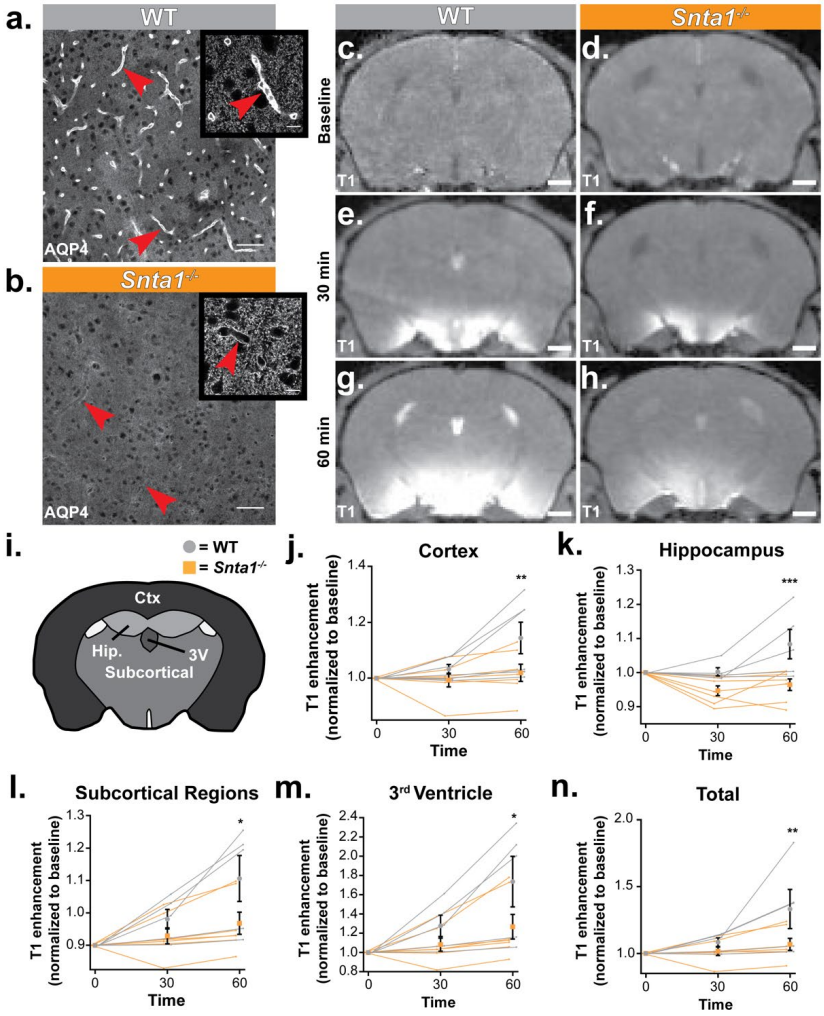

Figure A.6. Deletion of the adapter protein α-syntrophin impairs AQP4 perivascular localization, and CSF influx into the brain parenchyma.

Dynamic contrast enhanced magnetic resonance imaging (DCE-MRI) was acquired on a 11.75 preclinical MRI scanner, and was used to characterize the effect of α-syntrophin deletion on gadoteridol influx into the brain. Representative images of AQP4 perivascular localization in wild type mice (a), and the loss of perivascular localization of AQP4 seen in the Snta1-/- mice (b). Scale bar: 50 µm, inset scale bar: 10 µm. (c-h) Coronal slice of T1-weighted images acquired by DCE-MRI demonstrate the reduced influx of gadoteridol contrast agent into the parenchyma in Snta1-/- mice relative to wild type mice at 30 and 60 minutes. Scale bar: 1mm. (i-n) Quantification of T1 weighted signal in various brain sub regions normalized to baseline at each time point. Traces for each individual animal are presented (lines) along with the summary statistics (mean ± SEM, 2-way ANOVA). WT n=5, ASYNKO n=7. CTx = cortex (P = 0.0035) Hip = hippocampus (P = 0.0003) Subcortical = subcortical regions (P = 0.0185) 3V = 3rd Ventricle (P = 0.0284) Total (P = 0.0085).

Insertion of an injection pipette in striatum is linked to a global suppression of CSF influx

Smith et al. (Smith et al., 2017) questioned the existence of bulk flow within the brain parenchyma based on imaging tracer dispersion following local injections in cortex or striatum. The tracers were delivered by glass pipettes inserted through a cranial burr hole. The surgical procedure associated with insertion of glass pipettes is obviously traumatic. Since acute and chronic traumatic injury markedly suppress CSF influx (Iliff et al., 2014), we questioned the validity of studying interstitial tracer dispersion using an invasive approach. To this end, we compared CSF tracer (BSA-647, 66 kDa) influx in 3 groups of mice anesthetized with KX: (i) controls with no surgery beyond CM injection, (ii) insertion of a glass pipette (12 μm diameter tip) and injection of 20 nl (4 nl/min) HiLyte 488-amyloid-$\beta_{1\text{-}40}$ in aCSF, or (iii) same as group 2 but HiLyte 488-amyloid-$\beta_{1\text{-}40}$ was not added to the 20 nl aCSF (Figure A.1f). One hour later, the BSA-647 tracer was injected into cisterna magna and allowed to circulate for 1 hr before the brain was harvested, immersion-fixed, and the distribution of BSA-647 analyzed in coronal brain sections (Figure A.7a-b). The analysis showed that the two groups exposed to invasive surgery exhibited markedly suppressed CSF tracer influx compared with the control group (Figure A.7c). The suppression of CSF tracer influx in animals with insertion of the glass pipettes was symmetric with no difference in tracer influx between the ipsilateral and the contralateral hemisphere ($P > 0.05$, 3-5 slices per animal, $n = 7$, Wilcoxon rank-sum test). These observations show that invasive procedures acutely suppresses brain-wide CSF influx and that tracer injection should not be used in the study of the glymphatic system.

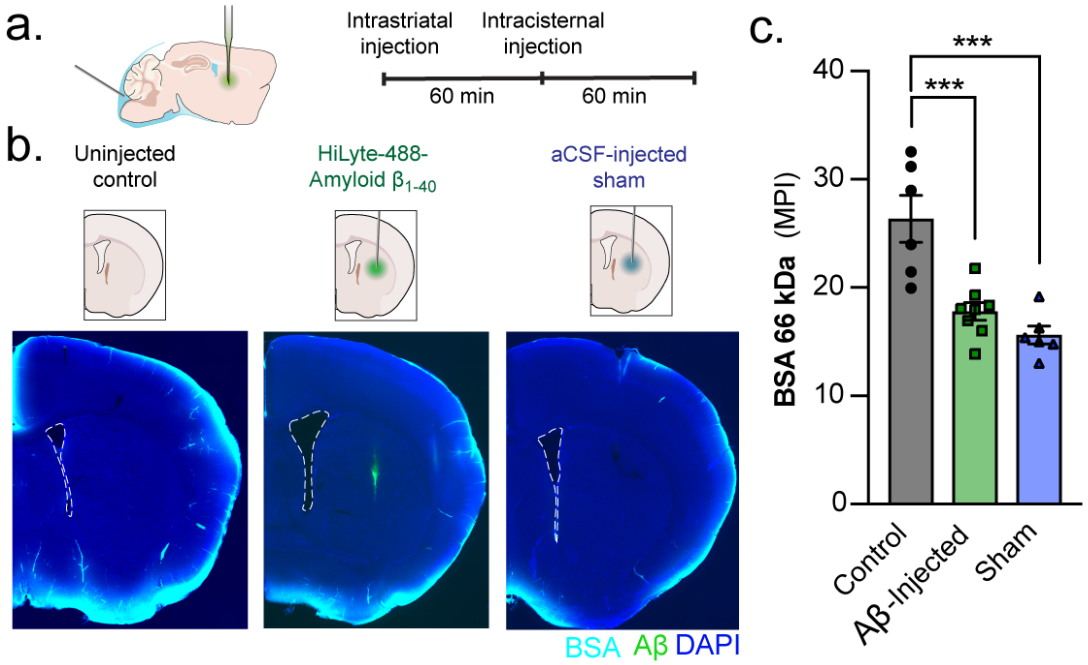

Figure A.7. A unilateral intrastriatal injection reduces global glymphatic function. (a) KX-anesthesized mice received an injection into striatum. After injection, the glass capillary was slowly removed and the skull sealed with silicone elastomer. One hour later, mice received an intracisternal injection of a 66 kDa BSA-647 tracer and brains were removed and drop fixed 60 min later. (b) Control mice only received the intracisternal injection but not the intrastriatal injection. Mice that received an intrastriatal injection were injected with either HiLyte 488-amyloid-β1-40 or an aCSF sham. (c) Global glymphatic tracer influx was quantified from a total of six coronal sections between +1.2 and -1.8 mm from bregma for each animal. Ordinary one-way ANOVA posthoc Tukey's multiple comparisons test, Control vs. Aβ-injected: ***P=0.0006; Control vs. Sham: ***P=0.0001; n=6-8/group.

Meta-analysis

A potential cause of conflicting results could be due to varying methodology used in each study. We used meta-analysis to evaluate this heterogeneity and better understand the relationship between AQP4 and CSF-ISF transport using all the available literature that evaluated tracer injections in global *Aqp4* KO and wildtype mice. Studies were largely divided into two types: 1) intracisternal and 2) intracerebral tracer injections (Figure A.8a-b), a separate meta-analysis was conducted for each of these two main experimental approaches.

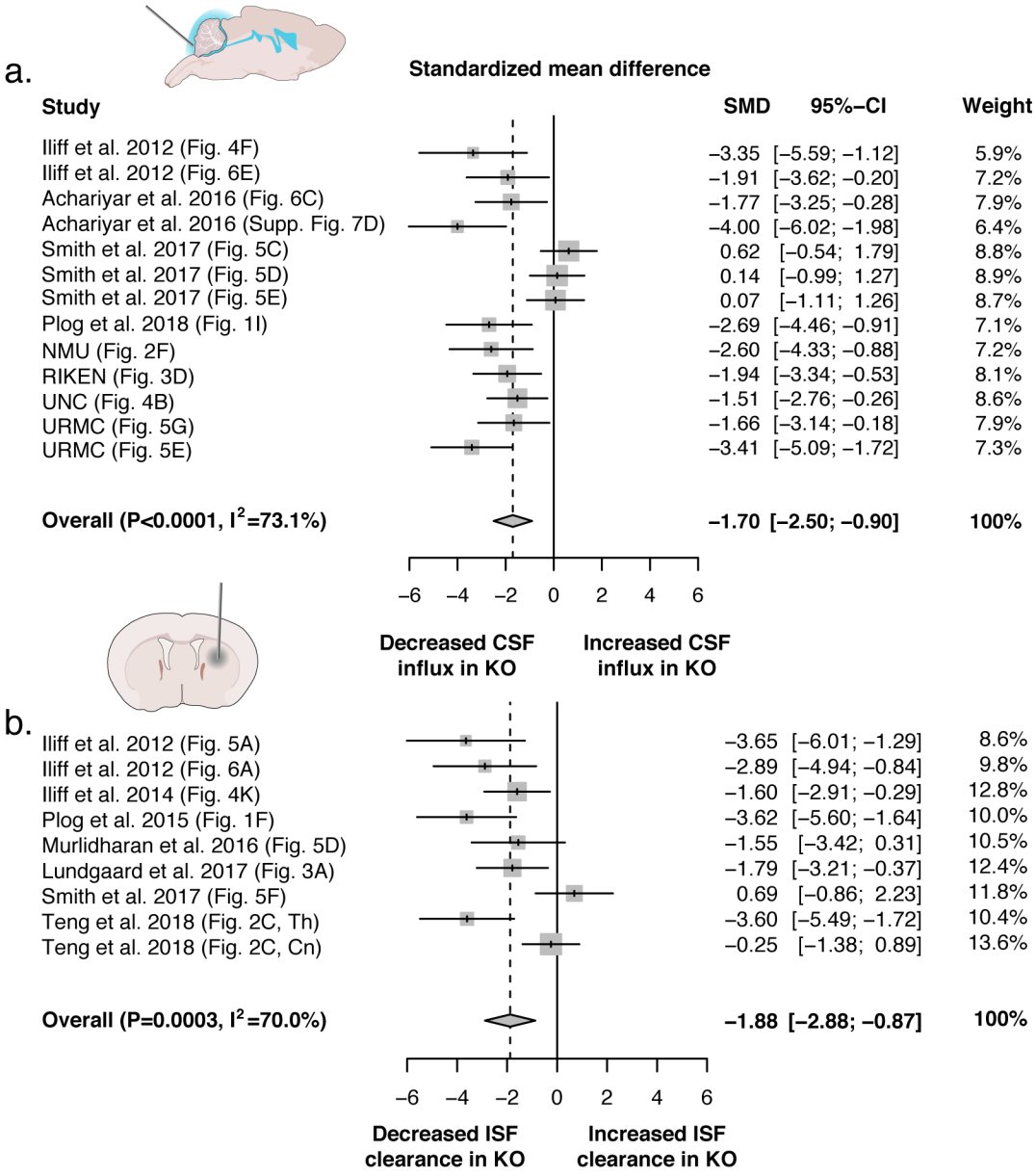

Figure A.8. Evidence evaluating the role of AQP4 in CSF influx and ISF efflux. (a) Meta-analysis from experiments that delivered either fluorescence- or radio-labeled tracers into the cisterna magna of both *Aqp4* KO and wildtype rodents. (b) Meta-analysis from studies that delivered intracerebral tracers to evaluate clearance or transport of tracers out of the brain. P value is from the overall random effects model. Data in forest plots presented as standardized mean difference (SMD) with a 95% confidence interval (CI). Th: thalamus; Cn: caudate nucleus.

1) *CSF Influx*: The search for studies that delivered tracers into the cisterna magna to evaluate CSF entry yielded a total of 13 eligible independent datasets from 6 different

laboratories. Experiments were done in a total of 144 mice (92.4%) and rats (7.6%) from 5 different *Aqp4* KO lines (UIO: 50.7%; UCSF mouse: 25.7%; RIKEN: 9.03%, UCSF rat: 7.64%, and NMU: 6.94%) with a wide age range (6-24 weeks), the age of the rat line was not reported. Results were obtained using three different anesthetic protocols (ketamine/xylazine: 68.8%; tribromoethanol: 24.3%; chloral hydrate: 6.94%) and it was not possible to determine sex due to variable reporting. Experiments consisted of the delivery of fluorescently- (86.1%) and radioisotope-labeled (13.9%) tracers that ranged in size (4.5-70 kDa) and concentration. Tracer delivery varied in total volume (5-10 µl) and the injection rate (1-2 µl/min) while experiment duration ranged from 15-30 min. Standardized mean differences (SMD) were used in the meta-analysis to account for different outcome measures (e.g. fluorescence intensity, thresholded area, % injected radiation), and demonstrated a significant overall decrease in tracer entry in *Aqp4* KO mice compared to controls (SMD with 95% confidence interval: -1.70 [-2.49; -0.90]; P< 0.0001) with a high degree of interstudy heterogeneity (I^2=73.1%; P<0.0001; Figure A.8a). Leave-one-out and meta-regression sensitivity analyses were used to explore the sources of heterogeneity. As expected based on the direction and magnitude of the effect estimates reported in the studies, the high degree of heterogeneity was primarily caused by three datasets extracted from Smith et al. We could not confidently determine from the text of these studies whether these experimental figures were based on separate, independent experiments, or whether they were data collected in the same set of mice. Due to this uncertainty, we conducted leave-one-out analyses that would recapitulate all possible scenarios. The analysis showed that when these data sets were excluded, there was a reduction in heterogeneity (I^2 =65.7%, 70.3%, and 71.4%; P = 0.0007, P = 0.0001 and P < 0.0001). When all three data sets from this publication were excluded, the heterogeneity becomes non-significant (I^2 = 0.0%, P = 0.4622). Using meta-regression to further explore sources of heterogeneity, we tested whether the: KO line, age, anesthesia type, tracer properties, injection paradigm, experiment duration, and detection method were significant covariates. The KO line used (P=0.0001, Test of Moderators), the age of the mice (P=0.0006), the anesthetic protocol (P<0.0001), and the injection rate (P<0.0001) explained a significant proportion of the observed variance between the datasets. The variables that explained the largest proportion of heterogeneity were

anesthesia type and injection rate. The three data sets that reported null results used tribromoethanol (Avertin), an anesthetic that was not used in any other studies (all of which found a significant association). The same three data sets were also the only ones to report variable injection rates (10 µl delivered over 5-7 min) in comparison with the remaining studies that used exact injection rates. Thus, it is possible that the choice of anesthesia type and injection rate could explain the heterogeneity. Animal age was also a significant source of heterogeneity, accounting for 85.28% of the variance between studies. This may be in part explained by the fact that two out of the three data sets that demonstrated no association were completed in mice that were older than the mice used in the majority of other studies and reported the largest age range (12-24 weeks). Although it is not possible to determine the exact role that these covariates played in the observed results, both anesthesia and aging have been shown to modify the degree of intracisternal tracer entry, providing another potential explanation for the observed heterogeneity (Benveniste et al., 2017; Kress et al., 2014). Similarly, the heterogeneity stemming from the KO line may also be explained by the fact that the majority of UCSF KO mice (72.9%) were in the null studies. Interestingly, the fourth study (UNC, this report) that utilized the UCSF KO mouse line, but an alternate anesthetic (ketamine/xylazine) observed a significant effect. Unfortunately, due to low study number we were unable to include two covariates (e.g. anesthesia type and KO line) in the meta-regression to test this interaction. Additional covariates including tracer properties, the injection paradigm, and the detection method were not significant sources of heterogeneity suggesting that multiple experimental methodologies should be able to observe an effect between KO and control.

2) *ISF Efflux*: There were 9 eligible studies produced by 4 independent research groups that injected tracers or contrast agents into the brain of *Aqp4* KO or wildtype rodents in order to evaluate brain clearance or ISF efflux. These experiments were conducted in a total of 87 rodents from both mouse (72.4%) and rat (27.6%) KO lines. There were 2 murine lines (UIO: 57.5%; UCSF: 14.9%) and 1 rat line (Beijing: 27.6%) generated by 3 separate groups. Age of the mouse lines ranged broadly (0-24 weeks) while the age of the rat line could not be confirmed but a weight range of 250-300g was reported. Four anesthetic protocols were used for these experiments (ketamine/xylazine:

57.5%; hypothermia: 6.9%; tribromoethanol: 8.0%; sodium pentobarbital: 27.6%). Fluorescence-conjugated tracers (14.9%), radio-labeled (57.5%) tracers, and gadolinium-based contrast agents (27.6%) that ranged in size (0.18-45 kDa), concentration, and where they were delivered within the brain (striatum: 40.2%; cortex: 39.1%; thalamus: 13.8%; lateral ventricle: 6.9%). Tracer delivery varied in total volume (0.02-3 µl) and injection rate (0.017-3 µl/min), differing based on the injection site or whether the experiment was done in mice or rats. Experiment durations ranged between 45-240 min and one of the studies (Smith et al.) did not report this. Results from the overall meta-analysis showed a significant decrease in the transport of the injected substance in *Aqp4* KO mice relative to controls (-1.88 [-2.88; -0.87]; P= 0.0003) with high heterogeneity (I^2=70.0%, P=0.0008; Figure A.8b). Similar to the previous model, leave-one-out analysis of the two null datasets reduced the heterogeneity (I^2 = 60.1%; P = 0.0143 and I^2 = 65.3%; P = 0.0053, respectively) and removing both datasets made the heterogeneity non-significant (I^2 = 17.2%; P = 0.299). The same covariates used in the first model were used for meta-regression analysis, in addition to an injection site variable. Meta-regression was unable to identify significant sources of heterogeneity; most likely because of two datasets from Teng et al. that found a difference in thalamus, but not in striatum, in the same rat line using identical methodology(Teng, 2018). Despite the potential biological significance of this, the study was the only one to use rats, MRI as the detection method, and had an experiment duration that was 4-fold longer than the other studies. Therefore, we decided to run a reduced model on all available mouse experiments using fluorescence or radioactivity detection methods. The meta-analysis was still highly significant and showed decreased clearance in the *Aqp4* KO mouse lines (-1.92 [-3.02; -0.82]; P= 0.0006) with a lower degree of heterogeneity (I^2=64.1%, P=0.0103). The KO line used (P=0.0205), age (P=0.0075), the anesthetic protocol (P=0.0075), the injection rate (P=0.0056), the experiment duration (P=0.0075), and the detection method (P=0.0205) explained a significant proportion of the observed variance between the datasets. Similar to previous results, tribromoethanol again seemed to function as a proxy for the null study from Smith et al. since none of the others used this anesthetic. The mouse KO line from UCSF explained a significant proportion of heterogeneity compared to the other lines, likely because the null dataset accounted for

half of the studies that used this line. Age of the experimental animals was also a significant source of heterogeneity and can be explained by the wide age range (0-24 weeks) found between the studies but the lack of specific age reporting could also potentially explain this. Injection rate accounted for the largest proportion of heterogeneity in this analysis. The injection rate used by Smith et al. (5 × 100 ms pulses at 1 Hz and 10 psi), was highly significant in the meta-regression model compared to the reference injection rate (0.017 µl/min, P = 0.0007), whereas all other injection paradigms were not significantly different. The Smith paradigm was therefore the driver of the explanatory value of the injection rate covariate in the meta-regression model. Similar to anesthesia type, this variable also functioned as a proxy for the null study since all other datasets reported an exact volumetric injection rate. The reported injection protocol was used for experiments performed in both mice and rats despite different injection volumes (~20 nl vs. 30,000 nl) suggesting that the rate varied significantly between experiments. The time the tracer was allowed to circulate after the injection (experiment duration) was also a highly significant source of variation between studies. The experiment duration that accounted for all the heterogeneity was the unreported time from the null study. Only one separate study evaluated a time point that did not report a significant difference between KO and control (30 min; Iliff et al. 2012). However, this study did report a difference at 60 min after injection, so it is possible that if Smith et al. used shorter experimental durations this could account for the observed heterogeneity (Iliff et al., 2012). The detection method (i.e. fluorescence, radioactivity, and MRI) used was also found to be a significant source of heterogeneity. The largest contributor to heterogeneity were fluorescent detection methods, mostly likely due to the fact that the study that obtained a null result used this approach despite most studies using radio-labeled tracers. The remaining covariates: species, tracer properties, the injection volume, and the injection site were not significant sources of heterogeneity in this analysis.

Discussion

This study evaluated the role of the astrocytic water channel AQP4 in the dispersion of fluorescent tracers or contrast agents by five independent groups. Four of the groups (NMU, RIKEN, UNC, URMC) injected CSF tracers in cisterna magna and

compared the influx of the tracer in coronal sections prepared from *Aqp4* KO and WT mice, whereas the OHSU group injected contrast agent in cisterna magna and then compared CSF transport by DCE-MRI in *Snta1* KO and WT mice. Compilation of data from the six independently-conducted experiments documented that deletion of *Aqp4* (*Aqp4* KO mice) or mis-localization of AQP4 (through *Snta1* gene deletion) suppressed influx of CSF tracers or contrast agents. In fact, a meta-analysis that included all reports published to date came to the same conclusion (Figure A.8). Thus, our observations provide strong and concordant support for the glymphatic model in which AQP4 supports the perivascular influx of CSF and efflux of ISF (Iliff et al., 2012). Supporting evidence of this has also been shown in humans; two independent single nucleotide polymorphism (SNP) variant association studies identified multiple SNPs in the *Aqp4* gene that were associated with cognitive decline in Alzheimer's disease (AD) and increased Aβ burden in humans with reduced sleep quality (Burfeind et al., 2017; Rainey-Smith et al., 2018). A separate study by the OHSU group also found that reduced perivascular polarization of AQP4 was a significant predictor of AD status in postmortem human brains (Zeppenfeld et al., 2017).

Independent replication studies of biological phenomena are essential, both to confirm novel experimental findings, as well as to extend and refine initial observations and interpretations. The original report from the URMC group on the glymphatic system showed that deletion of astrocytic water channels suppressed both the influx of CSF tracers injected into the cisterna magna and the efflux of tracer infused directly into striatum (Iliff et al., 2012). Follow-up of that finding by the NMU group documented that Aβ accumulation and cerebral amyloid angiopathy were significantly increased in a double-hit murine model with *Aqp4* deletion and Aβ over-expression (Xu et al., 2015). The URMC/OHSU groups subsequently reported that deletion of *Aqp4* aggravated neurofibrillary pathology following TBI (Iliff et al., 2014), whereas the UNC group showed that deletion of *Aqp4* significantly reduced clearance of AAV (Murlidharan et al., 2016). Thus, these reports conceptually address the same idea, although the replications entailed different approaches and methodologies. The dissenting report from Dr. Verkman's laboratory belongs to the rarer category of replication studies, which (as their title states) seeks to test directly the glymphatic hypothesis and the AQP4-dependence of

solute transport in brain. Since their study was intended to gauge the veracity of the original findings, it should be expected that it follow the experimental design and data analysis of the original study (Picho et al., 2016), and their methodology should be presented in sufficient detail to allow the reader to assess the fidelity of their replication (Brandt et al., 2014). However, Smith et al. (Smith et al., 2017) failed to meet these requirements in several key respects. First, their methodologies deviate from the original report in critical ways. In particular, Iliff et al. used ketamine/xylazine (KX) anesthesia rather than tribromoethanol (Avertin) (Iliff et al., 2012). Xylazine is an α_2 adrenergic agonist that blocks release of norepinephrine from the locus coeruleus projections across the neuraxis. This is an important point, because norepinephrine has been identified as the key humoral regulator of glymphatic solute transport (Xie et al., 2013), and norepinephrine attenuates glymphatic function. However, with the exception of the photo-bleaching experiments carried out only in WT mice, Smith et al. (Smith et al., 2017) anesthetized their mice with Avertin, an injectable anesthetic with an unknown mechanism of action. Avertin is not approved for use in several European countries and is restricted to terminal procedures in the US (Arras et al., 2001; Meyer and Fish, 2005). The importance of the anesthetic agent in the present context was first highlighted by Groothius et al., (Groothuis et al., 2007), who reported that parenchymal solute efflux was 100-fold slower in rats anesthetized with pentobarbital than those that received ketamine/xylazine. Anesthesia-dependent effects were also noted by Benveniste et al., that reported a marked difference in influx of contrast agents in isoflurane-anesthetized animals versus low-dose isoflurane plus dexmedetomidine (an α_2 agonist) (Benveniste et al., 2017). The importance of anesthesia is supported by the experiments reported here: The UNC group used ketamine/xylazine anesthesia and observed AQP4-dependent glymphatic transport (Figure A.4), despite using the same *Aqp4* KO mouse line as in the Smith et al. (Smith et al., 2017). In addition, we note that key methodological details, such as the injection approach and rate, anesthesia, or the age of the animals were not provided for data collected in rats in Smith et al. Neither did the investigators assess whether *Aqp4* was deleted in CNS albeit this was the first report utilizing *Aqp4* KO rats. In fact, no such data have been published so far to our knowledge (Smith et al., 2017). For these reasons, the present study is not a replication study of Smith et al (Smith et al.,

2017). Instead we used the methodology reported in Iliff et al., 2012 (Iliff et al., 2012) and further optimized it in subsequent studies (Iliff et al., 2013a; Kress et al., 2014).

It is also important to note that the recovery period that follows general anesthesia differs from the awake state. A recent study reported that increasing anesthesia concentration decreased glymphatic function (Gakuba et al., 2018), as opposed to the original finding that the glymphatic system is maximally active during natural sleep or anesthesia (Xie et al., 2013). However, the recent study injected CSF tracers under inhalation anesthesia followed by a short recovery period (Gakuba et al., 2018). This is not a valid approach, because brain function does not immediately normalize after general anesthesia: awakening is associated with cognitive disturbances (Numan et al., 2017; Paredes et al., 2016; Su et al., 2016) and inhaled anesthetics in particular are linked to a high rate of delirium upon emergence from anesthesia (Brioni et al., 2017). Close evaluation of the imaging in Gakuba et al. shows a failed intracisternal injection, as enhancement of contrast agent is evident in the paraspinal muscles and extracranial spaces (Gakuba et al., 2018). In our experience, experimenter error during cisterna magna injections is a significant source of variability. Thus, careful consideration of the anesthesic regimen and long periods of post-anesthesia recoveries are essential when studying the glymphatic system.

The initial study articulating the glymphatic hypothesis confirmed seminal work by Cserr and colleagues that interstitial tracers are cleared from brain tissue at rates that are independent of molecular weight (Cserr et al., 1981; Iliff et al., 2012). While these early studies support the role of bulk flow in the clearance of interstitial solutes from the brain interstitium, they lacked the spatial resolution necessary to resolve whether bulk flow was occurring throughout the entire brain interstitium or was restricted to a subset of compartments permissive to flow. A large body of indirect experimental evidence supports the occurrence of bulk flow in the periarterial space in the brain (see reviews by Hladky and Barrand (Hladky and Barrand, 2014) and Nicholson and Hrabetova (Nicholson and Hrabetova, 2017)). Smith et al. (Smith et al., 2017) themselves provide such evidence, stating that “occasionally, when the injected dextran entered the perivascular space of vessels near the injection site, both large and small dextrans traveled substantial distances away from the injection site” (Smith et al., 2017). There is

also indirect evidence that this flow is peristaltic, propelled by pulsations of the arterial walls (e.g., Hadaczek 2006, (Hadaczek et al., 2006a)). This mechanism has recently been confirmed by direct observations of pulsatile flow in periarterial spaces (Bedussi et al., 2018; Mestre et al., 2018b). Using two-photon microscopy and particle-tracking velocimetry, Mestre et al. gathered hundreds of thousands of velocity measurements at sampling rates up to 30 Hz over half hour experiments, mapping the perivascular flow in space and time in great detail: their results show that the flow pulses in synchrony with the heartbeat, is driven by pulsations of the arterial wall, and produces a net (average) flow in the same direction as the blood flow. This flow is in accordance with several earlier fluid-dynamic models and experimental studies (Bilston et al., 2003; Iliff et al., 2013b; Rennels et al., 1985; Schley et al., 2006; Wang and Olbricht, 2011), and with in vivo dynamic imaging studies, including MRI experiments in human subjects, demonstrating the rapid distribution of CSF tracers into and through the brain interstitium along peri-arterial routes (Eide and Ringstad, 2015; Iliff et al., 2013a; Ringstad et al., 2017). In addition to perivascular spaces, white matter tracts also serve as permissive routes for interstitial solute and fluid movement (Ohata and Marmarou, 1992; Rosenberg and Kyner, 1980).

As a consequence of the now well-established bulk flow along periarterial spaces, there must be an outlet for this directional flow: conservation of mass - as expressed by the continuity equation - demands that this volumetric flow must continue through other parts of the glymphatic system – i.e., in the neuropil and the perivenous spaces. Although the full volumetric net flow must pass through the neuropil, flow speeds will be lower there because of the much larger total cross-sectional area of the available extracellular flow channels, and due to the availability of the gap junction-coupled astroglial syncytium as an intracellular route for water and solute movement(Asgari et al., 2016). In fact, a meta-analysis that include the more than 200 *Aqp4* KO mice and rats studied so far added further support to the finding that glymphatic influx and efflux are both highly dependent upon AQP4 expression (Figure A.8). The meta-analysis identified the anesthesia protocol, wide age range of the experimental animals and the injection paradigm are potential causes for the conflicting data reported by Smith et al. However, it is important to note that glymphatic transport is affected by multiple pathways other than

AQP4. For example, the sleep-wake cycle (Xie et al., 2013), brain injury in the setting of trauma or ischemia (Iliff et al., 2014; Wang et al., 2017), exercise (He et al., 2017; von Holstein-Rathlou et al., 2018; Yin et al., 2018), amyloid-β accumulation and acute amyloid-β toxicity (Peng et al., 2016; Xu et al., 2015), omega-3 fatty acids (Ren et al., 2017), plasma osmolarity (Plog et al., 2018), and aging (Kress et al., 2014) are important regulators of glymphatic transport. How AQP4 on a cellular level facilitates CSF/ISF exchange remains to be firmly established. The primary role of AQP channels is to lower the driving forces for fluid transport across the plasma membranes (Verkman et al., 2017). AQP4 is highly enriched in astrocytic endfeet facing the perivascular space and thus strategically positioned for facilitate CSF exchange with interstitial fluid. Accordingly, loss of the polarized expression of AQP4 in reactive astrocytes lead to a reduction in parenchymal CSF tracer influx (Iliff et al., 2014; Kress et al., 2014). Moreover, deletion of AQP4 potentiated the increases in intracranial pressure in a murine model of hydrocephalus consistent with the notion that AQP4 supports and facilitates intraparenchymal fluid flow (Bloch et al., 2006).

The claim by Smith et al. (Smith and Verkman, 2018) that solute transport in the parenchyma is primarily driven by diffusion rather than convection (bulk flow) is based on their finding of a dependence of this transport on the size of the solute particles. They claim that diffusive transport depends strongly on particle size, whereas convective transport does not, so long as the ratio of the particle size to the pore or channel size is less than about 0.5. In support of this claim, they cite a single reference (Dechadilok and Deen, 2009), which does not actually support their claim, but instead shows a significant dependence of flow resistance on particle size for much smaller particles. The influence of solutes or suspended particles on flow through narrow channels is a complicated problem in hydrodynamics, entailing many factors, including solute concentration, electrical charge, shape of the particle, channel geometry, tortuosity, and possible obstructions (Nicholson and Hrabetova, 2017). Hence, it would require a very sophisticated theoretical model to evaluate the role of bulk flow in the transport observed experimentally by Smith et al (Smith et al., 2017). Their findings are in general agreement with recent modeling studies suggesting that at the smallest microscopic scales, encompassing small numbers of vessels and the interposed neuropil, diffusion is

sufficient to account for observed solute movement (Asgari et al., 2016; Holter et al., 2017; Jin et al., 2016). However, it is important to note that these findings do not exclude a contribution of bulk flow within the entire interstitium, and do not determine whether the experimental approaches used to detect flow on the microscopic scale are sufficiently sensitive to detect bulk flow occurring at very low flow rates. Also, the majority of the studies contradicting the glymphatic model are based on theoretical modeling and not experimental evidence(Asgari et al., 2016; Faghih and Sharp, 2018; Jin et al., 2016). We suspected that the surgical procedures required for intraparenchymal tracer injections utilized in Smith et al. (Smith et al., 2017) might suppress influx of CSF tracers. To formally test this potential caveat, CSF tracer influx was analyzed in mice in which a glass pipette was inserted in striatum 1 hr earlier (Figure A.7). The analysis showed that insertion of a glass pipette suppressed CSF tracer influx significantly and independently of intrastriatal injection of aCSF with or without HiLyte 488-amyloid-$\beta_{1\text{-}40}$ compared to non-surgical controls. We conclude that dispersion of tracers in CNS should not be studied using invasive procedures. Thus, as articulated by Holter et al. in their recent modeling study (Holter et al., 2017), there is a need to develop more appropriate technical approaches for evaluating slow interstitial bulk flow over long distances (Ratner et al., 2017), such as DCE-MRI in nonhuman primates or human subjects. Until then, the glymphatic model of CNS fluid and solute flow should properly include the rapid exchange of CSF with the brain ISF along perivascular spaces, with CSF principally entering along peri-arterial spaces and ISF draining towards the ventricular and CSF compartments along peri-venous pathways and along cranial and spinal nerves, supported by AQP4-dependent astroglial water transport. On this last element, the present findings from five independent groups do not concur with the negative findings reported by Smith et al. (Smith et al., 2017). Instead, our compiled data provides strong and consistent support for our claim that solute transport in the rodent brain is facilitated by the polarized expression of AQP4 in astrocytic endfeet.

Methods

Generation of transgenic mouse lines

NMU: *Aqp4* KO mice were generated by Dr. Fan Yan by targeted gene disruption as described previously (Fan et al., 2005). In brief, an AQP4 replacement targeting vector was constructed using the positive-negative selection cassettes derived from the vectors pPolII long neo bpA and pXhoMC1TK, containing the neoR and HSVtk genes, respectively. The targeting construct was linearized with NotI and introduced into E14K ES cells by electroporation. ES cell clones that were G418/gancyclovir-resistant were isolated, amplified, and screened for targeting fidelity using Southern blot analysis. Cells from two targeted clones were microinjected into CD1 blastocysts and implanted into pseudopregnant recipients (Fan et al., 2005). Five-month old *Aqp4* KO and WT mice were used in the present study.

RIKEN: *Aqp4* null/eGFP knock-in mice (SJL.Cg-Aqp4<tm1.1(GFP)Mysi>/MysiRbrc) were generated as described previously (Ikeshima-Kataoka et al., 2013). Briefly, knockout of AQP4 was accomplished by replacing the 250 nucleotides in exon 1 (corresponding to the region from Ser 18 to Thr 101) with eGFP cDNA and a PGK-neomycin cassette flanked by flippase recombination target sequences. The targeting vector was electroporated into TT2 ES cells derived from a C57BL/6 female and a CBA male. The PGK-neomycin cassette was removed by crossing with B6-Tg (CAG-FLPe) 37 (Kanki et al., 2006). The resultant mice were backcrossed with the SJL/J strain (Charles River, Japan) for more than 12 times (RIKEN CDB accession no. CDB0758K-1; http://www.clst.riken.jp/arg/mutant%20mice%20list.html). Both B6-Tg (CAG-FLPe) 37 and SJL.Cg-Aqp4<tm1.1(GFP)Mysi>/MysiRbrc> mice are provided by the RIKEN BRC through the National Bio-Resource Project of MEXT, Japan (accession no. RBRC01835 and RBRC06500, respectively).

UNC: The constitutive *Aqp4* KO mouse model was generated by Dr. Alan Verkman (Ma et al., 1997). In brief, *Aqp4* KO mice were generated on a CD1 background, following the construction of a targeting vector for homologous recombination of a 7-kb SacI AQP4 genomic fragment, in which part of the exon 1

coding sequence was deleted. All animal experiments reported in this study were conducted on *Aqp4* KO mice (B6/129), B6/129 controls, and wildtype C57BL/6 mice.

URMC: *Aqp4* KO mice were generated by Dr. Ole Petter Ottersen using GenOway technique, as described previously (Thrane et al., 2011). Their strategy involved cloning and sequencing of a targeted region of the murine *Aqp4* gene in a 129/Sv genetic background. Identification of a targeted locus of the *Aqp4* gene permitted the delete exons 1–3 to avoid any expression of putative splice variants. Hence, a flippase recognition target (FRT)-neomycin-FRT-LoxP–validated cassette was inserted downstream of exon 3, and a LoxP site was inserted upstream of exon 1 (Thrane et al., 2011). The mice were backcrossed for 20+ generations with C57BL/6N mice prior to experimentation.

OHSU: The *Snta1* KO mouse line was generated by Dr. Stanley Froehner (Adams et al., 2000), and was purchased through The Jackson Laboratory (*Snta1*^{tm1Scf}/J, *#012940*). In brief, exon 1 of the mouse *Snta1* gene was replaced with a neomycin resistance cassette. The resulting construct was electroporated into 129P2/OlaHsd-derived E14 embryonic, and these cells were then injected into C57BL/6J blastocysts. The resulting mice were bred with C57BL/6J mice for at least 11 generations before the colony was established. Adult male and female mice (WT 15.4 ± 1.6 weeks, *Snta1* KO 14.7 ± 1.6 weeks) were used in these studies.

Injection, imaging and analysis of CSF tracers or contrast agents

NMU:

Intracisternal Tracer Injections. Intracisternal injections of Texas Red conjugated dextran (TRd3; 3 kDa, Invitrogen) were adapted from a previous report (Iliff et al., 2012). In brief, the mice were anesthetized by a 4% chloral hydrate solution. A ten-microliter volume of 0.5% TRd3 dissolved in artificial CSF was infused into the cisterna magna through a 50 μL syringe mounted with a 27-gauge needle (Hamilton, Reno, NV, USA), connected to a constant current syringe pump (TJ-2A/L07-2A, Suzhou Wen Hao Chip Technology Co. Ltd., Jiangsu, China). The intracisternal injection was carried out at a rate of 2 μL/min. Thirty min after the start of injection, the still deeply anesthetized

animals were perfused trans-cardially with 4% paraformaldehyde (PFA), and the brains removed and post-fixed in the same fixative for 24 hours.

Tissue processing and image analysis of fluorescent tracer. A subset of WT and *Aqp4* KO brains (N = 4 per genotype) were scanned by an ex vivo near infrared (NIR) fluorescence imaging system (Azure biosystems c600, CA, USA). Briefly, the ventral and dorsal brains were imaged (excitation length 660 nm, exposure time: 50 ms), as well as the corresponding bright-field images. The fluorescence and bright field images were superimposed using Adobe Photoshop 8.0. Based on the Mouse Brain Atlas, fluorescence was measured along anterior-posterior axis based on the localization of bregma using NIH Image J software (Figure A.2a). The mean integrated optical density (MIOD) of TRd3 at a total of 80 sites were sequentially measured from 4 mm anterior to 8 mm posterior to the bregma. In addition, the telencephalon from 5 mice per genotype was cut into 100 μm coronal sections using a vibratome (Leica, Wetzlar, Germany). Sections were mounted on gelatin-coated slides, washed, and cover-slipped with the slices coated in PBS/glycerol. Images of 6-8 coronal sections collected sequentially from 1.7 mm anterior to 0.7 mm posterior of the bregma were imaged by a Leica DM4000B digital microscope (Leica Microsystems, Wetzlar, Germany) under a 1.25x objective, with uniform exposure time, offset, and gain. The distribution of the tracer (TRd3) was quantified using NIH Image J software as described previously (Iliff et al., 2012). In brief, the fluorescent tracer coverage within the whole section was detected using the same threshold and constant settings for minimum and maximum intensities. Subregional analysis of CSF tracer distribution was analyzed in coronal section at the level of 0.5 mm anterior to the bregma. Tracer penetration along perivascular spaces and into brain parenchyma was quantified on high magnification images of the hypothalamus, which were captured with 10x objective. The fluorescence intensity within the perivascular space was measured along large vessels (diameter >20 μm) extending 500 μm below the brain surface. Two or three separate vessels from each image were analyzed and the data averaged. The fluorescence intensity in the brain parenchyma was also determined along a corresponding linear region adjacent to the vessels (Figure A.2e). The imaging and subsequent analysis was performed by an investigator who was blind to animal genotype.

RIKEN:

Adult mice (postnatal 10 to 23 weeks old, mixed gender) were anesthetized by a ketamine-xylazine cocktail (70mg/kg of ketamine and 10mg/kg of xylazine) and fixed to a stereotaxic frame. The membrane of the cisterna magna was exposed by surgical procedures. A glass micropipette (tip diameter ~50 μm, preloaded with 0.5% biotinylated dextran amine in saline (BDA, 70 kDa, D1957, Molecular Probes), was carefully pierced through the cisterna magna membrane using a manipulator. A total of 10 μL of the BDA containing solution was infused at a rate of 1 μL/min using a syringe driver (KDS Legato Series, KD Scientific, USA). Thereafter, two supplementary ketamine-xylazine administrations were made (30 min apart, 50% of the initial dose). Five minutes after the second supplementary anesthesia, Mice were transcardially perfused with fixative containing 4% paraformaldehyde in 0.1 M phosphate buffer. After one day of post-fixation in the same fixative, 60 μm slices were incubated in 0.1% triton-X TBS containing Alexa-594-conjugated SA (1:1000) for one hour. Images of SA-processed brain sections were acquired using a standard fluorescent microscope (Olympus BX51 equipped with a DP74 digital camera). An offset, defined as the median of the top 1% of pixel intensities of an unprocessed brain section, is subtracted from the raw image of the SA-processed brain section. For depth profiles were calculated from the pial position of 3 mm from the midline using ImageJ.

UNC:

Intracisternal Tracer Injections. The experiments were performed as described previously(Iliff et al., 2012). In brief, mice (15-18 weeks old) were anesthetized with ketamine/xylazine (100/10 mg/kg) and then a cannula was surgically implanted into the cisterna magna(Xavier et al., 2018). Afterwards, an Alexa Fluor 647-conjugated bovine serum albumin tracer was infused into the cistern (0.5% in aCSF; 10 μl at 1μl/min for 10 min) and allowed to circulate for 30 min. Body temperature was maintained throughout the experiment. Perfusion-fixation is expected to alter intracranial pulsatility, a process that has been shown to drive CSF flow(Iliff et al., 2013b); therefore, thirty minutes post injection the mice were decapitated, and the brain drop fixed in 4% PFA.

Tissue processing and microscopy. The mouse brains were post-fixed prior to sectioning. In brief, 100 µm thick coronal plane vibratome sections were obtained using a Leica VT 1200S apparatus (Leica Biosystems, IL). Free-floating mouse brain sections were mounted with ProLong™ Gold Antifade Mounting Media with DAPI (Life Technologies, CA). We used an epifluorescent macroscope for imaging mouse brain sections (Olympus). The images were pseudocolored and analyzed on FIJI software. The sections were analyzed following methodology from both Iliff et al.(Iliff et al., 2012) and Smith et al(Smith et al., 2017). Mean pixel intensity was calculated for six coronal sections covering +1.2 to -1.8 mm from anterior to posterior relative to bregma. Subregional analysis of the coronal section at position +0.6 mm was conducted to identify which regions accounted for the differences in CSF influx(Kress et al., 2014).

URMC:

Intracisternal Tracer Injections. Mice (8-10 week old males) were anesthetized with ketamine/xylazine (100/10mg/kg) and fixed in a stereotaxic frame whereupon the posterior atlanto-occipital membrane overlying the cisterna magna was surgically exposed. For all CSF tracer experiments, Alexa 647-conjugated bovine serum albumin (BSA-647; 66 kDa; 0.5%) was injected into the subarachnoid CSF via cisterna magna puncture, at a rate of 1 or 2 µL/min for a period of five min (5 µL or 10 µL total volume) through a 30-gauge syringe pump (Harvard Apparatus). To visualize penetration of fluorescent CSF tracers into the brain parenchyma ex vivo, anesthetized animals were decapitated at 30 min after the start of the injection, a time point previously identified to correspond to robust tracer penetration of similar molecular weight compounds in young male C57BL/6 mice (Iliff et al., 2012). Brains were then removed and post-fixed in 4% PFA for 24 hours before being sliced with a vibratome into 100 µm coronal sections which were slide-mounted using PROLONG anti-fade gold with DAPI (Invitrogen).

In vivo transcranial optical imaging. Transcranial optical imaging was performed in KX-anesthetized mice as recently described (Plog et al., 2018). To prepare the mouse, the skin overlying the dorsal convexity was reflected and afterwards the cisterna magna was cannulated as described above. Fluorescent CSF tracers Texas Red 3 kDa dextran and BSA-647 (10 µl at 2 µl/ min, 0.5% in aCSF) were injected into the cisterna magna

and imaged using a fluorescent macroscope (MVX10, Olympus) using a PRIOR Lumen 1600-LED light source and ORCA Flash 4.0 digital camera (Hamamatsu). The mouse's head was stabilized with ear bars using a customized stereotaxic frame and placed under the microscope stage. Imaging was done at a 20x magnification and acquired in the far-red emission channel (647 nm). Due to high scattering at the excitation/emission wavelength of the Texas Red 3 kDa dextran through the intact skull this channel was not acquired. Images were collected every minute for 30 minutes following the start of the injection. MetaMorph Basic imaging software was used for image acquisition (Molecular Devices). The same exposure time (100 ms) was used throughout the experiment and between the WT and KO groups. After 30 min, the brain was extracted and fixed as described below.

Intrastriatal tracer injections. KX-anesthetized mice were placed in a stereotaxic apparatus and the skin was opened to expose the skull. Carefully, periosteum was removed and bregma was identified with a surgical microscope. A burr hole was done with a hand-held drill on the coordinates AP: +0.5 DV: +3.0 LM: +2.0 mm from bregma, using a 27G needle to break the meningeal layer. A pulled glass capillary (TW100-3, World Precision Instruments) with a 12 μm tip diameter was introduced in the brain parenchyma. Once in place, 20 nL of 0.5% Amyloid-$\beta_{1\text{-}40}$ in aCSF (as a sham) was delivered in a perfusion rate of 4 nL/second by a micropump (UMP3 UltraMicroPump with Micro4 controller, World Precision Instruments) as done by Smith et al. Control mice did not receive an injection. The micropipette remained in place for 5 minutes and then was very slowly withdrew, to avoid any possible backflow. If backflow was observed, the animal was excluded from the experiment. Immediately after the capillary was removed, a small amount of Kwik-Cast Sealant (KWIK-CAST, World Precision Instruments) was applied to seal the site of injection. After 60 minutes, mice received an injection in cisterna magna with BSA-647 (1% in aCSF) as descried above to evaluate glymphatic function.

Ex-vivo imaging of fluorescent CSF tracers. BSA-647 and TxRd 3 kDa dextran circulation along perivascular pathways and penetration into the brain parenchyma was visualized by conventional fluorescence microscopy of 100 μm vibratome coronal brain sections, as described previously (Iliff et al., 2012). For coronal section quantification, six

brain sections (per animal were imaged and analyzed by a blinded investigator using an Olympus fluorescence macroscope (MVX10) under 20x magnification to generate whole-slice images (using the MetaMorph software, Molecular Devices). High magnification montage images of coronal sections were acquired using an Olympus BX51 fluorescent microscope at 4x objective magnification using cellSens software (Olympus). Tracer penetration was quantified using NIH Image J software as described previously (Iliff et al., 2012). The first slice was collected at the beginning at the anterior aspect of the corpus callosum, one section was collected every 500 μm apart until a total of six sections had been collected for each animal. Fluorescence of the CSF tracer BSA-647 was measured in each slice as mean pixel intensity (MPI). The MPI from the six brain slices from each animal were averaged to define CSF penetration within a single biological replicate. For the ipsilateral to contralateral comparison, 3 to 5 slices from the injection site where selected from each mouse, and their tracer penetration was quantified, averaged and analyzed by Wilcoxon rank-sum test using different ROIs for each hemisphere. A subset of brain slices were immunostained for AQP4 as previously described (Kress et al., 2014). Tracer penetration depth was evaluated using Fiji and Matlab. A coronal section obtained from bregma from each mouse was used for the analysis. In the KO mice, a 500 μm line was placed orthogonal to the cortical surface at the most dorsal position where tracer could be found at the pial surface (Figure A.5f). Tracer depth in the WT mice was measured at the same position as the KO mouse despite there being more tracer spread over the dorsal convexity. The line profile was normalized to the maximum fluorescence at the cortical surface ($\Delta F/F_{max}$). Tracer penetration depth was quantified as the distance at which F_{max} was reduced by half ($d_{1/2}$) similar to Smith et al (Smith et al., 2017).

OHSU:

Dynamic contrast enhanced magnetic resonance imaging (DCE-MRI) of glymphatic transport. 3-6-month-old mice were anesthetized with isoflurane, with induction at 3-5%. The posterior atlanto-occipital membrane was exposed surgically. To enable the contrast injection during MRI scanning, we used a pulled glass micropipette with trimmed end (external diameter of approximately .016 mm) to perform the injection.

The micropipette was fixed in place for the duration of the imaging session with superglue. Gadoteridol (68 mM, osmotically adjusted), a contrast medium was infused by syringe pump (Harvard Apparatus) at a rate of 500 nl/min for 20 minutes (10 µl total volume), with a 2 µl chase of saline.

MR imaging. CSF circulation was quantified by dynamic contrast-enhanced magnetic resonance imaging (DCE-MRI). All imaging was performed using a Bruker-Biospec 11.75 T preclinical scanner equipped with a 20 mm I.D. quadrature RF volume-coil with a specially designed head holder. Heart rate, oxygen saturation and respiratory rate were monitored, and core temperature was maintained at 37 °C using a warm air temperature control system (SA Instruments). Upon placement of the glass micropipette, isoflurane anesthesia was switched to ketamine-xylazine (100-10mg/kg) for the duration of the experiment. Consecutive T_1 weighted 3D FLASH images were obtained at 10-minute intervals (TR/TE 16/2.8 ms, flip angle 15°, matrix 256x192x192, 100x100x100 µm resolution), for a total of 90 minutes. Injection was initiated after acquiring the first image. If no elevation in signal was detectable in the cortical or subcortical brain regions or the basal cistern within the first 30 minutes, the imaging session was aborted, and the animal was excluded from further analysis.

MR data analysis. Due to frequent occurrence of motion artifact during the last 30 minutes of acquisition (70-90 minutes), these three time points were excluded from analysis, and those animals showing movement artifacts during the first 60 minutes of acquisition were also excluded. Linear rigid body registration was used to spatially align the image series to the baseline image (FSL). Regions of interest (ROIs) were drawn on a coronal image slice best matching that depicted in Figure 6I, and mean intensity values were determined with FIJI software. Repeated measures two-way ANOVA with Sidak multiple comparisons correction was used to analyze the data. Multiple comparisons were used to determine the significance of genotype differences at each time point.

Meta-analysis. *Literature search:* A review of the literature on PubMed and Google Scholar was conducted for all studies published to date (November 2018) on global *Aqp4* KO models in rodents. *Inclusion criteria:* Out of 6,527 studies that were retrieved from the online search, only tracer studies that evaluated fluid flow in the brain in *Aqp4* KO versus wildtype controls were included. *Exclusion criteria:* Studies were

excluded if either mean, standard deviation, or sample size could not be extracted. Studies that evaluated tracer transport in a disease model were also eliminated. Non-English studies were not excluded. Only one study Binder et al. 2004 was excluded due to the inability to estimate sample size(Binder et al., 2004). After exclusion, a total of 11 studies satisfied the selection criteria. Five data sets from the present study (NMU, RIKEN, UNC, URMC) were also included. *Data extraction:* Means, standard deviations, and sample sizes for each experiment were extracted from the text where possible. If exact numbers were not reported, we used graphical extraction using FIJI. When standard error of the mean was reported, standard deviation was calculated using the square root of the sample size. In cases where sample size was reported as a range, the lowest number was chosen for analysis. In one study, it was impossible to determine if two separate analyses were derived from the same group of mice. In order to avoid inadvertently excluding data (e.g. If the study was in fact conducted in 2 separate sets of mice) we included both experimental data sets in the meta-analysis(Smith et al., 2017).

Data analysis: Studies addressed mainly two parts of intracranial fluid flow: 1) CSF influx to brain after delivery of tracers to the cisterna magna and 2) tracer transport after being injected into the interstitial fluid in the brain parenchyma. To address these two types of experiments, we decided to run two separate models using the inverse variance method for meta-analysis. Since these were evaluated using different outcome measures between fluorescence (fluorescence intensity and thresholding approaches), radioisotope, and MRI experiments we opted for a standardized mean difference (SMD) using the Cohen's D method for the final analysis. After data was extracted, analysis was done in R (R-Project). Due to high heterogeneity (I^2 >70%), a random effects model was selected after attempting to reduce heterogeneity by implementing alternate standardized mean difference formulas (e.g. Glass's delta, Hedge's G), however these attempts did not eliminate heterogeneity. Sources of heterogeneity were then explored using mixed-effects model meta-regression. Candidate predictors of heterogeneity included: anesthesia type, species, strain, age, tracer properties, injection properties, injection location, and experimental method. Inclusion of more than one covariate in the meta-regression resulted in model non-convergence due to the relatively small number of studies and the distribution of these factors across studies so covariates were included one at a time. Data

in forest plots is shown as SMD with 95% confidence intervals (CI) and P values less than 0.05 were considered significant.

Bibliography

2011. Allen Mouse Brain Connectivity Atlas. In Allen Institute for Brain Science.

Abbott, N.J. 2004. Evidence for bulk flow of brain interstitial fluid: significance for physiology and pathology. *Neurochemistry international* 45:545-552.

Abbott, N.J., M.E. Pizzo, J.E. Preston, D. Janigro, and R.G. Thorne. 2018. The role of brain barriers in fluid movement in the CNS: is there a 'glymphatic' system? *Acta neuropathologica* 135:387-407.

Achariyar, T.M., B. Li, W. Peng, P.B. Verghese, Y. Shi, E. McConnell, A. Benraiss, T. Kasper, W. Song, T. Takano, D.M. Holtzman, M. Nedergaard, and R. Deane. 2016. Glymphatic distribution of CSF-derived apoE into brain is isoform specific and suppressed during sleep deprivation. *Mol Neurodegener* 11:74.

Adams, M.E., N. Kramarcy, S.P. Krall, S.G. Rossi, R.L. Rotundo, R. Sealock, and S.C. Froehner. 2000. Absence of alpha-syntrophin leads to structurally aberrant neuromuscular synapses deficient in utrophin. *The Journal of cell biology* 150:1385-1398.

Agrawal, S., P. Anderson, M. Durbeej, N. van Rooijen, F. Ivars, G. Opdenakker, and L.M. Sorokin. 2006. Dystroglycan is selectively cleaved at the parenchymal basement membrane at sites of leukocyte extravasation in experimental autoimmune encephalomyelitis. *The Journal of experimental medicine* 203:1007-1019.

Akanuma, S., T. Sakurai, M. Tachikawa, Y. Kubo, and K. Hosoya. 2015. Transporter-mediated L-glutamate elimination from cerebrospinal fluid: possible involvement of excitatory amino acid transporters expressed in ependymal cells and choroid plexus epithelial cells. *Fluids Barriers CNS* 12:11.

Albeck, M.J., C. Skak, P.R. Nielsen, K.S. Olsen, S.E. Borgesen, and F. Gjerris. 1998. Age dependency of resistance to cerebrospinal fluid outflow. *Journal of neurosurgery* 89:275-278.

Amiry-Moghaddam, M., T. Otsuka, P.D. Hurn, R.J. Traystman, F.M. Haug, S.C. Froehner, M.E. Adams, J.D. Neely, P. Agre, O.P. Ottersen, and A. Bhardwaj. 2003. An alpha-syntrophin-dependent pool of AQP4 in astroglial end-feet confers bidirectional water flow between blood and brain. *Proceedings of the National Academy of Sciences of the United States of America* 100:2106-2111.

Andriezen, W.L. 1893. The Neuroglia Elements in the Human Brain. *British medical journal* 2:227-230.

Angot, E., J.A. Steiner, C. Hansen, J.Y. Li, and P. Brundin. 2010. Are synucleinopathies prion-like disorders? *The Lancet. Neurology* 9:1128-1138.

Arras, M., P. Autenried, A. Rettich, D. Spaeni, and T. Rulicke. 2001. Optimization of intraperitoneal injection anesthesia in mice: drugs, dosages, adverse effects, and anesthesia depth. *Comparative medicine* 51:443-456.

Asgari, M., D. de Zelicourt, and V. Kurtcuoglu. 2015. How astrocyte networks may contribute to cerebral metabolite clearance. *Sci Rep* 5:15024.

Asgari, M., D. de Zelicourt, and V. Kurtcuoglu. 2016. Glymphatic solute transport does not require bulk flow. *Sci Rep* 6:38635.

Aspelund, A., S. Antila, S.T. Proulx, T.V. Karlsen, S. Karaman, M. Detmar, H. Wiig, and K. Alitalo. 2015. A dural lymphatic vascular system that drains brain interstitial fluid and macromolecules. *The Journal of experimental medicine* 212:991-999.

Assentoft, M., S. Kaptan, R.A. Fenton, S.Z. Hua, B.L. de Groot, and N. MacAulay. 2013. Phosphorylation of rat aquaporin-4 at Ser(111) is not required for channel gating. *Glia* 61:1101-1112.

Attems, J., K. Jellinger, D.R. Thal, and W. Van Nostrand. 2011. Review: sporadic cerebral amyloid angiopathy. *Neuropathology and applied neurobiology* 37:75-93.

Audrey, D., A. Misa, N.U. Valentin, S. Hédi, and B. Hugues. 2019. Simulation of calcium signaling in fine astrocytic processes: effect of spatial properties on spontaneous activity. *bioRxiv* 567388.

Bakker, E.N., B.J. Bacskai, M. Arbel-Ornath, R. Aldea, B. Bedussi, A.W. Morris, R.O. Weller, and R.O. Carare. 2016. Lymphatic Clearance of the Brain: Perivascular, Paravascular and Significance for Neurodegenerative Diseases. *Cellular and molecular neurobiology* 36:181-194.

Bartholomaus, I., N. Kawakami, F. Odoardi, C. Schlager, D. Miljkovic, J.W. Ellwart, W.E. Klinkert, C. Flugel-Koch, T.B. Issekutz, H. Wekerle, and A. Flugel. 2009. Effector T cell interactions with meningeal vascular structures in nascent autoimmune CNS lesions. *Nature* 462:94-98.

Bedussi, B., M. Almasian, J. de Vos, E. VanBavel, and E.N. Bakker. 2018. Paravascular spaces at the brain surface: Low resistance pathways for cerebrospinal fluid flow. *J Cereb Blood Flow Metab* 38:719-726.

Bedussi, B., M.G. van Lier, J.W. Bartstra, J. de Vos, M. Siebes, E. VanBavel, and E.N. Bakker. 2015. Clearance from the mouse brain by convection of interstitial fluid towards the ventricular system. *Fluids Barriers CNS* 12:23.

Belanger, M., I. Allaman, and P.J. Magistretti. 2011. Brain energy metabolism: focus on astrocyte-neuron metabolic cooperation. *Cell metabolism* 14:724-738.

Bell, R.D., R. Deane, N. Chow, X. Long, A. Sagare, I. Singh, J.W. Streb, H. Guo, A. Rubio, W. Van Nostrand, J.M. Miano, and B.V. Zlokovic. 2009. SRF and myocardin regulate LRP-mediated amyloid-beta clearance in brain vascular cells. *Nature cell biology* 11:143-153.

Ben-Zvi, A., B. Lacoste, E. Kur, B.J. Andreone, Y. Mayshar, H. Yan, and C. Gu. 2014. Mfsd2a is critical for the formation and function of the blood-brain barrier. *Nature* 509:507-511.

Bennett, M.V., J.E. Contreras, F.F. Bukauskas, and J.C. Saez. 2003. New roles for astrocytes: gap junction hemichannels have something to communicate. *Trends in neurosciences* 26:610-617.

Benveniste, H., H. Lee, F. Ding, Q. Sun, E. Al-Bizri, R. Makaryus, S. Probst, M. Nedergaard, E.A. Stein, and H. Lu. 2017. Anesthesia with Dexmedetomidine and Low-dose Isoflurane Increases Solute Transport via the Glymphatic Pathway in Rat Brain When Compared with High-dose Isoflurane. *Anesthesiology* 127:976-988.

Billingsley, M.L., and R.L. Kincaid. 1997. Regulated phosphorylation and dephosphorylation of tau protein: effects on microtubule interaction, intracellular trafficking and neurodegeneration. *The Biochemical journal* 323 (Pt 3):577-591.

Bilston, L.E., D.F. Fletcher, A.R. Brodbelt, and M.A. Stoodley. 2003. Arterial pulsation-driven cerebrospinal fluid flow in the perivascular space: a computational model. *Computer methods in biomechanics and biomedical engineering* 6:235-241.

Binder, D.K., M.C. Papadopoulos, P.M. Haggie, and A.S. Verkman. 2004. In vivo measurement of brain extracellular space diffusion by cortical surface photobleaching. *J Neurosci* 24:8049-8056.

Bindocci, E., I. Savtchouk, N. Liaudet, D. Becker, G. Carriero, and A. Volterra. 2017. Three-dimensional Ca(2+) imaging advances understanding of astrocyte biology. *Science (New York, N.Y.)* 356:

Black, P.M., A. Tzouras, and L. Foley. 1985. Cerebrospinal fluid dynamics and hydrocephalus after experimental subarachnoid hemorrhage. *Neurosurgery* 17:57-62.

Blanchette, M., and R. Daneman. 2015. Formation and maintenance of the BBB. *Mechanisms of development* 138 Pt 1:8-16.

Blasberg, R., D. Johnson, and J. Fenstermacher. 1981. Absorption resistance of cerebrospinal fluid after subarachnoid hemorrhage in the monkey; effects of heparin. *Neurosurgery* 9:686-691.

Bloch, O., K.I. Auguste, G.T. Manley, and A.S. Verkman. 2006. Accelerated progression of kaolin-induced hydrocephalus in aquaporin-4-deficient mice. *J Cereb Blood Flow Metab* 26:1527-1537.

Boisvert, M.M., G.A. Erikson, M.N. Shokhirev, and N.J. Allen. 2018. The Aging Astrocyte Transcriptome from Multiple Regions of the Mouse Brain. *Cell reports* 22:269-285.

Boor, I., M. Nagtegaal, W. Kamphorst, P. van der Valk, J.C. Pronk, J. van Horssen, A. Dinopoulos, K.E. Bove, I. Pascual-Castroviejo, F. Muntoni, R. Estevez, G.C. Scheper, and M.S. van der Knaap. 2007. MLC1 is associated with the dystrophin-glycoprotein complex at astrocytic endfeet. *Acta neuropathologica* 114:403-410.

Boulay, A.C., B. Saubamea, N. Adam, S. Chasseigneaux, N. Mazare, A. Gilbert, M. Bahin, L. Bastianelli, C. Blugeon, S. Perrin, J. Pouch, B. Ducos, S. Le Crom, A. Genovesio, F. Chretien, X. Decleves, J.L. Laplanche, and M. Cohen-Salmon. 2017. Translation in astrocyte distal processes sets molecular heterogeneity at the gliovascular interface. *Cell discovery* 3:17005.

Boulay, A.C., B. Saubamea, S. Cisternino, V. Mignon, A. Mazeraud, L. Jourdren, C. Blugeon, and M. Cohen-Salmon. 2015. The Sarcoglycan complex is expressed in the cerebrovascular system and is specifically regulated by astroglial Cx30 channels. *Frontiers in cellular neuroscience* 9:9.

Bousset, L., L. Pieri, G. Ruiz-Arlandis, J. Gath, P.H. Jensen, B. Habenstein, K. Madiona, V. Olieric, A. Bockmann, B.H. Meier, and R. Melki. 2013. Structural and functional characterization of two alpha-synuclein strains. *Nature communications* 4:2575.

Braak, H., and E. Braak. 1995. Staging of Alzheimer's disease-related neurofibrillary changes. *Neurobiol Aging* 16:271-278; discussion 278-284.

Braak, H., K. Del Tredici, U. Rub, R.A. de Vos, E.N. Jansen Steur, and E. Braak. 2003. Staging of brain pathology related to sporadic Parkinson's disease. *Neurobiol Aging* 24:197-211.

Bragg, A.D., M. Amiry-Moghaddam, O.P. Ottersen, M.E. Adams, and S.C. Froehner. 2006. Assembly of a perivascular astrocyte protein scaffold at the mammalian blood-brain barrier is dependent on alpha-syntrophin. *Glia* 53:879-890.

Bragg, A.D., S.S. Das, and S.C. Froehner. 2010. Dystrophin-associated protein scaffolding in brain requires alpha-dystrobrevin. *Neuroreport* 21:695-699.

Brandt, M., H. IJzerman, A. Dijksterhuis, F. Farachc, J. Geller, R. Giner-Sorolla, J. Grange, Perugini, J. Spies, and A. Veer. 2014. The Replication Recipe: What makes for a convincing replication? *Journal of Experimental Social Psychology* 50:217-224.

Brinker, T., V. Seifert, and D. Stolke. 1991. Effect of intrathecal fibrinolysis on cerebrospinal fluid absorption after experimental subarachnoid hemorrhage. *Journal of neurosurgery* 74:789-793.

Brinker, T., E. Stopa, J. Morrison, and P. Klinge. 2014. A new look at cerebrospinal fluid circulation. *Fluids Barriers CNS* 11:10.

Brioni, J.D., S. Varughese, R. Ahmed, and B. Bein. 2017. A clinical review of inhalation anesthesia with sevoflurane: from early research to emerging topics. *Journal of anesthesia* 31:764-778.

Broekman, M.L., L.A. Comer, B.T. Hyman, and M. Sena-Esteves. 2006. Adeno-associated virus vectors serotyped with AAV8 capsid are more efficient than AAV-1 or -2 serotypes for widespread gene delivery to the neonatal mouse brain. *Neuroscience* 138:501-510.

Broux, B., E. Gowing, and A. Prat. 2015. Glial regulation of the blood-brain barrier in health and disease. *Seminars in immunopathology* 37:577-590.

Burbulla, L.F., P. Song, J.R. Mazzulli, E. Zampese, Y.C. Wong, S. Jeon, D.P. Santos, J. Blanz, C.D. Obermaier, C. Strojny, J.N. Savas, E. Kiskinis, X. Zhuang, R. Kruger, D.J. Surmeier, and D. Krainc. 2017. Dopamine oxidation mediates mitochondrial and lysosomal dysfunction in Parkinson's disease. *Science (New York, N.Y.)* 357:1255-1261.

Burfeind, K.G., C.F. Murchison, S.K. Westaway, M.J. Simon, D. Erten-Lyons, J.A. Kaye, J.F. Quinn, and J.J. Iliff. 2017. The effects of noncoding aquaporin-4 single-nucleotide polymorphisms on cognition and functional progression of Alzheimer's disease. *Alzheimers Dement (N Y)* 3:348-359.

Burre, J., M. Sharma, and T.C. Sudhof. 2014. alpha-Synuclein assembles into higher-order multimers upon membrane binding to promote SNARE complex formation. *Proceedings of the National Academy of Sciences of the United States of America* 111:E4274-4283.

Bushong, E.A., M.E. Martone, Y.Z. Jones, and M.H. Ellisman. 2002. Protoplasmic astrocytes in CA1 stratum radiatum occupy separate anatomical domains. *J Neurosci* 22:183-192.

Cahoy, J.D., B. Emery, A. Kaushal, L.C. Foo, J.L. Zamanian, K.S. Christopherson, Y. Xing, J.L. Lubischer, P.A. Krieg, S.A. Krupenko, W.J. Thompson, and B.A. Barres. 2008. A transcriptome database for astrocytes, neurons, and

oligodendrocytes: a new resource for understanding brain development and function. *J Neurosci* 28:264-278.

Carlos, T.M., R.S. Clark, D. Franicola-Higgins, J.K. Schiding, and P.M. Kochanek. 1997. Expression of endothelial adhesion molecules and recruitment of neutrophils after traumatic brain injury in rats. *Journal of leukocyte biology* 61:279-285.

Chau, K.F., M.W. Springel, K.G. Broadbelt, H.Y. Park, S. Topal, M.P. Lun, H. Mullan, T. Maynard, H. Steen, A.S. LaMantia, and M.K. Lehtinen. 2015. Progressive Differentiation and Instructive Capacities of Amniotic Fluid and Cerebrospinal Fluid Proteomes following Neural Tube Closure. *Developmental cell* 35:789-802.

Cirrito, J.R., J.E. Kang, J. Lee, F.R. Stewart, D.K. Verges, L.M. Silverio, G. Bu, S. Mennerick, and D.M. Holtzman. 2008. Endocytosis is required for synaptic activity-dependent release of amyloid-beta in vivo. *Neuron* 58:42-51.

Cirrito, J.R., K.A. Yamada, M.B. Finn, R.S. Sloviter, K.R. Bales, P.C. May, D.D. Schoepp, S.M. Paul, S. Mennerick, and D.M. Holtzman. 2005. Synaptic activity regulates interstitial fluid amyloid-beta levels in vivo. *Neuron* 48:913-922.

Clancy, B., R.B. Darlington, and B.L. Finlay. 2001. Translating developmental time across mammalian species. *Neuroscience* 105:7-17.

Clarke, L.E., S.A. Liddelow, C. Chakraborty, A.E. Münch, M. Heiman, and B.A. Barres. 2018. Normal aging induces A1-like astrocyte reactivity. *Proceedings of the National Academy of Sciences of the United States of America* 115:E1896-E1905.

Constantin, B. 2014. Dystrophin complex functions as a scaffold for signalling proteins. *Biochim Biophys Acta* 1838:635-642.

Crane, J.M., A.N. Van Hoek, W.R. Skach, and A.S. Verkman. 2008. Aquaporin-4 dynamics in orthogonal arrays in live cells visualized by quantum dot single particle tracking. *Molecular biology of the cell* 19:3369-3378.

Cserr, H.F. 1971. Physiology of the choroid plexus. *Physiol Rev* 51:273-311.

Cserr, H.F. 1988. Role of secretion and bulk flow of brain interstitial fluid in brain volume regulation. *Annals of the New York Academy of Sciences* 529:9-20.

Cserr, H.F., D.N. Cooper, P.K. Suri, and C.S. Patlak. 1981. Efflux of radiolabeled polyethylene glycols and albumin from rat brain. *The American journal of physiology* 240:F319-328.

Dalloz, C., R. Sarig, P. Fort, D. Yaffe, A. Bordais, T. Pannicke, J. Grosche, D. Mornet, A. Reichenbach, J. Sahel, U. Nudel, and A. Rendon. 2003. Targeted inactivation of dystrophin gene product Dp71: phenotypic impact in mouse retina. *Human molecular genetics* 12:1543-1554.

Damkier, H.H., P.D. Brown, and J. Praetorius. 2013. Cerebrospinal fluid secretion by the choroid plexus. *Physiol Rev* 93:1847-1892.

Dandy, W.E. 1918. EXTIRPATION OF THE CHOROID PLEXUS OF THE LATERAL VENTRICLES IN COMMUNICATING HYDROCEPHALUS. *Annals of surgery* 68:569-579.

Daneman, R., L. Zhou, A.A. Kebede, and B.A. Barres. 2010. Pericytes are required for blood-brain barrier integrity during embryogenesis. *Nature* 468:562-566.

Danzer, K.M., W.P. Ruf, P. Putcha, D. Joyner, T. Hashimoto, C. Glabe, B.T. Hyman, and P.J. McLean. 2011. Heat-shock protein 70 modulates toxic extracellular alpha-synuclein oligomers and rescues trans-synaptic toxicity. *FASEB journal : official*

publication of the Federation of American Societies for Experimental Biology 25:326-336.

Davson, H. 1963. THE CEREBROSPINAL FLUID. *Ergebnisse der Physiologie, biologischen Chemie und experimentellen Pharmakologie* 52:20-72.

Davson, H., and M.B. Segal. 1995. Physiology of the CSF and Blood Brain Bariers. CRC-Press,

De Bellis, M., F. Pisani, M.G. Mola, S. Rosito, L. Simone, C. Buccoliero, M. Trojano, G.P. Nicchia, M. Svelto, and A. Frigeri. 2017. Translational readthrough generates new astrocyte AQP4 isoforms that modulate supramolecular clustering, glial endfeet localization, and water transport. *Glia* 65:790-803.

De Pittà, M., E. Ben-Jacob, and H. Berry. 2019. G Protein-Coupled Receptor-Mediated Calcium Signaling in Astrocytes. In Computational Glioscience. M. De Pittà, and H. Berry, editors. Springer International Publishing, Cham. 115-150.

de Rougemont, J., A. Ames, 3rd, F.B. Nesbett, and H.F. Hofmann. 1960. Fluid formed by choroid plexus; a technique for its collection and a comparison of its electrolyte composition with serum and cisternal fluids. *Journal of neurophysiology* 23:485-495.

Deane, R., R.D. Bell, A. Sagare, and B.V. Zlokovic. 2009. Clearance of amyloid-beta peptide across the blood-brain barrier: implication for therapies in Alzheimer's disease. *CNS & neurological disorders drug targets* 8:16-30.

Dechadilok, P., and W.M. Deen. 2009. Electrostatic and electrokinetic effects on hindered convection in pores. *Journal of colloid and interface science* 338:135-144.

Dermietzel, R. 1973. Visualization by freeze-fracturing of regular structures in glial cell membranes. *Die Naturwissenschaften* 60:208.

Derouiche, A., T. Pannicke, J. Haseleu, S. Blaess, J. Grosche, and A. Reichenbach. 2012. Beyond polarity: functional membrane domains in astrocytes and Muller cells. *Neurochemical research* 37:2513-2523.

Desplats, P., H.J. Lee, E.J. Bae, C. Patrick, E. Rockenstein, L. Crews, B. Spencer, E. Masliah, and S.J. Lee. 2009. Inclusion formation and neuronal cell death through neuron-to-neuron transmission of alpha-synuclein. *Proceedings of the National Academy of Sciences of the United States of America* 106:13010-13015.

Deverman, B.E., P.L. Pravdo, B.P. Simpson, S.R. Kumar, K.Y. Chan, A. Banerjee, W.L. Wu, B. Yang, N. Huber, S.P. Pasca, and V. Gradinaru. 2016. Cre-dependent selection yields AAV variants for widespread gene transfer to the adult brain. *Nature biotechnology* 34:204-209.

Dreha-Kulaczewski, S., A.A. Joseph, K.D. Merboldt, H.C. Ludwig, J. Gartner, and J. Frahm. 2015. Inspiration is the major regulator of human CSF flow. *J Neurosci* 35:2485-2491.

Eid, T., T.S. Lee, M.J. Thomas, M. Amiry-Moghaddam, L.P. Bjornsen, D.D. Spencer, P. Agre, O.P. Ottersen, and N.C. de Lanerolle. 2005. Loss of perivascular aquaporin 4 may underlie deficient water and K+ homeostasis in the human epileptogenic hippocampus. *Proceedings of the National Academy of Sciences of the United States of America* 102:1193-1198.

Eide, P.K., and G. Ringstad. 2015. MRI with intrathecal MRI gadolinium contrast medium administration: a possible method to assess glymphatic function in human brain. *Acta Radiol Open* 4:2058460115609635.

Eng, L.F., J.J. Vanderhaeghen, A. Bignami, and B. Gerstl. 1971. An acidic protein isolated from fibrous astrocytes. *Brain Res* 28:351-354.

Engelhardt, B., and C. Coisne. 2011. Fluids and barriers of the CNS establish immune privilege by confining immune surveillance to a two-walled castle moat surrounding the CNS castle. *Fluids Barriers CNS* 8:4.

Engelhardt, B., and R.M. Ransohoff. 2012. Capture, crawl, cross: the T cell code to breach the blood-brain barriers. *Trends in immunology* 33:579-589.

Enger, R., G.A. Gundersen, N.N. Haj-Yasein, M. Eilert-Olsen, A.E. Thoren, G.F. Vindedal, P.H. Petersen, O. Skare, M. Nedergaard, O.P. Ottersen, and E.A. Nagelhus. 2012. Molecular scaffolds underpinning macroglial polarization: an analysis of retinal Muller cells and brain astrocytes in mouse. *Glia* 60:2018-2026.

Erdo, F., L. Denes, and E. de Lange. 2016. Age-associated physiological and pathological changes at the blood-brain barrier: A review. *J Cereb Blood Flow Metab*

Erecinska, M., S. Cherian, and A.S. I. 2005. Brain development and susceptibility to damage; ion levels and movements. *Current topics in developmental biology* 69:139-186.

Eusebi, P., D. Giannandrea, L. Biscetti, I. Abraha, D. Chiasserini, M. Orso, P. Calabresi, and L. Parnetti. 2017. Diagnostic utility of cerebrospinal fluid alpha-synuclein in Parkinson's disease: A systematic review and meta-analysis. *Mov Disord* 32:1389-1400.

Faghih, M.M., and M.K. Sharp. 2018. Is bulk flow plausible in perivascular, paravascular and paravenous channels? *Fluids Barriers CNS* 15:17.

Fan, Y., J. Zhang, X.L. Sun, L. Gao, X.N. Zeng, J.H. Ding, C. Cao, L. Niu, and G. Hu. 2005. Sex- and region-specific alterations of basal amino acid and monoamine metabolism in the brain of aquaporin-4 knockout mice. *Journal of neuroscience research* 82:458-464.

Feinberg, D.A., and A.S. Mark. 1987. Human brain motion and cerebrospinal fluid circulation demonstrated with MR velocity imaging. *Radiology* 163:793-799.

Flugge, G., C. Araya-Callis, E. Garea-Rodriguez, C. Stadelmann-Nessler, and E. Fuchs. 2014. NDRG2 as a marker protein for brain astrocytes. *Cell and tissue research* 357:31-41.

Frigeri, A., M.A. Gropper, F. Umenishi, M. Kawashima, D. Brown, and A.S. Verkman. 1995. Localization of MIWC and GLIP water channel homologs in neuromuscular, epithelial and glandular tissues. *Journal of cell science* 108 (Pt 9):2993-3002.

Frost, B., R.L. Jacks, and M.I. Diamond. 2009. Propagation of tau misfolding from the outside to the inside of a cell. *The Journal of biological chemistry* 284:12845-12852.

Frydenlund, D.S., A. Bhardwaj, T. Otsuka, M.N. Mylonakou, T. Yasumura, K.G. Davidson, E. Zeynalov, O. Skare, P. Laake, F.M. Haug, J.E. Rash, P. Agre, O.P. Ottersen, and M. Amiry-Moghaddam. 2006. Temporary loss of perivascular aquaporin-4 in neocortex after transient middle cerebral artery occlusion in mice.

Proceedings of the National Academy of Sciences of the United States of America 103:13532-13536.

Fukuda, A.M., V. Pop, D. Spagnoli, S. Ashwal, A. Obenaus, and J. Badaut. 2012. Delayed increase of astrocytic aquaporin 4 after juvenile traumatic brain injury: possible role in edema resolution? *Neuroscience* 222:366-378.

Furman, C.S., D.A. Gorelick-Feldman, K.G. Davidson, T. Yasumura, J.D. Neely, P. Agre, and J.E. Rash. 2003. Aquaporin-4 square array assembly: opposing actions of M1 and M23 isoforms. *Proceedings of the National Academy of Sciences of the United States of America* 100:13609-13614.

Gaberel, T., C. Gakuba, R. Goulay, S. Martinez De Lizarrondo, J.L. Hanouz, E. Emery, E. Touze, D. Vivien, and M. Gauberti. 2014. Impaired glymphatic perfusion after strokes revealed by contrast-enhanced MRI: a new target for fibrinolysis? *Stroke* 45:3092-3096.

Gakuba, C., T. Gaberel, S. Goursaud, J. Bourges, C. Di Palma, A. Quenault, S.M. de Lizarrondo, D. Vivien, and M. Gauberti. 2018. General Anesthesia Inhibits the Activity of the "Glymphatic System". *Theranostics* 8:710-722.

Gardner, R.C., J.F. Burke, J. Nettiksimmons, S. Goldman, C.M. Tanner, and K. Yaffe. 2015. Traumatic brain injury in later life increases risk for Parkinson disease. *Annals of neurology* 77:987-995.

Gato, A., M.I. Alonso, C. Martin, E. Carnicero, J.A. Moro, A. De la Mano, J.M. Fernandez, F. Lamus, and M.E. Desmond. 2014. Embryonic cerebrospinal fluid in brain development: neural progenitor control. *Croatian medical journal* 55:299-305.

Gesemann, M., A. Brancaccio, B. Schumacher, and M.A. Ruegg. 1998. Agrin is a high-affinity binding protein of dystroglycan in non-muscle tissue. *The Journal of biological chemistry* 273:600-605.

Ghersi-Egea, J.F., W. Finnegan, J.L. Chen, and J.D. Fenstermacher. 1996. Rapid distribution of intraventricularly administered sucrose into cerebrospinal fluid cisterns via subarachnoid velae in rat. *Neuroscience* 75:1271-1288.

Giaume, C., A. Koulakoff, L. Roux, D. Holcman, and N. Rouach. 2010. Astroglial networks: a step further in neuroglial and gliovascular interactions. *Nature reviews. Neuroscience* 11:87-99.

Goldman, S.M., C.M. Tanner, D. Oakes, G.S. Bhudhikanok, A. Gupta, and J.W. Langston. 2006. Head injury and Parkinson's disease risk in twins. *Annals of neurology* 60:65-72.

Groothuis, D.R., M.W. Vavra, K.E. Schlageter, E.W. Kang, A.C. Itskovich, S. Hertzler, C.V. Allen, and H.L. Lipton. 2007. Efflux of drugs and solutes from brain: the interactive roles of diffusional transcapillary transport, bulk flow and capillary transporters. *J Cereb Blood Flow Metab* 27:43-56.

Gunnarson, E., G. Axehult, G. Baturina, S. Zelenin, M. Zelenina, and A. Aperia. 2005. Lead induces increased water permeability in astrocytes expressing aquaporin 4. *Neuroscience* 136:105-114.

Guo, J.L., and V.M. Lee. 2011. Seeding of normal Tau by pathological Tau conformers drives pathogenesis of Alzheimer-like tangles. *The Journal of biological chemistry* 286:15317-15331.

Guo, J.L., and V.M. Lee. 2014. Cell-to-cell transmission of pathogenic proteins in neurodegenerative diseases. *Nature medicine* 20:130-138.

Guo, Z., L.A. Cupples, A. Kurz, S.H. Auerbach, L. Volicer, H. Chui, R.C. Green, A.D. Sadovnick, R. Duara, C. DeCarli, K. Johnson, R.C. Go, J.H. Growdon, J.L. Haines, W.A. Kukull, and L.A. Farrer. 2000. Head injury and the risk of AD in the MIRAGE study. *Neurology* 54:1316-1323.

Hablitz, L.M., H.S. Vinitsky, Q. Sun, F.F. Staeger, B. Sigurdsson, K.N. Mortensen, T.O. Lilius, and M. Nedergaard. 2019. Increased glymphatic influx is correlated with high EEG delta power and low heart rate in mice under anesthesia. *Science advances* 5:eaav5447.

Hadaczek, P., M. Kohutnicka, M.T. Krauze, J. Bringas, P. Pivirotto, J. Cunningham, and K. Bankiewicz. 2006a. Convection-enhanced delivery of adeno-associated virus type 2 (AAV2) into the striatum and transport of AAV2 within monkey brain. *Human gene therapy* 17:291-302.

Hadaczek, P., Y. Yamashita, H. Mirek, L. Tamas, M.C. Bohn, C. Noble, J.W. Park, and K. Bankiewicz. 2006b. The "perivascular pump" driven by arterial pulsation is a powerful mechanism for the distribution of therapeutic molecules within the brain. *Molecular therapy : the journal of the American Society of Gene Therapy* 14:69-78.

Hadjihambi, A., I.F. Harrison, M. Costas-Rodriguez, F. Vanhaecke, N. Arias, R. Gallego-Duran, S. Mastitskaya, P.S. Hosford, S.W.M. Olde Damink, N. Davies, A. Habtesion, M.F. Lythgoe, A.V. Gourine, and R. Jalan. 2018. Impaired brain glymphatic flow in experimental hepatic encephalopathy. *Journal of hepatology*

Haglund, M., U. Passant, M. Sjobeck, E. Ghebremedhin, and E. Englund. 2006. Cerebral amyloid angiopathy and cortical microinfarcts as putative substrates of vascular dementia. *International journal of geriatric psychiatry* 21:681-687.

Han, Z., M.B. Wax, and R.V. Patil. 1998. Regulation of aquaporin-4 water channels by phorbol ester-dependent protein phosphorylation. *The Journal of biological chemistry* 273:6001-6004.

Hardy, J., and D.J. Selkoe. 2002. The amyloid hypothesis of Alzheimer's disease: progress and problems on the road to therapeutics. *Science (New York, N.Y.)* 297:353-356.

Hawkes, C.A., W. Hartig, J. Kacza, R. Schliebs, R.O. Weller, J.A. Nicoll, and R.O. Carare. 2011. Perivascular drainage of solutes is impaired in the ageing mouse brain and in the presence of cerebral amyloid angiopathy. *Acta neuropathologica* 121:431-443.

He, X.F., D.X. Liu, Q. Zhang, F.Y. Liang, G.Y. Dai, J.S. Zeng, Z. Pei, G.Q. Xu, and Y. Lan. 2017. Voluntary Exercise Promotes Glymphatic Clearance of Amyloid Beta and Reduces the Activation of Astrocytes and Microglia in Aged Mice. *Frontiers in molecular neuroscience* 10:144.

Henneberger, C., L. Bard, A. Panatier, J.P. Reynolds, N.I. Medvedev, D. Minge, M.K. Herde, S. Anders, I. Kraev, J.P. Heller, O. Kopach, S. Rama, K. Zheng, T.P. Jensen, I. Sanchez-Romero, H. Janovjak, O.P. Ottersen, E.A. Nagelhus, S.H.R. Oliet, M.G. Stewart, U.V. Nägerl, and D.A. Rusakov. 2019. LTP induction drives remodeling of astroglia to boost glutamate escape from synapses. *bioRxiv* 349233.

Hertz, L., M.E. Gibbs, and G.A. Dienel. 2014. Fluxes of lactate into, from, and among gap junction-coupled astrocytes and their interaction with noradrenaline. *Frontiers in neuroscience* 8:261.

Hiroaki, Y., K. Tani, A. Kamegawa, N. Gyobu, K. Nishikawa, H. Suzuki, T. Walz, S. Sasaki, K. Mitsuoka, K. Kimura, A. Mizoguchi, and Y. Fujiyoshi. 2006. Implications of the aquaporin-4 structure on array formation and cell adhesion. *Journal of molecular biology* 355:628-639.

Hirt, L., B. Ternon, M. Price, N. Mastour, J.F. Brunet, and J. Badaut. 2009. Protective role of early aquaporin 4 induction against postischemic edema formation. *J Cereb Blood Flow Metab* 29:423-433.

His, W. 1865. Über ein perivasculäres Canalsystem in den nervösen Centralorganen und über dessen Beziehungen zum Lymphsystem. *Zeitschrift für wissenschaftliche Zoologie* 15:127-141.

Hladky, S.B., and M.A. Barrand. 2014. Mechanisms of fluid movement into, through and out of the brain: evaluation of the evidence. *Fluids Barriers CNS* 11:26.

Hladky, S.B., and M.A. Barrand. 2016. Fluid and ion transfer across the blood-brain and blood-cerebrospinal fluid barriers; a comparative account of mechanisms and roles. *Fluids Barriers CNS* 13:19.

Hokama, M., S. Oka, J. Leon, T. Ninomiya, H. Honda, K. Sasaki, T. Iwaki, T. Ohara, T. Sasaki, F.M. LaFerla, Y. Kiyohara, and Y. Nakabeppu. 2014. Altered expression of diabetes-related genes in Alzheimer's disease brains: the Hisayama study. *Cerebral cortex (New York, N.Y. : 1991)* 24:2476-2488.

Holmes, B.B., and M.I. Diamond. 2014. Prion-like properties of Tau protein: the importance of extracellular Tau as a therapeutic target. *The Journal of biological chemistry* 289:19855-19861.

Holter, K.E., B. Kehlet, A. Devor, T.J. Sejnowski, A.M. Dale, S.W. Omholt, O.P. Ottersen, E.A. Nagelhus, K.A. Mardal, and K.H. Pettersen. 2017. Interstitial solute transport in 3D reconstructed neuropil occurs by diffusion rather than bulk flow. *Proceedings of the National Academy of Sciences of the United States of America* 114:9894-9899.

Holth, J.K., S.K. Fritschi, C. Wang, N.P. Pedersen, J.R. Cirrito, T.E. Mahan, M.B. Finn, M. Manis, J.C. Geerling, P.M. Fuller, B.P. Lucey, and D.M. Holtzman. 2019. The sleep-wake cycle regulates brain interstitial fluid tau in mice and CSF tau in humans. *Science (New York, N.Y.)* 363:880-884.

Hoshi, A., A. Tsunoda, M. Tada, M. Nishizawa, Y. Ugawa, and A. Kakita. 2017. Expression of Aquaporin 1 and Aquaporin 4 in the Temporal Neocortex of Patients with Parkinson's Disease. *Brain Pathol* 27:160-168.

Hsiao, K., P. Chapman, S. Nilsen, C. Eckman, Y. Harigaya, S. Younkin, F. Yang, and G. Cole. 1996. Correlative memory deficits, Abeta elevation, and amyloid plaques in transgenic mice. *Science (New York, N.Y.)* 274:99-102.

Huber, V.J., H. Igarashi, S. Ueki, I.L. Kwee, and T. Nakada. 2018. Aquaporin-4 facilitator TGN-073 promotes interstitial fluid circulation within the blood-brain barrier: [17O]H2O JJVCPE MRI study. *Neuroreport* 29:697-703.

Iba, M., J.L. Guo, J.D. McBride, B. Zhang, J.Q. Trojanowski, and V.M. Lee. 2013. Synthetic tau fibrils mediate transmission of neurofibrillary tangles in a transgenic mouse model of Alzheimer's-like tauopathy. *J Neurosci* 33:1024-1037.

Iba, M., J.D. McBride, J.L. Guo, B. Zhang, J.Q. Trojanowski, and V.M. Lee. 2015. Tau pathology spread in PS19 tau transgenic mice following locus coeruleus (LC) injections of synthetic tau fibrils is determined by the LC's afferent and efferent connections. *Acta neuropathologica* 130:349-362.

Ichimura, T., P.A. Fraser, and H.F. Cserr. 1991. Distribution of extracellular tracers in perivascular spaces of the rat brain. *Brain Res* 545:103-113.

Ikeshima-Kataoka, H., Y. Abe, T. Abe, and M. Yasui. 2013. Immunological function of aquaporin-4 in stab-wounded mouse brain in concert with a pro-inflammatory cytokine inducer, osteopontin. *Mol Cell Neurosci* 56:65-75.

Iliff, J.J., M.J. Chen, B.A. Plog, D.M. Zeppenfeld, M. Soltero, L. Yang, I. Singh, R. Deane, and M. Nedergaard. 2014. Impairment of glymphatic pathway function promotes tau pathology after traumatic brain injury. *J Neurosci* 34:16180-16193.

Iliff, J.J., H. Lee, M. Yu, T. Feng, J. Logan, M. Nedergaard, and H. Benveniste. 2013a. Brain-wide pathway for waste clearance captured by contrast-enhanced MRI. *J Clin Invest* 123:1299-1309.

Iliff, J.J., M. Wang, Y. Liao, B.A. Plogg, W. Peng, G.A. Gundersen, H. Benveniste, G.E. Vates, R. Deane, S.A. Goldman, E.A. Nagelhus, and M. Nedergaard. 2012. A paravascular pathway facilitates CSF flow through the brain parenchyma and the clearance of interstitial solutes, including amyloid beta. *Sci Transl Med* 4:147ra111.

Iliff, J.J., M. Wang, D.M. Zeppenfeld, A. Venkataraman, B.A. Plog, Y. Liao, R. Deane, and M. Nedergaard. 2013b. Cerebral arterial pulsation drives paravascular CSF-interstitial fluid exchange in the murine brain. *J Neurosci* 33:18190-18199.

Jafari, S., M. Etminan, F. Aminzadeh, and A. Samii. 2013. Head injury and risk of Parkinson disease: a systematic review and meta-analysis. *Mov Disord* 28:1222-1229.

Jeon, I., F. Cicchetti, G. Cisbani, S. Lee, E. Li, J. Bae, N. Lee, L. Li, W. Im, M. Kim, H.S. Kim, S.H. Oh, T.A. Kim, J.J. Ko, B. Aube, A. Oueslati, Y.J. Kim, and J. Song. 2016. Human-to-mouse prion-like propagation of mutant huntingtin protein. *Acta neuropathologica* 132:577-592.

Jessen, N.A., A.S. Munk, I. Lundgaard, and M. Nedergaard. 2015. The Glymphatic System: A Beginner's Guide. *Neurochemical research*

Jin, B.J., A.J. Smith, and A.S. Verkman. 2016. Spatial model of convective solute transport in brain extracellular space does not support a "glymphatic" mechanism. *J Gen Physiol* 148:489-501.

Johanson, C., E. Stopa, A. Baird, and H. Sharma. 2011. Traumatic brain injury and recovery mechanisms: peptide modulation of periventricular neurogenic regions by the choroid plexus-CSF nexus. *Journal of neural transmission (Vienna, Austria : 1996)* 118:115-133.

Johanson, C.E., J.A. Duncan, 3rd, P.M. Klinge, T. Brinker, E.G. Stopa, and G.D. Silverberg. 2008. Multiplicity of cerebrospinal fluid functions: New challenges in health and disease. *Cerebrospinal fluid research* 5:10.

Ju, Y.S., S.J. Ooms, C. Sutphen, S.L. Macauley, M.A. Zangrilli, G. Jerome, A.M. Fagan, E. Mignot, J.M. Zempel, J. Claassen, and D.M. Holtzman. 2017. Slow wave sleep disruption increases cerebrospinal fluid amyloid-beta levels. *Brain* 140:2104-2111.

Jucker, M., and L.C. Walker. 2013. Self-propagation of pathogenic protein aggregates in neurodegenerative diseases. *Nature* 501:45-51.

Kang, J.E., M.M. Lim, R.J. Bateman, J.J. Lee, L.P. Smyth, J.R. Cirrito, N. Fujiki, S. Nishino, and D.M. Holtzman. 2009. Amyloid-beta dynamics are regulated by orexin and the sleep-wake cycle. *Science (New York, N.Y.)* 326:1005-1007.

Kanki, H., H. Suzuki, and S. Itohara. 2006. High-efficiency CAG-FLPe deleter mice in C57BL/6J background. *Experimental animals* 55:137-141.

Kao, L., L.M. Kurtz, X. Shao, M.C. Papadopoulos, L. Liu, D. Bok, S. Nusinowitz, B. Chen, S.L. Stella, M. Andre, J. Weinreb, S.S. Luong, N. Piri, J.M. Kwong, D. Newman, and I. Kurtz. 2011. Severe neurologic impairment in mice with targeted disruption of the electrogenic sodium bicarbonate cotransporter NBCe2 (Slc4a5 gene). *The Journal of biological chemistry* 286:32563-32574.

Karran, E., M. Mercken, and B. De Strooper. 2011. The amyloid cascade hypothesis for Alzheimer's disease: an appraisal for the development of therapeutics. *Nature reviews. Drug discovery* 10:698-712.

Kastritsis, C.H., A.K. Salm, and K. McCarthy. 1992. Stimulation of the P2Y purinergic receptor on type 1 astroglia results in inositol phosphate formation and calcium mobilization. *Journal of neurochemistry* 58:1277-1284.

Kervezee, L., R. Hartman, D.J. van den Berg, S. Shimizu, Y. Emoto-Yamamoto, J.H. Meijer, and E.C. de Lange. 2014. Diurnal variation in P-glycoprotein-mediated transport and cerebrospinal fluid turnover in the brain. *The AAPS journal* 16:1029-1037.

Kettenmann, H., and A. Verkhratsky. 2011. [Neuroglia--living nerve glue]. *Fortschritte der Neurologie-Psychiatrie* 79:588-597.

Kim, K.J., J.A. Iddings, J.E. Stern, V.M. Blanco, D. Croom, S.A. Kirov, and J.A. Filosa. 2015. Astrocyte contributions to flow/pressure-evoked parenchymal arteriole vasoconstriction. *J Neurosci* 35:8245-8257.

Kishore, B.K., J.M. Terris, and M.A. Knepper. 1996. Quantitation of aquaporin-2 abundance in microdissected collecting ducts: axial distribution and control by AVP. *The American journal of physiology* 271:F62-70.

Kitchen, P., R.E. Day, L.H. Taylor, M.M. Salman, R.M. Bill, M.T. Conner, and A.C. Conner. 2015. Identification and Molecular Mechanisms of the Rapid Tonicity-induced Relocalization of the Aquaporin 4 Channel. *The Journal of biological chemistry* 290:16873-16881.

Konsman, J.P., V. Tridon, and R. Dantzer. 2000. Diffusion and action of intracerebroventricularly injected interleukin-1 in the CNS. *Neuroscience* 101:957-967.

Korogod, N., C.C. Petersen, and G.W. Knott. 2015. Ultrastructural analysis of adult mouse neocortex comparing aldehyde perfusion with cryo fixation. *eLife* 4:

Kress, B.T., J.J. Iliff, M. Xia, M. Wang, H.S. Wei, D. Zeppenfeld, L. Xie, H. Kang, Q. Xu, J.A. Liew, B.A. Plog, F. Ding, R. Deane, and M. Nedergaard. 2014. Impairment of paravascular clearance pathways in the aging brain. *Annals of neurology* 76:845-861.

Langer, J., N.J. Gerkau, A. Derouiche, C. Kleinhans, B. Moshrefi-Ravasdjani, M. Fredrich, K.W. Kafitz, G. Seifert, C. Steinhauser, and C.R. Rose. 2017. Rapid

sodium signaling couples glutamate uptake to breakdown of ATP in perivascular astrocyte endfeet. *Glia* 65:293-308.

Langfelder, P., and S. Horvath. 2008. WGCNA: an R package for weighted correlation network analysis. *BMC bioinformatics* 9:559.

Langfelder, P., and S. Horvath. 2012. Fast R Functions for Robust Correlations and Hierarchical Clustering. *Journal of statistical software* 46:

Lehmenkuhler, A., E. Sykova, J. Svoboda, K. Zilles, and C. Nicholson. 1993. Extracellular space parameters in the rat neocortex and subcortical white matter during postnatal development determined by diffusion analysis. *Neuroscience* 55:339-351.

Lehtinen, M.K., M.W. Zappaterra, X. Chen, Y.J. Yang, A.D. Hill, M. Lun, T. Maynard, D. Gonzalez, S. Kim, P. Ye, A.J. D'Ercole, E.T. Wong, A.S. LaMantia, and C.A. Walsh. 2011. The cerebrospinal fluid provides a proliferative niche for neural progenitor cells. *Neuron* 69:893-905.

Lennon, V.A., T.J. Kryzer, S.J. Pittock, A.S. Verkman, and S.R. Hinson. 2005. IgG marker of optic-spinal multiple sclerosis binds to the aquaporin-4 water channel. *The Journal of experimental medicine* 202:473-477.

Lennon, V.A., D.M. Wingerchuk, T.J. Kryzer, S.J. Pittock, C.F. Lucchinetti, K. Fujihara, I. Nakashima, and B.G. Weinshenker. 2004. A serum autoantibody marker of neuromyelitis optica: distinction from multiple sclerosis. *Lancet (London, England)* 364:2106-2112.

Li, J.Y., E. Englund, J.L. Holton, D. Soulet, P. Hagell, A.J. Lees, T. Lashley, N.P. Quinn, S. Rehncrona, A. Bjorklund, H. Widner, T. Revesz, O. Lindvall, and P. Brundin. 2008a. Lewy bodies in grafted neurons in subjects with Parkinson's disease suggest host-to-graft disease propagation. *Nature medicine* 14:501-503.

Li, Y., Y. Song, L. Zhao, G. Gaidosh, A.M. Laties, and R. Wen. 2008b. Direct labeling and visualization of blood vessels with lipophilic carbocyanine dye DiI. *Nature protocols* 3:1703-1708.

Liddelow, S.A., K.A. Guttenplan, L.E. Clarke, F.C. Bennett, C.J. Bohlen, L. Schirmer, M.L. Bennett, A.E. Munch, W.S. Chung, T.C. Peterson, D.K. Wilton, A. Frouin, B.A. Napier, N. Panicker, M. Kumar, M.S. Buckwalter, D.H. Rowitch, V.L. Dawson, T.M. Dawson, B. Stevens, and B.A. Barres. 2017. Neurotoxic reactive astrocytes are induced by activated microglia. *Nature* 541:481-487.

Lien, C.F., S.K. Mohanta, M. Frontczak-Baniewicz, J.D. Swinny, B. Zablocka, and D.C. Gorecki. 2012. Absence of glial alpha-dystrobrevin causes abnormalities of the blood-brain barrier and progressive brain edema. *The Journal of biological chemistry* 287:41374-41385.

Liu, L., V. Drouet, J.W. Wu, M.P. Witter, S.A. Small, C. Clelland, and K. Duff. 2012. Trans-synaptic spread of tau pathology in vivo. *PloS one* 7:e31302.

Longden, T.A., D.C. Hill-Eubanks, and M.T. Nelson. 2016. Ion channel networks in the control of cerebral blood flow. *J Cereb Blood Flow Metab* 36:492-512.

Louveau, A., I. Smirnov, T.J. Keyes, J.D. Eccles, S.J. Rouhani, J.D. Peske, N.C. Derecki, D. Castle, J.W. Mandell, K.S. Lee, T.H. Harris, and J. Kipnis. 2015. Structural and functional features of central nervous system lymphatic vessels. *Nature* 523:337-341.

Lu, D.C., Z. Zador, J. Yao, F. Fazlollahi, and G.T. Manley. 2011. Aquaporin-4 Reduces Post-Traumatic Seizure Susceptibility by Promoting Astrocytic Glial Scar Formation in Mice. *Journal of neurotrauma*

Lu, M., M.D. Lee, B.L. Smith, J.S. Jung, P. Agre, M.A. Verdijk, G. Merkx, J.P. Rijss, and P.M. Deen. 1996. The human AQP4 gene: definition of the locus encoding two water channel polypeptides in brain. *Proceedings of the National Academy of Sciences of the United States of America* 93:10908-10912.

Lucchinetti, C.F., B.F. Popescu, R.F. Bunyan, N.M. Moll, S.F. Roemer, H. Lassmann, W. Bruck, J.E. Parisi, B.W. Scheithauer, C. Giannini, S.D. Weigand, J. Mandrekar, and R.M. Ransohoff. 2011. Inflammatory cortical demyelination in early multiple sclerosis. *The New England journal of medicine* 365:2188-2197.

Luk, K.C., V. Kehm, J. Carroll, B. Zhang, P. O'Brien, J.Q. Trojanowski, and V.M. Lee. 2012a. Pathological alpha-synuclein transmission initiates Parkinson-like neurodegeneration in nontransgenic mice. *Science (New York, N.Y.)* 338:949-953.

Luk, K.C., V.M. Kehm, B. Zhang, P. O'Brien, J.Q. Trojanowski, and V.M. Lee. 2012b. Intracerebral inoculation of pathological alpha-synuclein initiates a rapidly progressive neurodegenerative alpha-synucleinopathy in mice. *The Journal of experimental medicine* 209:975-986.

Lunde, L.K., L.M. Camassa, E.H. Hoddevik, F.H. Khan, O.P. Ottersen, H.B. Boldt, and M. Amiry-Moghaddam. 2015. Postnatal development of the molecular complex underlying astrocyte polarization. *Brain structure & function* 220:2087-2101.

Lundgaard, I., M.L. Lu, E. Yang, W. Peng, H. Mestre, E. Hitomi, R. Deane, and M. Nedergaard. 2017. Glymphatic clearance controls state-dependent changes in brain lactate concentration. *J Cereb Blood Flow Metab* 37:2112-2124.

Ma, T., B. Yang, A. Gillespie, E.J. Carlson, C.J. Epstein, and A.S. Verkman. 1997. Generation and phenotype of a transgenic knockout mouse lacking the mercurial-insensitive water channel aquaporin-4. *J Clin Invest* 100:957-962.

Martin, K.R., R.L. Klein, and H.A. Quigley. 2002. Gene delivery to the eye using adeno-associated viral vectors. *Methods (San Diego, Calif.)* 28:267-275.

Masaki, H., Y. Wakayama, H. Hara, T. Jimi, A. Unaki, S. Iijima, H. Oniki, K. Nakano, K. Kishimoto, and Y. Hirayama. 2010. Immunocytochemical studies of aquaporin 4, Kir4.1, and alpha1-syntrophin in the astrocyte endfeet of mouse brain capillaries. *Acta histochemica et cytochemica* 43:99-105.

Masseguin, C., S. LePanse, B. Corman, J.M. Verbavatz, and J. Gabrion. 2005. Aging affects choroidal proteins involved in CSF production in Sprague-Dawley rats. *Neurobiol Aging* 26:917-927.

Mathiisen, T.M., K.P. Lehre, N.C. Danbolt, and O.P. Ottersen. 2010. The perivascular astroglial sheath provides a complete covering of the brain microvessels: an electron microscopic 3D reconstruction. *Glia* 58:1094-1103.

Mawuenyega, K.G., W. Sigurdson, V. Ovod, L. Munsell, T. Kasten, J.C. Morris, K.E. Yarasheski, and R.J. Bateman. 2010. Decreased clearance of CNS beta-amyloid in Alzheimer's disease. *Science (New York, N.Y.)* 330:1774.

McCandless, E.E., L. Piccio, B.M. Woerner, R.E. Schmidt, J.B. Rubin, A.H. Cross, and R.S. Klein. 2008. Pathological expression of CXCL12 at the blood-brain barrier correlates with severity of multiple sclerosis. *The American journal of pathology* 172:799-808.

McCandless, E.E., Q. Wang, B.M. Woerner, J.M. Harper, and R.S. Klein. 2006. CXCL12 limits inflammation by localizing mononuclear infiltrates to the perivascular space during experimental autoimmune encephalomyelitis. *Journal of immunology (Baltimore, Md. : 1950)* 177:8053-8064.

McCarthy, K.D., and J. de Vellis. 1980. Preparation of separate astroglial and oligodendroglial cell cultures from rat cerebral tissue. *The Journal of cell biology* 85:890-902.

McCaslin, A.F., B.R. Chen, A.J. Radosevich, B. Cauli, and E.M. Hillman. 2011. In vivo 3D morphology of astrocyte-vasculature interactions in the somatosensory cortex: implications for neurovascular coupling. *J Cereb Blood Flow Metab* 31:795-806.

McComb, J.G. 1983. Recent research into the nature of cerebrospinal fluid formation and absorption. *Journal of neurosurgery* 59:369-383.

Mestre, H., L.M. Hablitz, A.L. Xavier, W. Feng, W. Zou, T. Pu, H. Monai, G. Murlidharan, R.M. Castellanos Rivera, M.J. Simon, M.M. Pike, V. Pla, T. Du, B.T. Kress, X. Wang, B.A. Plog, A.S. Thrane, I. Lundgaard, Y. Abe, M. Yasui, J.H. Thomas, M. Xiao, H. Hirase, A. Asokan, J.J. Iliff, and M. Nedergaard. 2018a. Aquaporin-4-dependent glymphatic solute transport in the rodent brain. *eLife* 7:

Mestre, H., J. Tithof, T. Du, W. Sog, W. Peng, A. Sweeney, G. Olveda, J. Thomas, M. Nedergaard, and D.H. Kelley. 2018b. Flow of cerebrospinal fluid is driven by arterial pulsations and is reduced in hypertension. *(Submitted)*

Mestre, H., J. Tithof, T. Du, W. Song, W. Peng, A.M. Sweeney, G. Olveda, J.H. Thomas, M. Nedergaard, and D.H. Kelley. 2018c. Flow of cerebrospinal fluid is driven by arterial pulsations and is reduced in hypertension. *Nature communications* 9:4878.

Meyer, R.E., and R.E. Fish. 2005. A review of tribromoethanol anesthesia for production of genetically engineered mice and rats. *Lab animal* 34:47-52.

Michalak, M., and M. Opas. 1997. Functions of dystrophin and dystrophin associated proteins. *Current opinion in neurology* 10:436-442.

Millar, I.D., and P.D. Brown. 2008. NBCe2 exhibits a 3 HCO3(-):1 Na+ stoichiometry in mouse choroid plexus epithelial cells. *Biochemical and biophysical research communications* 373:550-554.

Miller, J.A., S.L. Ding, S.M. Sunkin, K.A. Smith, L. Ng, A. Szafer, A. Ebbert, Z.L. Riley, J.J. Royall, K. Aiona, J.M. Arnold, C. Bennet, D. Bertagnolli, K. Brouner, S. Butler, S. Caldejon, A. Carey, C. Cuhaciyan, R.A. Dalley, N. Dee, T.A. Dolbeare, B.A. Facer, D. Feng, T.P. Fliss, G. Gee, J. Goldy, L. Gourley, B.W. Gregor, G. Gu, R.E. Howard, J.M. Jochim, C.L. Kuan, C. Lau, C.K. Lee, F. Lee, T.A. Lemon, P. Lesnar, B. McMurray, N. Mastan, N. Mosqueda, T. Naluai-Cecchini, N.K. Ngo, J. Nyhus, A. Oldre, E. Olson, J. Parente, P.D. Parker, S.E. Parry, A. Stevens, M. Pletikos, M. Reding, K. Roll, D. Sandman, M. Sarreal, S. Shapouri, N.V. Shapovalova, E.H. Shen, N. Sjoquist, C.R. Slaughterbeck, M. Smith, A.J. Sodt, D. Williams, L. Zollei, B. Fischl, M.B. Gerstein, D.H. Geschwind, I.A. Glass, M.J. Hawrylycz, R.F. Hevner, H. Huang, A.R. Jones, J.A. Knowles, P. Levitt, J.W. Phillips, N. Sestan, P. Wohnoutka, C. Dang, A. Bernard, J.G. Hohmann, and E.S. Lein. 2014. Transcriptional landscape of the prenatal human brain. *Nature* 508:199-206.

Mirra, S.S., A. Heyman, D. McKeel, S.M. Sumi, B.J. Crain, L.M. Brownlee, F.S. Vogel, J.P. Hughes, G. van Belle, and L. Berg. 1991. The Consortium to Establish a Registry for Alzheimer's Disease (CERAD). Part II. Standardization of the neuropathologic assessment of Alzheimer's disease. *Neurology* 41:479-486.

Mishra, A., J.P. Reynolds, Y. Chen, A.V. Gourine, D.A. Rusakov, and D. Attwell. 2016. Astrocytes mediate neurovascular signaling to capillary pericytes but not to arterioles. *Nature neuroscience* 19:1619-1627.

Mitsuma, T., K. Tani, Y. Hiroaki, A. Kamegawa, H. Suzuki, H. Hibino, Y. Kurachi, and Y. Fujiyoshi. 2010. Influence of the cytoplasmic domains of aquaporin-4 on water conduction and array formation. *Journal of molecular biology* 402:669-681.

Moeller, H.B., R.A. Fenton, T. Zeuthen, and N. Macaulay. 2009. Vasopressin-dependent short-term regulation of aquaporin 4 expressed in Xenopus oocytes. *Neuroscience* 164:1674-1684.

Murlidharan, G., A. Crowther, R.A. Reardon, J. Song, and A. Asokan. 2016. Glymphatic fluid transport controls paravascular clearance of AAV vectors from the brain. *JCI insight* 1:e88034.

Musa-Aziz, R., L.M. Chen, M.F. Pelletier, and W.F. Boron. 2009. Relative CO2/NH3 selectivities of AQP1, AQP4, AQP5, AmtB, and RhAG. *Proceedings of the National Academy of Sciences of the United States of America* 106:5406-5411.

Nagelhus, E.A., and O.P. Ottersen. 2013. Physiological roles of aquaporin-4 in brain. *Physiol Rev* 93:1543-1562.

Nakamura, K., I. Kosugi, D.Y. Lee, A. Hafner, D.A. Sinclair, A. Ryo, and K.P. Lu. 2012. Prolyl isomerase Pin1 regulates neuronal differentiation via beta-catenin. *Molecular and cellular biology* 32:2966-2978.

Nedergaard, M. 2013. Neuroscience. Garbage truck of the brain. *Science (New York, N.Y.)* 340:1529-1530.

Nedergaard, M., B. Ransom, and S.A. Goldman. 2003. New roles for astrocytes: redefining the functional architecture of the brain. *Trends in neurosciences* 26:523-530.

Neely, J.D., M. Amiry-Moghaddam, O.P. Ottersen, S.C. Froehner, P. Agre, and M.E. Adams. 2001. Syntrophin-dependent expression and localization of Aquaporin-4 water channel protein. *Proceedings of the National Academy of Sciences of the United States of America* 98:14108-14113.

Neely, J.D., B.M. Christensen, S. Nielsen, and P. Agre. 1999. Heterotetrameric composition of aquaporin-4 water channels. *Biochemistry* 38:11156-11163.

Nicholson, C., and S. Hrabetova. 2017. Brain Extracellular Space: The Final Frontier of Neuroscience. *Biophysical journal* 113:2133-2142.

Nicholson, C., J.M. Phillips, and A.R. Gardner-Medwin. 1979. Diffusion from an iontophoretic point source in the brain: role of tortuosity and volume fraction. *Brain Res* 169:580-584.

Nico, B., A. Frigeri, G.P. Nicchia, P. Corsi, D. Ribatti, F. Quondamatteo, R. Herken, F. Girolamo, A. Marzullo, M. Svelto, and L. Roncali. 2003. Severe alterations of endothelial and glial cells in the blood-brain barrier of dystrophic mdx mice. *Glia* 42:235-251.

Nielsen, S., E.A. Nagelhus, M. Amiry-Moghaddam, C. Bourque, P. Agre, and O.P. Ottersen. 1997. Specialized membrane domains for water transport in glial cells:

high-resolution immunogold cytochemistry of aquaporin-4 in rat brain. *J Neurosci* 17:171-180.

Nielsen, S., B.L. Smith, E.I. Christensen, and P. Agre. 1993. Distribution of the aquaporin CHIP in secretory and resorptive epithelia and capillary endothelia. *Proceedings of the National Academy of Sciences of the United States of America* 90:7275-7279.

Nilsson, C., F. Stahlberg, C. Thomsen, O. Henriksen, M. Herning, and C. Owman. 1992. Circadian variation in human cerebrospinal fluid production measured by magnetic resonance imaging. *The American journal of physiology* 262:R20-24.

Noel, G., D.K. Tham, and H. Moukhles. 2009. Interdependence of laminin-mediated clustering of lipid rafts and the dystrophin complex in astrocytes. *The Journal of biological chemistry* 284:19694-19704.

Noell, S., P. Fallier-Becker, C. Beyer, S. Kroger, A.F. Mack, and H. Wolburg. 2007. Effects of agrin on the expression and distribution of the water channel protein aquaporin-4 and volume regulation in cultured astrocytes. *The European journal of neuroscience* 26:2109-2118.

Noell, S., P. Fallier-Becker, U. Deutsch, A.F. Mack, and H. Wolburg. 2009. Agrin defines polarized distribution of orthogonal arrays of particles in astrocytes. *Cell and tissue research* 337:185-195.

Noell, S., K. Wolburg-Buchholz, A.F. Mack, A.M. Beedle, J.S. Satz, K.P. Campbell, H. Wolburg, and P. Fallier-Becker. 2011. Evidence for a role of dystroglycan regulating the membrane architecture of astroglial endfeet. *The European journal of neuroscience* 33:2179-2186.

Nonaka, T., M. Masuda-Suzukake, T. Arai, Y. Hasegawa, H. Akatsu, T. Obi, M. Yoshida, S. Murayama, D.M. Mann, H. Akiyama, and M. Hasegawa. 2013. Prion-like properties of pathological TDP-43 aggregates from diseased brains. *Cell reports* 4:124-134.

Nordstrom, P., K. Michaelsson, Y. Gustafson, and A. Nordstrom. 2014. Traumatic brain injury and young onset dementia: a nationwide cohort study. *Annals of neurology* 75:374-381.

Numan, T., A.J.C. Slooter, A.W. van der Kooi, A.M.L. Hoekman, W.J.L. Suyker, C.J. Stam, and E. van Dellen. 2017. Functional connectivity and network analysis during hypoactive delirium and recovery from anesthesia. *Clinical neurophysiology : official journal of the International Federation of Clinical Neurophysiology* 128:914-924.

Oberheim, N.A., T. Takano, X. Han, W. He, J.H. Lin, F. Wang, Q. Xu, J.D. Wyatt, W. Pilcher, J.G. Ojemann, B.R. Ransom, S.A. Goldman, and M. Nedergaard. 2009. Uniquely hominid features of adult human astrocytes. *J Neurosci* 29:3276-3287.

Oh, S.W., J.A. Harris, L. Ng, B. Winslow, N. Cain, S. Mihalas, Q. Wang, C. Lau, L. Kuan, A.M. Henry, M.T. Mortrud, B. Ouellette, T.N. Nguyen, S.A. Sorensen, C.R. Slaughterbeck, W. Wakeman, Y. Li, D. Feng, A. Ho, E. Nicholas, K.E. Hirokawa, P. Bohn, K.M. Joines, H. Peng, M.J. Hawrylycz, J.W. Phillips, J.G. Hohmann, P. Wohnoutka, C.R. Gerfen, C. Koch, A. Bernard, C. Dang, A.R. Jones, and H. Zeng. 2014. A mesoscale connectome of the mouse brain. *Nature* 508:207-214.

Ohata, K., and A. Marmarou. 1992. Clearance of brain edema and macromolecules through the cortical extracellular space. *Journal of neurosurgery* 77:387-396.

Oshio, K., H. Watanabe, Y. Song, A.S. Verkman, and G.T. Manley. 2005. Reduced cerebrospinal fluid production and intracranial pressure in mice lacking choroid plexus water channel Aquaporin-1. *FASEB journal : official publication of the Federation of American Societies for Experimental Biology* 19:76-78.

Osterberg, V.R., K.J. Spinelli, L.J. Weston, K.C. Luk, R.L. Woltjer, and V.K. Unni. 2015. Progressive aggregation of alpha-synuclein and selective degeneration of lewy inclusion-bearing neurons in a mouse model of parkinsonism. *Cell reports* 10:1252-1260.

Palygin, O., U. Lalo, A. Verkhratsky, and Y. Pankratov. 2010. Ionotropic NMDA and P2X1/5 receptors mediate synaptically induced Ca2+ signalling in cortical astrocytes. *Cell calcium* 48:225-231.

Paredes, S., L. Cortinez, V. Contreras, and B. Silbert. 2016. Post-operative cognitive dysfunction at 3 months in adults after non-cardiac surgery: a qualitative systematic review. *Acta anaesthesiologica Scandinavica* 60:1043-1058.

Paresce, D.M., R.N. Ghosh, and F.R. Maxfield. 1996. Microglial cells internalize aggregates of the Alzheimer's disease amyloid beta-protein via a scavenger receptor. *Neuron* 17:553-565.

Pascale, C.L., M.C. Miller, C. Chiu, M. Boylan, I.N. Caralopoulos, L. Gonzalez, C.E. Johanson, and G.D. Silverberg. 2011. Amyloid-beta transporter expression at the blood-CSF barrier is age-dependent. *Fluids Barriers CNS* 8:21.

Patlak, C.S., and J.D. Fenstermacher. 1975. Measurements of dog blood-brain transfer constants by ventriculocisternal perfusion. *The American journal of physiology* 229:877-884.

Patterson, B.W., D.L. Elbert, K.G. Mawuenyega, T. Kasten, V. Ovod, S. Ma, C. Xiong, R. Chott, K. Yarasheski, W. Sigurdson, L. Zhang, A. Goate, T. Benzinger, J.C. Morris, D. Holtzman, and R.J. Bateman. 2015. Age and amyloid effects on human central nervous system amyloid-beta kinetics. *Annals of neurology* 78:439-453.

Peng, C., R.J. Gathagan, D.J. Covell, C. Medellin, A. Stieber, J.L. Robinson, B. Zhang, R.M. Pitkin, M.F. Olufemi, K.C. Luk, J.Q. Trojanowski, and V.M. Lee. 2018. Cellular milieu imparts distinct pathological alpha-synuclein strains in alpha-synucleinopathies. *Nature* 557:558-563.

Peng, W., T.M. Achariyar, B. Li, Y. Liao, H. Mestre, E. Hitomi, S. Regan, T. Kasper, S. Peng, F. Ding, H. Benveniste, M. Nedergaard, and R. Deane. 2016. Suppression of glymphatic fluid transport in a mouse model of Alzheimer's disease. *Neurobiology of disease* 93:215-225.

Pfefferbaum, A., D.H. Mathalon, E.V. Sullivan, J.M. Rawles, R.B. Zipursky, and K.O. Lim. 1994. A quantitative magnetic resonance imaging study of changes in brain morphology from infancy to late adulthood. *Archives of neurology* 51:874-887.

Picho, K., L.A. Maggio, and A.R. Artino, Jr. 2016. Science: the slow march of accumulating evidence. *Perspectives on medical education* 5:350-353.

Pixley, S.K., and J. de Vellis. 1984. Transition between immature radial glia and mature astrocytes studied with a monoclonal antibody to vimentin. *Brain Res* 317:201-209.

Pizzo, M.E., D.J. Wolak, N.N. Kumar, E. Brunette, C.L. Brunnquell, M.J. Hannocks, N.J. Abbott, M.E. Meyerand, L. Sorokin, D.B. Stanimirovic, and R.G. Thorne. 2018. Intrathecal antibody distribution in the rat brain: surface diffusion, perivascular transport and osmotic enhancement of delivery. *The Journal of physiology* 596:445-475.

Plassman, B.L., R.J. Havlik, D.C. Steffens, M.J. Helms, T.N. Newman, D. Drosdick, C. Phillips, B.A. Gau, K.A. Welsh-Bohmer, J.R. Burke, J.M. Guralnik, and J.C. Breitner. 2000. Documented head injury in early adulthood and risk of Alzheimer's disease and other dementias. *Neurology* 55:1158-1166.

Plog, B.A., M.L. Dashnaw, E. Hitomi, W. Peng, Y. Liao, N. Lou, R. Deane, and M. Nedergaard. 2015. Biomarkers of traumatic injury are transported from brain to blood via the glymphatic system. *J Neurosci* 35:518-526.

Plog, B.A., H. Mestre, G.E. Olveda, A.M. Sweeney, H.M. Kenney, A. Cove, K.Y. Dholakia, J. Tithof, T.D. Nevins, I. Lundgaard, T. Du, D.H. Kelley, and M. Nedergaard. 2018. Transcranial optical imaging reveals a pathway for optimizing the delivery of immunotherapeutics to the brain. *JCI insight* 3:

Pollay, M., and F. Curl. 1967. Secretion of cerebrospinal fluid by the ventricular ependyma of the rabbit. *The American journal of physiology* 213:1031-1038.

Pooler, A.M., E.C. Phillips, D.H. Lau, W. Noble, and D.P. Hanger. 2013. Physiological release of endogenous tau is stimulated by neuronal activity. *EMBO reports* 14:389-394.

Porter-Stransky, K.A., S.W. Centanni, S.L. Karne, L.M. Odil, S. Fekir, J.C. Wong, C. Jerome, H.A. Mitchell, A. Escayg, N.P. Pedersen, D.G. Winder, D.A. Mitrano, and D. Weinshenker. 2019. Noradrenergic Transmission at Alpha1-Adrenergic Receptors in the Ventral Periaqueductal Gray Modulates Arousal. *Biological psychiatry* 85:237-247.

Preston, J.E. 2001. Ageing choroid plexus-cerebrospinal fluid system. *Microscopy research and technique* 52:31-37.

Proescholdt, M.G., B. Hutto, L.S. Brady, and M. Herkenham. 2000. Studies of cerebrospinal fluid flow and penetration into brain following lateral ventricle and cisterna magna injections of the tracer [14C]inulin in rat. *Neuroscience* 95:577-592.

Rainey-Smith, S.R., G.N. Mazzucchelli, V.L. Villemagne, B.M. Brown, T. Porter, M. Weinborn, R.S. Bucks, L. Milicic, H.R. Sohrabi, K. Taddei, D. Ames, P. Maruff, C.L. Masters, C.C. Rowe, O. Salvado, R.N. Martins, and S.M. Laws. 2018. Genetic variation in Aquaporin-4 moderates the relationship between sleep and brain Abeta-amyloid burden. *Translational psychiatry* 8:47.

Rash, J.E., T. Yasumura, C.S. Hudson, P. Agre, and S. Nielsen. 1998. Direct immunogold labeling of aquaporin-4 in square arrays of astrocyte and ependymocyte plasma membranes in rat brain and spinal cord. *Proceedings of the National Academy of Sciences of the United States of America* 95:11981-11986.

Ratner, V., Y. Gao, H. Lee, R. Elkin, M. Nedergaard, H. Benveniste, and A. Tannenbaum. 2017. Cerebrospinal and interstitial fluid transport via the glymphatic pathway modeled by optimal mass transport. *NeuroImage* 152:530-537.

Ray, L., J.J. Iliff, and J.J. Heys. 2019. Analysis of convective and diffusive transport in the brain interstitium. *Fluids Barriers CNS* 16:6.

Reboldi, A., C. Coisne, D. Baumjohann, F. Benvenuto, D. Bottinelli, S. Lira, A. Uccelli, A. Lanzavecchia, B. Engelhardt, and F. Sallusto. 2009. C-C chemokine receptor 6-regulated entry of TH-17 cells into the CNS through the choroid plexus is required for the initiation of EAE. *Nature immunology* 10:514-523.

Recasens, A., B. Dehay, J. Bove, I. Carballo-Carbajal, S. Dovero, A. Perez-Villalba, P.O. Fernagut, J. Blesa, A. Parent, C. Perier, I. Farinas, J.A. Obeso, E. Bezard, and M. Vila. 2014. Lewy body extracts from Parkinson disease brains trigger alpha-synuclein pathology and neurodegeneration in mice and monkeys. *Annals of neurology* 75:351-362.

Reemst, K., S.C. Noctor, P.J. Lucassen, and E.M. Hol. 2016. The Indispensable Roles of Microglia and Astrocytes during Brain Development. *Frontiers in human neuroscience* 10:566.

Ren, H., C. Luo, Y. Feng, X. Yao, Z. Shi, F. Liang, J.X. Kang, J.B. Wan, Z. Pei, and H. Su. 2017. Omega-3 polyunsaturated fatty acids promote amyloid-beta clearance from the brain through mediating the function of the glymphatic system. *FASEB journal : official publication of the Federation of American Societies for Experimental Biology* 31:282-293.

Ren, Z., J.J. Iliff, L. Yang, J. Yang, X. Chen, M.J. Chen, R.N. Giese, B. Wang, X. Shi, and M. Nedergaard. 2013. 'Hit & Run' model of closed-skull traumatic brain injury (TBI) reveals complex patterns of post-traumatic AQP4 dysregulation. *J Cereb Blood Flow Metab* 33:834-845.

Rennels, M.L., O.R. Blaumanis, and P.A. Grady. 1990. Rapid solute transport throughout the brain via paravascular fluid pathways. *Advances in neurology* 52:431-439.

Rennels, M.L., T.F. Gregory, O.R. Blaumanis, K. Fujimoto, and P.A. Grady. 1985. Evidence for a 'paravascular' fluid circulation in the mammalian central nervous system, provided by the rapid distribution of tracer protein throughout the brain from the subarachnoid space. *Brain Res* 326:47-63.

Ribeiro Mde, C., L. Hirt, J. Bogousslavsky, L. Regli, and J. Badaut. 2006. Time course of aquaporin expression after transient focal cerebral ischemia in mice. *Journal of neuroscience research* 83:1231-1240.

Ringstad, G., S.A.S. Vatnehol, and P.K. Eide. 2017. Glymphatic MRI in idiopathic normal pressure hydrocephalus. *Brain* Epub ahead of print:

Ritchie, M.E., B. Phipson, D. Wu, Y. Hu, C.W. Law, W. Shi, and G.K. Smyth. 2015. limma powers differential expression analyses for RNA-sequencing and microarray studies. *Nucleic acids research* 43:e47.

Rodriguez, J.J., M. Olabarria, A. Chvatal, and A. Verkhratsky. 2009. Astroglia in dementia and Alzheimer's disease. *Cell death and differentiation* 16:378-385.

Roemer, S.F., J.E. Parisi, V.A. Lennon, E.E. Benarroch, H. Lassmann, W. Bruck, R.N. Mandler, B.G. Weinshenker, S.J. Pittock, D.M. Wingerchuk, and C.F. Lucchinetti. 2007. Pattern-specific loss of aquaporin-4 immunoreactivity distinguishes neuromyelitis optica from multiple sclerosis. *Brain* 130:1194-1205.

Rogers, J., R. Strohmeyer, C.J. Kovelowski, and R. Li. 2002. Microglia and inflammatory mechanisms in the clearance of amyloid beta peptide. *Glia* 40:260-269.

Roh, J.H., Y. Huang, A.W. Bero, T. Kasten, F.R. Stewart, R.J. Bateman, and D.M. Holtzman. 2012. Disruption of the sleep-wake cycle and diurnal fluctuation of β-amyloid in mice with Alzheimer's disease pathology. *Science translational medicine* 4:150ra122-150ra122.

Rosenberg, G.A., and W.T. Kyner. 1980. Gray and white matter brain-blood transfer constants by steady-state tissue clearance in cat. *Brain Res* 193:59-66.

Rosenberg, G.A., W.T. Kyner, and E. Estrada. 1980. Bulk flow of brain interstitial fluid under normal and hyperosmolar conditions. *The American journal of physiology* 238:F42-49.

Samuel, F., W.P. Flavin, S. Iqbal, C. Pacelli, S.D. Sri Renganathan, L.E. Trudeau, E.M. Campbell, P.E. Fraser, and A. Tandon. 2016. Effects of Serine 129 Phosphorylation on alpha-Synuclein Aggregation, Membrane Association, and Internalization. *The Journal of biological chemistry* 291:4374-4385.

Sapkota, D., A.M. Lake, W. Yang, C. Yang, H. Wesseling, A. Guise, C. Uncu, J.S. Dalal, A.W. Kraft, J.M. Lee, M.S. Sands, J.A. Steen, and J.D. Dougherty. 2019. Cell-Type-Specific Profiling of Alternative Translation Identifies Regulated Protein Isoform Variation in the Mouse Brain. *Cell reports* 26:594-607.e597.

Sauvageot, C.M., and C.D. Stiles. 2002. Molecular mechanisms controlling cortical gliogenesis. *Current opinion in neurobiology* 12:244-249.

Schindelin, J., I. Arganda-Carreras, E. Frise, V. Kaynig, M. Longair, T. Pietzsch, S. Preibisch, C. Rueden, S. Saalfeld, B. Schmid, J.Y. Tinevez, D.J. White, V. Hartenstein, K. Eliceiri, P. Tomancak, and A. Cardona. 2012. Fiji: an open-source platform for biological-image analysis. *Nature methods* 9:676-682.

Schley, D., R. Carare-Nnadi, C.P. Please, V.H. Perry, and R.O. Weller. 2006. Mechanisms to explain the reverse perivascular transport of solutes out of the brain. *Journal of theoretical biology* 238:962-974.

Schreiner, A.E., S. Durry, T. Aida, M.C. Stock, U. Ruther, K. Tanaka, C.R. Rose, and K.W. Kafitz. 2014. Laminar and subcellular heterogeneity of GLAST and GLT-1 immunoreactivity in the developing postnatal mouse hippocampus. *The Journal of comparative neurology* 522:204-224.

Schreiner, S.J., L.L. Imbach, E. Werth, R. Poryazova, H. Baumann-Vogel, P.O. Valko, T. Murer, D. Noain, and C.R. Baumann. 2019. Slow-wave sleep and motor progression in Parkinson disease. *Annals of neurology* 85:765-770.

Science, A.I.f.B. 2015. Allen Cell Types Database.

Semyanov, A. 2019. Spatiotemporal pattern of calcium activity in astrocytic network. *Cell calcium* 78:15-25.

Serrano-Pozo, A., M.P. Frosch, E. Masliah, and B.T. Hyman. 2011. Neuropathological alterations in Alzheimer disease. *Cold Spring Harbor perspectives in medicine* 1:a006189.

Sharma, H.S., J.A. Duncan, and C.E. Johanson. 2006. Whole-body hyperthermia in the rat disrupts the blood-cerebrospinal fluid barrier and induces brain edema. *Acta neurochirurgica. Supplement* 96:426-431.

Shimozawa, A., M. Ono, D. Takahara, A. Tarutani, S. Imura, M. Masuda-Suzukake, M. Higuchi, K. Yanai, S.I. Hisanaga, and M. Hasegawa. 2017. Propagation of pathological alpha-synuclein in marmoset brain. *Acta neuropathologica communications* 5:12.

Shokri-Kojori, E., G.J. Wang, C.E. Wiers, S.B. Demiral, M. Guo, S.W. Kim, E. Lindgren, V. Ramirez, A. Zehra, C. Freeman, G. Miller, P. Manza, T. Srivastava, S. De Santi, D. Tomasi, H. Benveniste, and N.D. Volkow. 2018. beta-Amyloid accumulation in the human brain after one night of sleep deprivation. *Proceedings of the National Academy of Sciences of the United States of America* 115:4483-4488.

Siler, D.A., J.A. Gonzalez, R.K. Wang, J.S. Cetas, and N.J. Alkayed. 2014. Intracisternal administration of tissue plasminogen activator improves cerebrospinal fluid flow and cortical perfusion after subarachnoid hemorrhage in mice. *Translational stroke research* 5:227-237.

Silverberg, G.D., G. Heit, S. Huhn, R.A. Jaffe, S.D. Chang, H. Bronte-Stewart, E. Rubenstein, K. Possin, and T.A. Saul. 2001. The cerebrospinal fluid production rate is reduced in dementia of the Alzheimer's type. *Neurology* 57:1763-1766.

Simon, M.J., and J.J. Iliff. 2016. Regulation of cerebrospinal fluid (CSF) flow in neurodegenerative, neurovascular and neuroinflammatory disease. *Biochim Biophys Acta* 1862:442-451.

Simon, M.J., C. Murchison, and J.J. Iliff. 2017. A transcriptome-based assessment of the astrocytic dystrophin-associated complex in the developing human brain. *Journal of neuroscience research*

Simon, M.J., M.X. Wang, C.F. Murchison, N.E. Roese, E.L. Boespflug, R.L. Woltjer, and J.J. Iliff. 2018. Transcriptional network analysis of human astrocytic endfoot genes reveals region-specific associations with dementia status and tau pathology. *Sci Rep* 8:12389.

Skoff, R.P. 1990. Gliogenesis in rat optic nerve: astrocytes are generated in a single wave before oligodendrocytes. *Developmental biology* 139:149-168.

Smith, A.J., T. Duan, and A.S. Verkman. 2019. Aquaporin-4 reduces neuropathology in a mouse model of Alzheimer’s disease by remodeling peri-plaque astrocyte structure. *Acta neuropathologica communications* 7:74.

Smith, A.J., B.J. Jin, and A.S. Verkman. 2015. Muddying the water in brain edema? *Trends in neurosciences* 38:331-332.

Smith, A.J., and A.S. Verkman. 2018. The "glymphatic" mechanism for solute clearance in Alzheimer's disease: game changer or unproven speculation? *FASEB journal : official publication of the Federation of American Societies for Experimental Biology* 32:543-551.

Smith, A.J., X. Yao, J.A. Dix, B.J. Jin, and A.S. Verkman. 2017. Test of the 'glymphatic' hypothesis demonstrates diffusive and aquaporin-4-independent solute transport in rodent brain parenchyma. *eLife* 6:

Smith, D.H., V.E. Johnson, and W. Stewart. 2013. Chronic neuropathologies of single and repetitive TBI: substrates of dementia? *Nature reviews. Neurology* 9:211-221.

Sohet, F., C. Lin, R.N. Munji, S.Y. Lee, N. Ruderisch, A. Soung, T.D. Arnold, N. Derugin, Z.S. Vexler, F.T. Yen, and R. Daneman. 2015. LSR/angulin-1 is a tricellular tight junction protein involved in blood-brain barrier formation. *The Journal of cell biology* 208:703-711.

Spector, R. 1989. Micronutrient homeostasis in mammalian brain and cerebrospinal fluid. *Journal of neurochemistry* 53:1667-1674.

Stohr, J., J.C. Watts, Z.L. Mensinger, A. Oehler, S.K. Grillo, S.J. DeArmond, S.B. Prusiner, and K. Giles. 2012. Purified and synthetic Alzheimer's amyloid beta (Abeta) prions. *Proceedings of the National Academy of Sciences of the United States of America* 109:11025-11030.

Stokum, J.A., D.B. Kurland, V. Gerzanich, and J.M. Simard. 2015. Mechanisms of astrocyte-mediated cerebral edema. *Neurochemical research* 40:317-328.

Su, X., Z.T. Meng, X.H. Wu, F. Cui, H.L. Li, D.X. Wang, X. Zhu, S.N. Zhu, M. Maze, and D. Ma. 2016. Dexmedetomidine for prevention of delirium in elderly patients after non-cardiac surgery: a randomised, double-blind, placebo-controlled trial. *Lancet (London, England)* 388:1893-1902.

Sun, H., R. Liang, B. Yang, Y. Zhou, M. Liu, F. Fang, J. Ding, Y. Fan, and G. Hu. 2016. Aquaporin-4 mediates communication between astrocyte and microglia: Implications of neuroinflammation in experimental Parkinson's disease. *Neuroscience* 317:65-75.

Surmeier, D.J., J.A. Obeso, and G.M. Halliday. 2017. Selective neuronal vulnerability in Parkinson disease. *Nature reviews. Neuroscience* 18:101-113.

Suzuki, H., K. Nishikawa, Y. Hiroaki, and Y. Fujiyoshi. 2008. Formation of aquaporin-4 arrays is inhibited by palmitoylation of N-terminal cysteine residues. *Biochim Biophys Acta* 1778:1181-1189.

Sykova, E. 2005. Glia and volume transmission during physiological and pathological states. *Journal of neural transmission (Vienna, Austria : 1996)* 112:137-147.

Sykova, E., and C. Nicholson. 2008. Diffusion in brain extracellular space. *Physiol Rev* 88:1277-1340.

Szabo, A., V. Jancsik, D. Mornet, and M. Kalman. 2004. Immunofluorescence mapping of dystrophin in the rat brain: astrocytes contain the splice variant Dp71f, but this is confined to subpopulations. *Anatomy and embryology* 208:463-477.

Szentistvanyi, I., C.S. Patlak, R.A. Ellis, and H.F. Cserr. 1984. Drainage of interstitial fluid from different regions of rat brain. *The American journal of physiology* 246:F835-844.

Tani, K., T. Mitsuma, Y. Hiroaki, A. Kamegawa, K. Nishikawa, Y. Tanimura, and Y. Fujiyoshi. 2009. Mechanism of aquaporin-4's fast and highly selective water conduction and proton exclusion. *Journal of molecular biology* 389:694-706.

Team, R.C. 2014. R: A Language and Environment for Statistical Computing.

Teng, Z., Wang, A, Wang, P, Wang, R, Wang, W, Han, H. 2018. The effect of aquaporin-4 knockout on interstitial fluid flow and the structure of the extracellular space in the deep brain. *Aging and Disease* 9:

Thrane, A.S., V. Rangroo Thrane, and M. Nedergaard. 2014. Drowning stars: reassessing the role of astrocytes in brain edema. *Trends in neurosciences* 37:620-628.

Thrane, A.S., V. Rangroo Thrane, B.A. Plog, and M. Nedergaard. 2015. Filtering the muddied waters of brain edema. *Trends in neurosciences* 38:333-335.

Thrane, A.S., P.M. Rappold, T. Fujita, A. Torres, L.K. Bekar, T. Takano, W. Peng, F. Wang, V. Rangroo Thrane, R. Enger, N.N. Haj-Yasein, O. Skare, T. Holen, A. Klungland, O.P. Ottersen, M. Nedergaard, and E.A. Nagelhus. 2011. Critical role of aquaporin-4 (AQP4) in astrocytic Ca2+ signaling events elicited by cerebral edema. *Proceedings of the National Academy of Sciences of the United States of America* 108:846-851.

Thrane, A.S., T. Takano, V. Rangroo Thrane, F. Wang, W. Peng, O.P. Ottersen, M. Nedergaard, and E.A. Nagelhus. 2013. In vivo NADH fluorescence imaging indicates effect of aquaporin-4 deletion on oxygen microdistribution in cortical spreading depression. *J Cereb Blood Flow Metab* 33:996-999.

Tien, A.C., H.H. Tsai, A.V. Molofsky, M. McMahon, L.C. Foo, A. Kaul, J.D. Dougherty, N. Heintz, D.H. Gutmann, B.A. Barres, and D.H. Rowitch. 2012. Regulated temporal-spatial astrocyte precursor cell proliferation involves BRAF signalling in mammalian spinal cord. *Development (Cambridge, England)* 139:2477-2487.

Tonnesen, J., V. Inavalli, and U.V. Nagerl. 2018. Super-Resolution Imaging of the Extracellular Space in Living Brain Tissue. *Cell* 172:1108-1121 e1115.

Tritsch, N.X., and D.E. Bergles. 2007. Defining the role of astrocytes in neuromodulation. *Neuron* 54:497-500.

Valdinocci, D., R.A. Radford, S.M. Siow, R.S. Chung, and D.L. Pountney. 2017. Potential Modes of Intercellular alpha-Synuclein Transmission. *Int J Mol Sci* 18:

van Raaij, M.E., J. van Gestel, I.M. Segers-Nolten, S.W. de Leeuw, and V. Subramaniam. 2008. Concentration dependence of alpha-synuclein fibril length assessed by quantitative atomic force microscopy and statistical-mechanical theory. *Biophysical journal* 95:4871-4878.

Verbavatz, J.M., T. Ma, R. Gobin, and A.S. Verkman. 1997. Absence of orthogonal arrays in kidney, brain and muscle from transgenic knockout mice lacking water channel aquaporin-4. *Journal of cell science* 110 (Pt 22):2855-2860.

Verkman, A.S., J. Ratelade, A. Rossi, H. Zhang, and L. Tradtrantip. 2011. Aquaporin-4: orthogonal array assembly, CNS functions, and role in neuromyelitis optica. *Acta pharmacologica Sinica* 32:702-710.

Verkman, A.S., L. Tradtrantip, A.J. Smith, and X. Yao. 2017. Aquaporin Water Channels and Hydrocephalus. *Pediatric neurosurgery* 52:409-416.

Vernadakis, A., and D.M. Woodbury. 1962. Electrolyte and amino acid changes in rat brain during maturation. *The American journal of physiology* 203:748-752.

Vindedal, G.F., A.E. Thoren, V. Jensen, A. Klungland, Y. Zhang, M.J. Holtzman, O.P. Ottersen, and E.A. Nagelhus. 2016. Removal of aquaporin-4 from glial and ependymal membranes causes brain water accumulation. *Mol Cell Neurosci* 77:47-52.

Vinters, H.V., W.G. Ellis, C. Zarow, B.W. Zaias, W.J. Jagust, W.J. Mack, and H.C. Chui. 2000. Neuropathologic substrates of ischemic vascular dementia. *Journal of neuropathology and experimental neurology* 59:931-945.

Virchow, R. 1855. Ein Fall von progressiver Muskelatrophie. *Archiv für pathologische Anatomie und Physiologie und für klinische Medicin* 8:537-540.

Volpicelli-Daley, L.A., K.C. Luk, T.P. Patel, S.A. Tanik, D.M. Riddle, A. Stieber, D.F. Meaney, J.Q. Trojanowski, and V.M. Lee. 2011. Exogenous alpha-synuclein fibrils induce Lewy body pathology leading to synaptic dysfunction and neuron death. *Neuron* 72:57-71.

von Holstein-Rathlou, S., N.C. Petersen, and M. Nedergaard. 2018. Voluntary running enhances glymphatic influx in awake behaving, young mice. *Neuroscience letters* 662:253-258.

Vorisek, I., and E. Sykova. 1997. Evolution of anisotropic diffusion in the developing rat corpus callosum. *Journal of neurophysiology* 78:912-919.

Walsh, D.M., and D.J. Selkoe. 2016. A critical appraisal of the pathogenic protein spread hypothesis of neurodegeneration. *Nature reviews. Neuroscience* 17:251-260.

Walz, T., Y. Fujiyoshi, and A. Engel. 2009. The AQP structure and functional implications. *Handbook of experimental pharmacology* 31-56.

Wang, H., B. Wang, K.P. Normoyle, K. Jackson, K. Spitler, M.F. Sharrock, C.M. Miller, C. Best, D. Llano, and R. Du. 2014. Brain temperature and its fundamental properties: a review for clinical neuroscientists. *Frontiers in neuroscience* 8:307.

Wang, M., F. Ding, S. Deng, X. Guo, W. Wang, J.J. Iliff, and M. Nedergaard. 2017. Focal Solute Trapping and Global Glymphatic Pathway Impairment in a Murine Model of Multiple Microinfarcts. *J Neurosci* 37:2870-2877.

Wang, M., J.J. Iliff, Y. Liao, M.J. Chen, M.S. Shinseki, A. Venkataraman, J. Cheung, W. Wang, and M. Nedergaard. 2012. Cognitive deficits and delayed neuronal loss in a mouse model of multiple microinfarcts. *J Neurosci* 32:17948-17960.

Wang, P., and W.L. Olbricht. 2011. Fluid mechanics in the perivascular space. *Journal of theoretical biology* 274:52-57.

Welch, K. 1963. SECRETION OF CEREBROSPINAL FLUID BY CHOROID PLEXUS OF THE RABBIT. *The American journal of physiology* 205:617-624.

Weller, R.O., E. Djuanda, H.Y. Yow, and R.O. Carare. 2009. Lymphatic drainage of the brain and the pathophysiology of neurological disease. *Acta neuropathologica* 117:1-14.

Wen, H., E.A. Nagelhus, M. Amiry-Moghaddam, P. Agre, O.P. Ottersen, and S. Nielsen. 1999. Ontogeny of water transport in rat brain: postnatal expression of the aquaporin-4 water channel. *The European journal of neuroscience* 11:935-945.

Whiting, J.L., L. Ogier, K.A. Forbush, P. Bucko, J. Gopalan, O.M. Seternes, L.K. Langeberg, and J.D. Scott. 2016. AKAP220 manages apical actin networks that coordinate aquaporin-2 location and renal water reabsorption. *Proceedings of the National Academy of Sciences of the United States of America* 113:E4328-4337.

Wilcock, D.M., M.P. Vitek, and C.A. Colton. 2009. Vascular amyloid alters astrocytic water and potassium channels in mouse models and humans with Alzheimer's disease. *Neuroscience* 159:1055-1069.

Williams, K., X. Alvarez, and A.A. Lackner. 2001. Central nervous system perivascular cells are immunoregulatory cells that connect the CNS with the peripheral immune system. *Glia* 36:156-164.

Willis, M., W.A. Kaufmann, G. Wietzorrek, B. Hutter-Paier, S. Moosmang, C. Humpel, F. Hofmann, M. Windisch, H.G. Knaus, and J. Marksteiner. 2010. L-type calcium channel CaV 1.2 in transgenic mice overexpressing human AbetaPP751 with the London (V717I) and Swedish (K670M/N671L) mutations. *Journal of Alzheimer's disease : JAD* 20:1167-1180.

Wolburg-Buchholz, K., A.F. Mack, E. Steiner, F. Pfeiffer, B. Engelhardt, and H. Wolburg. 2009. Loss of astrocyte polarity marks blood-brain barrier impairment during experimental autoimmune encephalomyelitis. *Acta neuropathologica* 118:219-233.

Wolburg, H., K. Wolburg-Buchholz, P. Fallier-Becker, S. Noell, and A.F. Mack. 2011. Structure and functions of aquaporin-4-based orthogonal arrays of particles. *International review of cell and molecular biology* 287:1-41.

Wolburg, H., K. Wolburg-Buchholz, S. Liebner, and B. Engelhardt. 2001. Claudin-1, claudin-2 and claudin-11 are present in tight junctions of choroid plexus epithelium of the mouse. *Neuroscience letters* 307:77-80.

Wosik, K., R. Cayrol, A. Dodelet-Devillers, F. Berthelet, M. Bernard, R. Moumdjian, A. Bouthillier, T.L. Reudelhuber, and A. Prat. 2007. Angiotensin II controls occludin function and is required for blood brain barrier maintenance: relevance to multiple sclerosis. *J Neurosci* 27:9032-9042.

Wu, Y.W., S. Gordleeva, X. Tang, P.Y. Shih, Y. Dembitskaya, and A. Semyanov. 2019. Morphological profile determines the frequency of spontaneous calcium events in astrocytic processes. *Glia* 67:246-262.

Wu, Z.Q., D. Li, Y. Huang, X.P. Chen, W. Huang, C.F. Liu, H.Q. Zhao, R.X. Xu, M. Cheng, M. Schachner, and Q.H. Ma. 2016. Caspr Controls the Temporal Specification of Neural Progenitor Cells through Notch Signaling in the Developing Mouse Cerebral Cortex. *Cerebral cortex (New York, N.Y. : 1991)*

Wyss-Coray, T., J.D. Loike, T.C. Brionne, E. Lu, R. Anankov, F. Yan, S.C. Silverstein, and J. Husemann. 2003. Adult mouse astrocytes degrade amyloid-beta in vitro and in situ. *Nature medicine* 9:453-457.

Xavier, A.L.R., N.L. Hauglund, S. von Holstein-Rathlou, Q. Li, S. Sanggaard, N. Lou, I. Lundgaard, and M. Nedergaard. 2018. Cannula Implantation into the Cisterna Magna of Rodents. *J Vis Exp*

Xie, L., H. Kang, Q. Xu, M.J. Chen, Y. Liao, M. Thiyagarajan, J. O'Donnell, D.J. Christensen, C. Nicholson, J.J. Iliff, T. Takano, R. Deane, and M. Nedergaard. 2013. Sleep drives metabolite clearance from the adult brain. *Science (New York, N.Y.)* 342:373-377.

Xu, Z., N. Xiao, Y. Chen, H. Huang, C. Marshall, J. Gao, Z. Cai, T. Wu, G. Hu, and M. Xiao. 2015. Deletion of aquaporin-4 in APP/PS1 mice exacerbates brain Abeta accumulation and memory deficits. *Mol Neurodegener* 10:58.

Yamada, K., J.K. Holth, F. Liao, F.R. Stewart, T.E. Mahan, H. Jiang, J.R. Cirrito, T.K. Patel, K. Hochgrafe, E.M. Mandelkow, and D.M. Holtzman. 2014. Neuronal activity regulates extracellular tau in vivo. *The Journal of experimental medicine* 211:387-393.

Yamada, S., M. Miyazaki, Y. Yamashita, C. Ouyang, M. Yui, M. Nakahashi, S. Shimizu, I. Aoki, Y. Morohoshi, and J.G. McComb. 2013. Influence of respiration on cerebrospinal fluid movement using magnetic resonance spin labeling. *Fluids Barriers CNS* 10:36.

Yang, J., L.K. Lunde, P. Nuntagij, T. Oguchi, L.M. Camassa, L.N. Nilsson, L. Lannfelt, Y. Xu, M. Amiry-Moghaddam, O.P. Ottersen, and R. Torp. 2011. Loss of astrocyte polarization in the tg-ArcSwe mouse model of Alzheimer's disease. *Journal of Alzheimer's disease : JAD* 27:711-722.

Yang, L., B.T. Kress, H.J. Weber, M. Thiyagarajan, B. Wang, R. Deane, H. Benveniste, J.J. Iliff, and M. Nedergaard. 2013. Evaluating glymphatic pathway function utilizing clinically relevant intrathecal infusion of CSF tracer. *Journal of translational medicine* 11:107.

Yao, X., S. Hrabetova, C. Nicholson, and G.T. Manley. 2008. Aquaporin-4-deficient mice have increased extracellular space without tortuosity change. *J Neurosci* 28:5460-5464.

Yin, M., T. Pu, L. Wang, C. Marshall, T. Wu, and M. Xiao. 2018. Astroglial water channel aquaporin 4-mediated glymphatic clearance function: A determined factor for time-sensitive treatment of aerobic exercise in patients with Alzheimer's disease. *Medical hypotheses* 119:18-21.

Zeisel, A., H. Hochgerner, P. Lonnerberg, A. Johnsson, F. Memic, J. van der Zwan, M. Haring, E. Braun, L.E. Borm, G. La Manno, S. Codeluppi, A. Furlan, K. Lee, N. Skene, K.D. Harris, J. Hjerling-Leffler, E. Arenas, P. Ernfors, U. Marklund, and S. Linnarsson. 2018. Molecular Architecture of the Mouse Nervous System. *Cell* 174:999-1014.e1022.

Zeppenfeld, D.M., M. Simon, J.D. Haswell, D. D'Abreo, C. Murchison, J.F. Quinn, M.R. Grafe, R.L. Woltjer, J. Kaye, and J.J. Iliff. 2017. Association of Perivascular Localization of Aquaporin-4 With Cognition and Alzheimer Disease in Aging Brains. *JAMA neurology* 74:91-99.

Zhang, B., and S. Horvath. 2005. A general framework for weighted gene co-expression network analysis. *Statistical applications in genetics and molecular biology* 4:Article17.

Zhang, E.T., C.B. Inman, and R.O. Weller. 1990. Interrelationships of the pia mater and the perivascular (Virchow-Robin) spaces in the human cerebrum. *Journal of anatomy* 170:111-123.

Zhang, Y., K. Chen, S.A. Sloan, M.L. Bennett, A.R. Scholze, S. O'Keeffe, H.P. Phatnani, P. Guarnieri, C. Caneda, N. Ruderisch, S. Deng, S.A. Liddelow, C. Zhang, R. Daneman, T. Maniatis, B.A. Barres, and J.Q. Wu. 2014. An RNA-sequencing transcriptome and splicing database of glia, neurons, and vascular cells of the cerebral cortex. *J Neurosci* 34:11929-11947.

Zhang, Y., S.A. Sloan, L.E. Clarke, C. Caneda, C.A. Plaza, P.D. Blumenthal, H. Vogel, G.K. Steinberg, M.S. Edwards, G. Li, J.A. Duncan, 3rd, S.H. Cheshier, L.M. Shuer, E.F. Chang, G.A. Grant, M.G. Gephart, and B.A. Barres. 2016. Purification and Characterization of Progenitor and Mature Human Astrocytes Reveals Transcriptional and Functional Differences with Mouse. *Neuron* 89:37-53.

Zhao, R., S.H. Min, Y. Wang, E. Campanella, P.S. Low, and I.D. Goldman. 2009. A role for the proton-coupled folate transporter (PCFT-SLC46A1) in folate receptor-mediated endocytosis. *The Journal of biological chemistry* 284:4267-4274.

Zhao, Z.A., P. Li, S.Y. Ye, Y.L. Ning, H. Wang, Y. Peng, N. Yang, Y. Zhao, Z.H. Zhang, J.F. Chen, and Y.G. Zhou. 2017. Perivascular AQP4 dysregulation in the hippocampal CA1 area after traumatic brain injury is alleviated by adenosine A2A receptor inactivation. *Sci Rep* 7:2254.

Zhu, L., A. Malatras, M. Thorley, I. Aghoghogbe, A. Mer, S. Duguez, G. Butler-Browne, T. Voit, and W. Duddy. 2015. CellWhere: graphical display of interaction networks organized on subcellular localizations. *Nucleic acids research* 43:W571-575.

Zolotukhin, S., B.J. Byrne, E. Mason, I. Zolotukhin, M. Potter, K. Chesnut, C. Summerford, R.J. Samulski, and N. Muzyczka. 1999. Recombinant adeno-associated virus purification using novel methods improves infectious titer and yield. *Gene therapy* 6:973-985.

Zou, W., T. Pu, W. Feng, M. Lu, Y. Zheng, R. Du, M. Xiao, and G. Hu. 2019. Blocking meningeal lymphatic drainage aggravates Parkinson's disease-like pathology in mice overexpressing mutated alpha-synuclein. *Translational neurodegeneration* 8:7.